
Strongly Coupled Models at the LHC

Dissertation

zur Erlangung des Doktorgrades
an der Fakultät für Mathematik,
Informatik und Naturwissenschaften
Fachbereich Physik
der Universität Hamburg

vorgelegt von

MAIKEL DE VRIES

aus

STADSKANAAL, DEN NIEDERLANDEN

Hamburg

2014

Gutachter/in der Dissertation:	Dr. Andreas Weiler Prof. Dr. Gudrid Moortgat-Pick
Gutachter/in der Disputation:	Dr. Jürgen Reuter Jun.-Prof. Dr. Christian Sander Prof. Dr. Sven-Olaf Moch
Datum der Disputation:	15. Oktober 2014
Vorsitzender des Prüfungsausschusses:	Prof. Dr. Dieter Horns
Vorsitzende des Promotionsausschusses:	Prof. Dr. Daniela Pfannkuche
Dekan des Fachbereichs Physik:	Prof. Dr. Heinrich Graener

Abstract

In this thesis strongly coupled models where the Higgs boson is composite are discussed. These models provide an explanation for the origin of electroweak symmetry breaking including a solution for the hierarchy problem. Strongly coupled models provide an alternative to the weakly coupled supersymmetric extensions of the Standard Model and lead to different and interesting phenomenology at the Large Hadron Collider (LHC). This thesis discusses two particular strongly coupled models, a composite Higgs model with partial compositeness and the Littlest Higgs model with T-parity — a composite model with collective symmetry breaking. The phenomenology relevant for the LHC is covered and the applicability of effective operators for these types of strongly coupled models is explored.

First, a composite Higgs model with partial compositeness is discussed. In this model right-handed light quarks could be significantly composite, yet compatible with experimental searches at the LHC and precision tests on Standard Model couplings. In these scenarios, which are motivated by flavour physics, large cross sections for the production of new resonances coupling to light quarks are expected. Experimental signatures of right-handed compositeness at the LHC are studied, and constraints on the parameter space of these models are derived using recent results by ATLAS and CMS. Furthermore, dedicated searches for multi-jet signals at the LHC are proposed which could significantly improve the sensitivity to signatures of right-handed compositeness.

The Littlest Higgs model with T-parity, providing an attractive solution to the fine-tuning problem, is discussed next. This solution is only natural if its intrinsic symmetry breaking scale f is relatively close to the electroweak scale. The constraints from the latest results of the 8 TeV run at the LHC are examined. The model's parameter space is being excluded based on a combination of electroweak precision observables, Higgs precision physics and direct searches at the LHC. These tests provide stringent limits on f and the parameter space is slowly driven into the TeV range. Furthermore, a strategy on how to optimise present supersymmetry searches for the Littlest Higgs model with T-parity is presented, with the goal to improve the constraints and yield more stringent limits on f .

Finally, the robustness of translating effective operator constraints to beyond the Standard Model (BSM) theories is treated and turns out to crucially depend on the mass and coupling of BSM particles. This is especially relevant for hadron colliders where the partonic centre of mass energy is around the typical energy scales of natural BSM theories. The caveats in applying limits from effective operators are discussed using Z' and G' models, illustrating the effects for a large class of models. This analysis shows that the applicability of effective operators mainly depends on the ratio of the transfer energy in the events and the mass scale of the full theory. Moreover, based on these results a method is developed to recast existing experimental limits on effective operators to the full theory parameter space.

It is concluded that strongly coupled models of electroweak symmetry breaking are still natural and compatible with LHC results. Moreover, these types of models provide new and interesting final state topologies for experimental searches at the LHC. For the high energy runs of the LHC these new searches will prove useful in determining the faith of composite models and maybe thereby the origin of electroweak symmetry breaking.

Zusammenfassung

In dieser Dissertation werden stark gekoppelte Modelle diskutiert, in denen das Higgs Boson kein elementares Teilchen ist, sondern zusammengesetzt ist. Diese Modelle liefern eine Erklärung für den Ursprung der elektroschwachen Symmetriebrechung, sowie eine Lösung des Hierarchieproblems. Stark gekoppelte Modelle stellen eine Alternative für schwach gekoppelte supersymmetrische Erweiterungen des Standardmodells dar und führen zu unterschiedlicher und interessanter Phänomenologie am Large Hadron Collider (LHC). In dieser Dissertation werden zwei bestimmte stark gekoppelte Modelle diskutiert, ein zusammengesetztes Higgs Modell mit partieller Zusammensetzung und das Littlest Higgs Modell mit T-Parität — ein zusammengesetztes Modell mit kollektiver Symmetriebrechung. Die Phänomenologie für den LHC wird in dieser Dissertation beschrieben und mit einem detaillierten Bericht über die Anwendbarkeit von effektiven Operatoren für diese Art von stark gekoppelten Modellen abgeschlossen.

Zuerst wird ein zusammengesetztes Higgs Modell mit partieller Zusammensetzung diskutiert. In diesem Modell können rechtshändige leichte Quarks signifikant zusammengesetzt sein, was dennoch kompatibel mit experimentellen Ergebnissen am LHC und mit Präzisionstests der Standardmodellkopplungen ist. In diesen Szenarien, welche ihre Motivation in der Flavourphysik haben, werden hohe Produktionswirkungsquerschnitte für neue Resonanzen erwartet, welche an leichte Quarks ankoppeln. Experimentelle Signaturen von rechtshändiger Zusammensetzung am LHC werden untersucht und Beschränkungen des Parameterraums dieser Modelle werden aus den neuesten Resultaten von ATLAS und CMS abgeleitet. Die Sensitivität des LHCs könnte durch gezielte Untersuchungen, insbesondere von Multi-Jet-Signalen, deutlich verbessert werden.

Das Littlest Higgs Modell mit T-Parität, welches eine attraktive Lösung des Hierarchieproblems liefert, wird danach diskutiert. Diese Lösung ist nur dann natürlich, wenn die intrinsische Symmetriebrechungsskala f relativ nahe an der elektroschwachen Skala liegt. Die Beschränkungen der neuesten Resultate des 8 TeV Durchlaufs am LHC wurden untersucht. Der Parameterraum des Modells wird, basierend auf einer Kombination aus elektroschwachen Präzisionsobservablen, Higgs Präzisionsphysik und direkten Untersuchungen am LHC, eingeschränkt. Diese Tests liefern stringente Grenzen für f und der Parameterraum wird langsam in das TeV Regime verschoben. Außerdem wird eine Strategie für das Optimieren von vorhandenen Supersymmetrie-Untersuchungen für das Littlest Higgs Modell mit T-Parität vorgestellt, mit dem Ziel der Verbesserung der Einschränkungen an den Parameterraum und der Erhöhung der Grenzen für f .

Schlussendlich wird die Robustheit der Anwendung von Beschränkungen durch effektive Operatoren auf Theorien jenseits des Standardmodells behandelt, was kritisch von der Masse und Kopplung des Teilchens abhängt. Dies ist besonders relevant für Hadronen-Beschleuniger, wo die partonische Schwerpunktsenergie sich um die typischen Energien von Theorien jenseits des Standardmodells befindet. Die Probleme der Anwendung von Grenzen durch effektive Operatoren werden für Z' und G' Modelle diskutiert, welche die Effekte für eine große Gruppe von Modellen illustrieren. Die Analyse zeigt, dass die Anwendbarkeit von effektiven Operatoren kritisch vom Verhältnis der Energie in Kollisionen und der Massenskala der vollständigen Theorie abhängt. Außerdem wird basierend auf diesen Resultaten eine Methode entwickelt, um experimentelle Grenzen durch effektive Operatoren auf Parameterräume der vollständigen Theorie um zu gestalten.

Es wird geschlossen, dass stark gekoppelte Modelle der elektroschwachen Symmetriebrechung natürlich und kompatibel mit Resultaten des LHCs sind. Außerdem liefert diese Art von Modellen neue und interessante Kollisionstopologien für experimentelle Untersuchungen am LHC. Für die Hochenergiedurchläufe des LHCs werden diese neuen Untersuchungen sich als sehr nützlich erweisen, um das Schicksal zusammengesetzter Modelle und somit vielleicht auch den Ursprung der elektroschwachen Symmetriebrechung zu bestimmen.

List of Publications

My research during the three years of my PhD has resulted in the following publications:

- [1] M. Redi, V. Sanz, M. de Vries, and A. Weiler, *Strong Signatures of Right-Handed Compositeness*, *JHEP* **1308** (2013) 008, [arXiv:1305.3818].
- [2] J. Reuter, M. Tonini, and M. de Vries, *Little Higgs Model Limits from LHC - Input for Snowmass 2013*, [arXiv:1307.5010].
- [3] J. Reuter, M. Tonini, and M. de Vries, *Littlest Higgs with T-parity: Status and Prospects*, *JHEP* **1402** (2014) 053, [arXiv:1310.2918].
- [4] M. de Vries, *Four-Quark Effective Operators at Hadron Colliders*, [arXiv:1409.4657].

Declaration on oath

I hereby declare, on oath, that I have written the present dissertation by my own and have not used other than the acknowledged resources and aids.

Hamburg, the 18th of August 2014

Maikel de Vries

Eidesstattliche Versicherung

Hiermit erkläre ich an Eides statt, dass ich die vorliegende Dissertationsschrift selbst verfasst und keine anderen als die angegebenen Quellen und Hilfsmittel benutzt habe.

Hamburg, den 18. August 2014

Maikel de Vries

Contents

1	Introduction	1
2	Strongly Coupled Models	5
2.1	Introduction	5
2.2	Electroweak Symmetry Breaking	6
2.3	Composite Higgs	13
2.4	Little Higgs	27
3	Composite Higgs	33
3.1	Introduction	33
3.2	Composite Light Quarks	34
3.3	Colour Octet	37
3.4	Bounds on Left-Handed Quark Partners	44
3.5	Bounds on Right-Handed Quark Partners	45
3.6	Dedicated Searches	54
4	Little Higgs	60
4.1	Introduction	60
4.2	LHT Model	61
4.3	LHT Phenomenology	69
4.4	Experimental Searches	74
4.5	Optimising Current SUSY Searches	85
5	Hadron Collider EFT	95
5.1	Introduction	95
5.2	Effective Operators	96
5.3	Experimental Analyses	101
5.4	Results	104
6	Conclusions	109
7	Acknowledgements	113
A	Appendix - Composite Higgs	114
A.1	Right-Handed Composite Model	114
A.2	Approximate p_T Distribution	116
B	Appendix - Little Higgs	118
B.1	Higgs Precision Data	118

B.2	LHT Topologies	119
B.3	EWPO & Precision Higgs: Case B	121
C	Appendix - Hadron Collider EFT	122
C.1	Toy Model	122
C.2	Dijet Cross Sections	125
C.3	Recast Example	129
	Bibliography	131

Chapter 1

Introduction

A new era in collider physics has begun with the impressive discovery of a Higgs-like boson in July 2012 at the Large Hadron Collider [1, 2]. The Standard Model (SM) of particle physics [3–5] has been completed with this discovery, explaining almost all results from collider experiments with an extremely high precision. Possibly all particles with masses around the electroweak scale have been found now and this pushes the focus into precision physics and the search for beyond the Standard Model (BSM) physics. In contrast to the Higgs discovery, experimental searches for beyond the Standard Model particles have been unsuccessful so far. All search channels from CMS and ATLAS are confirming the Standard Model, in some cases even up to partonic centre of mass energies of roughly 4 TeV [6, 7]. On the precision physics front, the couplings of the Higgs-like boson appear to be consistent with and very similar to the Standard Model, leaving increasingly less room for BSM physics. However, there are several BSM theories predicting Higgs bosons with similar properties to the Standard Model, thereby saving their validity for now. In this work we discuss a few of those theories, which are strongly coupled, as opposed to popular supersymmetric extensions of the Standard Model.

The discovery of the Higgs-like boson and thereby the first confirmation of the Higgs mechanism [8–10] raises the question about the generation of the Higgs potential and the origin of electroweak symmetry breaking (EWSB). In the Standard Model the Higgs field has a potential defined ad hoc with a non-trivial vacuum which breaks electroweak symmetry down to electromagnetism. It is not at all obvious why such a potential exists and why its vacuum breaks the electroweak symmetry of the Standard Model, moreover providing masses for the fermions and gauge bosons in the model. In fact most of the beyond the Standard Model theories include an explanation for the form of the potential and the specific symmetry breaking pattern.

Another issue not addressed within the context of the Standard Model is the effect of radiative corrections to the Higgs potential and Higgs mass. In the SM the Higgs mass receives radiative corrections which scale quadratically with the UV cut-off of the theory, coming from loops involving gauge bosons, fermions and the Higgs itself [11]. The Higgs boson is special in this regard, since its scalar nature does not protect it against these quadratic divergences. Based on the assumption that the SM is valid up to the GUT scale — the scale where the gauge couplings meet in Grand Unified Theories — or the Planck scale, the experimentally measured Higgs mass of 125 GeV must equal the bare mass plus large corrections of the order of Λ_{GUT}^2 . This implies that the bare mass must be fine-tuned to a large degree, which is called the fine-tuning or hierarchy problem [12–15]. The hierarchy problem can be addressed in different ways: one method is to introduce a symmetry which protects the scalar mass from receiving quadratic divergences. Supersymmetric theories

are an example for these kinds of models [16–19]. Another method is to lower the cut-off scale by introducing BSM physics around the TeV scale, thereby significantly reducing the amount of fine-tuning. Strongly coupled theories implement this feature naturally. Here, the Higgs boson is a composite state and therefore does not receive quadratically divergent corrections at higher energies [20, 21].

At the Large Hadron Collider the main experimental efforts relevant to the origin of EWSB go into the direction of Higgs precision measurements, searches for supersymmetry and searches for exotic particles. The Higgs precision measurements currently consist of mass determination and the measurement of the coupling strengths to the Standard Model fermions and gauge bosons [22, 23]. Precise measurements of these coupling strengths and the mass may indirectly constrain BSM physics, which modifies these couplings either directly or through intermediate heavy particles in Higgs production or decay processes. A generic feature shared among BSM theories are the conjectured new particles with masses higher than the electroweak scale. For example in supersymmetry there is a partner for each Standard Model particle with opposite spin statistics and with masses higher than the electroweak scale due to supersymmetry breaking. There are numerous dedicated experimental searches for supersymmetric partners and no deviation from the Standard Model has been found so far [24, 25]. The same is true for strongly coupled theories, where also heavy partners of the SM particles are conjectured, but have not been discovered at LHC yet [26, 27]. With every LHC run at higher energies and luminosities the exclusion limits on BSM theories are pushed into higher energy regimes, which leads to more fine-tuning. At some point these BSM theories do not provide a natural description of nature any more, however, at the LHC naturalness may be used as a guiding principle to design experimental searches.

Even after the Higgs discovery the field of particle physics is still thriving. In 2015 the LHC will start running again after an upgrade from 7 and 8 TeV to 13 or 14 TeV centre of mass energy. The increase in centre of mass energy implies that particles with higher masses can be produced at threshold and might be discovered through direct detection in one of the experimental analysis. If such particles are found this will be a clear indication for BSM physics. On the other hand if the LHC does not discover any new physics, the International Linear Collider (ILC) which is being considered by the international community [28–31], might play a crucial role in understanding the mechanism behind EWSB. Currently Japan has indicated their serious interest in hosting the ILC, a linear e^+e^- collider running at a centre of mass energy of 500 GeV. This collider is especially suited for precision measurements involving the Higgs, due to the more precise nature of leptons and the fact that it can scan over various threshold productions involving the Higgs boson [29, 32]. The precise determination of Higgs properties might then indirectly reveal more about the nature of electroweak symmetry breaking.

This thesis has been divided into four parts according to the different subjects: introduction to strongly coupled physics, composite Higgs models, Little Higgs models and validity of effective operator limits. The organisation of this thesis is described in the following paragraphs.

In **Chapter 2** strongly coupled physics is discussed. First the mechanism for electroweak

symmetry breaking is discussed in the context of the Standard Model, showing that the Higgs boson unitarises WW scattering. Then strongly coupled models with modified Higgs couplings are introduced which still unitarise WW scattering, though only up to a specific energy scale. The dynamical origin of the potential and therefore of EWSB is explained and experimental constraints from collider and flavour physics are discussed. To meet those constraints the concept of partial compositeness in composite Higgs models is introduced, and several phenomenological aspects relevant to the LHC are treated. Based on the composite Higgs framework Little Higgs models are discussed. In these types of models collective symmetry breaking is implemented to alleviate the amount of fine-tuning in strongly coupled models.

The concept of partial compositeness is further explored in **chapter 3** where a specific model is introduced. In this model the compositeness of the fermions is implemented such that only one chirality of Standard Model fermions is largely composite. Minimal Flavour Violation is then realised by assuming universal couplings for either the left-handed or right-handed fermions. This implementation leads to large couplings between light quarks and heavy resonances, which are then copiously produced at the LHC giving rise to interesting signatures. In this chapter these signatures and exclusion limits for the heavy partners of the gluons and the quarks will be discussed. Furthermore, search strategies for three and four-jet final states — which have not been explored at the LHC in full detail yet — are proposed.

Then we switch gears in **chapter 4** and discuss another type of strongly coupled physics, namely Little Higgs models. In this chapter we focus on the Littlest Higgs with T-parity (LHT), where the collective symmetry breaking structure is minimal and T-parity prevents large contributions to electroweak precision observables. This ensures that the still allowed parts of parameter space in this model have relatively little fine-tuning and that the model is still a realistic candidate for discovery at the LHC. In this chapter a comprehensive method of constraining the parameter space of this model based on searches for supersymmetry is developed. We will show that constraints from indirect and direct searches are comparable and continue to drive the LHT parameter space into more fine-tuned regions. However, our findings show that the amount of fine-tuning is still comparable to natural supersymmetric models like the Minimal Supersymmetric Standard Model. This chapter concludes with optimisation proposals aimed at the LHT model for searches with missing transverse energy at the Large Hadron Collider.

Exclusion limits for strongly coupled physics often originate from bounds on effective operators, which are also extracted from LHC data. In **chapter 5** the applicability of effective operator constraints from hadron colliders to strongly coupled BSM physics is discussed. The validity of translating effective operator constraints to strongly coupled theories depends on the mass and coupling of the new heavy partners. For hadron colliders where the partonic centre of mass energy is around the typical energy scales of natural BSM theories deviations between the effective and full description arise. The caveats in applying the limits are discussed for Z' and G' models, illustrating the effects for a large class of strongly coupled models. Based on these results a bound from effective operators on the composite model discussed in chapter 3 is revisited and its validity is improved.

In **chapter 6** conclusions for each of the discussed topics and general conclusions for strongly coupled physics at the LHC are presented. Moreover, for each of the discussed topics there are additional results, which are discussed in the **appendices A, B and C**.

Finally a few remarks on this work have to be made. Many of the results presented in this thesis are based on a collaborative effort with the co-authors listed in the list of publications. In accordance with the dissertation requirements, there is an indication on which works the main chapters are based and what my involvement has been. Furthermore, important formulae and results are presented in grey boxes. Then finally the acknowledgements can be found at the end of this thesis in **chapter 7**, where detailed information about the licensing of this work is given, as well.

Chapter 2

Strongly Coupled Models

This chapter provides a brief introduction to the theoretical models used for the work in chapters 3 and 4. The models considered in these chapters are based on the strongly coupled models known as composite Higgs and Little Higgs models. This chapter provides a general introduction to these classes of models and chapters 3 and 4 both contain introductions tailored for the specific models considered there. This introduction is based on references [33–35] for section 2.2 on electroweak symmetry breaking and section 2.3 on composite Higgs models and references [36, 37] for section 2.4 on Little Higgs models. Since this chapter provides an introduction to the models discussed in this thesis, none of the parts here are derived from my work.

2.1 Introduction

The first models based on a strongly coupled description of electroweak symmetry breaking date back to the late seventies and early eighties. In the late seventies, a new model was based on QCD using a new strong gauge interaction whose global chiral symmetry is spontaneously broken by a QCD-like condensate [38, 39]. Then, if part of the global symmetry is weakly gauged the spontaneous breaking is transferred to the electroweak symmetry, causing masses for the electroweak gauge bosons. If the symmetry breaking is around the electroweak scale this mechanism is able to accommodate the weak gauge boson masses, notably without introducing a new scalar particle like the Higgs boson. This class of theories is known as Technicolor. Later, in the early eighties similar theories based on the breaking of global symmetries of strongly interaction theories at higher scales were developed. In here the Higgs is a pseudo Nambu-Goldstone boson which appears from a broken global symmetry [20, 21], and the Higgs boson is naturally lighter than the scale of symmetry breaking in theory, because of its Goldstone nature. These models are generally known as composite Higgs models.

The naturally light nature of the Higgs boson makes composite models an attractive alternative to supersymmetric extensions of the Standard Model. In composite Higgs models there is a separation of scales between the electroweak scale and the scale of symmetry breaking which suppresses the corrections to oblique parameters and other precisely measured quantities in the Standard Model. This feature combined with the discovery of a Higgs-like boson makes composite Higgs models a more attractive alternative than Technicolor theories. The details of the symmetry breaking and the lightness of the Higgs is discussed later in this chapter. Composite Higgs models also predict other particles, typically heavy partners of SM particles with masses around and above the global symmetry breaking scale. These particles make composite Higgs models phenomenologically extremely interesting for the

Large Hadron Collider, since it will be able to probe the existence of many of the composite partners.

The pseudo-Goldstone nature of the Higgs explains its lightness compared to the scale of global symmetry breaking in composite Higgs models. However, there are still increasing amounts of fine-tuning involved as the scale of symmetry breaking becomes larger. An additional suppression of the Higgs mass is therefore an attractive option provided by Little Higgs models which are an alternative to composite Higgs models [40]. In Little Higgs models the global symmetry is collectively broken by two non-zero coupling constants. If either one of these couplings vanishes a global symmetry acting on the Higgs field is restored and the Little Higgs masslessness is obtained. This translates directly into the absence of quadratic divergences at one-loop in the Higgs potential, thereby introducing an additional loop factor in the scale separation. In conclusion the more advanced symmetry structure of Little Higgs models leads to less fine-tuning compared to generic composite Higgs models. Similarly as for the composite Higgs model, Little Higgs models also predict additional heavy partners of SM particles relevant to LHC phenomenology.

This thesis is based on two specific implementations of strongly coupled models, one based on the composite Higgs models and another based on Little Higgs models. For composite Higgs models recently the concept of partial compositeness has been revived [35], where SM particles are mixtures of states from an elementary and composite sector. In this thesis we focus on a specific model where minimal flavour violation is realised by having only one chirality of Standard Model fermions largely composite [41]. The concept of partial compositeness is discussed later in this chapter, however, the details of this specific model are discussed in chapter 3. The Little Higgs model we consider is the Littlest Higgs with T-parity [42, 43] where the symmetry breaking structure is kept relatively simple and T-parity leads to the absence of severe constraints from electroweak precision physics. Little Higgs models are discussed in the last section of this chapter and the phenomenology for the specific model in chapter 4.

In this chapter strongly coupled physics will be discussed based on the concept of electroweak symmetry breaking in the Standard Model. Since these theories provide alternative descriptions of EWSB it is crucial to understand the basic concepts in the Standard Model. We discuss the breakdown of unitarity in a Standard Model with ad-hoc masses for the gauge bosons and fermions and discuss the regularising role of the Higgs boson. Then we introduce strongly coupled models like Technicolor and the composite Higgs and show that they also save the problem of unitarity, although deviating from the Standard Model description. Composite Higgs models are discussed in detail, describing the structure of symmetry breaking, the nature of the Higgs, the dynamical generation of the potential and partial compositeness. In the last section we then discuss Little Higgs models, building on the concepts of composite Higgs models.

2.2 Electroweak Symmetry Breaking

The starting point of this discussion of strongly coupled physics is the structure of electroweak symmetry breaking and the role of the Higgs boson. The Standard Model descrip-

tion of electroweak symmetry breaking can then be extended to possible strongly coupled models and their effects are more straightforwardly interpreted. The role of the Higgs in the Standard Model is best described by the problems which arise without the Higgs. For this reason let the Higgs be absent and consider the massless Standard Model Lagrangian

$$\mathcal{L}_0 = -\frac{1}{4}W_{\mu\nu}^a W^{a\mu\nu} - \frac{1}{4}B_{\mu\nu}B^{\mu\nu} - \frac{1}{4}G_{\mu\nu}^a G^{a\mu\nu} + \sum_{j=1}^3 \bar{\Psi}^{(j)} i \not{D} \Psi^{(j)}. \quad (2.1)$$

In here we have the usual kinetic terms for gauge bosons and fermions. Experimental measurements, of course, dictate masses for the fermions and the electroweak gauge bosons. These are described by the Lagrangian

$$\mathcal{L}_{\text{mass}} = m_W^2 W_\mu^+ W^{-\mu} + \frac{1}{2}m_Z^2 Z_\mu Z^\mu - \sum_{i,j} \left(\bar{u}_L^{(i)} m_{ij}^u u_R^{(j)} + \bar{d}_L^{(i)} m_{ij}^d d_R^{(j)} \right), \quad (2.2)$$

where only the quarks are considered in the fermion sector.

Comparing the two Lagrangians in equations (2.1) and (2.2) leads to the observation that the interactions among particles are invariant under an $SU(2)_L \times U(1)_Y$ symmetry, whereas the mass terms are not. The electroweak symmetry is hidden, or rather spontaneously broken by the vacuum. At energies much higher than the electroweak scale this formulation leads to inconsistencies in perturbation theory. For example the scattering amplitude involving four longitudinal W bosons $W_L^+ W_L^- \rightarrow W_L^+ W_L^-$ grows as E^2 for energies $E \gg m_W$. Scattering amplitudes which grow with energy violate the unitarity bound, which will be discussed in more detail in section 2.2.1.

To investigate the unitarity of these scattering amplitudes in detail, the Nambu-Goldstone bosons that correspond to the longitudinal polarisations of the massive gauge bosons are introduced. The mass Lagrangian in equation (2.2) is then written as

$$\mathcal{L}_{\text{mass}} = \frac{v^2}{4} \text{Tr} \left[(D_\mu \Sigma)^\dagger (D^\mu \Sigma) \right] - \frac{v}{\sqrt{2}} \sum_{i,j} \left(\bar{u}_L^{(i)} \bar{d}_L^{(i)} \right) \Sigma \begin{pmatrix} \lambda_{ij}^u u_R^{(j)} \\ \lambda_{ij}^d d_R^{(j)} \end{pmatrix} + \text{h.c.} \quad (2.3)$$

The field Σ contains the Goldstone bosons χ^a in a non-linear way as

$$\Sigma(x) = \exp \left[\frac{i\sigma^a \chi^a(x)}{v} \right], \quad D_\mu \Sigma = \partial_\mu \Sigma - ig \frac{\sigma^a}{2} W_\mu^a \Sigma + ig' \Sigma \frac{\sigma^3}{2} B_\mu. \quad (2.4)$$

In this chiral form the electroweak symmetry $SU(2)_L \times U(1)_Y$ manifests itself, since Σ transforms as

$$\Sigma(x) \rightarrow U_L(x) \Sigma(x) U_Y^\dagger(x). \quad (2.5)$$

We see that the symmetry is non-linearly realised on the Goldstone bosons χ^a , indicating that the symmetry is hidden or spontaneously broken by the mass terms. In the unitary gauge, that is $\langle \Sigma \rangle = 1$, the familiar masses for the gauge bosons and fermions from equation (2.2) are reproduced.

Moreover the relation

$$\rho \equiv \frac{m_W^2}{m_Z^2 \cos^2 \theta_W} = 1 \quad (2.6)$$

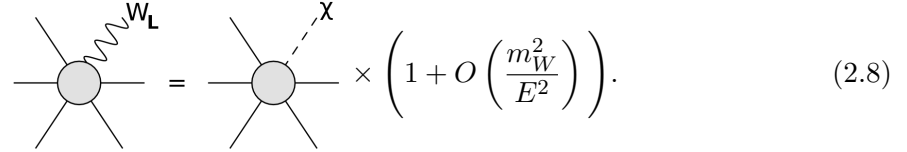
is obtained for $\langle \Sigma \rangle = 1$, consistent with the experimental measurement to good accuracy. This is connected to the invariance under global $SU(2)_L \times SU(2)_R$ transformations

$$\Sigma(x) \rightarrow U_L \Sigma(x) U_R^\dagger. \quad (2.7)$$

This symmetry is broken diagonally by $\langle \Sigma \rangle = 1$, resulting in the custodial symmetry $SU(2)_c$ giving $m_W = m_Z$ for $g' = 0$ and $\lambda_{ij}^u = \lambda_{ij}^d$. Then for a non-zero g' one obtains the relation in equation (2.6) and further loop corrections are proportional to g' and $\lambda^u - \lambda^d$.

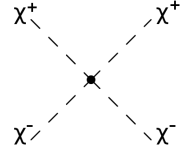
2.2.1 Violation of Unitarity

As argued earlier in this chapter, the Standard Model with masses given by equation (2.2) or (2.3) has problems with perturbative unitarity. It predicts amplitudes that grow with energy and then at some high energies perturbation theory breaks down and the theory loses its validity. These amplitudes which grow with energy occur in the scattering of the longitudinal modes of the massive gauge bosons. The derivation of violation of unitarity is based on the equivalence theorem which states that the amplitude for a longitudinal gauge boson is equal to the amplitude for its respective Goldstone boson at sufficiently high energies



$$\text{Diagram with } W_L = \text{Diagram with } \chi \times \left(1 + O\left(\frac{m_W^2}{E^2}\right) \right). \quad (2.8)$$

With the use of the equivalence theorem the scattering amplitude $W_L^+ W_L^- \rightarrow W_L^+ W_L^-$ can be approximated by the amplitude for $\chi^+ \chi^- \rightarrow \chi^+ \chi^-$ at leading order in E/m_W . At this order the scattering amplitude reads



$$\mathcal{A}(\chi^+ \chi^- \rightarrow \chi^+ \chi^-) = \frac{1}{v^2}(s + t). \quad (2.9)$$

The growth with energy originates from the derivative interaction among four Goldstone bosons obtained when expanding equation (2.3). The unitarity bound prescribes that when the amplitude is projected on partial waves, each partial wave must satisfy $\text{Re}(a_l) > \pi/2$, see reference [33] for more details. Therefore, we project the amplitude in equation (2.9) on partial wave amplitudes, using the Legendre polynomials ($P_0(x) = 1$, $P_1(x) = x$, $P_2(x) = 3x^2/2 - 1/2$, \dots)

$$a_l = \frac{1}{32\pi} \int_{-1}^{+1} d\cos\theta \mathcal{A}(s, \theta) P_l(\cos\theta). \quad (2.10)$$

The s -wave amplitude then reads

$$a_0(W_L^+ W_L^- \rightarrow W_L^+ W_L^-) \simeq \frac{1}{32\pi} \frac{s}{v^2}, \quad (2.11)$$

which leads to the bound $\sqrt{s} \simeq \Lambda \leq 4\pi v$.

Ultimately the loss of perturbative unitarity can be traced back to the non-renormalisability of the chiral Lagrangian in equation (2.3). This is related to the fact that the chiral Lagrangian is an effective field theory which breaks down at some energy scale. For chiral theories in general we have that the break down scale is $\Lambda = 4\pi v$, where v is the scale of spontaneous symmetry breaking [44]. Now we have two possibilities: either cure the problem by introducing new degrees of freedom which restore perturbative unitarity or let the theory become strongly coupled at some higher energy. Both scenarios indicate the emergence and therefore the need for new physics and we conclude that there has to be some symmetry breaking dynamics as a UV-completion of the chiral Lagrangian.

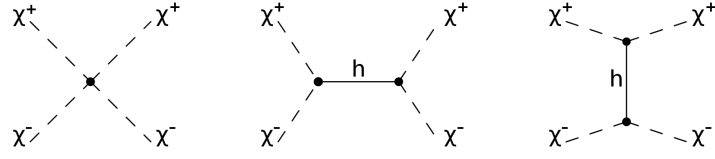
2.2.2 Higgs Model

The most straightforward way to solve the unitarity problem discussed in the last section is adding a single scalar h which is a singlet under $SU(2)_L \times SU(2)_R$ with arbitrary couplings to gauge bosons and fermions. So instead of the chiral mass Lagrangian we now have [45] (to quadratic order in the scalar h)

$$\begin{aligned} \mathcal{L}_H = & \frac{1}{2} (\partial_\mu h)^2 + V(h) + \frac{v^2}{4} \text{Tr} \left[(D_\mu \Sigma)^\dagger (D_\mu \Sigma) \right] \left(1 + 2a \frac{h}{v} + b \frac{h^2}{v^2} + \dots \right) \\ & - \frac{v}{\sqrt{2}} \sum_{i,j} \left(\bar{u}_L^{(i)} \bar{d}_L^{(i)} \right) \Sigma \left(1 + c \frac{h}{v} + \dots \right) \begin{pmatrix} \lambda_{ij}^u u_R^{(j)} \\ \lambda_{ij}^d d_R^{(j)} \end{pmatrix} + \text{h.c.} \end{aligned} \quad (2.12)$$

where a , b and c are arbitrary couplings and $V(h)$ is the potential for the scalar field. Based on this Lagrangian, the effects of this scalar degree of freedom on the high energy properties of the theory are analysed.

The first possible amplitude which might grow with energy is $\chi^+ \chi^- \rightarrow \chi^+ \chi^-$ scattering and at leading order we find the diagrams and amplitude

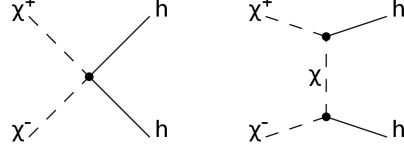


$$\begin{aligned} \mathcal{A}(\chi^+ \chi^- \rightarrow \chi^+ \chi^-) = & \frac{1}{v^2} \left[s - a^2 \frac{s^2}{s - m_h^2} + (s \leftrightarrow t) \right] \\ = & \frac{s+t}{v^2} (1 - a^2) + O\left(\frac{m_h^2}{E^2}\right). \end{aligned} \quad (2.13)$$

Interestingly, the observation is made that for $a = 1$ this amplitude does not grow with energy any more and the scalar h unitarises this part of the theory.

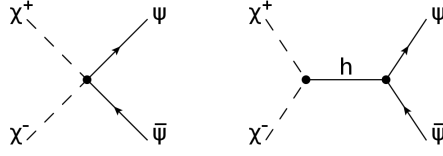
A second possibility is the amplitude for $\chi^+ \chi^- \rightarrow hh$ scattering and the leading order

diagrams and amplitudes are



$$\mathcal{A}(\chi^+ \chi^- \rightarrow hh) = \frac{s}{v^2} (b - a^2) + O\left(\frac{m_h^2}{E^2}\right). \quad (2.14)$$

These types of processes are unitarised if the double Higgs coupling equals $b = a^2$. The third and final option is the amplitude for $\chi^+ \chi^- \rightarrow \psi \bar{\psi}$ scattering which results in diagrams and amplitudes



$$\mathcal{A}(\chi^+ \chi^- \rightarrow \psi \bar{\psi}) = \frac{m_\psi \sqrt{s}}{v^2} (1 - ac) + O\left(\frac{m_h^2}{E^2}\right). \quad (2.15)$$

From these results we find that gauge boson to fermion scattering is unitary if the relation $ac = 1$ holds.

From the $\chi^+ \chi^- \rightarrow \chi^+ \chi^-$ scattering result we observe that now the theory is perturbative until a higher scale

$$\Lambda(a) = \frac{4\pi v}{\sqrt{1 - a^2}}, \quad (2.16)$$

and similarly for the other amplitudes. Hence, an additional scalar degree of freedom with couplings to gauge bosons and fermions increases the energy scale until which this theory is unitary. The combination of the three constraints from the amplitudes above leads to

$$\left. \begin{array}{l} a^2 = 1 \\ b = a^2 \\ ac = 1 \end{array} \right\} \Rightarrow a = b = c = 1. \quad (2.17)$$

It is exactly this point in parameter space that completely unitarises the Lagrangian in equation (2.12), if higher order terms vanish. This parameter space point coincides with the Standard Model Higgs description and the Lagrangian in equation (2.12) can be rewritten in terms of the familiar Higgs doublet

$$H(x) = \frac{1}{\sqrt{2}} e^{i\sigma^a \chi^a(x)/v} \begin{pmatrix} 0 \\ v + h(x) \end{pmatrix}. \quad (2.18)$$

With the use of this rewriting, the familiar Standard Model Lagrangian describing electroweak symmetry breaking appears. The renormalisability of this Lagrangian with maximally dimensions-four operators ensures the unitarity for all energies.

The introduction of a weakly interacting Higgs boson is an interesting solution due to two properties. First the model's calculability is theoretically attractive and secondly it is phenomenological successful, since it satisfies measurements at LHC [22, 23] and precision tests from LEP and SLD [46]. However, a light scalar boson as the Higgs is an unnatural solution as it is quadratically unstable under radiative corrections as we will show in the next paragraph.

Hierarchy Problem

The biggest shortcoming of the Standard Model is the lack of protection against quadratically divergent radiative corrections to the Higgs mass, known as the hierarchy problem or the fine-tuning problem [12–15]. In the Standard Model the gauge and fermionic degrees of freedom have masses whose radiative corrections are protected by gauge and chiral symmetries, respectively. These masses are naturally small, since setting them to zero restores a symmetry in the Lagrangian, which is called 't Hooft naturalness [15]. The Higgs mass on the other hand is not protected by any symmetry. Formulated alternatively: setting the Higgs mass to zero does not restore any symmetry in the Standard Model Lagrangian, this is a general property of elementary scalar fields.

The hierarchy problem appears when extrapolating the Standard Model to higher energies. Beyond the Standard Model there is an energy scale at which new physics starts playing a role, at the latest this will be the Planck scale where the strength of gravity becomes comparable to the SM gauge theories. However, new physics is expected to appear earlier as an explanation for either dark matter, unification of gauge couplings or the hierarchy in Yukawa couplings. Indeed, it is then assumed that the Standard Model is at least valid up to an energy scale Λ_{NP} , which indicates the appearance of new physics.

In the case of unification or the Planck scale, there is a large hierarchy between v the scale of the SM and $\Lambda_{\text{NP}} \sim 10^{15} - 10^{19}$ GeV. It is exactly this hierarchy that appears in the corrections to the Higgs mass. The Higgs mass receives corrections at one-loop from diagrams involving gauge bosons, fermions and the Higgs itself. If regularised using a cut-off scheme these corrections scale as [11, 47]

$$\delta m_h^2 = \frac{3}{8\pi^2} \frac{\Lambda_{\text{NP}}^2}{v^2} [m_h^2 + 2m_W^2 + m_Z^2 - 4m_t^2]. \quad (2.19)$$

The observed mass in nature is then given by $m_h^2 = m_{h,\text{bare}}^2 + \delta m_h^2$, where $m_{h,\text{bare}}^2$ is the bare mass in the SM Lagrangian, which is a free parameter. If the scale Λ_{NP} is of the order of 10^{15} GeV then the bare mass needs to be fine-tuned to at least 30 decimal places to obtain a Higgs mass around the electroweak scale v . This problem is known as the fine-tuning problem and is a motivation to look for new physics beyond the Standard Model.

The hierarchy problem leads to the believe that the Higgs might rather be the parametrisation for the physics responsible for the dynamical origin of electroweak symmetry breaking. An interesting solution for this problem is found in supersymmetric theories where the Higgs mass is protected by a symmetry which connects fermionic with bosonic degrees of freedom and vice versa. However, in this work the focus is on strongly coupled solutions where the Higgs is a composite state at higher energies above and around the TeV scale. A

simple example based on QCD will be discussed in the next section and later in section 2.3 a detailed account of composite Higgs theories is presented.

2.2.3 Strongly Coupled EWSB

Although the Higgs model might be the most straightforward method to solve the unitarity problem, there is already an example in nature which does the same, namely QCD. At low energies QCD breaks a global $SU(2)_L \times SU(2)_R$ chiral symmetry to the vectorial $SU(2)_V$ via the known condensates, like the pions and ρ mesons. It is therefore interesting to look at QCD in terms of unitarity and electroweak symmetry breaking. In this section we present this solution to the unitarity problem, as an example for strongly coupled solutions to electroweak symmetry breaking. The chiral Lagrangian for the pions is given by

$$\mathcal{L}_\pi = \frac{f_\pi^2}{4} \text{Tr} \left[(\partial_\mu \Sigma)^\dagger (\partial^\mu \Sigma) \right], \quad \Sigma(x) = \exp \left[\frac{i\sigma^a \pi^a(x)}{f_\pi} \right], \quad (2.20)$$

where $f_\pi = 92$ MeV is the pion decay constant. Here the pions play the same role as the Goldstone bosons do in the Lagrangian from equation (2.3). The pion-pion scattering described by this Lagrangian suffers from the same unitarity problems as before. However, in the case of QCD there is no Higgs-like resonance which unitarises the theory. Instead, the tower of resonances in QCD, which is exchanged in pion-pion scattering at high energies enforces unitarity.

QCD breaks electroweak symmetry, which is observed when the electroweak interactions are turned on in equation (2.20). There is a global symmetry breaking of $SU(2)_L \times SU(2)_R \times U(1)_B \rightarrow SU(2)_V \times U(1)_B$ of which only the $SU(2)_L \times U(1)_Y$ part will be gauged. In this way an explicit breaking of the global symmetry is introduced and the QCD vacuum breaks the electroweak invariance and the pions act as eaten Goldstone bosons to give mass to the W and the Z . More explicitly the chiral Lagrangian is gauged

$$\mathcal{L}_\pi = \frac{f_\pi^2}{4} \text{Tr} \left[(D_\mu \Sigma)^\dagger (D^\mu \Sigma) \right], \quad (2.21)$$

where the covariant derivative is defined as in equation (2.4). Then expanding around the vacuum $\langle \Sigma \rangle = 1$ results in the gauge boson masses

$$\mathcal{L}_{\text{mass}} = \frac{g^2 f_\pi^2}{4} W_\mu^+ W^{\mu-} + \frac{g^2 + g'^2}{8} f_\pi^2 Z_\mu Z^\mu. \quad (2.22)$$

This implies that the W mass equals $m_W \simeq 29$ MeV, which is significantly below the experimental value. However, QCD is qualitatively a good example of electroweak symmetry breaking, and in the Standard Model the pions also form a small contribution to the gauge boson masses.

An up-scaled version of QCD could then actually provide the dynamics for EWSB, where the pion decay constant is now larger: $f_\pi \rightarrow F_\pi \simeq v$. These types of theories are known as Technicolor [38, 39], where possibly a different $SU(N_{TC})$ gauge group with a global $SU(2)_L \times SU(2)_R$ invariance breaks down to $SU(2)_V$ at low energies due to confinement. A linear combination of the QCD pions and the new technipions are eaten and form the

longitudinal components of the weak gauge bosons. The other combination forms the physical pions observed in nature. Actually for any EWSB description, there is always a small component of the gauge boson masses which comes from the pions of QCD. In Technicolor theories there is no Higgs to unitarise the pion-pion scattering, however there are heavy resonances unitarising the theory. In these theories the lightest resonances have masses of $m_\rho \simeq g_\rho F_\pi$.

In this section two models which resolve the unitarity problem and generate a viable mechanism for EWSB were introduced, one weakly coupled and one strongly coupled. However, both of them are not completely satisfying solutions. The Higgs model has a hierarchy problem and it is generally believed that a more symmetric theory like supersymmetry might address this. Although Technicolor has no Higgs and therefore no hierarchy problem, it is roughly excluded by experimental searches. First of all a light bosonic resonance similar to the Higgs is found [1, 2], moreover Technicolor predicts too high contributions to flavour changing neutral currents and the S parameter [48–51]. Therefore, in the next sections we look into alternative implementations of strongly coupled descriptions of EWSB including a light Higgs.

2.3 Composite Higgs

An interesting interpolation between the previously discussed Higgs model and Technicolor is the composite Higgs paradigm, where the Higgs is a bound state from a strongly interacting sector. In particular the Higgs will emerge as a pseudo Goldstone boson of an enlarged global symmetry of this strong sector. This will assure that it is naturally lighter than the other resonances of the strong sector as was first discussed in the eighties [20, 21]. The mass of the composite Higgs boson does not receive corrections from the Planck scale similarly to the mass of the pion in QCD and thereby solves the hierarchy problem of the Standard Model. Therefore the composite Higgs boson is an attractive alternative for the Standard Model [45, 52, 53], even more since the in contrast to Technicolor a light Higgs aids in satisfying electroweak precision tests.

In this section first the general principles for a successful construction of the Higgs as a pseudo Goldstone boson will be discussed. Then, the minimal custodial implementation of a composite Higgs is discussed on which the model discussed in chapter 3 is based. For this model we give a short review on the couplings of the composite Higgs to gauge bosons and fermions. Furthermore, the concept of partial compositeness is discussed on which most successful implementations of composite Higgs models are based. Finally, the dynamical generation of the potential which breaks electroweak symmetry is discussed and we conclude with a short review on the phenomenology relevant to the Large Hadron Collider.

The composite Higgs paradigm is based on two general principles: there is a strongly coupled theory with a global symmetry \mathcal{G} which is dynamically broken to \mathcal{H}_1 at an energy scale f , from this symmetry breaking the Higgs arises as a composite pseudo Goldstone boson. Furthermore, the global symmetry \mathcal{G} needs to be partially gauged by external vector bosons from a subgroup $\mathcal{H}_0 \subset \mathcal{G}$. These external vector bosons must minimally contain the electroweak bosons and for simplicity we assume that $\mathcal{H}_0 = \mathcal{G}_{\text{SM}} = SU(2)_L \times U(1)_Y$. The

external gauging explicitly breaks the global symmetry \mathcal{G} . In this picture the Standard Model fields — gauge bosons and fermions — are external to the strong sector and are elementary.

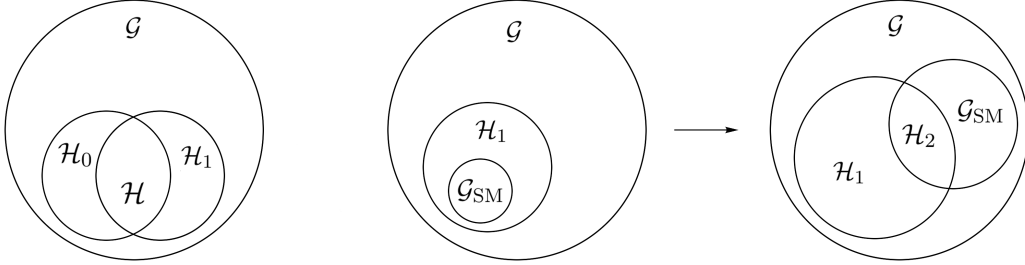


Figure 2.1. Overview of the global symmetry breaking patterns in composite Higgs models. On the left the case is shown where the gauging subgroup \mathcal{H}_0 is not fully contained in \mathcal{H}_1 . It is normally assumed that \mathcal{H}_0 is the electroweak group and is fully contained in \mathcal{H}_1 , this is shown in the middle. The right figure shows the global symmetries after the loop induced two step symmetry breaking, where only the electromagnetic symmetry $U(1)_{\text{em}} \subset \mathcal{H}_2$ remains unbroken.

Since the strong sector should not break electroweak symmetry directly, the electroweak group must be embeddable in the unbroken group $\mathcal{H}_0 = \mathcal{G}_{\text{SM}} \subset \mathcal{H}_1$. Furthermore the symmetry breaking coset $\mathcal{G}/\mathcal{H}_1$ should contain Goldstone bosons that transform as the $SU(2)_L$ Higgs doublet. Then the global symmetry breaking $\mathcal{G} \rightarrow \mathcal{H}_1$ implies $n = \dim(\mathcal{G}) - \dim(\mathcal{H}_1)$ Goldstone bosons, of which $n_0 = \dim(\mathcal{H}_0) - \dim(\mathcal{H})$ are eaten by the vector bosons, where $\mathcal{H} = \mathcal{H}_1 \cap \mathcal{H}_0$ is the unbroken gauge group. In the simple case where $\mathcal{H}_0 = \mathcal{G}_{\text{SM}} \subset \mathcal{H}_1$ none of the Goldstone bosons are eaten and $n_0 = 0$. An overview of the symmetry breaking pattern is given in figure 2.1.

The realisation of the above conditions then implies that \mathcal{G}_{SM} is unbroken at tree level and the Higgs doublet consists of the pseudo Nambu-Goldstone bosons living on the coset $\mathcal{G}/\mathcal{H}_1$. A possible Higgs potential is zero at tree level due to the Goldstone symmetry, however, the global symmetry \mathcal{G} is explicitly broken by couplings with the external Standard Model fields. Then loops of Standard Model fermions and gauge bosons generate a Higgs potential, a dynamical potential which possibly breaks the electroweak symmetry. Conclusively, we observe that composite Higgs models may provide a dynamical explanation for electroweak symmetry breaking, the exact details are postponed to later sections of this chapter.

The total picture can then be viewed as a two step breaking $\mathcal{G} \xrightarrow{f} \mathcal{H}_1 \xrightarrow{v} \mathcal{H}_2$, where only the $U(1)_{\text{em}}$ part of \mathcal{H}_2 is gauged, see figure 2.1. Since the electroweak scale is dynamically generated it can be smaller than the symmetry breaking scale f . An important difference to Technicolor where no such separation of scales exist. The ratio $\xi = v^2/f^2$ is determined by the degree of misalignment of the true vacuum of the Higgs potential, which may be interpreted as the orientation of \mathcal{G}_{SM} with respect to \mathcal{H} . Corrections to electroweak precision observables are suppressed by this ratio and the scale separation between v and f directly translates into a more natural EWSB description than Technicolor. Typical strong sector resonances have masses of the order $m_\rho \sim g_\rho f$ and the Higgs mass is around $m_h \sim g_{\text{SM}} v$, where the couplings roughly satisfy $g_{\text{SM}} \lesssim 1 \lesssim g_\rho \lesssim 4\pi$.

It is interesting to observe that the composite Higgs model in fact interpolates between the Standard Model and Technicolor. In the limit of $\xi \rightarrow 0$ while keeping v fixed, the Higgs bosons remain light and all other resonances become infinitely heavy. Moreover corrections to the Standard Model — since proportional to ξ — vanish, more details on this follow in the next sections when specific models are discussed. On the other hand in the limit of $\xi \rightarrow 1$, the scale separation disappears and the composite Higgs resembles Technicolor with a light Higgs.

2.3.1 Minimal Custodial Model: $SO(5)/SO(4)$

For the purpose of this thesis it is most instructive to consider a particular implementation of the composite Higgs, namely the simplest custodially invariant one based on the symmetry breaking pattern $SO(5)/SO(4)$ [52, 54]. The model discussed in chapter 3 is based on this model and therefore other models are not considered. Required is the construction of the minimal model which can accommodate EWSB, the Higgs doublet and does respect the custodial symmetry of the Standard Model. A coset which contains at least four real Goldstone bosons is needed, the simplest solution is $SU(3)/SU(2) \times U(1)$ giving the required Goldstone bosons. However, the requirement of custodial symmetry is not satisfied here, since custodial symmetry is guaranteed by an $SU(2)_L \times SU(2)_R$ symmetry which is broken to the diagonal by EWSB. Requiring unbroken custodial symmetry, the minimal choice is $SO(4) \simeq SU(2)_L \times SU(2)_R$. The minimal symmetry breaking pattern is $SO(5)/SO(4) = S^4$, where the coset is the surface of a sphere in five dimensions containing the $\dim SO(5) - \dim SO(4) = 10 - 6 = 4$ Goldstone bosons. For constructing a realistic embedding of the hypercharge an extra $U(1)_X$ symmetry is needed [52]. The symmetry breaking pattern then equals $SO(5) \times U(1)_X / SO(4) \times U(1)_X$, where the factor $U(1)_X$ does not play a role in the symmetry breaking. The $SU(2)_L \times U(1)_Y$ symmetry part of the unbroken $SU(2)_L \times SU(2)_R \times U(1)_X$ is gauged, which gives a hypercharge $Y = T_{3R} + X$.

First we analyse the Goldstone bosons and their parametrisation both for the strong sector breaking and for electroweak symmetry breaking. The goal is to derive an effective action which describes the composite Higgs and the Standard Model elementary fields. From this result we can then derive the Higgs potential and the couplings of the Higgs to other Standard Model particles, this will be discussed later in this chapter. The Goldstone bosons living on the $SO(5)/SO(4)$ coset can be parametrised in the usual CCWZ formalism [55, 56] as

$$\Phi(x) = \exp \left[i\sqrt{2}\pi^{\hat{a}}(x)T^{\hat{a}}/f \right] \begin{pmatrix} 0 \\ 0 \\ 0 \\ 0 \\ 1 \end{pmatrix}, \quad (2.23)$$

where $T^{\hat{a}}$ are the broken $SO(5)/SO(4)$ generators. The basis used for the fundamental

representation of $SO(5)$ when broken to $SO(4)$ is

$$\begin{aligned} T_{ij}^a &= -\frac{i}{2} \left[\frac{1}{2} \epsilon^{abc} \left(\delta_i^b \delta_j^c - \delta_j^b \delta_i^c \right) \pm \left(\delta_i^a \delta_j^4 - \delta_j^a \delta_i^4 \right) \right] \\ T_{ij}^{\hat{a}} &= -\frac{i}{\sqrt{2}} \left(\delta_i^{\hat{a}} \delta_j^5 - \delta_j^{\hat{a}} \delta_i^5 \right), \end{aligned} \quad (2.24)$$

where the first expression depicts the unbroken and the second expression the broken generators. The parametrisation $\Phi(x)$ then is readily expressed in explicit form by defining $\pi = \sqrt{(\pi^{\hat{a}})^2}$ and $\hat{\pi}^{\hat{a}} = \pi^{\hat{a}}/\pi$, and by expanding the exponentiated matrix we find

$$\Phi(x) = \begin{pmatrix} \sin(\pi/f) \begin{pmatrix} \hat{\pi}^1 \\ \hat{\pi}^2 \\ \hat{\pi}^3 \\ \hat{\pi}^4 \end{pmatrix} \\ \cos(\pi/f) \end{pmatrix}. \quad (2.25)$$

At tree level, where the $SO(4)$ symmetry is unbroken this is the final result and no electroweak symmetry breaking is induced.

The potential generated by Standard Model loop contributions may trigger electroweak symmetry breaking. Assuming this is the case, the three Goldstone bosons from the $SO(4)/SO(3)$ breaking — these in the end are eaten by the W and the Z gauge bosons — can be parametrised as usual as $\Sigma(x) = \exp[i\chi^i(x)\sigma^i/v]$. Then after spontaneous symmetry breaking the vacuum can be defined as $\langle \pi \rangle = \theta \cdot f$ where θ is the amount of misalignment. The misalignment θ is related to the vacuum expectation value v of EWSB, the exact identification is connected to the derivation of the W mass, provided later in this section. Expanding around the vacuum $\pi(x) \rightarrow \theta \cdot f + h(x)$, where $h(x)$ is the Standard Model Higgs, gives

$$\Phi(x) = \begin{pmatrix} \sin(\theta + h(x)/f) \Sigma(x) \begin{pmatrix} 0 \\ 0 \\ 0 \\ 1 \end{pmatrix} \\ \cos(\theta + h(x)/f) \end{pmatrix}. \quad (2.26)$$

This is how the fields are embedded in the two step symmetry breaking $SO(5) \xrightarrow{f} SO(4) \xrightarrow{v} SO(3)$, where $SO(4)$ is gauged under the electroweak symmetry which is then broken $SO(3)$ with only the electromagnetic gauging.

This parametrisation for $\Phi(x)$ can then be directly used in the CCWZ prescription to obtain the Higgs couplings. This prescription dictates that the gauge couplings for the Goldstone bosons are given by the $SO(5)$ invariant Lagrangian

$$\mathcal{L} = \frac{f^2}{2} (D_\mu \Phi)^T (D^\mu \Phi), \quad (2.27)$$

where the covariant derivative is given analogously to equation (2.4).

2.3.2 Higgs Couplings to Gauge Bosons

A very interesting feature with regard to the LHC is the strength of the couplings between the Higgs and the other Standard Model particles, which are tested and will be tested with more accuracy in the future. This will be a distinguishing feature in the future for BSM models which predict modified Higgs couplings. For the minimal model $SO(5)/SO(4)$ we will use an effective description for the couplings at low energy with respect to the strong sector. The Lagrangian and therefore the couplings are then fully determined by symmetry arguments. The phenomenological implications of this derivation will be further discussed in section 2.3.6.

The starting point of the derivation of the gauge couplings is the CCWZ Lagrangian from equation (2.27) and the expression from equation (2.26) for $\Phi(x)$. Combining the two leads to

$$\begin{aligned} \mathcal{L} = & \frac{f^2}{2} \left[D_\mu \sin \left(\theta + \frac{h(x)}{f} \right) \Sigma \right]^T \left[D^\mu \sin \left(\theta + \frac{h(x)}{f} \right) \Sigma \right] \\ & + \frac{f^2}{2} \partial_\mu \cos \left(\theta + \frac{h(x)}{f} \right) \partial^\mu \cos \left(\theta + \frac{h(x)}{f} \right), \end{aligned} \quad (2.28)$$

since the covariant derivative does not act on the fifth component of the $SO(5)$ parametrisation. Expanding this result further, while only keeping terms relevant for the gauge boson masses and Higgs to gauge couplings we find

$$\begin{aligned} \mathcal{L} \supset & \frac{f^2}{2} \left[(D_\mu \Sigma)^T (D^\mu \Sigma) \right] \sin^2 \left(\theta + \frac{h(x)}{f} \right) \\ & + \frac{f^2}{2} \partial_\mu \sin \left(\theta + \frac{h(x)}{f} \right) \partial^\mu \sin \left(\theta + \frac{h(x)}{f} \right) + \{\sin \rightarrow \cos\} \\ & \supset \frac{1}{2} \partial_\mu h \partial^\mu h + \frac{f^2}{4} \text{Tr} \left[(D_\mu \Sigma)^\dagger (D^\mu \Sigma) \right] \sin^2 \left(\theta + \frac{h(x)}{f} \right). \end{aligned} \quad (2.29)$$

In order to have successful EWSB we need to reproduce the electroweak gauge boson masses, this will provide a relation between the misalignment θ and the parameters v and f . For this purpose only look at the vacuum term where where $\langle \Sigma \rangle = 1$ and retain only the θ terms, then the W mass is given by

$$m_W^2 = \frac{g^2 f^2}{4} \sin^2 \theta \quad \Rightarrow \quad \sin^2 \theta = \frac{v^2}{f^2} = \xi. \quad (2.30)$$

Using the explicit result for the misalignment parameter θ , equation (2.28) can be expanded around the vacuum to find the couplings for the Higgs to gauge bosons

$$\begin{aligned} \mathcal{L} \supset & \frac{f^2}{4} \text{Tr} \left[(D_\mu \Sigma)^\dagger (D^\mu \Sigma) \right] \left[\sin^2 \theta + \frac{h(x)}{f} \sin 2\theta + \frac{h(x)^2}{f^2} \cos 2\theta + \dots \right] \\ = & \frac{v^2}{4} \text{Tr} \left[(D_\mu \Sigma)^\dagger (D^\mu \Sigma) \right] \left[1 + 2 \frac{h(x)}{v} \sqrt{1 - \xi} + \frac{h(x)^2}{v^2} (1 - 2\xi) + \dots \right]. \end{aligned} \quad (2.31)$$

Comparing with the effective Higgs Lagrangian from equation (2.12) the Higgs to gauge boson coupling constants are given by

$$a = \sqrt{1 - \xi}, \quad b = 1 - 2\xi. \quad (2.32)$$

These expressions confirm the fact that for $\xi \rightarrow 0$ the composite Higgs models resembles the Standard Model. Interestingly, the coupling structure to gauge bosons in this effective description using the CCWZ prescription is completely determined by symmetry arguments. Therefore, all composite Higgs models with the $SO(5) \rightarrow SO(4)$ symmetry breaking pattern have the same coupling structure between the Higgs and gauge bosons.

2.3.3 Partial Compositeness

Before discussing Higgs to fermion couplings in the next section, it is necessary to elaborate on the different methods to implement fermions into the effective description for the composite Higgs. In the Standard Model the fermions are elementary particles which couple directly to Higgs boson and the gauge bosons. The composite Higgs introduces a strongly coupled sector which can facilitate additional fermions with the same spin and charges as the Standard Model fermions. In fact these fermions of the strong sector could in principle be the fermions of the Standard Model. On the other hand the Standard Model fermions could be fully elementary or could be a mixture of the fermions from the elementary and strongly coupled sectors. This last option is most viable and is known as partial compositeness. In this section the three options are briefly discussed and then a detailed description of partial compositeness is provided. Of course, the amount of compositeness can be different depending on fermion flavours, this is discussed later as well.

- **Total compositeness:** In the total compositeness scenario, the Standard Model fermions are totally composite and couple directly to the strong sector [57]. This implementation results in large tension with electroweak precision observables, more specifically bounds on lepton compositeness. The tension directly translates into a large fine-tuning, rendering this class of models less attractive.
- **Bilinear coupling:** In this case the Standard Model fermions are completely elementary and couple directly to the strong sector including the Higgs in a bilinear fashion. This type of coupling corresponds to extensions of Technicolor theories [58, 59]. Constraints from conformal field theories result in tension between the Higgs mass operator and flavour operators, which disfavours these models [60].
- **Partial compositeness:** The fermions from the strongly coupled sector mix with the elementary sector, the light states are the Standard Model fermions, whereas the heavy states are new resonances at the TeV scale. The mixing directly provides the couplings for the new light states to the strong sector resonances including the Higgs [35, 61]. In this approach the mixings dictate the strength of the couplings of the Standard Model fermions to the strong sector and thereby the effects of strong sector resonances on the precision and flavour observables. Specific implementations then allow to alleviate the problems of flavour and precision physics which composite models typically have.

In this work the idea of partial compositeness is explored further, mainly in chapter 3. Therefore, in this section a detailed account of the idea is presented, which was first discussed in the nineties after the discovery of composite models [61]. Only in this century the

idea gained traction through the connection of strongly coupled physics with an extra dimensional dual theory [62]. In these extra dimensional theories the concept of partial compositeness appears naturally in the strongly coupled physics in four dimensions. Here only a description of the phenomenologically relevant four dimensional theory in terms of an effective expansion in the strongly coupled sector is given, based on reference [35].

The idea of partial compositeness is based on the existence of an elementary sector and a strongly coupled sector — for example the composite Higgs model discussed in the previous section. The elementary sector contains weakly interacting elementary particles, roughly comparable to the massless Standard Model Lagrangian

$$\mathcal{L}_{\text{elementary}} = -\frac{1}{4}F_{\mu\nu}^2 + \bar{\psi}_L i\not{D}\psi_L + \bar{\psi}_R i\not{D}\psi_R. \quad (2.33)$$

The gauge fields correspond to the Standard Model gauge symmetry and are given by $A_\mu \equiv \{G_\mu, W_\mu, B_\mu\}$ and the fermions in the model are given by $\psi_L \equiv \{q_L, \ell_L\}$ and $\psi_R \equiv \{u_R, d_R, \nu_R, e_R\}$, where the flavour and colour indices are omitted. In here we have the elementary gauge couplings which are denoted as g_{e1}, g_{e2}, g_{e3} , these turn out to be approximately equal to the Standard Model gauge couplings. At high energy scales the effect of flavour and CP violating operators constructed out of the elementary fields in this Lagrangian are negligible. Therefore, effects of flavour and CP violation must be generated in the strongly coupled sector.

The strongly coupled sector contains the Higgs boson and lots of additional resonances, however, typically these resonances come in towers with increasing masses. Only the resonances with lowest mass and which correspond to the SM gauge bosons and fermions are considered in the effective picture. The validity of this picture then of course only extends to energies where the heavier resonances are not excited. The LHC energies must at least reach the mass of the lightest resonances in the strong sector and the next to lowest resonance typically have twice the mass of the lightest resonance. Therefore we can conclude that the effective expansion introduces errors roughly of $(1/2)^2 = 1/4$. This description is, however, still very useful at the LHC as a guiding principle for experimental searches and as rough first interpretation tool for composite Higgs physics.

For every elementary fermion and gauge boson there is a partner in the effective description of the strong sector. These partners provide composite content to the Standard Model fermions and gauge bosons and this determines to which extent these particles couple to the Higgs boson. The composite Lagrangian is given by

$$\begin{aligned} \mathcal{L}_{\text{composite}} = & -\frac{1}{4}\rho_{\mu\nu}^2 + \frac{m_\rho^2}{2}\rho_\mu^2 + |D_\mu H|^2 - V(H) + \bar{\chi} (i\not{D} - m_\chi) \chi + \bar{\xi} (i\not{D} - m_\xi) \xi \\ & - \chi \left(Y_u \tilde{H} \xi^u + Y_d H \xi^d \right) + \text{h.c.} \end{aligned} \quad (2.34)$$

This Lagrangian represents the lowest resonances of the strongly coupled theory in an effective description, where ρ represents the gauge partners and χ, ξ represent the fermionic partners corresponding to the Standard Model states. Their masses are given by m_ρ, m_χ and m_ξ and are roughly of the order of the symmetry breaking scale f . Moreover, the strong sector contains a Higgs which is described like in the Standard Model and has strong Yukawa couplings Y_u, Y_d to the fermionic partners.

The Standard Model gauge bosons and fermions are a mixture of the elementary and composite fields, to that extend a Lagrangian which mixes both sectors must be introduced. This is done in a renormalisable way using mass mixing terms and leads to the Lagrangian

$$\mathcal{L}_{\text{mixing}} = -m_\rho^2 \frac{g_{\text{el}}}{g_\rho} A_\mu \rho^\mu + \frac{m_\rho^2}{2} \left(\frac{g_{\text{el}}}{g_\rho} A_\mu \right)^2 + (\bar{\psi}_L \Delta_L \chi_R + \bar{\psi}_R \Delta_R \xi_L + \text{h.c.}). \quad (2.35)$$

In this equation g_ρ represents the gauge couplings of the strong sector, which are also appearing in the Lagrangian in equation (2.34) in the $\rho_{\mu\nu}$ tensor. The mixing strength between the elementary and composite fields is represented by the parameters $\Delta_{L/R}$ with mass dimension one.

Diagonalisation

The particles observed in experiment and described by the Standard Model are in this model a mixture of elementary and composite particles. To obtain the exact expressions for these states the total Lagrangian

$$\mathcal{L} = \mathcal{L}_{\text{elementary}} + \mathcal{L}_{\text{composite}} + \mathcal{L}_{\text{mixing}} \quad (2.36)$$

needs to be diagonalised. Both the kinetic and the mass terms need to be diagonalised and the Lagrangian then obtained contains the physical states, of which the lighter ones can be identified with the Standard Model particles.

For the gauge fields the transformation

$$\begin{pmatrix} A_\mu \\ \rho_\mu \end{pmatrix} \rightarrow \begin{pmatrix} \cos \theta & -\sin \theta \\ \sin \theta & \cos \theta \end{pmatrix} \begin{pmatrix} A_\mu \\ \rho_\mu \end{pmatrix}, \quad \tan \theta = \frac{g_{\text{el}}}{g_\rho} \quad (2.37)$$

achieves this for each of the gauge couplings $\theta = \theta_1, \theta_2, \theta_3$. From this it is directly seen that the SM gauge fields are given by the superposition

$$\frac{g_\rho}{\sqrt{g_\rho^2 + g_{\text{el}}^2}} A_\mu + \frac{g_{\text{el}}}{\sqrt{g_\rho^2 + g_{\text{el}}^2}} \rho_\mu, \quad (2.38)$$

and the SM gauge couplings read

$$g = \frac{g_{\text{el}} g_\rho}{\sqrt{g_\rho^2 + g_{\text{el}}^2}} \simeq g_{\text{el}}, \quad \text{if } g_{\text{el}} \ll g_\rho. \quad (2.39)$$

The last condition is typically satisfied for strongly coupled theories and therefore leads to the fact that the Standard Model gauge fields are mostly elementary. The other superposition is the vector meson of partial compositeness. The gauge boson part of the new diagonalised Lagrangian contains the following terms¹

$$\mathcal{L}_{\text{gauge}} \supset -\frac{1}{4} F_{\mu\nu}^2 + \frac{m_\rho^2}{2 \cos^2 \theta} \rho_\mu^2. \quad (2.40)$$

¹This Lagrangian also contains kinetic terms for the ρ and interaction terms between the SM gauge bosons and their heavy partners, more details can be found in [35].

In here the covariant derivative for the three SM gauge symmetries is defined as in the Standard Model with the coupling constant equal to $g = g_\rho \sin \theta = g_{el} \cos \theta$. From this Lagrangian it is observed that before electroweak symmetry breaking the Standard Model gauge bosons have their original kinetic term and remain massless. The vector mesons ρ_μ have already masses before electroweak symmetry breaking.

The transformation needed to diagonalise the fermion sector is

$$\begin{pmatrix} \psi_L \\ \chi_L \end{pmatrix} \rightarrow \begin{pmatrix} \cos \varphi_L & -\sin \varphi_L \\ \sin \varphi_L & \cos \varphi_L \end{pmatrix} \begin{pmatrix} \psi_L \\ \chi_L \end{pmatrix}, \quad \tan \varphi_L = \frac{\Delta_L}{m_\chi}, \quad (2.41)$$

and the same for the right-handed elementary field using the replacements $\psi_L \rightarrow \psi_R$, $\chi_L \rightarrow \xi_R$, $\varphi_L \rightarrow \varphi_R$, $\Delta_L \rightarrow \Delta_R$ and $m_\chi \rightarrow m_\xi$. In here the mixing angles φ_L and φ_R range over all the different fermion types and flavours. After diagonalisation the Lagrangian for fermions contains the terms²

$$\begin{aligned} \mathcal{L}_{\text{fermion}} \subset & \bar{\psi}_L i \not{D} \psi_L + \bar{\chi} (i \not{D} - m_\chi^*) \chi \\ & + g \bar{\psi}_L (\sin^2 \varphi_L \cot \theta - \cos^2 \varphi_L \tan \theta) \rho_\mu \gamma^\mu \psi_L \\ & + g \bar{\psi}_L \left(\frac{\sin \varphi_L \cos \varphi_L}{\sin \theta \cos \theta} \right) \rho_\mu \gamma^\mu \chi_L + \text{h.c.} \\ & + g \bar{\chi}_L (\cos^2 \varphi_L \cot \theta - \sin^2 \varphi_L \tan \theta) \rho_\mu \gamma^\mu \chi_L \\ & + \{L \rightarrow R, \chi \rightarrow \xi, \varphi_L \rightarrow \varphi_R, m_\chi^* \rightarrow m_\xi^*\}. \end{aligned} \quad (2.42)$$

The mass of the Standard Model fermions before EWSB vanishes as expected and the mass of the heavy partners is given by

$$m_\chi^* = \sqrt{\Delta_L^2 + m_\chi^2}, \quad m_\xi^* = \sqrt{\Delta_R^2 + m_\xi^2}. \quad (2.43)$$

There are also terms which involve couplings of the fermions and gauge bosons with the composite Higgs³. As for the other terms, these terms as well describe the Standard Model and composite sector before electroweak symmetry breaking. For example schematically the Standard Model Yukawa couplings are given by

$$y_{\text{SM}} = \sin \phi_L \cdot Y \cdot \sin \phi_R, \quad (2.44)$$

where Y denotes the Yukawa-like couplings in the strong sector. Even though the Standard Model Yukawas are off-diagonal and hierarchical the strong sector Yukawas do not have to be, since the mixing angles can provide the flavour structure. This is a great achievement of partial compositeness and aids in satisfying flavour and CP constraints. Discussion of these matters is postponed to section 3 and is detailed there. Based on the concept of partial compositeness also the Higgs to fermion couplings can be obtained, for which the Lagrangian after electroweak symmetry breaking is needed. This is discussed in the following section.

²This Lagrangian also contains additional interactions between the fermions and the vector mesons of the strong sector, more details can be found in [35].

³The couplings between fermions and gauge bosons and the Higgs doublet are detailed in [35].

2.3.4 Higgs Couplings to Fermions

An interesting quantity is the coupling strength of the composite Higgs to Standard Model fermions. From the previous section it was observed that in the context of partial compositeness these couplings are the product of Yukawas in the strong sector and mixing angles. Equation (2.44) dictates that the Standard Model fermion mass is proportional to the mixings and therefore light fermions are mainly elementary and heavy fermions are largely composite. Based on the idea of partial compositeness we now examine the $SO(5)/SO(4)$ model as considered previously for the gauge bosons to Higgs couplings.

In this minimal custodial example of the composite Higgs model there is the freedom to specify how the fermions transform under the $SO(5)$ symmetry. This will affect the coupling strength between fermions and the composite Higgs. Two possibilities will be discussed, one where the fermions transform under the spinorial representation of $SO(5)$ [52] and another where the fermions transform under the fundamental of $SO(5)$ [54, 63]. A detailed derivation of these couplings strengths is given in reference [33], here we provide a short account focussing on obtaining the coupling strengths.

Analogously to the derivation of partial compositeness a mixing Lagrangian can be formulated. Since we are only interested in the generic scaling of the coupling with $\xi = v^2/f^2$ a simplified mixing Lagrangian for one generation can be used

$$\mathcal{L} = \lambda_q \bar{q}_L O_q + \lambda_u \bar{u}_R O_u + \lambda_d \bar{d}_R O_d + \text{h.c.} \quad (2.45)$$

Using this Lagrangian, an effective action for the elementary quarks is derived in the background of a composite Higgs without any further resonances. This allows to make a first estimate of the fermionic couplings, without including the mixing effects which arise in the framework of partial compositeness.

Spinorial Representation

In this case the operators in equation (2.45) transform as spinors of $SO(5)$, and because of the linear coupling also the SM quarks do. A spinor of $SO(5)$ decomposes as a 4 of $SO(4)$ which is a $(2, 1) + (1, 2)$ of $SU(2)_R \times SU(2)_L$, so the SM quarks are embedded in the following way

$$\Psi_q = \begin{bmatrix} q_L \\ Q_L \end{bmatrix}, \quad \Psi_u = \begin{bmatrix} q_R^u \\ u_R \\ d_R' \end{bmatrix}, \quad \Psi_d = \begin{bmatrix} q_R^d \\ u_R' \\ d_R \end{bmatrix}. \quad (2.46)$$

Progressing along the same lines as the CCWZ formalism for the gauge Lagrangian, we write down an effective Lagrangian with the most general $SO(5)$ invariant couplings for quarks with the composite Higgs

$$\mathcal{L}_\Psi = \sum_{r=q,u,d} \bar{\Psi}_r i \not{\partial} \Psi_r + i\lambda f \sum_{r=u,d} \bar{\Psi}_q \Gamma^i \Phi^i \Psi_r. \quad (2.47)$$

In here Φ denotes the same Goldstone fields as in (2.26) and the Γ^i denote the spinorial representation of $SO(5)$

$$\Gamma^{\hat{a}} = \begin{bmatrix} 0 & \sigma^{\hat{a}} \\ \sigma^{\hat{a}\dagger} & 0 \end{bmatrix}, \quad \Gamma^5 = \begin{bmatrix} \mathbf{1} & 0 \\ 0 & -\mathbf{1} \end{bmatrix}, \quad \sigma^{\hat{a}} = \{\vec{\sigma}, -i\mathbf{1}\}. \quad (2.48)$$

With the use of these expressions the relevant term determining the fermion to Higgs couplings can be expanded as

$$\Gamma^i \Phi^i = \begin{pmatrix} \cos(\theta + h(x)/f) \mathbf{1} & -i \sin(\theta + h(x)/f) \Sigma(x) \\ i \sin(\theta + h(x)/f) \Sigma(x) & -\cos(\theta + h(x)/f) \mathbf{1} \end{pmatrix}. \quad (2.49)$$

Plugging these expressions into the Lagrangian and only keeping the q_L and the u_R we find

$$\mathcal{L}_\Psi \supset \bar{q}_L i \not{\partial} q_L + \bar{u}_R i \not{\partial} u_R + \lambda f \sin(\theta + h/f) \bar{q}_L \Sigma u_R. \quad (2.50)$$

Expanding the last term around the vacuum gives

$$\begin{aligned} \mathcal{L}_\Psi &\supset \lambda f \bar{q}_L \Sigma u_R \left(\sin \theta + \frac{h(x)}{f} \cos \theta + \dots \right) \\ &= \lambda v \bar{q}_L \Sigma u_R \left(1 + \frac{h(x)}{v} \sqrt{1 - \xi} + \dots \right), \end{aligned} \quad (2.51)$$

where λ must be identified with the Yukawa coupling and we omitted generation indices. The parameter for the Higgs to fermion coupling is easily identified as

$$c = \sqrt{1 - \xi}. \quad (2.52)$$

Fundamental Representation

This case dictates that the operators in equation (2.45) transform as fundamentals of $SO(5)$ and analogously for the quarks. The same steps as for the spinorial case should be taken and lead to the result [54, 64, 65]

$$c = \frac{1 - 2\xi}{\sqrt{1 - \xi}}. \quad (2.53)$$

In section 2.3.6 both these results for the spinorial and fundamental representation of the fermions are compared to Higgs precision data. This is one of the indirect methods of constraining the composite Higgs parameter space.

2.3.5 Dynamical Potential

The pseudo Nambu-Goldstone nature of the Higgs explains its lightness, though it does not give any insight into the origin of electroweak symmetry breaking. In composite Higgs models the potential for the Higgs doublet is generated through loop diagrams and introduces the concept of dynamical breaking of electroweak symmetry. It is this explanation for the origin of EWSB that gives composite Higgs models additional value with respect to the rather ad hoc Standard Model description of the Higgs mechanism, which is rather a

parametrisation. However, if a dynamical potential is generated at loop level it must satisfy at least two criteria. The generated potential must allow for a spontaneous breaking and the minimum of the potential must break both the global $SO(4)$ invariance and the electroweak gauge invariance. Furthermore a light Higgs boson mass is required and therefore the induced breaking should be relatively small.

Deriving the Higgs potential for the minimal composite Higgs is rather lengthy and beyond the scope of this introduction to composite Higgs models, however based on recent results [64, 66] we indicate the important features. There are two main contributions from Standard Model particles, those induced by gauge bosons loops and those induced from the top quark loops. The gauge boson contribution is completely determined by the structure of global symmetry breaking of the minimal composite Higgs and is given by

$$V_{\text{gauge}}(h) = \alpha \sin^2 \frac{h}{f} + \beta \sin^4 \frac{h}{f} + \dots . \quad (2.54)$$

The expressions for α and β are given in [64] and the important result is that $\alpha > 0$. This directly implies that a dynamically generated potential in minimal composite Higgs model from gauge contributions alone can not induce electroweak symmetry breaking.

However, the contributions from top quark loops are usually dominant and might induce EWSB. The top quark induced potential for the fundamental representation is given by the expansion

$$V_{\text{top}}(h) = \alpha \sin^2 \frac{h}{f} - \beta \sin^2 \frac{h}{f} \cos^2 \frac{h}{f} + \dots . \quad (2.55)$$

Expanding the trigonometric functions indicates that for $\alpha < \beta$ and $\beta \geq 0$ EWSB is induced, and these values can indeed be obtained as is detailed in [64]. The minimum of the potential is given by

$$\left\langle \sin \frac{h}{f} \right\rangle \equiv \frac{v}{f} \equiv \sqrt{\xi} \simeq \sqrt{\frac{\beta - \alpha}{2\beta}}, \quad (2.56)$$

which leads to an expression for the Higgs mass

$$m_h^2 \simeq \frac{8\beta}{f^2} \left\langle \sin^2 \frac{h}{f} \cos^2 \frac{h}{f} \right\rangle. \quad (2.57)$$

This expression is rather involved when written out in full detail and therefore in this context it is more interesting to give a naive dimensional estimate for the potential [45]

$$V(h) \simeq \frac{m_\rho^4}{g_\rho^2} \times \frac{y_t g_\rho}{16\pi^2} \times \hat{V}(h/f), \quad (2.58)$$

where the potential is the usual Higgs potential with order one couplings $V(h/f) \sim (h/f)^2 + (h/f)^4$. This leads to a quartic coupling $\lambda \sim (g_\rho/4\pi)^3 4\pi y_t$. The resulting Higgs boson mass roughly equals

$$m_h \simeq \left(\frac{g_\rho}{4\pi} \right)^{3/2} \sqrt{4\pi v m_t} \simeq 150 \text{ GeV}. \quad (2.59)$$

Hence a relatively light Higgs is feasible within these theories. There are more involved calculations which express the Higgs mass as a function of the mass of the heavy fermion partners. Implication from the measurement of a light Higgs on the fermion partner masses are discussed in the next section.

2.3.6 Higgs Phenomenology

The Higgs results from the first run of the LHC at 7 and 8 TeV have resulted in two interesting methods to constrain and generically test composite Higgs models. The first is the measurement of the Higgs couplings to an already remarkable precisions, which can provide the first clues about the composite nature of the Higgs boson. Secondly, the measurement of the Higgs mass puts constraints on the parameter space of composite Higgs models, especially if these are assumed to provide a solution to the hierarchy problem. Both constraining methods are briefly discussed here to give an introduction to LHC phenomenology for composite Higgs models, then later in chapter 3 other approaches for specific models are described. For a recent overview of the phenomenology of a large number of composite Higgs models see reference [67].

Modified Couplings

First the effects of the modified couplings of the Higgs boson to gauge bosons and fermions for composite Higgs models are discussed. For the most simple composite Higgs model based on the coset $SO(5)/SO(4)$ these were derived in the previous sections and from equations (2.32), (2.52) and (2.53) one finds

$$a = \sqrt{1 - \xi}, \quad b = 1 - 2\xi, \quad c = \begin{cases} \sqrt{1 - \xi} & \text{spinorial} \\ \frac{1 - 2\xi}{\sqrt{1 - \xi}} & \text{fundamental} \end{cases}, \quad \text{where } \xi = \frac{v^2}{f^2}. \quad (2.60)$$

In here a, b, c represent the coupling strengths between fermions and gauge bosons and the Higgs in an effective description as defined in equation (2.12).

The LHC experiments started scrutinising the Higgs coupling strengths after the Higgs discovery and produced results where the Higgs couplings are grouped into two categories [70, 71]. First the Higgs coupling to gauge bosons which is probed in the ZZ and WW decay channels and the Higgs coupling to fermions which is probed in the $\gamma\gamma$, $\tau\tau$ and $b\bar{b}$ decay channels and the gluon fusion production mode which involves the Higgs to top quark coupling. These two categories form a direct map on the parameters a and c in the effective description of equation (2.12). The constraints from the LHC experiments on these parameters are shown in figure 2.2, which includes an adaptation for the minimal composite Higgs model. From these results it can be concluded that values of $\xi > 0.2$ are excluded at 95% CL. Conclusively, since ξ is proportional to the the amount of fine-tuning, these measurements of the coupling strengths slowly drive the composite Higgs models into a more fine-tuned regime.

Higgs Mass Implications

As discussed in section 2.3.5 the Higgs mass depends on the mass of the heavy fermionic partners in the composite Higgs model. This dependence is rather dominant and the interesting observation is made that for light Higgs masses as have been measured at the LHC [71, 72], the heavy top partners must be rather light in natural composite Higgs models

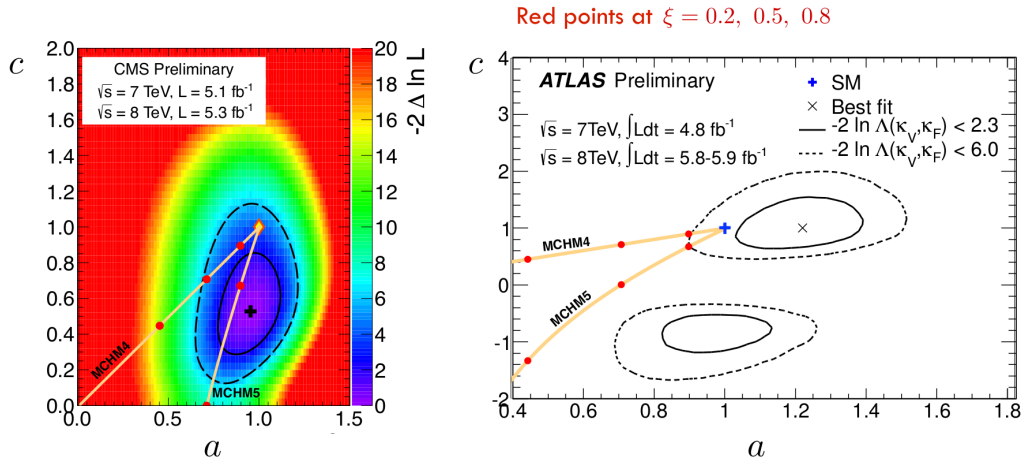


Figure 2.2. Experimental constraints on the a and c parameter in the effective description of the Higgs couplings from CMS and ATLAS, with the composite Higgs predictions. The solid and dashed lines represent 68% and 95% CL contours respectively and MCHM4 denotes the composite Higgs with fermions in the spinorial representation, whereas MCHM5 denotes fermions in the fundamental representation. Figure has been taken from [34] adapted from the combination of experimental results presented in [68, 69].

[64, 66, 73–75]. In conclusion, the lightness of the Higgs sets an upper bound on the mass of the heavy top partners.

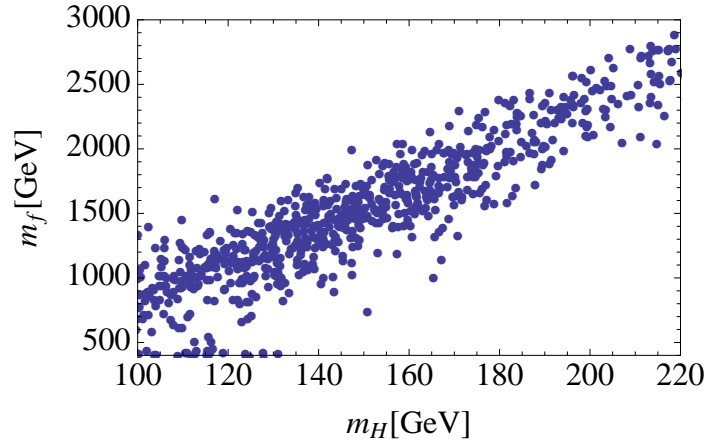


Figure 2.3. Relation between the top partner mass and the Higgs mass for symmetry breaking scale $f = 800$ TeV in the minimal composite Higgs model with minimal flavour violation. Figure has been taken from [74].

In figure 2.3 the relation between the fermion partner masses and the Higgs mass is shown. Assuming a Higgs mass around 125 GeV — as has been measured — results in an upper bound on the fermion partner masses

$$m_{\text{partner}} \lesssim 1500 \text{ GeV}, \quad (2.61)$$

for $f = 800$ TeV. This bound is phenomenologically relevant for the model considered in chapter 3, since it reduces the parameter space for experimental searches and provides an indication for where to expect new resonances at the Large Hadron Collider. These aspects will be discussed further in chapter 3. Constraints on the heavy fermion partners for other models are similar and can be found in the provided references.

2.4 Little Higgs

Little Higgs models are strongly coupled models based on the composite Higgs paradigm. Their attractive feature is the absence of quadratically divergent corrections to the Higgs mass at one-loop due to collective symmetry breaking [40, 76]. In Little Higgs models the global symmetry is explicitly broken only when two or more coupling constants are non-zero. When either of these couplings vanishes the symmetry is restored and the Little Higgs is massless. Later it will be shown that in specific implementations of Little Higgs models there are no quadratically divergent one-loop diagrams involving more than one coupling, thereby protecting the Higgs mass at one-loop level. Moreover, the mechanism of collective symmetry breaking naturally generates a scale separation between v and f .

Little Higgs models come in different guises based on the pattern of collective symmetry breaking, though also based on additional features like discrete symmetry protection for electroweak precision observables. In this dissertation in chapter 4 the Large Hadron Collider phenomenology for the Littlest Higgs with T-parity is discussed in detail. In there, the aspects of the model relevant for LHC phenomenology are discussed in a rather self contained introduction. A full treatment of Little Higgs models is beyond the scope of this work, however, a short introduction to Little Higgs models is provided. This introduction discusses the collective symmetry breaking mechanism in some more detail and is based on the Littlest Higgs model [77] where needed. Comprehensive introductions to Little Higgs models are given in [36, 37] on which the review in this section is based.

2.4.1 Collective Symmetry Breaking

Little Higgs models try to avoid quadratic divergences to the Higgs potential at one-loop level by using collective symmetry breaking. Each of the sectors which induces quadratic divergences needs to be changed to accommodate collective symmetry breaking. This is discussed in this section for the gauge, fermion and scalar sector. In each of these sectors the Higgs potential receives quadratic corrections to the mass and quartic coupling, which need to be cancelled by additional structures introduced in the Little Higgs paradigm. Then in this section the structure is detailed and we see how these additional fields appear. For some of the sectors a model independent approach is possible, however, if needed the discussion is based on the Littlest Higgs model [77].

As for composite Higgs models a global symmetry breaking structure is essential to Little Higgs models, for the Littlest Higgs we have

$$SU(5)/SO(5). \tag{2.62}$$

As for the non-linear sigma models in composite Higgs theories, the Goldstone bosons on the coset of the symmetry breaking at a scale f can be parametrised as

$$\Sigma = \exp [2i\Pi/f] \langle \Sigma \rangle \quad (2.63)$$

where

$$\Pi = \pi^a X^a, \quad \langle \Sigma \rangle = \begin{pmatrix} \mathbf{0}_{2 \times 2} & \mathbf{0}_{2 \times 1} & \mathbf{1}_2 \\ \mathbf{0}_{1 \times 2} & 1 & \mathbf{0}_{1 \times 2} \\ \mathbf{1}_2 & \mathbf{0}_{2 \times 1} & \mathbf{0}_{2 \times 2} \end{pmatrix}, \quad (2.64)$$

and X^a are the $24 - 10 = 14$ broken generators spanning the $SU(5)/SO(5)$ coset. The vacuum expectation value $\langle \Sigma \rangle$ ensures the specific breaking.

The Littlest Higgs is a product group model: a Little Higgs model where the $SU(2)_L$ weak symmetry is embedded in a product gauge group contained in this case in $SU(5)$. In the Littlest Higgs we have that a $[SU(2) \times U(1)]^2$ subgroup of $SU(5)$ is gauged. In the next paragraph when the gauge sector is discussed we see that this gauged symmetry is broken to the diagonal $[SU(2) \times U(1)]^2 \rightarrow SU(2)_L \times U(1)_Y$ through the vacuum expectation value $\langle \Sigma \rangle$ at the scale f . Hence, we have a massless electroweak gauged group which can be identified with the SM electroweak gauge group and another copy of the electroweak gauge group with masses around the scale f .

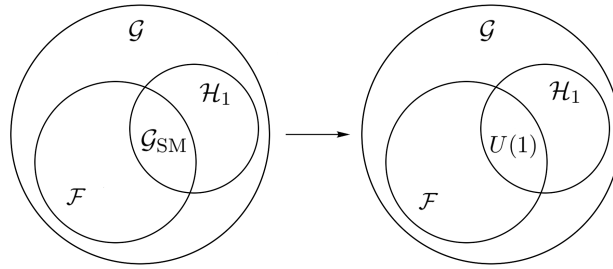


Figure 2.4. Overview of the global symmetry breaking patterns in Little Higgs models. On the left the symmetry breaking pattern of Little Higgs before electroweak symmetry breaking is shown. On the right EWSB is included and induces a misalignment breaking the Standard Model gauge group down to electromagnetism.

Before turning to the gauge sector, we discuss the general pattern of collective symmetry breaking in Little Higgs models and compare it to composite Higgs models. A cartoon has been provided in figure 2.4 and can be compared to the composite Higgs cartoon in figure 2.1. Similar to composite Higgs models we have the global symmetry breaking $\mathcal{G} \rightarrow \mathcal{H}_1$ at a scale f in Little Higgs models. A subgroup $\mathcal{F} \subset \mathcal{G}$ of the global symmetry is gauged, in product group models \mathcal{F} contains the product gauge group. The other variant are called simple group models where the weak gauge group is embedded in a larger group, for a discussion on these types of models we refer to references [36, 37]. Parts of the gauged \mathcal{F} subgroup are unbroken and are contained in \mathcal{H}_1 . This group can be identified with the Standard Model gauge group $\mathcal{G}_{\text{SM}} = \mathcal{F} \cap \mathcal{H}_1$ and remains massless before EWSB. The other part of the gauge group $\mathcal{F} \setminus \mathcal{H}_1$ contains the gauge bosons which correspond to a broken symmetry and acquire masses of the order of f .

Turning back to the Littlest Higgs model we see that the symmetry breaking results in 14 Nambu-Goldstone bosons of which 4 will be eaten by the heavy vectors corresponding to the part of the gauged group $[SU(2) \times U(1)]^2$ which is not contained in the unbroken group \mathcal{H}_1 . Therefore there are 10 Goldstone bosons remaining before EWSB of which 4 will form the Higgs doublet. The details will be discussed in the next paragraph on the gauge sector.

Gauge Sector

This paragraph focuses on the principle of collective symmetry breaking in the gauge sector, different aspects are explained by using the Littlest Higgs model as an example. As in the section before we use the CCWZ formalism to write down kinetic terms for the Goldstone bosons

$$\mathcal{L} = \frac{f^2}{8} \text{Tr} \left[(D_\mu \Sigma)^\dagger D_\mu \Sigma \right], \quad (2.65)$$

where the covariant derivative is defined as

$$D_\mu \Sigma = \partial_\mu \Sigma - i \sum_{j=1}^2 \left[g_j \left(W_j^a (Q_j^a \Sigma + \Sigma Q_j^{aT}) \right) + g'_j B_j (Y_j \Sigma + \Sigma Y_j^T) \right]. \quad (2.66)$$

The generators for the $SU(2)$ and $U(1)$ symmetries are given by

$$\begin{aligned} Q_1^a &= \begin{pmatrix} \sigma^a/2 & 0 & 0 \\ 0 & 0 & 0 \\ 0 & 0 & 0 \end{pmatrix} & Y_1 &= \frac{1}{10} \text{diag} (3, 3, -2, -2, -2) \\ Q_2^a &= \begin{pmatrix} 0 & 0 & 0 \\ 0 & 0 & 0 \\ 0 & 0 & -\sigma^{a*}/2 \end{pmatrix} & Y_2 &= \frac{1}{10} \text{diag} (2, 2, 2, -3, -3). \end{aligned} \quad (2.67)$$

The symmetry breaking as argued before consists of two steps, namely $[SU(2) \times U(1)]^2 \rightarrow SU(2)_L \times U(1)_Y \rightarrow U(1)_{\text{em}}$. In the first steps the heavy gauge bosons obtain their masses and in the EWSB breaking the Standard Model bosons acquire masses, the mass expressions can be found in section 4.2.

It is interesting to observe the collective symmetry breaking at work here. First, we note that the generators for the gauge bosons in equation (2.67) are embedded in $SU(5)$. Actually, the first copy of generators commute with an $SU(3)$ subgroup embedded in the lower right corner of the $SU(5)$ matrices and the second copy of the gauge generators commute with the $SU(3)$ in the upper left corner. Hence, if either one pair of gauge couplings (g_1, g'_1 or g_2, g'_2) is set to zero, there is an exact $SU(3)$ symmetry which is broken down to $SU(2)$ by the vacuum expectation value $\langle \Sigma \rangle$. The Nambu Goldstone bosons of this breaking are exactly the Higgs doublet. Therefore, the Higgs is exactly massless at all orders in perturbation theory.

Now, corrections to the Higgs mass must involve the combination of at least the two groups of gauge couplings. Then, if we look at diagrams with intermediate gauge bosons which could cause corrections to the Higgs mass, we see that at one-loop level these only involve

a single gauge field. Therefore, either these contributions cancel between themselves or are non existing in the Littlest Higgs model. Either case implies there are no one-loop quadratic divergences to the Higgs mass in the gauge sector.

Scalar Sector

For the scalar sector a model independent description of collective symmetry breaking can be formulated, a brief review is given based on references [78, 79]. From general arguments we know that the Higgs potential and especially its mass are protected by a shift symmetry in composite and Little Higgs models

$$h \rightarrow h + \epsilon. \quad (2.68)$$

For collective symmetry breaking in the scalar sector additional pseudo Nambu-Goldstone bosons are required. Then terms in the potential which are invariant under the combination include

$$V \supset \lambda_1 f^2 \left| \phi + \frac{h^2}{f} \right|^2 + \lambda_2 f^2 \left| \phi - \frac{h^2}{f} \right|^2, \quad (2.69)$$

in schematic form. These terms can generate a quartic coupling while still protecting the Higgs mass from quadratic corrections. In order to compensate the shift symmetry on h for either one of the two terms, the field ϕ has transformations

$$\phi \rightarrow \phi \pm \frac{h\epsilon + \epsilon h}{f}, \quad (2.70)$$

An explicit expression for the potential in the Littlest Higgs model can be found in reference [37]. As usual f is the scale of symmetry breaking in the strongly coupled sector. Neither of the two terms in equation (2.69) can induce a potential by itself, since they are invariant under the transformation in equation (2.68) and either one in equation (2.70). Then the Higgs is an exact Goldstone boson, more explicitly, the Higgs quartic interaction can be removed by the field redefinition $\phi \rightarrow \phi \pm h^2/f$. The terms in equation (2.69) lead to a mass for the ϕ field equal to $m_\phi = f\sqrt{\lambda_1 + \lambda_2}$, which is around the scale f . When both operators are present and the couplings are non-zero a Higgs quartic interaction is generated when ϕ is integrated out and equals

$$V \supset 4 \frac{\lambda_1 \lambda_2}{\lambda_1 + \lambda_2} h^4. \quad (2.71)$$

The potential in equation (2.69) generates a correction to the Higgs mass which scales only logarithmically in the cut-off Λ

$$\Delta m_h^2 \sim \frac{4}{16\pi^2} \frac{\lambda_1 \lambda_2}{\lambda_1 + \lambda_2} m_\phi^2 \log \frac{\Lambda^2}{m_\phi^2}. \quad (2.72)$$

This is the mechanism of collective symmetry breaking at work, only diagrams proportional to λ_1 and λ_2 contribute to the Higgs potential at one-loop order. These diagrams are only logarithmically divergent. Thereby, a separation of scales between v and f is provided for and the fields ϕ are responsible for counteracting the the quadratic divergences to the Higgs mass.

Fermion Sector

For each of the three quadratically divergent contributions to the Higgs mass collective symmetry breaking needs to be implemented, the last sector involves fermions. Only the top Yukawa coupling significantly contributes to the quadratic divergence of the Higgs mass, therefore in a minimal model only partners for the top quark need to be introduced. For the Littlest Higgs model the gauge sector had two parts transforming under different $SU(3)$ symmetries which were then broken to the $SU(2)$ electroweak symmetry. In the fermion sector the same can be done for the top quark by embedding the fields as

$$\Psi = \begin{pmatrix} ib_L \\ -it_{1L} \\ t_{2L} \\ 0 \end{pmatrix} \equiv \begin{pmatrix} q_L \\ t_{2L} \\ 0 \end{pmatrix}. \quad (2.73)$$

The gauge invariant Yukawa Lagrangian then reads

$$\mathcal{L}_Y \supset \frac{\lambda_1}{2} f (\epsilon_{ijk} \epsilon_{mn} \bar{\Psi}_i \Sigma_{jm} \Sigma_{kn} t_{1R}) + \lambda_2 f (\bar{t}_{2L} t_{2R}) + \text{h.c.} \quad (2.74)$$

where $i, j, k = 1, 2, 3$ and $m, n = 4, 5$. The collective symmetry breaking appears here as well, setting $\lambda_1 = 0$ decouples the Higgs from the top sector completely. When on the other hand $\lambda_2 = 0$, the upper left corner $SU(3)$ is unbroken and the three upper components of the Ψ field transform as a fundamental under this symmetry. Then, as before the Higgs is an exact Goldstone boson. Since, as for the gauge sector, one-loop diagrams must involve both λ_1 and λ_2 , they are at most logarithmically divergent. Expanding the Lagrangian in equation (2.74) results in a Yukawa interaction for the top quark with strength

$$\lambda_t = \sqrt{2} \frac{\lambda_1 \lambda_2}{\sqrt{\lambda_1^2 + \lambda_2^2}}. \quad (2.75)$$

As expected this result dictates that corrections to the Higgs mass originating from top quark loops are proportional to λ_1 times λ_2 in agreement with the results from collective symmetry breaking.

2.4.2 Littlest Higgs with T-Parity

Most of the early constructions of Little Higgs models are constrained severely by electroweak precision tests. One of these models is the simplest Little Higgs [80, 81] based on the coset $[SU(3) \times U(1)]^2 / [SU(2) \times U(1)]^2$. In reference [82] the latest constraints on the symmetry breaking scale have been obtained from EWPT and Higgs precision physics (from 7 TeV data) and were found to be $f \gtrsim 3.26$ TeV at 95% CL. Moreover, there the parameter space of the Littlest Higgs was scrutinised as well and led to the constraint $f \gtrsim 3.58$ TeV at 95% CL. A large separation between the electroweak scale v and the scale of these Little Higgs models is observed, implying the models are highly fine-tuned. Hence, even though these models are designed to be a natural description of EWSB, measurements dictate their unnaturalness. Furthermore, a high symmetry breaking scale f implies high masses for

the Little Higgs partners, which renders them almost undetectable at the Large Hadron Collider.

In these models the most stringent constraints arise due to the tree level-exchange of heavy gauge bosons in electroweak precision observables. In the Littlest Higgs model the introduction of a discrete symmetry removes these tree-level contributions and ameliorates the tension with precision physics. This extension to the Littlest Higgs model is the Littlest Higgs with T-parity [42, 43] and this discrete symmetry reduces the constraints on symmetry breaking scale to $f \gtrsim 0.47$ TeV at 95% CL [82]. This low symmetry breaking scale gives plenty of opportunities of exploring this model at the LHC, and first steps for this endeavour are made in chapter 4. In this section we briefly explain how T-parity is introduced in the Littlest Higgs model, the phenomenologically relevant details can be found in the corresponding chapter.

In the Littlest Higgs with T-parity the discrete symmetry acts as an exchange symmetry between $[SU(2) \times U(1)]_1$ and $[SU(2) \times U(1)]_2$ gauge copies. For the kinetic term in equation (2.65) to be invariant it is required that $g_1 = g_2$ and $g'_1 = g'_2$. Then, before EWSB the gauge boson mass eigenstates equal

$$W_{\pm}^a = \frac{1}{\sqrt{2}} (W_1^a \pm W_2^a), \quad B_{\pm} = \frac{1}{\sqrt{2}} (B_1 \pm B_2), \quad (2.76)$$

where W_+^a and B_+ are identified with the Standard Model gauge bosons. These bosons are even under T-parity and the heavy partners of the Standard Model gauge bosons are T-odd. Since the Standard Model fields are all even under T-parity, this model is protected from tree-level exchange of heavy gauge bosons.

In the scalar sector schematically there are the Higgs fields and other scalar pseudo Nambu-Goldstone bosons called ϕ , actually in the Littlest Higgs model these additional fields are gathered in an $SU(2)$ triplet. This triplet is odd under T-parity, and since the Higgs is even under T-parity, couplings of the type $H^\dagger \phi H$ are forbidden. Therefore no triplet vacuum expectation value is generated and tree-level violation of custodial symmetry is prevented. For the fermion sector the inclusion of T-parity requires the introduction of additional fermionic fields and chapter 4 contains further details for the fermionic spectrum of the Littlest Higgs with T-parity.

Chapter 3

Composite Higgs

This chapter is based on the publication [83] about LHC signatures of partial compositeness written by my collaborators and myself. My involvement in this work covers sections 3.3 and 3.5, where I produced the results and explanatory text. In sections 3.4 and 3.6 I aided in the creation of the results and figures. Furthermore, I helped formulating the introduction and conclusions.

3.1 Introduction

In the previous chapter composite models and the concept of partial compositeness were discussed. In this chapter we build a specific model on top of this hypothesis, where each SM state has a heavy partner with equal quantum numbers under the SM symmetries, see [33, 52, 84–86] and references therein for more details. Until recently most studies focused on the so called “anarchic scenario” where the SM light quarks are mostly elementary and the top largely composite [87–90]. This hypothesis hides strong coupling effects from flavour and electroweak observables but also eliminates the typical collider signatures of compositeness.

In references [41, 91–93] it was shown that a different philosophy is possible within the partial compositeness paradigm. In here one chirality of SM light quarks has large compositeness and these scenarios are in fact strongly motivated by flavour physics. Assuming universal couplings for either left-handed or right-handed fermions allows the realisation of the Minimal Flavour Violation (MFV) hypothesis [94] in strongly coupled theories, solving the flavour problem of composite Higgs models [95–98]. Here the compositeness of the up quark cannot be small, it being connected to the one of the top. However, generalisations allowing to split the third generation can also be considered [99, 100].

In this chapter we will focus on the phenomenologically attractive scenario of composite right-handed quarks that is weakly constrained by precision electroweak tests allowing a large degree of compositeness, see [101] for a recent discussion. The collider phenomenology will be studied in detail, extending and updating the results in [41]. The experimental signatures are dramatically different from the ones in the widely studied anarchic models [102–106]. In these models the proton constituents are elementary, which makes it difficult to produce the new states at the LHC. If right-handed up and down quarks are composite instead, the couplings to the strong sector will be large. This implies larger production cross sections for the heavy states that are within the reach of the current LHC runs.

The typical collider signatures of our scenario are final states involving jets. In particular, a strong bound on gluon resonances from the latest dijet and $t\bar{t}$ searches at LHC is derived. The phenomenology of heavy fermions depends on the chirality of the associated

SM particles. Partners of left-handed quarks can be singly produced through electroweak interactions with large cross sections already at the 7 TeV LHC. This places a stringent and rather model independent bound that can be extracted from an ATLAS search [107]. Partners of right-handed quarks are instead more difficult to produce and detect and lead to final states with up to six jets and no missing energy. We find that present multi-jet LHC searches, tailored for supersymmetric scenarios, are mostly insensitive to this signature even in the R-parity violation case. Bounds could be significantly improved with dedicated searches and we suggest some possibilities that could be explored by the experimental collaborations.

The organisation of this chapter is as follows: In section 3.2 we review the model and discuss the relevant features of right-handed compositeness with particular emphasis on the importance of chromomagnetic interactions. In section 3.3 we discuss the phenomenology of the colour octet. The relevant experimental searches will be discussed and limits on the octet mass extracted. In sections 3.4 and 3.5 the collider signatures of heavy quark partners will be discussed. Available searches will be analysed and dedicated search strategies will be proposed in section 3.6. The conclusions are presented in the general conclusions in chapter 6. In appendix A.1 the model used in the collider simulations is presented and in appendix A.2 the p_T distribution in single production of heavy quark partners is discussed.

3.2 Composite Light Quarks

As was shown in the previous chapter, within the framework of partial compositeness SM fields mix with states of the composite sector of equal quantum numbers under the SM symmetries. In this section we briefly discuss the idea of right-handed compositeness, its attractive features and phenomenological details. More details about the structure of the Lagrangian can be found in appendix A.1 and all the details of the model are presented in reference [41].

All the new states are classified according to representations of the composite sector global symmetry. The minimal assumption is made that this contains the symmetry $SU(3)_c \times SU(2)_L \times SU(2)_R \times U(1)_X$. The SM Yukawa couplings are schematically given by

$$y_{\text{SM}} = \sin \phi_L \cdot Y \cdot \sin \phi_R, \tag{3.1}$$

where $\sin \phi_{L,R}$ are the mixings matrices of left and right chiralities of the SM quarks with the composite states. The coupling Y , in general a matrix, has a typical strength that characterises the composite sector. For simplicity we will often assume this to be equal to the coupling of spin-1 resonances g_ρ but it should be kept in mind that these are in principle independent parameters.

The standard assumption, naturally realised in Randall-Sundrum scenarios, is that the degree of compositeness is controlled by the mass of the SM states. This logic implies that the light generations are practically elementary and couple only through mixing of the SM gauge fields. This property makes the new states experimentally well hidden both from direct and indirect searches. It was pointed out, however, that at least the right-handed chiralities of the light generations could be composite [41, 92, 108]. In this case the effects

of compositeness are more visible at LHC because the proton constituents are strongly coupled to the composite states. Despite the large degree of compositeness, corrections to precisions observables measured at LEP are small and can be compatible with experimental bounds¹. This perhaps counter-intuitive possibility is in fact quite naturally realised if the right-handed quarks couple to singlets of the custodial symmetry. Moreover, this possibility is automatic in scenarios that realise the MFV hypothesis [41], because a flavour symmetry relates the compositeness of the up quark to the necessarily large compositeness of the top. In contrast to anarchic scenarios, composite light quarks have striking experimental signatures that could be seen at LHC. Among the new states, the lightest partners of the up and down quarks are considered in this chapter. For the right-handed quarks we assume that these are singlets of $SU(2)_L \times SU(2)_R$ while left-handed quarks will be associated to bi-doublets. For the up sector we have,

$$L_U = (\mathbf{2}, \mathbf{2})_{\frac{2}{3}} = \begin{pmatrix} U & U_{\frac{5}{3}} \\ D & U_{\frac{2}{3}} \end{pmatrix}, \quad \tilde{U} = (\mathbf{1}, \mathbf{1})_{\frac{2}{3}}. \quad (3.2)$$

The full model can be found in appendix A.1, in this section we further focus on the phenomenological details.

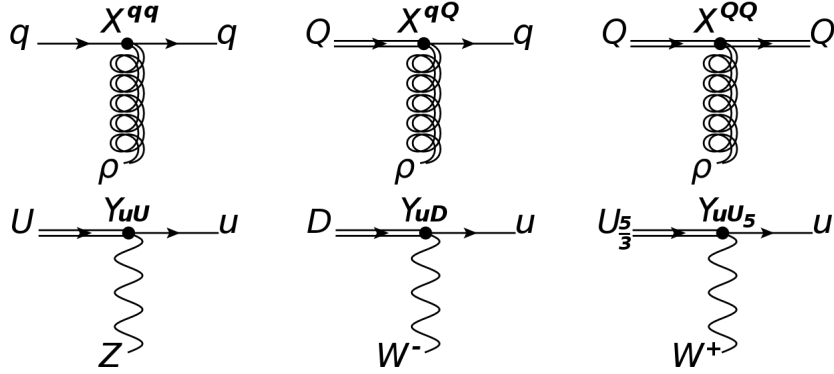


Figure 3.1. The diagrams above show the couplings of the colour octet to SM quarks and their heavy partners. The diagrams below show the couplings to electroweak gauge bosons.

The model contains several composite spin one states, however, we only include the gluon partner, a massive colour octet vector. The colour octet is most relevant in this scenario due to its significant couplings with the Standard Model quarks and gluons. Electroweak resonances will not be studied here, though we expect the rough features to be similar to the coloured sector. The colour octet couples as a gauge field with strength g_ρ . The mixing with

¹Modified Higgs couplings could also be obtained. See reference [109] for the discussion of Higgs precision phenomenology in models with composite right-handed quarks and reference [110] for related work.

SM quarks generates the trilinear couplings of the heavy gluon of figure 3.1 with strengths

$$\begin{aligned} X_R^{qq} &= g_s (\sin^2 \phi_{Rq} \cot \theta - \cos^2 \phi_{Rq} \tan \theta) \\ X_R^{qQ} &= g_s \frac{\sin \phi_{Rq} \cos \phi_{Rq}}{\sin \theta \cos \theta} \\ X_R^{QQ} &= g_s (\cos^2 \phi_{Rq} \cot \theta - \sin^2 \phi_{Rq} \tan \theta). \end{aligned} \quad (3.3)$$

where $\tan \theta = g_s/g_\rho$. For this model we denote by q a light SM quark and by Q a heavy partner quark and analogous formulae hold for the left-handed chiralities. We are interested in the situation where the right-handed up and down quarks are significantly composite. Strictly in MFV models $\sin \phi_{Ru} = \sin \phi_{Rt} > \lambda_t/g_\rho$ but this can be relaxed in more general constructions based on $SU(2)$ flavour symmetries [99, 100]. The SM right-handed quarks can couple to gluon resonances with a trilinear coupling $qq\rho$ as large as $g_\rho \sin^2 \phi_{Rq}$. Moreover the partners of right-handed quarks can be produced and decay through the heavy-light vertex in figure 3.1. On the other hand the vertex with left-handed partners is negligible because the compositeness of left-handed light quarks is extremely small.

For electroweak interactions the situation is exactly inverted, see figure 3.1. In the limit of zero quark masses in the up sector the relevant vertices are

$$\begin{aligned} Y_{uD} &= Y_{uU_{\frac{5}{3}}} = \frac{g}{\sqrt{2}} \frac{Y_U v}{\sqrt{2} m_Q} \sin \phi_{Ru} \\ Y_{uU} &= -Y_{uU_{\frac{2}{3}}} = \frac{g}{2 \cos \theta_W} \frac{Y_U v}{\sqrt{2} m_Q} \sin \phi_{Ru} \end{aligned} \quad (3.4)$$

where $v = 246$ GeV and Y_U is the up sector fermionic coupling, see appendix A.1. These interactions allow to singly produce the partners of left-handed quarks. Higgs interactions are also generated but we will not study them here, for more information see reference [111]. The last important ingredient in our analysis will be the chromomagnetic operator which couples the SM gluon to one light and one heavy quark, a coupling which is absent in the renormalisable Lagrangian. The operator is given by the expression

$$\mathcal{L}_{\text{chromo}}^{\text{SM}} = \kappa \frac{g_s}{m_Q} \bar{U}_L \sigma_{\mu\nu} T^a u_R G_{\mu\nu}^a + \text{h.c.} \quad (3.5)$$

This dimension five operator is relevant in our analysis because it controls the decay of the right-handed partners in the region $m_\rho > m_Q$ where the decay into $Q \rightarrow \rho q$ is kinematically forbidden. It is generated by loops of the strong sector fields with a size

$$\kappa \sim \frac{g_\rho^2}{16\pi^2} \frac{m_Q^2}{m_\rho^2} \sin \phi_{uR}, \quad (3.6)$$

as obtained in appendix A.1.

Finally, a brief comment on the scenario where left-handed quarks are strongly composite is given. Here precision electroweak tests, in particular modified coupling to the Z , strongly disfavours large compositeness. In reference [41] it is found that

$$\sin \phi_{Lq} \lesssim \frac{\lambda_t}{2g_\rho} \left(\frac{m_\rho}{3 \text{ TeV}} \right). \quad (3.7)$$

Repeating the analysis above implies that cross sections lower than in the anarchic scenario will be obtained, at least for the scales and couplings in natural composite models that address the hierarchy problem. In fact due to the opposite sign of the two contributions in equation (3.3), the couplings may even turn out to be smaller. In what follows we will only consider the scenario with composite right-handed quarks.

Simulations

In this chapter we study the phenomenology of the gluon resonance, partners of left-handed quarks $(\mathbf{2}, \mathbf{2})_{2/3}$ and partners of right-handed quarks, $\mathbf{1}_{2/3}$ and $\mathbf{1}_{-1/3}$. We focus on the first generation partners whose mass is, however, equal to the one of the top partners under the MFV hypothesis. The searches are very sensitive to the spectrum of the new states. We will mostly work under the assumption that the fermionic scale m_Q is smaller than m_ρ . This hypothesis appears to be necessary for the theory to be natural, given that spin one particles lighter than 2 TeV are disfavoured. On the other hand new vectorial fermions, which are the most relevant from the naturalness point of view, have weaker direct bounds. In our simulations we generate event samples with MadGraph5 [112], using a model² generated with Feynrules 1.6 [113]. The parton level events are passed to Pythia 6.4 [114] to simulate the effects of parton showering, and then to Delphes 2.0 [115] or ATLFast [116] for a fast detector simulation. We use the default CMS and ATLAS parameters for Delphes depending on what experimental analysis are being considered, and reconstruct jets with the anti- k_T algorithm [117] using a radius parameter of 0.5 and 0.7, respectively. These simulated events are then analysed using the experimental analyses, providing a method to interpret the relevant experimental searches in terms of our model.

3.3 Colour Octet

Among possible spin-1 resonances we will focus on the gluon partner, a colour octet with mass m_ρ , which is a free parameter in the model. In this section we discuss the experimental searches for dijets and $t\bar{t}$ resonances by CMS and ATLAS and try to constrain the parameter space of our model. Furthermore, constraints on four-quark effective operators are used, which appear when the colour octet is integrated out. It is to be noted that constraints on spin-one resonances from flavour physics are not necessarily negligible, even if MFV is realised. Certain operators — in particular $(\bar{q}_L y_u y_u^\dagger q_L)^2$ — are generated at tree level [99, 100]. Nevertheless, these bounds are more model dependent and can for example be avoided in extensions of MFV. We will not include them here, however, see reference [101] for a discussion.

3.3.1 Octet Phenomenology

The colour octet can be produced through the Drell-Yan like process $q\bar{q} \rightarrow \rho$ of figure 3.2. Through the coupling with light quarks (3.3), it can be copiously produced at LHC if

²The FeynRules implementation of the right-handed partial compositeness model is available upon request by the authors.

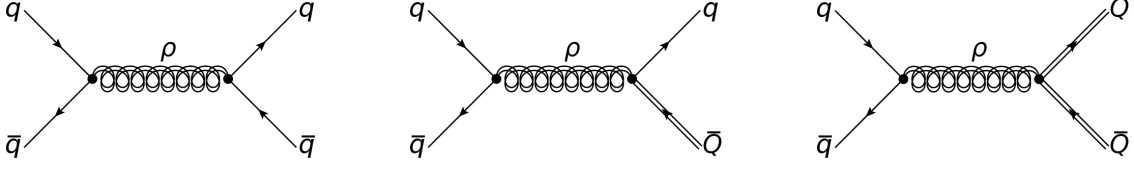


Figure 3.2. The heavy colour octet is dominantly produced from a quark anti-quark pair and then decays into any kinematically accessible combination of light and heavy quarks.

$\sin \phi_{Ru}$ is sufficiently large. Note that the processes which involves two gluons fusing to a single ρ is impossible due to gauge invariance.

The decay of the ρ plays an important role in the phenomenology for resonance searches. The decay into SM right-handed quarks is equal for all generations while only the one into t_L is relevant for left-handed quarks. If the heavy fermions are lighter than the colour octet the decay into a single heavy and one SM fermion or two heavy fermions (for $2m_Q < m_\rho$) is open. Since the couplings to the composite states are large this can strongly affect the phenomenology.

The decay modes are displayed in figure 3.2 and analytic formulae for these partial widths equal

$$\begin{aligned}
 \Gamma(\rho \rightarrow q\bar{q}) &= \frac{\alpha_s}{12} m_\rho \left[(X_L^{qq})^2 + (X_R^{qq})^2 \right] \\
 \Gamma(\rho \rightarrow q\bar{Q}, Q\bar{q}) &= \frac{\alpha_s}{12} m_\rho \left(1 - \frac{m_Q^2}{m_\rho^2} \right) \left(1 - \frac{m_Q^2}{2m_\rho^2} - \frac{m_Q^4}{2m_\rho^4} \right) \left[(X_L^{qQ})^2 + (X_R^{qQ})^2 \right] \\
 \Gamma(\rho \rightarrow Q\bar{Q}) &= \frac{\alpha_s}{12} m_\rho \sqrt{1 - \frac{4m_Q^2}{m_\rho^2}} \left[\left(1 - \frac{m_Q^2}{m_\rho^2} \right) \left[(X_L^{QQ})^2 + (X_R^{QQ})^2 \right] + 6 \frac{m_Q^2}{m_\rho^2} X_L^{QQ} X_R^{QQ} \right],
 \end{aligned} \tag{3.8}$$

in the limit $m_q \ll m_Q$. The couplings $X_{L/R}$'s are defined in equation (3.3). As shown in figure 3.3 the width of the colour octet changes drastically when the decay modes to either one or two heavy fermions open up. In the last case the resonance is very broad, affecting the applicability of resonance searches.

3.3.2 Compositeness Bounds

First we consider the compositeness bounds reported by ATLAS and CMS, see also [41, 118]. In the large m_ρ limit we can integrate out the colour octet and replace it with an effective four-fermion operator. Such an operator produces dijets with an angular distribution different from the QCD that allows to distinguish it from the background. In particular, the experiments place a bound on the effective operators with light quarks

$$c_{LL} (\bar{q}_L \gamma^\mu q_L)^2 + c_{RR} (\bar{q}_R \gamma^\mu q_R)^2 + 2c_{LR} (\bar{q}_L \gamma^\mu q_L) (\bar{q}_R \gamma_\mu q_R), \tag{3.9}$$

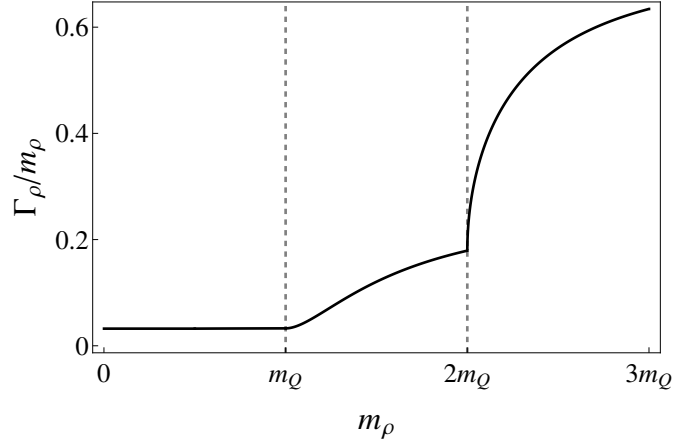


Figure 3.3. Typical behaviour of the colour octet width as a function of the octet mass, for $g_\rho = 3$. The width increases significantly as the decay channels to the quark partners open up, these qualitative features hold independently of the mixings.

that can be recast in our scenario. Recent experimental results on the angular distributions of dijet final states by both ATLAS [119] and CMS [120] imply

$$\begin{aligned} c_{LL,RR}^{(+)} &\lesssim 0.10 \text{ TeV}^{-2} && \text{ATLAS} \\ c_{LL,RR}^{(-)} &\lesssim 0.06 \text{ TeV}^{-2} && \text{CMS.} \end{aligned} \quad (3.10)$$

The \pm superscript refers to the sign of the coefficient, and the ATLAS analysis only considers the case of destructive interference. CMS provides an exclusion for both signs of the coefficient and the most constraining one is used. Note that the operators with heavy quarks (such as $u\bar{u}c\bar{c}$) are expected to be less relevant at LHC. Dijet production requires a quark-antiquark initial state, in this case the process is suppressed by the proton's parton density functions. Integrating out the heavy colour octet generates the four-fermion operator [41]

$$-\frac{g_\rho^2}{6m_\rho^2} \sin^4 \phi_{L,Rq} (\bar{q}_{L,Rq} \gamma^\mu q_{L,Rq})^2. \quad (3.11)$$

Using the strongest bound reported by CMS and the coefficient in equation (3.11)³ we derive

$$\sin^2 \phi_{Ru} \lesssim \frac{0.6}{g_\rho} \left(\frac{m_\rho}{\text{TeV}} \right). \quad (3.12)$$

Both constraints by ATLAS and CMS are represented by the blue areas and are presented in figure 3.4 in the m_ρ versus $\sin \phi_{Rq}$ plane. The compositeness of right-handed down quarks is slightly less constrained due to the predominance of up quarks in the proton. However, in figure 3.4 both constraints are combined through the assumption that $\phi_{Ru} = \phi_{Rd}$. Note that the sign of the coefficient obtained when integrating out heavy vectors (a similar conclusion

³Note that in reference [83] on which this chapter is based, the sign of this operator is displayed incorrectly, here the minus sign corresponds to the constructive interference with the QCD background and is most constraining.

holds for scalars) is fixed and corresponds to the most constrained sign in the CMS analysis. Hence, it is useful that the experiments report the bound for both signs of the operator.

Sophisticated Analysis

In chapter 5 a detailed account of the applicability of effective operators is presented. It is argued there, that large errors are introduced whenever the mass of the particle under consideration is small compared to the transfer energy in the events used for constraining the operator. At the LHC these effects are particularly important and should be taken into account. Section 5.4 provides a method to quantify the errors being made by using the effective description and proposes a recasting procedure to obtain more reliable estimates. In appendix C.3 this procedure has been applied to the model discussed here and the limits presented in figure 3.4 are rescaled and become less constraining. Consult chapter 5 and in particular appendix C.3 and figure C.1 for more details. We note here that the constraints on the colour octet mass from the combination of different observables obtained later in this section still remain valid. However, it is strongly recommended to rescale limits from effective operators using the procedure described in chapter 5.

3.3.3 Resonance Searches

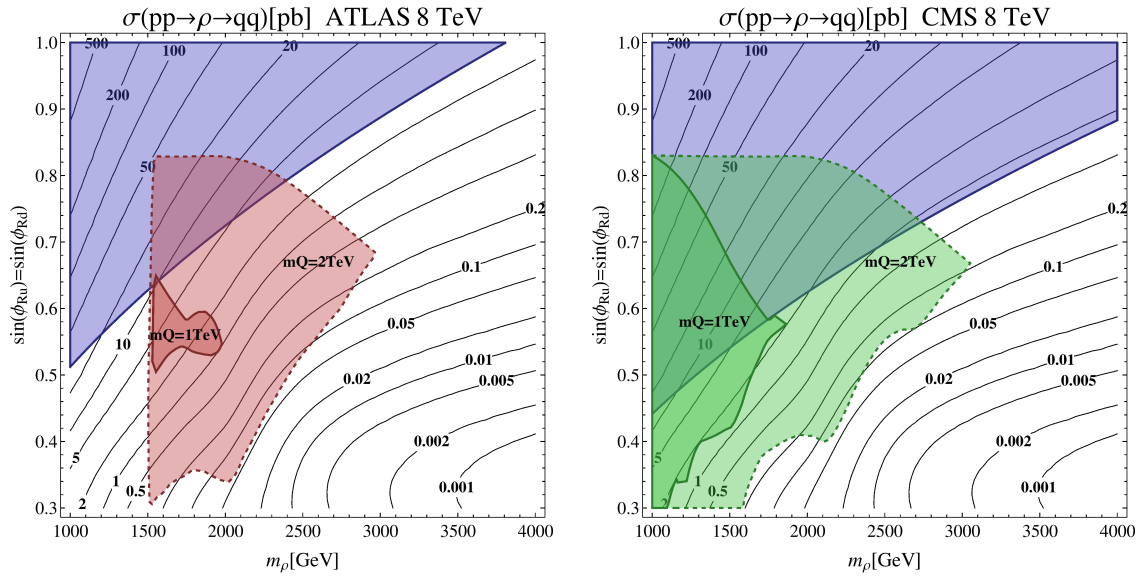


Figure 3.4. Exclusion plot for a colour octet with $g_\rho = 3$. In blue, region excluded by compositeness bounds. In red (ATLAS) and green (CMS) exclusion from direct production. The different regions correspond to 95% confidence level exclusion for two hypothetical scenarios where the quark partners are light ($m_Q = 1$ TeV, solid contour) or heavy ($m_Q = 2$ TeV, dashed contour).

If the ρ resonance is sufficiently light it can be produced on-shell in pp collisions at the LHC and then decay into jets. The natural search strategy is to look for a bump in the invariant mass distribution of dijets. We emphasise that this search is of a very different nature compared to compositeness bounds that rely on the angular distribution of dijets to distinguish new physics effects from the enormous QCD background. The resonance searches are

susceptible to the details of the bump and become less useful for wide resonances, which often appear in strongly coupled models.

We use the most recent analyses of ATLAS [121] and CMS [122, 123] based on 8 TeV data. The experiments provide a limit on $\sigma(pp \rightarrow \rho) \times \text{BR}(\rho \rightarrow q\bar{q})$ of resonances coupled to light quarks that can be applied to our scenario. We follow the procedure given by ATLAS for a Gaussian resonance with a particular width ranging from zero to 15%. Roughly the same strategy is applied to the CMS search, which provides limits on $\sigma \times \text{BR} \times \epsilon$. Our bounds are conservative as we explicitly take into account the width of the resonance. Both ATLAS and CMS perform a search for a relatively narrow resonance through a bump hunter algorithm. If the width of the the resonance exceeds a certain threshold the bump hunter search is invalidated and hence we discard the limit whenever the colour octet width is above 15%. In the m_ρ versus mixing angle plane, a grid of points is generated for which $\sigma \times \text{BR}$ are computed, and the efficiencies of the experimental cuts are analysed. The results are compared to the experimental limit, that only depends on the resonance mass, and are then interpolated to form exclusion regions.

The limits are obtained for a resonance with $g_\rho = 3$ and are presented in figure 3.4. The blue region corresponds to the bound on the effective four-fermion operators discussed in the previous section. The exclusions due to resonance searches for on-shell production are given by the red and green regions. These exclusion limits depend strongly on the fermionic spectrum, because of two effects. First, the increase in the width of the resonance, when decays to heavy partners open, possibly invalidates the search. This becomes particularly relevant when the decay into two heavy partners is kinematically accessible, see figure 3.3. Moreover, when other channels open up the signal strength is reduced through the branching ratios, since only the decay into SM quarks will generate a bump in the invariant mass distribution of the two leading jets. For this reason the region with $m_Q = 1$ TeV is more weakly constrained⁴. Note also that independent on the details of the model the region of high compositeness is not constrained because the width is in this case always too large.

3.3.4 $t\bar{t}$ Searches

In anarchic scenarios gluon resonances like the ρ are strongly coupled to the third generation and decay mostly into top quarks. For example in Randall-Sundrum scenarios, as considered in reference [102], one finds that the branching of heavy gluons into top right is almost 100%. To connect with our parametrisation, this model roughly corresponds to $g_\rho = 5$, $\sin \phi_{Rq} \approx 0$ for the light quarks and $\sin \phi_{Rt} = 1$ for the top quark. A strong bound on gluon resonances is obtained through searches of resonances that decay into $t\bar{t}$ pairs. Exclusion limits for this benchmark point have been reported in the searches from ATLAS [124] and CMS [125]. In the case of the Randall-Sundrum benchmark the heavy gluon resonance is excluded below 1.5 TeV at 95% confidence level.

In models that realise MFV, or more generally models with composite light quarks, the situation is different both for the production and decay of the heavy gluon, and one may

⁴We do not include here the partners of left-handed down quarks that would further increase the width if the decay into two heavy quarks is kinematically accessible.

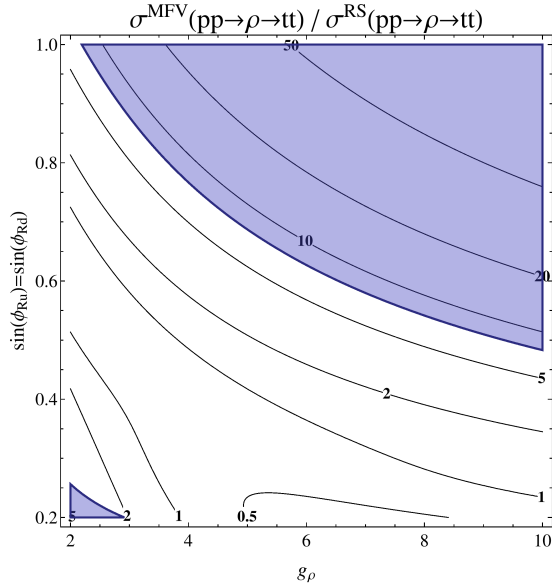


Figure 3.5. Ratio of $\sigma(pp \rightarrow \rho \rightarrow t\bar{t})$ in MFV models compared to the experimental benchmark Randall-Sundrum model. The blue region corresponds to a width greater than $0.2 m_\rho$ where the experimental bounds are not applicable. In this comparison the assumption is made that the decay to heavy fermions is kinematically forbidden.

obtain an even stronger bound. In these models the decay into third generation is typically not dominant. This depletion of the signal is however easily compensated by the increased production cross section. To get an idea of the bounds in this case, we can estimate $\sigma(pp \rightarrow \rho) \times \text{BR}(\rho \rightarrow t\bar{t})$ by rescaling the couplings of the anarchic scenario⁵. The numerical result is presented in figure 3.5. We see that the cross section in $t\bar{t}$ is typically larger than in anarchic scenarios, consequently slightly stronger bound will appear.

One caveat must be considered: similarly to the dijet searches, the experimental bound is obtained by looking for bumps in the invariant mass spectrum of $t\bar{t}$ pairs. This procedure depends on the width of the resonance and becomes inefficient for large widths. In anarchic scenarios the resonances are relatively broad. In the example of [102] the width is below 20% of the mass. The width can be larger in the MFV scenario due to multiplicity factors and the decay to heavy quark partners, as explained in the section before. The blue region in figure 3.5 corresponds to a width greater than $0.2 m_\rho$. In this region the experimental bound must be reconsidered. This region is, however, excluded by compositeness bounds discussed in the previous section. To compare the limits with the dijet searches also an exclusion plot in the m_ρ versus $\sin \phi_{Rq}$ plane is provided in figure 3.6. These exclusion plots have been obtained in a similar fashion as for the dijet limits from the previous section, including a careful treatment of the width of the heavy partners possibly invalidating the $t\bar{t}$ search.

It should be mentioned that in extensions of the MFV scenario based on $SU(2)$ rather than

⁵For simplicity we assume equal compositeness of up and down type right-handed quarks. The result is then approximately independent of parton density functions.

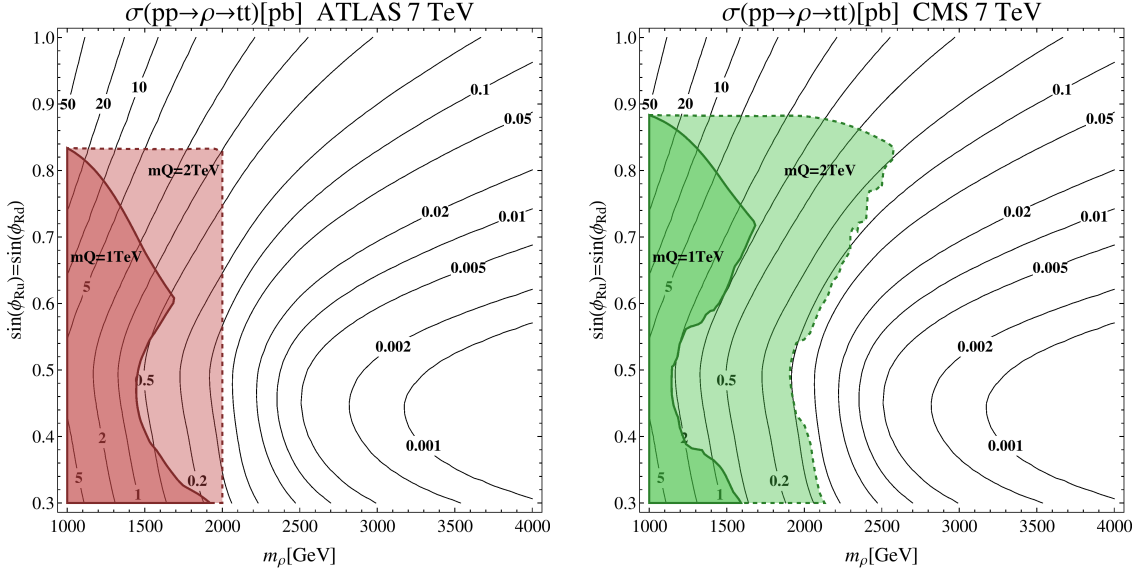


Figure 3.6. Constraints from $t\bar{t}$ searches by ATLAS (red) and CMS (green). The exclusion limits correspond to 95% confidence level for two hypothetical scenarios where the quark partners are light ($m_Q = 1$ TeV, solid contour) and where they are heavy ($m_Q = 2$ TeV, dashed contour).

$SU(3)$ flavour symmetries, the compositeness of the third generation can be different from the first two generations [99, 100]. Those scenarios are attractive phenomenologically as the light generations can be mostly elementary, avoiding compositeness bounds but with the same virtues as MFV for what concerns flavour. In this case the phenomenology of heavy gluons will be similar to anarchic scenarios.

3.3.5 Combined Bounds

The different bounds can be combined into a single statement on the mass of the colour octet, which provides a summary of the constraints obtained in this section. However, the direct limits on the colour octet depend heavily on the fermionic spectrum. Therefore, we differentiate two scenarios, one with light fermionic partners, $1 \text{ TeV} < m_Q < 2 \text{ TeV}$ and one with heavier partners $m_Q > 2 \text{ TeV}$. In the first we find

$$m_\rho > 1500 \text{ GeV} \quad (3.13)$$

at 95% confidence level. For the heavy scenario we find the constraint

$$m_\rho > 2000 \text{ GeV} \quad (3.14)$$

that is slightly stronger than the bound in anarchic scenarios. This constraint holds for all values of the mixings $\sin \phi_{Rq}$ and tighter bounds on the octet mass are obtained for specific mixings. More stringent bounds can be inferred from flavour physics and precision tests, though these rely on extra assumptions on the structure of the theory. Moreover, these bounds do not directly test the hypothesis of large compositeness of the first and second generation.

3.4 Bounds on Left-Handed Quark Partners

The fermionic partners can be divided into two categories, the left-handed and the right-handed sector. In this section we discuss fermionic partners in the left-handed sector and in the next section the right-handed sector is discussed. We focus in particular on the $(\mathbf{2}, \mathbf{2})_{2/3}$ coloured fermions. These states can of course be pair produced through strong interactions, see [126] for a study in anarchic scenarios. The double production is equal for both left-handed and right-handed partners and in the next section a bound is obtained from the experimental analysis in reference [127]. When translated to MFV scenarios the exclusion for these states is around 600 GeV. Here we derive the bound obtained from single production through the electroweak vertices of figure 3.3. The experimental results in reference [107] allow to derive a bound significantly stronger than the top partners bounds. The single production of left-handed partners is dominated by t -channel exchange of electroweak gauge bosons producing a forward jet ($p_T \sim m_W$) and a heavy quark. The heavy quark decays mainly through weak interactions into jets and W , Z or Higgs⁶. The jet has the same flavour as the mother particle, therefore only light quark jets are present in the final state.

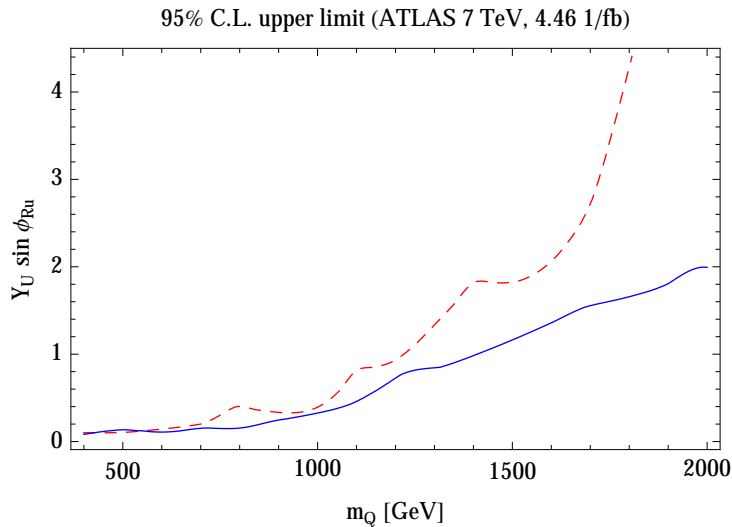


Figure 3.7. Exclusion of left-handed partners of the up quark by ATLAS [107]. The red dashed (blue solid) line shows the 95% CL observed upper limit on $Y_U \sin \phi_{Ru}$ obtained from the search of charge 2/3 (5/3) heavy quarks. The regions above the lines are excluded.

In the anarchic scenarios only third generation quarks can be produced this way, because the coupling is proportional to the degree of compositeness which is significant only for the third generation. To produce third generation partners one needs to scatter a W or Z boson and a top, the latter originating from the splitting of a gluon. This will be perhaps the most promising channel for the production of heavy fermions at LHC14 [128, 129] but in the present run suppression from parton density functions and low luminosity is too severe

⁶We do not include the decay into Higgs in our analysis. This was recently studied in [111].

for this process to be dominant. This is different with composite light quarks since the heavy partners can be directly produced with the proton constituents. In this case one can produce the left-handed partners through diagram b) in figure 3.8 with access to the valence quarks of the proton. A connected aspect is that the width of the resonance is larger than in anarchic scenarios.

The search for vector like quarks coupled to the first generation was performed by the ATLAS collaboration based on [130], see also references [131–134]. This search can be applied to our scenario, and we use the most recent results in [107] obtained with 4.64 fb^{-1} luminosity and 7 TeV centre of mass energy. The search directly constrains the combination $Y_U \sin \phi_{Ru}$. The derived exclusion is shown in figure 3.7 for the charge 2/3 and exotic charge 5/3 states, the latter being the strongest. Recall that in MFV scenarios there is a constraint

$$Y_U \sin \phi_{Ru} \gtrsim 1, \tag{3.15}$$

necessary to reproduce the top mass. From this it follows that the left-handed partners are often excluded up to 2 TeV and always below 1.5 TeV. This can only be avoided in extensions of MFV where the third generations can be split [99, 100].

We emphasise that this is an extremely strong bound that pushes the model into fine-tuning territory. In view of the recent discovery of a 125 GeV resonance [1, 2] some of the fermions associated with the top should be light if the theory shall remain natural. Recent analyses have shown that the lightest top partner should be typically below 1 TeV in a natural theory [64, 66, 73–75, 135]. In MFV scenarios the mass of the top partners is the same as the one of the light generations, up to mixing effects. Hence, we can translate the bound on the light generations into a bound on the top partners.

3.5 Bounds on Right-Handed Quark Partners

The phenomenology of partners of right-handed quarks is entirely different. The single production through electroweak interactions for these partners is absent and they mostly decay into two or three jets leading to multi-jet final states. The majority of multi-jet searches at LHC, being motivated by supersymmetry, assume a large missing energy typically of the order of few hundreds GeV or more. In our scenario, the missing energy in the event is a consequence of jet calibration accumulated by all jets, typically below 50 GeV. Therefore, we do not expect regular supersymmetric searches to play a role in constraining the parameter space of right-handed compositeness. Analysis of the relevant ATLAS and CMS searches will be done in the next two sections, divided into single production (through heavy resonances) and double production (both through QCD and heavy resonances). Dedicated searches that could improve the experimental reach will be discussed in the section 3.6. Before analysing the different searches at the LHC we first review production modes and decay channels in detail.

Production Modes

The heavy fermions associated to the first generation can be singly produced in association

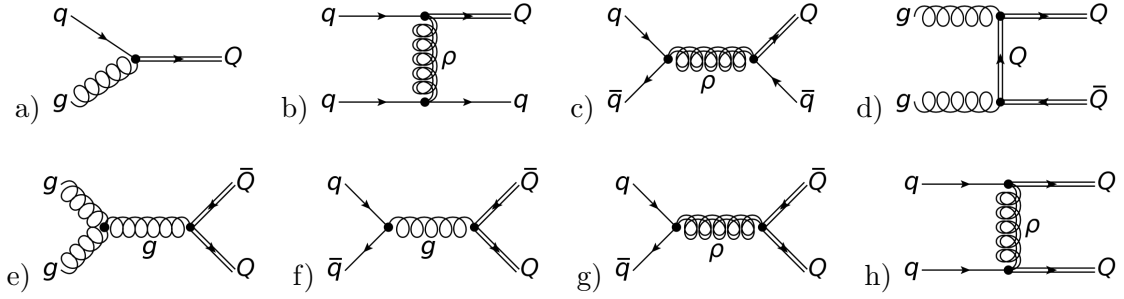


Figure 3.8. Examples for the fermion production modes: a) chromomagnetic s -channel, b)-c) single production and d)-h) double production.

with a quark via a t -channel exchange of the colour octet⁷. Double production of heavy fermions proceeds through s -channel gluon or colour octet exchange or a t -channel colour octet or heavy fermion. Both the production modes with either an s -channel or a t -channel colour octet dominate. The various production modes are depicted in figure 3.8. The relevant production modes can be summarised in associate single production and double production. For these modes the production cross section as a function of the colour octet mass and the heavy quark mass is given in figure 3.9.

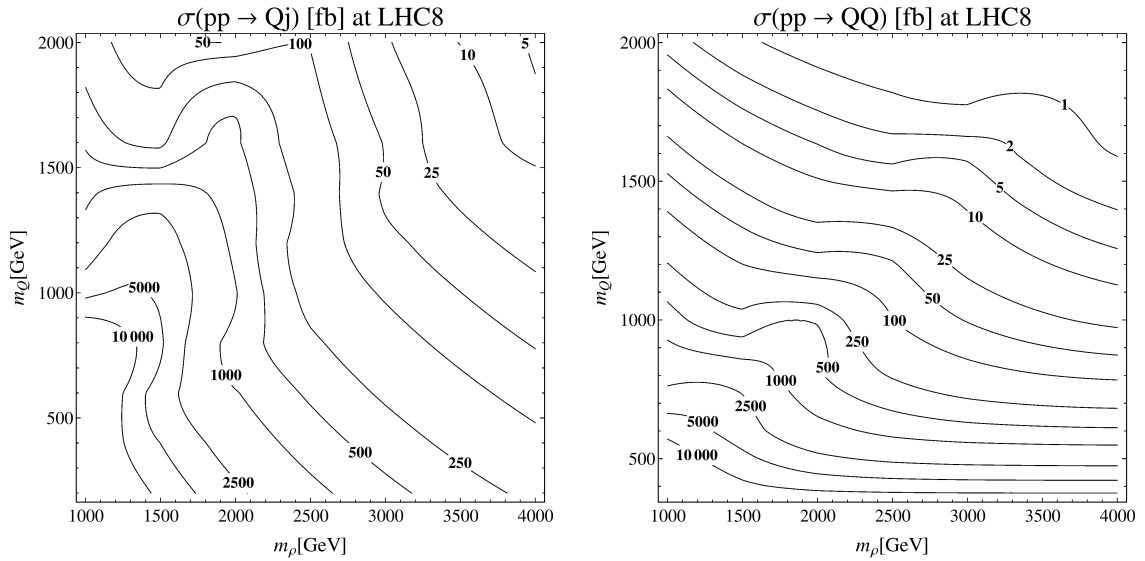


Figure 3.9. Displayed on the left is the total cross section of associated production of a heavy quark partner at LHC8 obtained with MadGraph [112] for $g_\rho = 3$, $\sin \phi_{Ru} = \sin \phi_{Ru} = 0.6$. On the right double production of right-handed quarks partners (t_R excluded) through QCD and heavy gluon exchange is presented.

Decay Channels

The heavy partners of SM right-handed quarks are singlets of $SO(4)$, because of this fact

⁷Single production via the chromomagnetic interaction (3.5) will be sub dominant from the observation that the coefficient is loop suppressed.

they decay almost entirely into jets. The different decay channels are displayed in figure 3.10. The chromomagnetic interaction induces a decay to a gluon and a quark and generates a width

$$\Gamma_{\text{chromo}}(Q \rightarrow qg) = \frac{4}{3} \alpha_s \kappa^2 \frac{1}{m_Q^5} |m_Q^2 - m_q^2|^3, \quad (3.16)$$

where κ contains the mixing angles for either up or down type quarks. This decay is induced at one-loop level and is typically very small, competing with three-body decay mediated by an off-shell ρ . An analytical expression for the three-body decay is quite lengthy and therefore we only give the limiting behaviour (with all light quark masses set to zero $m_q = m_{q'} = 0$ and narrow width approximation for the ρ : $\Gamma_\rho \ll m_\rho$)

$$\Gamma_{3\text{-body}}^\rho(Q \rightarrow qq'\bar{q}') = \begin{cases} \frac{\alpha_s^2}{12\pi} \left[(X_L^{qQ})^2 + (X_R^{qQ})^2 \right] \sum_{q'} \left[(X_L^{q'q'})^2 + (X_R^{q'q'})^2 \right] \times \\ \left[\frac{6m_\rho^4 - 3m_Q^2 m_\rho^2 - m_Q^4}{6m_Q m_\rho^2} + \frac{m_\rho^2 (m_\rho^2 - m_Q^2)}{m_Q^3} \log \frac{m_\rho^2 - m_Q^2}{m_\rho^2} \right] & \text{if } m_Q < m_\rho \\ \frac{\alpha_s}{6} \left(\frac{m_Q^6 - 3m_Q^2 m_\rho^4 + 2m_\rho^6}{m_Q^3 m_\rho^2} \right) \left[(X_L^{qQ})^2 + (X_R^{qQ})^2 \right] & \text{if } m_Q \gg m_\rho \end{cases} \quad (3.17)$$

The full analytic expression including the width of the heavy colour octet has been used for the analyses. This decay suffers from the octet being off-shell and phase space suppression. Finally a decay to SM quarks plus a longitudinal W , Z or Higgs [35] is possible and leads to a partial width equal to

$$\Gamma_{2\text{-body}}^{\text{EW}}(Q \rightarrow qH) \approx \frac{1}{4\pi} \frac{m_q^2 \cos^2 \phi_{Ru}}{v^2 \sin^2 \phi_{Ru}} m_Q. \quad (3.18)$$

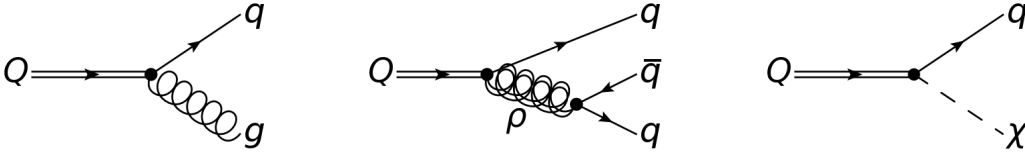


Figure 3.10. Fermion decay channels: shown are two-body decay via the chromomagnetic operators, three-body decay via an off-shell colour octet and electroweak two-body decay.

In the MFV scenario the electroweak two-body decay is completely negligible for the first generation as it is suppressed by the light quark mass over the vacuum expectation value. It is also sub-leading for the second while it is certainly dominant for the third generation. Note that this conclusion does not hold in the anarchic scenario, in that case $\sin \phi_{Ru}$ is smaller and the decay through electroweak interactions dominates producing $W, Z, h + jets$ final states.

The phenomenology and experimental strategies are strongly dependent on whether the two-body or three-body decay dominates, since this will result in either two or three jet final states. One interesting fact is that for $m_Q < m_\rho$ two-body and three-body decay scale

in the same way with the masses. In figure 3.11 it is shown in what regions of parameter space the two-body or three-body decay dominates. One should however keep in mind that other contributions could exist which possibly spoil this conclusion. Indeed, the decay widths are in any case extremely small and so even normally sub-leading effects could be important.

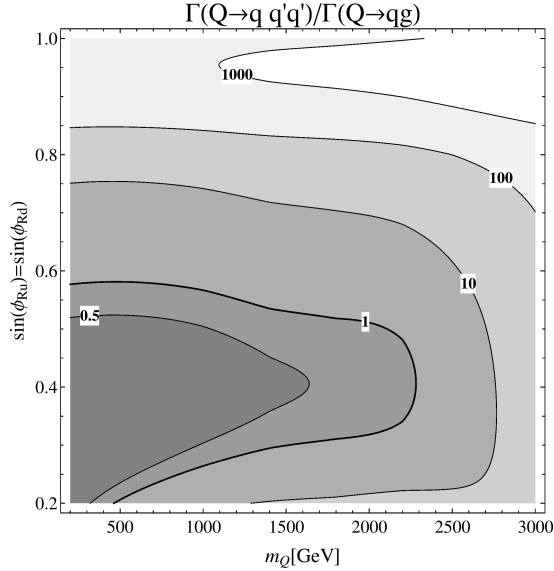


Figure 3.11. Relevance of the heavy fermion three-body decay compared to the two-body chromomagnetic decay displayed in the $(m_Q, \sin \phi_{Rq})$ plane for $m_\rho = 2.5$ TeV and $g_\rho = 3$. The thicker contour line indicates where the two and three-body branching fractions exactly equal each other.

Bounds on 3rd Generation Partners

Before delving into the direct searches of partners of the light generations let us consider the indirect bounds that can be derived from top partner constraints. Third generation partners behave very differently from light ones. Compositeness of left-handed top and bottom is sizeable so even the right-handed partners decay through electroweak interactions as in the anarchic scenario. ATLAS places a strong bound on these states [127]. The precise bound depends on the branching fraction (in the model under consideration the singlet \tilde{T} decays in Wb , Zt and ht) but in any case it typically ranges between 500 and 700 GeV. If \tilde{T} is at the bottom of the spectrum then the branching fractions can be predicted, $\text{BR}(\tilde{T} \rightarrow Wb) \simeq 2\text{BR}(\tilde{T} \rightarrow ht) \simeq 2\text{BR}(\tilde{T} \rightarrow Zt)$, corresponding to an exclusion around 600 GeV.

In models that realise MFV this bound translates into a bound on the mass of light generation right-handed partners. This can only be avoided in extensions of MFV that allow to split the third generation [99, 100]. However, this can only be done at the price of making the third generation partners heavier than the first two, which conflicts with naturalness. With this in mind we proceed to extract the direct exclusion limits from the LHC, which as we will show are still rather weak.

3.5.1 Single Production

In these scenarios the heavy quark is singly produced in association with a light quark. This leads to three or four-jet final states at parton level, depending on whether chromomagnetic or colour octet mediated decay prevails.

Chromomagnetic Decay Scenario

The topology of the event is a pair of jets (one quark jet and one gluon jet) with the invariant mass of the heavy partner and a third jet from the spectator quark. The bump hunter search of resonances decaying into dijets already considered in section 3.3 looks for features in the invariant mass of the two leading jets, where leading refers to p_T ordering. Therefore this search will be effective if the heavy fermion is the father of the two leading jets, a situation that depends on m_Q as we now explain.

First, we discuss the p_T distribution of the recoiling jet due to the t -channel production of the heavy quark. One might think that the typical p_T of the recoiling quark is controlled by the mass of the heavy fermion. In our region of parameter space however this is not true due to parton density function (PDF) suppression. In fact we find that the average p_T is almost independent on m_Q being controlled by the total energy. This can be seen in figure 3.12 on the left. The solid line is the average p_T of recoiling quark obtained with $m_\rho = 2$ TeV. For $E_{CM} = 8$ TeV this is around 500 GeV. Moreover this feature persists for different values of m_ρ . In fact since as we have seen m_ρ cannot be light, approximating the interaction with an effective operator is always a good approximation. Changing m_ρ simply rescales the cross section. Quantitatively, a good approximation for the cross section is given by

$$\frac{d\sigma}{d|p_T|} \propto \frac{1}{S} \frac{p_T^2}{m_\rho^4} \left(p_T + \sqrt{m_Q^2 + p_T^2} \right) \left(\frac{p_T^2 + m_Q^2 + p_T \sqrt{m_Q^2 + p_T^2}}{S} \right)^{-\alpha}, \quad (3.19)$$

where $\alpha \sim 3 - 6$ is a slowly varying function of \hat{s} determined by the PDFs. This result is derived in appendix A.2.

Given the p_T of the recoiling quark we can derive the p_T ordering of the jets in an event. Neglecting spin effects, the jets from the heavy quark will be isotropically distributed in their centre of mass frame with $p_T \simeq m_Q/2$. Boosting to the lab frame one finds $p_T^{1,2} \simeq \left| p_T^{\text{spectator}} \pm m_Q/2 \right|$. Therefore, for large m_Q we expect the two jets to be leading and the opposite for small m_Q .

This is confirmed by our simulation. In figure 3.12 on the right we plot the probability of the spectator quark to be the first, second or third jet in p_T . As we increase m_Q the spectator quark tends to have the lowest p_T . Therefore in this region the standard dijet search will capture the signal. However, with the production cross sections given in figure 3.9 no bound is obtained in our model if we perform a recast. Moreover, recent updates of dijet searches require a cut on the invariant mass of the jet pair to exceed 1 TeV so this search is unlikely to produce a bound even in the future. The situation for $m_Q < 1.5$ TeV is even less promising, as in this case the spectator quark often gives rise to the first or second jet so the dijet search will not be efficient. In this case a different ordering of jets should

be considered. Indeed requiring at least three jets in the final state and looking for bumps in the invariant mass of the second and third jet seems a promising strategy to reduce the background.

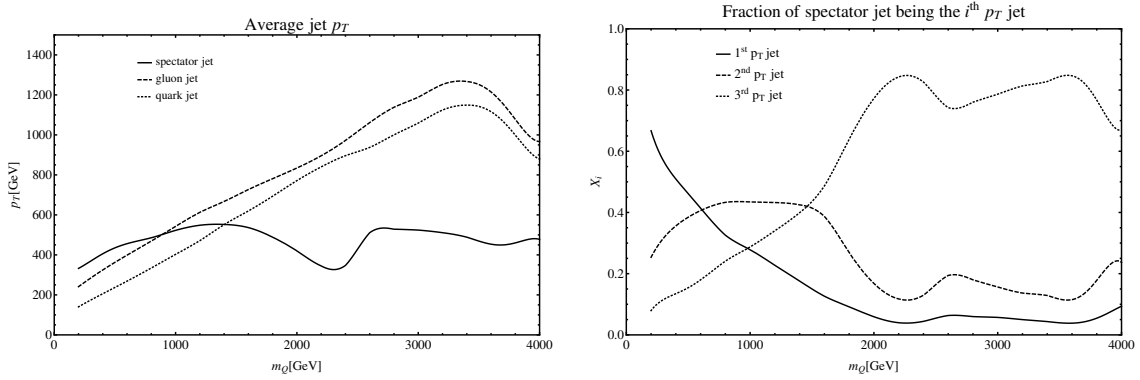


Figure 3.12. Plots of the p_T spectrum of the three jet final state. On the left the average p_T of the three different jets in the event as a function of m_Q are displayed. On the right the fraction of events with the spectator jet being the i^{th} p_T jet for LHC8.

Three Body Decay Scenario

In this case we have a four jet final state with three jets reconstructing the mass of the heavy quark. The searches for four jets by ATLAS [136, 137] and CMS [138] with no missing energy cuts are optimised for pair production of a heavy resonance, both decaying into two jets. Although these searches share the same final state, they have a low efficiency for our signal, because of the different three plus one jet topology. From these experimental searches no exclusion limit for the model considered can be obtained.

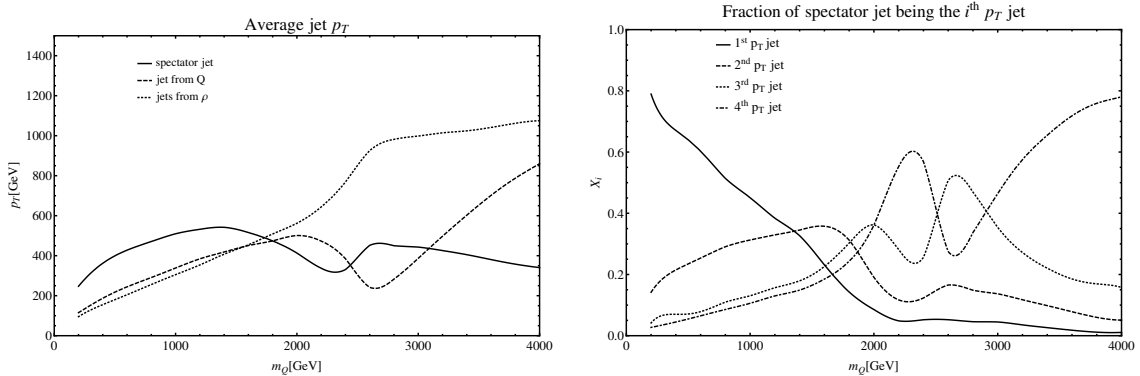


Figure 3.13. Plots of the p_T spectrum of the four jet final state. On the left the average p_T of the four different jets in the event as a function of m_Q are displayed. On the right the fraction of events with the spectator jet being the i^{th} p_T jet for LHC8.

A search strategy optimised for this signal should obviously try to capture the bump in the invariant mass of the trijets. As for the previous case an important element is the ordering of jets, which is shown in figure 3.13 on the right. Qualitatively, this is similar to the

two-body decay, however, as expected the recoiling jet is more likely to be the leading jet. This happens 50% of the times for a fermion with mass of 1 TeV. Therefore, in this case a dedicated search pairing the second, third and fourth jet is expected to be very effective. A detailed discussion for a proposal search for this final state is presented in section 3.6.

3.5.2 Double Production

In the case of double production of two heavy partners, final states with four or six jets are possible at parton level. Five jets could also be obtained in certain regions of parameters where 2-body and 3-body decay are comparable but we will neglect this possibility. In the four jet case two pairs of jets form the same invariant mass equal to the heavy quark mass. In the six jet case two sets of three jets each form the invariant mass of the heavy quark. Both scenarios are discussed in the remainder of this section.

Chromomagnetic Decay Scenario

CMS and ATLAS analysed double dijets final states, where they look for a pair-produced heavy resonance decaying into two jets in [136–138]. The ATLAS analysis only considers a mass region between 150 and 350 GeV, whereas CMS considers a region from 320 to 1200 GeV. Since our interest is mainly in the mass region up to around 1 TeV for the heavy quark partners, only the CMS analysis is considered for this topology. This search is expected to be effective for relatively low partner masses since for high masses the three-body decay is favoured, see figure 3.11.

The CMS analysis investigates events with at least four jets with $|\eta| < 2.5$ and $p_T > 150$ GeV and then combines the four highest- p_T jets into dijet combinations with $\Delta R_{jj} > 0.7$. Then the dijet pair combination with minimal $\Delta m/m_{\text{avg}}$ is selected, where $\Delta m = |m_{\text{jj}}^{(1)} - m_{\text{jj}}^{(2)}|$ and $m_{\text{avg}} = \frac{1}{2}(m_{\text{jj}}^{(1)} + m_{\text{jj}}^{(2)})$, with a maximum $\Delta m/m_{\text{avg}} < 0.15$ to suppresses the QCD background. Then a last requirement is

$$\Delta = \sum_{i=1,2} p_{T,i} - m_{\text{avg}} > 25 \text{ GeV}, \quad (3.20)$$

ensuring a smoothly falling paired dijet mass spectrum. In the absence of any observed resonances CMS then provides the limits on the folded $\sigma \times \text{BR} \times \epsilon$ as a function of the resonance mass, to which our scenario will be compared to obtain limits.

Our scenario is almost completely equivalent to the coloron model considered in the CMS analysis only differing in the production modes. Therefore we expect similar final state topology and the selection criteria to be close to optimal. To compare with the coloron exclusion limits we generate the dijet resonances using our FeynRules-MadGraph-Pythia-Delphes chain. Note that also for the model considered here the width of the heavy resonance is negligible compared to the experimental resolution. For a set of points in the m_Q versus $\sin \phi_R$ plane we analyse the efficiencies and obtain a value for $\sigma \times \text{BR} \times \epsilon$ to be compared to the CMS limit.

We are interested in the possible exclusion potential, and therefore we plot the limiting cross section σ_{lim} divided by the new physics cross section σ_{NP} of our model which removes the dependence on branching ratios and acceptances. This gives a good indication of the

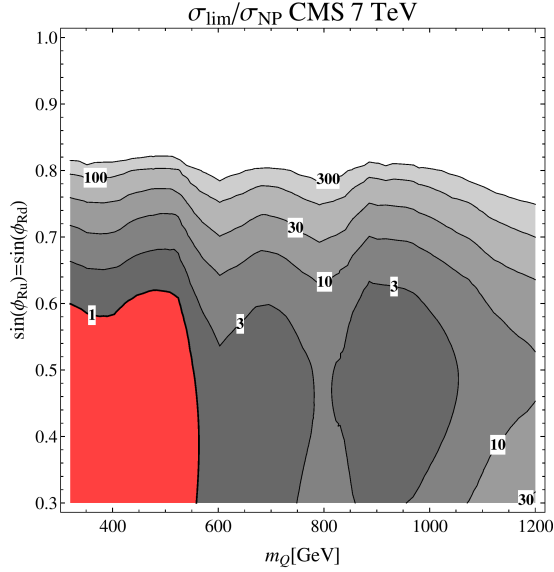


Figure 3.14. Constraints from the CMS double dijet search [138] for the double production combined with chromomagnetic decay scenario for $g_\rho = 3$ and $m_\rho = 2.5$ TeV. Displayed is the limit cross section over the new physics cross section in the m_Q versus $\sin \phi_R$ plane. The red region is already excluded at 95% CL by the current searches, whereas the grey contours give an indication for the needed increase in sensitivity to exclude further regions. The peculiar shape, the “island” in particular, is accounted for by upward fluctuations in the data around 600 and 800 GeV.

increase in sensitivity required to exclude certain regions of parameter space. The resulting contour plot is given in figure 3.14. Any region with $\sigma_{\text{lim}}/\sigma_{\text{NP}} \leq 1$ is excluded by the current searches, this is the red contour with the thick edge. We conclude that heavy partners with masses between 320 and 500 GeV are excluded, provided that the chromomagnetic decay dominates.

Three Body Decay Scenario

In this case there is a six jet final state, where two combinations of three jets originate from identical mother particles. The search closest to this topology is performed by CMS [139] where they look for the invariant mass of three jets in events with at least six jets with $p_T > 70$ GeV and $|\eta| < 3.0$. Furthermore, the total scalar sum of p_T is required to be higher than 900 GeV for each event. The search aims to capture pair produced trijet resonances and is interpreted in terms of RPV gluinos decaying into three jets. The six highest p_T jets are combined into all 20 three-jet combinations and in order to reduce both combinatorial and QCD background the requirement

$$M_{jjj} < \sum_{i=1}^3 p_T^i - \Delta, \quad (\Delta = 160 \text{ GeV}) \quad (3.21)$$

for each triplet is imposed. The acceptance is then defined as all the events with at least one triplet of jets passing this cut. The experiment provides the 95% CL limits on $\sigma \times \text{BR}$ as a function of the resonance mass in the range from 280 up to 1000 GeV.

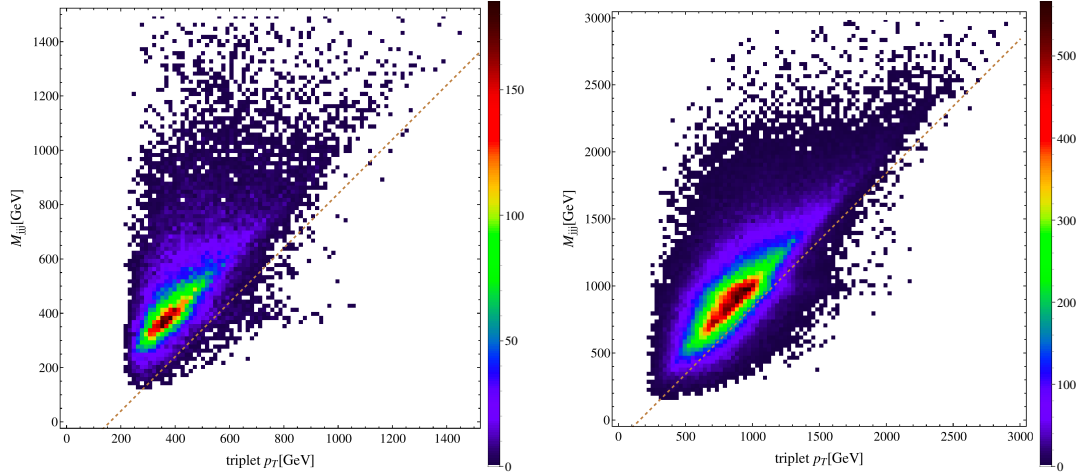


Figure 3.15. Distribution of the triplet mass M_{jjj} versus the triplet scalar p_T of all 20 triplets in each event for LHC7. The distributions are shown for quark partner masses of 400 GeV (left) and 1000 GeV (right). In these figures the selection criterion from equation (3.21) is given by the orange dashed line. These plots give an indication of the leakage of combinatorial background into the signal region.

Even though our topology shares the same final state as the RPV gluinos studied in the CMS analysis the kinematics are quite different. One of the main differences is that the quark partners are produced mostly by the colour octet rather than the gluon. Moreover the gluino decay is modelled by a four-fermion effective interaction, whereas the heavy quark decay proceeds through an off-shell colour octet. Hence, for the analysis to be applicable, roughly the same acceptances for both scenarios should be obtained. Especially the selection criterion in equation (3.21) should have the same effect on the combinatorial background and the trijets coming from the decay of the heavy partner. This is relevant since after this selection criterion a resonance search in the triplet invariant mass spectrum is performed. In order to analyse the effect of the cuts, in particular (3.21), our signal has been simulated and the distribution of events in the trijet mass versus triplet scalar p_T has been plotted in figure 3.15.

The CMS analysis is optimised for the gluino scenario choosing $\Delta = 160$ GeV and for triplets originating from the gluino the probability for passing this selection criterion ranges between 2% and 13% depending on the gluino mass. In figure 3.16 the acceptance for our signal is plotted, from which one can see that the acceptances are generally higher, however, also the combinatorial background grows rapidly. At high masses we observe that the combinatorial background starts to dominate over the signal, hence the selection as in equation (3.21) is not efficient for our topology. Therefore, no significant bound can be extracted. However, the search for this final state is potentially interesting and could be optimised for the topology of right-handed compositeness.

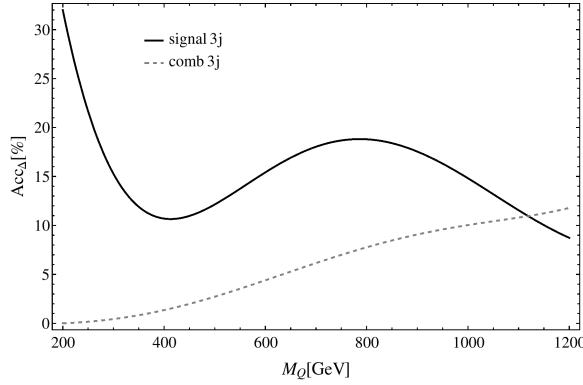


Figure 3.16. Acceptance of triplet events for the selection criterion in equation (3.21). The black line shows the acceptance for the triplets originating from one of the heavy quarks, whereas the grey dashed line shows the acceptance for the other triplets forming combinatorial background.

3.6 Dedicated Searches

In the previous section the existing multi-jet searches of ATLAS and CMS were recasted to set limits on the heavy quark partners. These limits are rather weak for the right-handed partners, see for example figure 3.14. The existing searches are not optimised to the most distinctive topology of the model, the single production of the heavy quark Q in association with a light jet. In this section we are going to propose searches that exploit the characteristic behaviour of this production mechanism, namely $pp \rightarrow Qq$. This leads to two plus one jet topologies for the two-body decay and three plus one jet topologies for the three-body decay of the heavy quark partners. The topology is characterised by at least three hard jets, where some of the jets reconstruct the mass of the fermion Q . The main background arise from QCD jets and is dominated by the diagrams given in figure 3.17.

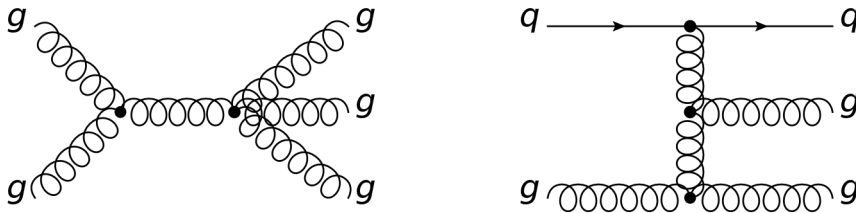


Figure 3.17. Typical QCD background events leading to three high- p_T jets.

When looking at dijet searches, a cut on the hardness of the third and fourth jet aids in reducing the background, but the effect is not too dramatic. For example, in 8 TeV QCD samples where the two leading jets have $p_T > 150$ GeV, asking for a third one with $p_T > (25, 70, 100 \text{ and } 150)$ GeV has an efficiency of (40, 9, 4 and 1)%. A larger reduction of the background can be achieved with more sophisticated cuts, for which we provide details later.

Other studies which have some overlap with the single production topology are the CMS and ATLAS studies of double dijets. In the previous section, we applied one of these searches to

double production $pp \rightarrow QQ$ where $Q \rightarrow jj$, concluding that the reach is rather weak. In the single production case the sensitivity is even lower, as the topology does not resemble the double dijet. For example, the efficiencies of the signal $pp \rightarrow qQ$ where $Q \rightarrow 3j$ to this search for $m_Q = 1, 2$ and 3 TeV is in the range of 1-4%. As in the case of dijet bump searches, a dedicated search needs to be performed. In the following we discuss the kinematic variables which show a better discrimination power for signal versus background in this topology. Two benchmark scenarios are considered which correspond to $m_\rho = 2500$ GeV, $g_\rho = 3$ and $\sin \phi_{R_{u,d}} = 0.6$, where the heavy fermion partner mass equals $m_Q = 600$ and 1200 GeV. The relevant kinematic variables are discussed in the next paragraphs.

The H_T Variable

We use the standard definition of the H_T variable

$$H_T = \sum_{i=\text{jets}} p_{T,i}. \quad (3.22)$$

In figure 3.18 (left) one can see that signal has a larger H_T distribution than the background, and it increases with m_Q . Note that in this plot and all the following ones, basic cuts on the jets are imposed and are given by $p_{T,j} > 70$ GeV and $|\eta_j| < 2.5$.

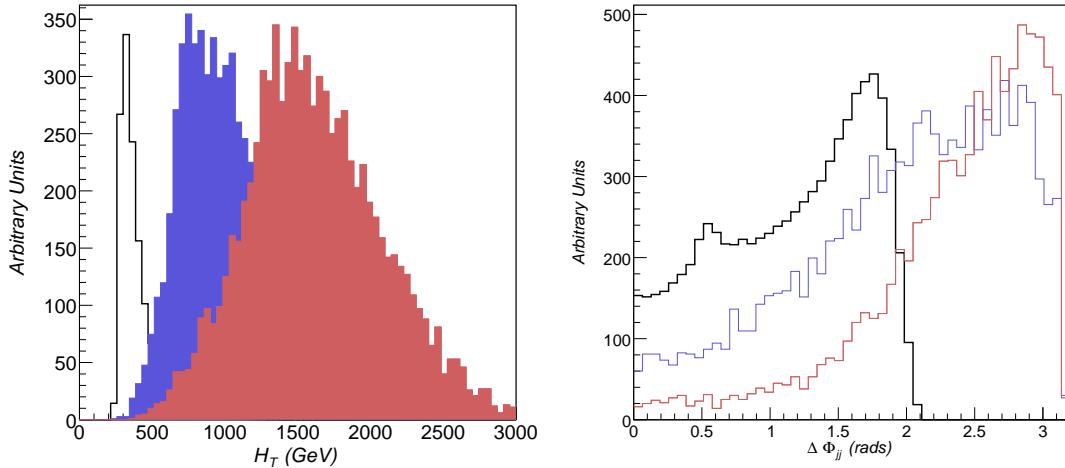


Figure 3.18. The left plot displays the H_T distribution for QCD events with $n_j \geq 3$ (black line), 2+1 signals with $m_Q = 600$ GeV (purple distribution) and $m_Q = 1200$ GeV (magenta distribution) in LHC8. The right plot presents the $\Delta\phi$ distributions between the two sub-leading QCD jets (black) and the dijets from the decaying Q particle, with $m_Q = 600$ (1200) GeV in blue (red). Both figures are generated at parton level, and in the right figure truth information is used to identify the jets from the heavy quark.

Angular Distribution

Since the heavy resonance is produced with little boost, one would expect a symmetric angular distribution among the jets coming from the decaying particle. In the $Q \rightarrow 2j$ case,

the daughter jets tend to be produced with $\Delta\phi = \pi$, whereas in the $Q \rightarrow 3j$ case one would expect a distribution near $\Delta\phi = 2\pi/3$.

In the QCD case, though, jets would not have such a preference. In three jet QCD events, like the ones in figure 3.17, one would expect a rather symmetric distribution of jets, more so as we increase the cut on p_T . This is seen in figure 3.19, where as we increase the p_T threshold, the distribution is more and more peaked towards $2\pi/3$, hence the *Mercedes* configurations. With the same cut on all jets, this configuration minimises the overall centre of mass energy of the three jet system, $M \sim 3p_{T,\min}$. For the configuration where the sub-leading jets are close and back-to-back with the leading jet, the minimal mass equals $M \sim 4p_{T,\min}$. Here the two sub-leading jets have $p_T = p_{T,\min}$ and the leading jet p_T is $2p_{T,\min}$ to balance momentum.

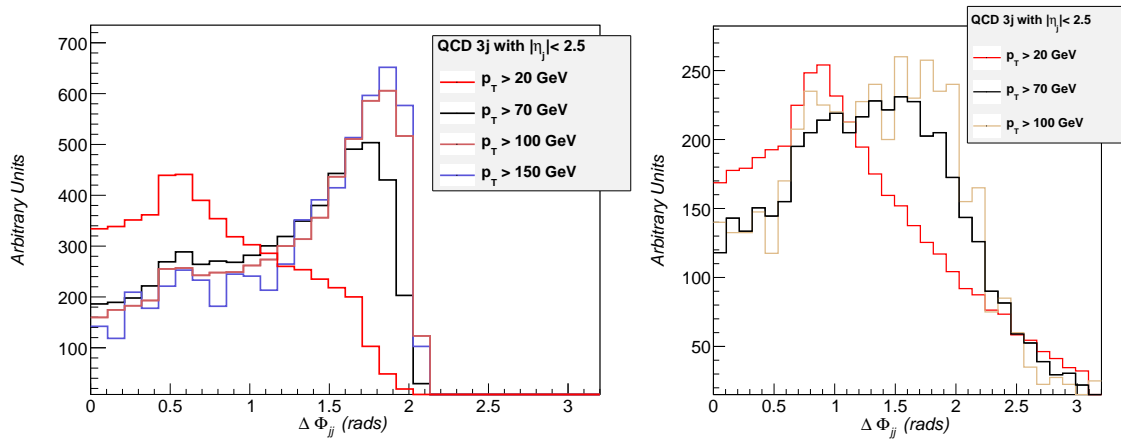


Figure 3.19. The angular distribution between the two sub-leading jets in QCD events, as a function of the p_T cuts on all jets for LHC8. The left plot is the partonic result and the plot on the right is reconstruction level.

This is shown in figure 3.18 (right), where we see that the jets from the Q decay tend to be symmetric, more so as the mass increases and the Q has smaller boosts. We find similar discriminating features when looking at the $Q \rightarrow 3j$ case, now with the peak at $\Delta\phi = 2\pi/3$ for the three jets from Q . Note, though, that figure 3.18 (right) has been done using parton level truth events (where the information of the mother particle was known). When showering, detector effects and combinatorial background are taken into account, the discriminating power of $\Delta\phi_{jj}$ is greatly reduced.

Mass Bump Reconstruction

An obvious characteristic of the signal is the presence of a mass bump, if the right combination of jets was chosen. In the previous section, we showed in figures 3.12 and 3.13 (right panels), that the leading jet tends to be the spectator jet for low $m_Q \lesssim 1$ TeV, more so for the 3+1 than the 2+1 topology. We then choose in each event the two (three) sub-leading jets and form an invariant mass. In figure 3.20 (left), we plot the invariant mass of the sub-leading jets for the 2+1 topology. The QCD distribution is peaked at low values, whereas

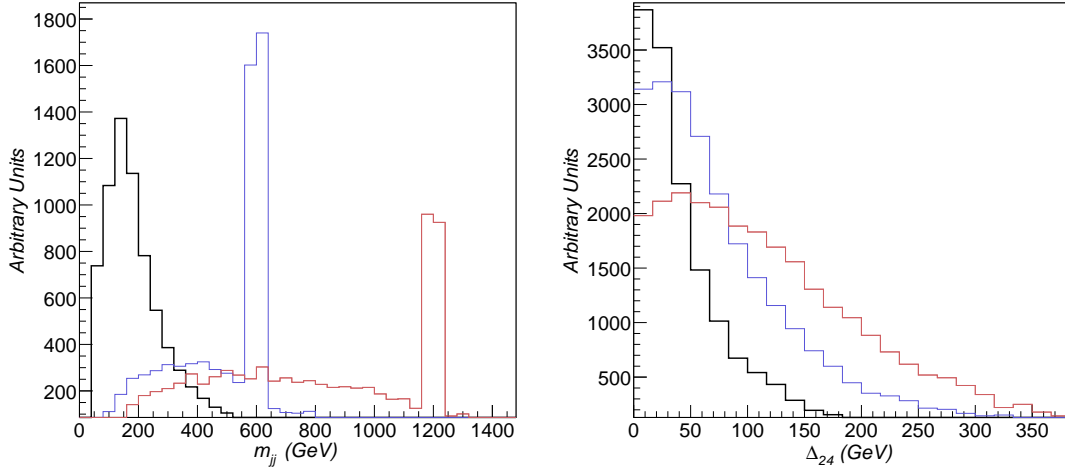


Figure 3.20. The left plot shows the invariant mass distribution of the two sub-leading jets for QCD events (black) and signal events in the 2+1 topology with $m_Q = 600$ (1200) GeV in blue (red) at LHC8. The right plot presents the distribution Δ_{24} for QCD events (black) and signal events in the 3+1 topology with $m_Q = 500$ (1000) GeV in blue (red) at LHC8. Both plots are generated at parton level.

there is a peak in the signal at high m_{jj} . The peak is more pronounced (lower combinatorial background) for low m_Q , but also the leakage of QCD events in the distribution is larger.

Kinematic Gap Variables

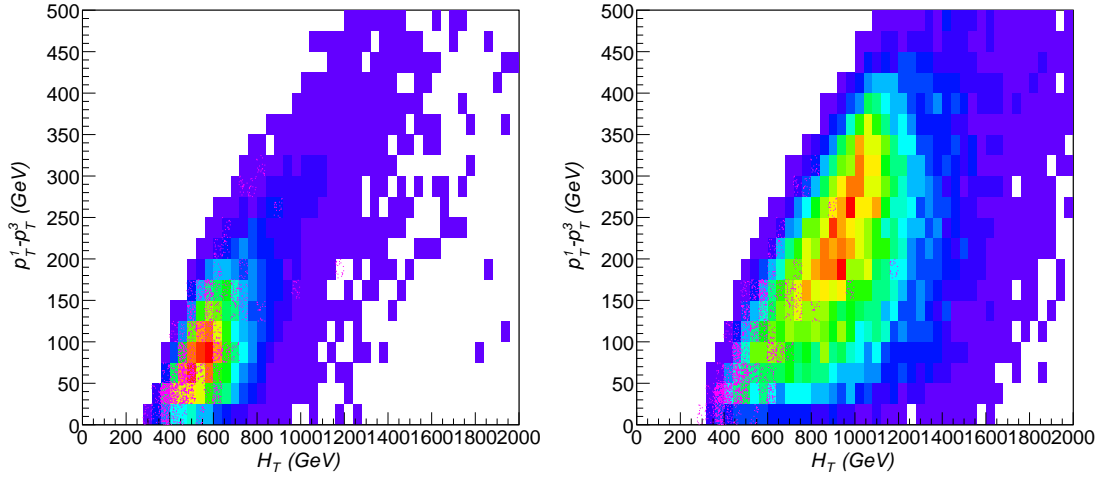


Figure 3.21. H_T versus $p_T^1 - p_T^3$ for the 3+1 topology at LHC8 for $m_Q = 500$ GeV (left) and 1 TeV (right). The pink-scatter plot corresponds to the QCD background. The events are at detector level for LHC8.

One could also exploit the gaps among the jet momenta and invariant masses. This is

especially interesting in the case of 3+1 topologies, on which we focus in the following. In figure 3.20 (right) we plot the variable $\Delta_{24} = \sum_{i=2,3,4} p_{T,i} - m_{234}$, a gap between the p_T 's and invariant mass. In the QCD background, the invariant mass and the p_T sum are close to each other, and we expect it to be peaked at low values. In the signal events, the invariant mass tends to be smaller than the scalar sum of p_T 's.

The gap between the jets in the event can also be used to discriminate between signal and background. In figure 3.21, we plot $H_T = \sum_{i=1}^4 p_T^i$ versus $\Delta_{13} = p_T^1 - p_T^3$, the p_T difference between the first and third jet, for $m_Q = 500$ GeV (left) and 1 TeV (right). The signal is characterised by a larger H_T and also by a larger hierarchy between the first and third jet. The differences between QCD and signal are weaker at low m_Q , and a harder cut on both variables should be done to keep QCD under control. Although the two variables are clearly correlated, a modified ABCD method could be used here to estimate the amount of QCD background leaking into the signal region.

Obtaining $S/B = 1$

Now we quantify the effect of the cuts on signal and QCD background using the variables described above. In table 3.1 we describe the cut-flow of those variables for the 2+1 case. The 3+1 case behaves very similarly in terms of signal efficiencies. Note that the QCD background of $n_j \gtrsim 3$, 4 jets with $p_T > 70$ GeV and $|\eta_j| < 2.5$ at LHC8 is 3×10^4 pb and 3×10^3 pb, respectively. The signal cross section can be read in figure 3.9 for specific values of g_ρ , $\sin \phi_{R_{u,d}}$, and it typically varies between 1 to 10 pb for $m_\rho \lesssim 2.5$ TeV. To achieve $S/B \sim 1$, one would need to have a relative suppression of efficiencies of $10^2 - 10^4$. In the table 3.1, one can see how this can be achieved by implementing cuts on the variables described above.

Cut-flow	$m_Q = 600$ GeV		$m_Q = 1200$ GeV	
	signal	QCD	signal	QCD
p_T leading jet > 450 GeV	0.51	0.0067	0.90	0.0067
$H_T > m_Q$	0.51	0.0067	0.80	0.0015
$ m_{jj} - m_Q < (30, 50)$ GeV	0.15	0.00037	0.11	2.5×10^{-5}
$\Delta\phi_{jj} > 1.5$	0.045	9.9×10^{-5}	0.060	2.1×10^{-7}

Table 3.1. Cut-flow demonstrating the effect on signal and background by applying cuts on the variables presented in the text. The numbers correspond to the efficiency to specified set of cumulative cuts. Here jj is the combination of the two sub-leading jets. For the background, the final numbers represent the cut-flow with either $m_Q = 600$ GeV or $m_Q = 1200$ GeV.

To produce this cut-flow, we took two benchmark masses, $m_Q = 600$ and 1200 GeV, and the 2+1 signature. The 2+1 topology was chosen, because it suffers from the largest background, still interesting S/B can be achieved using these cuts. Note that we have not truly optimised the cuts to a specific signal, and the intention of the table is to show that a background reduction in the required range is possible. Note also that we have not made use of the gap variables in this cut-flow, which could improve the sensitivity of the search.

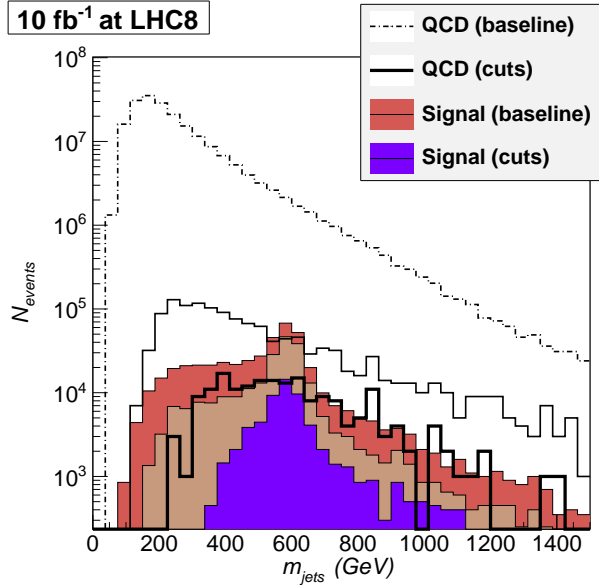


Figure 3.22. QCD background (black lines) and signal (solid colours) when the cuts on the table 3.1 are applied, except the one on m_{jj} . See text for further details.

The cut-flow table and figure are produced using detector level events showered with Pythia with MLM matching [140, 141] and simulated with Delphes [115] with anti- k_T jets of $R = 0.7$. In figure 3.22 we illustrate this cut-flow with a normalised background for 10 fb^{-1} of luminosity and a signal of $m_Q = 600 \text{ GeV}$ and $\sigma = 5 \text{ pb}$. In this figure, the three black lines correspond cumulatively to cuts on the three jet QCD background

1. $p_T > 70 \text{ GeV}$ and $|\eta_j| < 2.5$
2. $p_T^{\text{leading}} > 450 \text{ GeV}$ and $H_T > m_Q$
3. $\Delta\phi_{jj} > 1.5$

Similarly, the solid histograms correspond to the same cuts, applied to the signal.

At 14 TeV, the production cross section for QCD with $n_j \geq 3$ and $p_T > 70 \text{ GeV}$, $|\eta_j| < 2.5$, increases by a factor three respect to the 8 TeV run. For the $m_Q = 600 \text{ GeV}$ cut-flow described in table 3.1, the efficiencies to pass the cuts increase by a factor $\mathcal{O}(2)$ from 14 TeV respect to the 8 TeV case. The $m_Q = 1200 \text{ GeV}$ is more dramatic, with an efficiency increase for the QCD case of at least $\mathcal{O}(10)$. As we already mentioned, the cut-flow presented here should be seen as indicative of the strategy to follow, and it is clear one would need to re-optimize when moving from the 8 TeV to the 14 TeV run.

Chapter 4

Little Higgs

This chapter is based on the publications [142, 143] about the status and prospects of the Littlest Higgs with T-parity at the LHC written by my collaborators and myself. My involvement almost covers the complete work, together with co-author Marco Tonini I produced all the results, figures and accompanying text in this chapter and I aided in the formulation of the model introduction and the conclusions.

4.1 Introduction

In the previous two chapters composite models and a detailed account of the phenomenology of a composite Higgs model with partial compositeness were discussed. In this chapter we focus on another class of composite Higgs models, namely Little Higgs models [40, 42, 43, 76, 77, 79–81, 144–149]. In chapter 2 we showed that Little Higgs models reduce the fine-tuning of the Higgs mass compared to generic composite models. This feature is especially intriguing now that a Higgs-like boson with a mass of 125 GeV has been discovered at the LHC [1, 2]. In the regime of weakly coupled physics, supersymmetry is the most promising candidate to regulate quadratically divergent contributions to the Higgs mass. This class of models has been scrutinised by a large number of experimental searches at the LHC. The opposite is true for Little Higgs models, which are barely covered by LHC searches and therefore exclusion limits on these models are either indirect or simply not known. In order to gain as much discriminative power from LHC data, it is therefore very important to undertake the endeavour and try to constrain Little Higgs models in a manner as exhaustive as is done for supersymmetry.

As was shown in section 2.4, Little Higgs models are a special class of composite models based on a collective symmetry breaking pattern, which ameliorates the fine-tuning in the model. For these models the key observation is that the fine-tuning is proportional to $(v/f)^2$. Here, $f = \Lambda/(4\pi)$ is the scale of collective symmetry breaking and Λ the UV cut-off of the model. Hence, to address the original purpose of Little Higgs models, the scale f should not exceed the value of 1 TeV too much, since that would already imply fine-tuning in the percent range. From this perspective it is interesting to evaluate constraints from electroweak precision physics, Higgs precision physics and direct searches for realistic implementations of Little Higgs models.

The original constructions of Little Higgs models suffered severely from electroweak precision tests (EWPT) [150–152]. As a solution for these issues, several extensions have been presented, for example the Littlest Higgs with T-parity [42, 43, 77, 145] which introduces a discrete symmetry called T-parity to suppress corrections to precision observables. Other examples include the recent Bestest Little Higgs [146] and Next to Littlest Higgs [147]

models. The fine-tuning for each of these extensions is less severe and for example for the T-parity scenario the symmetry breaking scale f is only excluded up to roughly 400 GeV. However, as a large number of LHC results become available, the limits on these models have to be revisited once again. In this chapter we consider the Littlest Higgs with T-parity (LHT) and provide an update for the constraints from Higgs precision physics as presented in [82]. In addition, all direct searches from CMS and ATLAS will be analysed and recasted for this model whenever feasible. Finally, this will result in a lower bound on the symmetry breaking scale f from all possible corners of collider physics and will provide the most stringent test on the compatibility of the LHT model with experimental data.

The structure of the chapter is the following. In section 4.2 we review the theoretical set-up of the Littlest Higgs model with T-parity based on section 2.4 with emphasis on the details relevant for LHC phenomenology. Section 4.3 contains a full treatment of the phenomenological details of the LHT model tailored to 8 TeV experimental searches. This includes an analysis of the experimental final states for this model which enables identification of the relevant searches by the ATLAS and CMS experiments for the 8 TeV run. In section 4.4 these results are used to obtain exclusion limits on the LHT parameter space. Based on these existing limits we present optimisations for the existing searches which apply to the LHT model in section 4.5. The conclusions of this chapter are presented in the general conclusions in chapter 6.

4.2 LHT Model

In this section the Littlest Higgs with T-parity model [42, 43, 77] is discussed, building on the introduction of Little Higgs models given in section 2.4 and on the presentations given in [152–158]. Note that the introduction of T-parity has the additional benefit of providing a stable, weakly interacting particle by means of the lightest particle odd under T-parity. The constraints from dark matter experiments and the cosmic microwave background for the LHT model are not discussed here: the latest results can be found in [159, 160]. In this brief introduction the focus will be on details relevant for LHC collider phenomenology: we will first discuss the gauge sector, then the scalar sector, and finally the fermionic sector of the model. This collects the independent parameters of the model, and their connection to the masses of the new states as well as their couplings.

4.2.1 Gauge Sector

Analogous to the Littlest Higgs model discussed in section 2.4, the global symmetry structure of the LHT model is defined by the coset space

$$SU(5)/SO(5). \quad (4.1)$$

Spontaneous symmetry breaking is realised at the scale f via the vacuum expectation value of an $SU(5)$ symmetric tensor field

$$\langle \Sigma \rangle = \begin{pmatrix} \mathbf{0}_{2 \times 2} & \mathbf{0}_{2 \times 1} & \mathbf{1}_2 \\ \mathbf{0}_{1 \times 2} & 1 & \mathbf{0}_{1 \times 2} \\ \mathbf{1}_2 & \mathbf{0}_{2 \times 1} & \mathbf{0}_{2 \times 2} \end{pmatrix}. \quad (4.2)$$

Fourteen Nambu-Goldstone Bosons (NGBs) Π^a with $a = 1, \dots, 14$ arise in this set-up, parametrised in the usual non-linear sigma model formalism as

$$\Sigma(x) = e^{2i\Pi^a X^a(x)/f} \langle \Sigma \rangle \equiv \xi^2(x) \langle \Sigma \rangle, \quad (4.3)$$

where X^a are the broken generators of the coset space (4.1).

This model belongs to the class of product group models, where the SM gauge group emerges from the diagonal breaking of the product of several gauged groups. There is indeed a local invariance under $[SU(2)_1 \times U(1)_1] \times [SU(2)_2 \times U(1)_1]$, embedded in the matrix structure, spontaneously broken via $\langle \Sigma \rangle$ to its diagonal subgroup, which is identified with the SM gauge group. Explicitly, the kinetic term for the NGB matrix can be expressed in the standard non-linear sigma model formalism as

$$\mathcal{L}_\Sigma = \frac{f^2}{8} \text{Tr} |D_\mu \Sigma|^2, \quad (4.4)$$

where the covariant derivative is defined as

$$D_\mu \Sigma = \partial_\mu \Sigma - i \sum_{j=1}^2 [g_j (W_j \Sigma + \Sigma W_j^T) + g'_j (B_j \Sigma + \Sigma B_j^T)]. \quad (4.5)$$

The generators of the gauged symmetries are explicitly given as

$$\begin{aligned} Q_1^a &= \begin{pmatrix} \sigma^a/2 & 0 & 0 \\ 0 & 0 & 0 \\ 0 & 0 & 0 \end{pmatrix} & Y_1 &= \frac{1}{10} \text{diag}(3, 3, -2, -2, -2) \\ Q_2^a &= \begin{pmatrix} 0 & 0 & 0 \\ 0 & 0 & 0 \\ 0 & 0 & -\sigma^{a*}/2 \end{pmatrix} & Y_2 &= \frac{1}{10} \text{diag}(2, 2, 2, -3, -3). \end{aligned} \quad (4.6)$$

In the gauge boson sector, T-parity is introduced as an exchange symmetry between the gauge bosons of the two different copies of the SM gauge group as

$$T : \quad W_{1\mu}^a \leftrightarrow W_{2\mu}^a, \quad B_{1\mu} \leftrightarrow B_{2\mu}. \quad (4.7)$$

This can be connected to the Lie algebra generators which have transformation properties such that T-parity distinguishes the broken generators from the unbroken ones [42, 43]. The gauge-kinetic Lagrangian (4.4) of the Littlest Higgs model is then invariant under T-parity if

$$g_1 = g_2 = \sqrt{2}g, \quad g'_1 = g'_2 = \sqrt{2}g'. \quad (4.8)$$

Before EWSB, a set of $SU(2) \times U(1)$ gauge bosons ($W^{a'}$, B') obtains a mass term of order f from (4.4), while the other set (W^a , B) remains massless and is identified with the SM gauge bosons. The mass eigenstates are related to the gauge eigenstates by the following field rotations

$$\begin{aligned} W^a &= \frac{1}{\sqrt{2}} (W_1^a + W_2^a) & B &= \frac{1}{\sqrt{2}} (B_1 + B_2) \\ W^{a'} &= \frac{1}{\sqrt{2}} (W_1^a - W_2^a) & B' &= \frac{1}{\sqrt{2}} (B_1 - B_2). \end{aligned} \quad (4.9)$$

Clearly, under T-parity (4.7) the heavy gauge bosons are odd while the SM ones are even. EWSB induces further mixing for the light and heavy gauge bosons separately: in particular the mass eigenstates in the neutral heavy sector will be a linear combination of $W^{3'}$ and B' , producing a heavy partner of the photon A_H and of the Z boson Z_H , with a mixing angle of the order of v^2/f^2

$$\sin \theta_H \simeq \frac{5gg'}{4(5g^2 - g'^2)} \frac{v^2}{f^2}. \quad (4.10)$$

In here v represents the vacuum expectation value of the Higgs doublet, whose dynamical generation will be described later in this section. At $\mathcal{O}(v^2/f^2)$ in the expansion of the Lagrangian (4.4), the mass spectrum after EWSB is given by

$$m_W = \frac{gv}{2} \left(1 - \frac{1}{12} \frac{v^2}{f^2}\right) \quad m_Z = \frac{gv}{2 \cos \theta_w} \left(1 - \frac{1}{12} \frac{v^2}{f^2}\right) \quad m_\gamma = 0 \quad (4.11)$$

$$m_{W_H} = m_{Z_H} = gf \left(1 - \frac{1}{8} \frac{v^2}{f^2}\right) \quad m_{A_H} = \frac{g'f}{\sqrt{5}} \left(1 - \frac{5}{8} \frac{v^2}{f^2}\right). \quad (4.12)$$

In order to match the Standard Model prediction for the gauge boson masses, the vacuum expectation value needs to be redefined in terms of the typical SM value $v_{\text{SM}} = 246$ GeV via the functional form

$$v = \frac{f}{\sqrt{2}} \arccos \left(1 - \frac{v_{\text{SM}}^2}{f^2}\right) \simeq v_{\text{SM}} \left(1 + \frac{1}{12} \frac{v_{\text{SM}}^2}{f^2}\right). \quad (4.13)$$

4.2.2 Scalar Sector

In the scalar sector we are interested in the fourteen Goldstone bosons of the $SU(5)/SO(5)$ global symmetry breaking. These transform under the unbroken $SU(2)_L \times U(1)_Y$ gauge symmetry as $\mathbf{1}_0$, $\mathbf{3}_0$, $\mathbf{2}_{1/2}$ and $\mathbf{3}_{\pm 1}$. The $\mathbf{2}_{1/2}$ component is identified with the Higgs doublet H , while the $\mathbf{3}_{\pm 1}$ component is a complex triplet under $SU(2)_L$ which forms a symmetric tensor

$$\Phi = \frac{-i}{\sqrt{2}} \begin{pmatrix} \sqrt{2}\phi^{++} & \phi^+ \\ \phi^+ & \phi^0 + i\phi^P \end{pmatrix}. \quad (4.14)$$

Both ϕ^0 and the pseudoscalar ϕ^P are real scalars, whereas the ϕ^{++} and ϕ^+ are complex scalars. The other Goldstone bosons are the longitudinal modes of the heavy gauge bosons and therefore will not appear in the unitary gauge. In the this gauge, the Goldstone boson matrix Π is given by

$$\Pi = \frac{1}{\sqrt{2}} \begin{pmatrix} 0 & H & \sqrt{2}\Phi \\ H^\dagger & 0 & H^T \\ \sqrt{2}\Phi^\dagger & H^* & 0 \end{pmatrix}. \quad (4.15)$$

The action for T-parity in the scalar sector is defined as

$$T : \quad \Pi \rightarrow -\Omega \Pi \Omega, \quad (4.16)$$

where $\Omega = \text{diag}(1, 1, -1, 1, 1)$ is introduced to give the Higgs positive parity while keeping the triplet odd.

The global symmetries prevent the appearance of a potential for the scalar fields at tree level. The scalar potential is indeed generated dynamically at one-loop and higher orders due to the interactions with gauge bosons and fermions, and is parametrised through the Coleman-Weinberg potential [161]. The most general scalar potential invariant under the SM gauge groups, involving one doublet field H and one triplet field ϕ can be written up to dimension-four operators as

$$\begin{aligned}
 V_{\text{CW}} = & \lambda_{\phi^2} f^2 \text{Tr} \left(\phi^\dagger \phi \right) + i \lambda_{h\phi h} f \left(H \phi^\dagger H^T - H^* \phi H^\dagger \right) - \mu^2 H H^\dagger \\
 & + \lambda_{h^4} \left(H H^\dagger \right)^2 + \lambda_{h\phi\phi h} H \phi^\dagger \phi H^\dagger + \lambda_{h^2\phi^2} H H^\dagger \text{Tr} \left(\phi^\dagger \phi \right) \\
 & + \lambda_{\phi^2\phi^2} \left[\text{Tr} \left(\phi^\dagger \phi \right) \right]^2 + \lambda_{\phi^4} \text{Tr} \left(\phi^\dagger \phi \phi^\dagger \phi \right). \tag{4.17}
 \end{aligned}$$

The coefficients μ^2 , $\lambda_{h^2\phi^2}$ and $\lambda_{h\phi h}$ do not receive a contribution from the quadratically divergent part of the one-loop Coleman-Weinberg potential, either because of the collective symmetry breaking mechanism (μ^2 , $\lambda_{h^2\phi^2}$) or because of T-parity ($\lambda_{h\phi h}$). Therefore they only receive log-divergent contributions at one-loop, and quadratically divergent contributions starting from the two-loop level. The latter suppression of μ^2 from an extra loop factor gives the natural hierarchy between the electroweak scale and the cut-off scale Λ : two and higher-loop contributions have not been calculated, and therefore μ^2 can be treated as a free parameter and its value is fixed by the observed Higgs mass (4.19). Since the quartics $\lambda_{h^2\phi^2}$, $\lambda_{h\phi h}$ are two-loop suppressed as well, they are negligible with respect to the other $\mathcal{O}(1)$ quartic couplings, and therefore we will not consider them.

The remaining coefficients can be expressed in terms of the fundamental parameters of the model

$$\begin{aligned}
 \lambda_{\phi^2} = 2(g^2 + g'^2) + 8\lambda_1^2 & & \lambda_{h^4} = \frac{1}{4}\lambda_{\phi^2} \\
 \lambda_{h\phi\phi h} = -\frac{4}{3}\lambda_{\phi^2} & & \lambda_{h^2\phi^2} = -16\lambda_1^2 \\
 \lambda_{\phi^4} = -\frac{8}{3}(g^2 + g'^2) + \frac{16}{3}\lambda_1^2, & & \tag{4.18}
 \end{aligned}$$

where $\lambda_1 = \lambda_1(R, m_t)$ is a parameter of the third generation fermion sector which will be explained in the next subsection. Minimising the potential to obtain the doublet vacuum expectation value v which triggers EWSB, one can express the parameters in the scalar potential in terms of the physical parameters f , m_h and v . Diagonalising the scalar mass matrix, one obtains the following spectrum

$$m_h = \sqrt{2}\mu \quad m_\Phi = \frac{\sqrt{2}m_h}{v} f, \tag{4.19}$$

where all components of the triplet $(\phi^{++}, \phi^+, \phi^0, \phi^P)$ are degenerate at the order we are considering. Since μ^2 is treated as a free parameter, we will assume the measured Higgs mass for the scalar doublet h , fixing therefore the value of μ .

4.2.3 Fermion Sector

To implement T-parity in the fermion sector one introduces two $SU(2)_A$ fermion doublets $q_A = (id_{L_A}, -iu_{L_A})^T$ with $A = 1, 2$. T-parity will then be defined such that

$$T : \quad q_1 \leftrightarrow -q_2. \quad (4.20)$$

The T-even combination $u_{L+} = (u_{L_1} - u_{L_2})/\sqrt{2}$ will be the up-type component of the SM fermion doublet, while the T-odd combination $u_{L-} = (u_{L_1} + u_{L_2})/\sqrt{2}$ will be its T-odd partner, and analogously for the down-type components. We require that the T-even (SM) eigenstates obtain a mass only from Yukawa-like interactions after EWSB, while forcing the masses of the T-odd eigenstates to be at the TeV scale. The standard procedure is to embed the q_A doublets into incomplete $SU(5)$ multiplets Ψ_A as $\Psi_1 = (q_1, 0, \mathbf{0}_{1 \times 2})^T$ and $\Psi_2 = (\mathbf{0}_{1 \times 2}, 0, q_2)^T$, with the following transformation rules

$$\begin{aligned} SU(5) : \quad & \Psi_1 \rightarrow V^* \Psi_1, \quad \Psi_2 \rightarrow V \Psi_2, \quad V \in SU(5) \\ T : \quad & \Psi_1 \leftrightarrow -\langle \Sigma \rangle \Psi_2. \end{aligned} \quad (4.21)$$

To give masses to the additional fermions, an $SO(5)$ multiplet Ψ_c is also introduced as $\Psi_c = (q_c, \chi_c, \tilde{q}_c)^T$, non-linearly transforming under the full $SU(5)$

$$\begin{aligned} SU(5) : \quad & \Psi_c \rightarrow U \Psi_c \\ T : \quad & \Psi_c \rightarrow -\Psi_c, \end{aligned} \quad (4.22)$$

where the matrix U is a non-linear transformation. The components of the latter Ψ_c multiplet are the so-called *mirror* fermions.

A possible $SU(5)$ - and T-invariant Lagrangian that could generate a TeV scale mass only for the T-odd combinations is finally given by

$$\begin{aligned} \mathcal{L}_k = & -kf \left(\bar{\Psi}_2 \xi \Psi_c + \bar{\Psi}_1 \langle \Sigma \rangle \Omega \xi^\dagger \Omega \Psi_c \right) - m_q \bar{u}'_c u_c - m_q \bar{d}'_c d_c - m_\chi \bar{\chi}'_c \chi_c + \text{h.c.} \\ & \supset -\sqrt{2}kf \left[\bar{d}_{L-} \tilde{d}_c + \frac{1+c_\xi}{2} \bar{u}_{L-} \tilde{u}_c - \frac{s_\xi}{\sqrt{2}} \bar{u}_{L-} \chi_c - \frac{1-c_\xi}{2} \bar{u}_{L-} u_c \right] + \\ & - m_q \bar{u}'_c u_c - m_q \bar{d}'_c d_c - m_\chi \bar{\chi}'_c \chi_c + \text{h.c.} \end{aligned} \quad (4.23)$$

where $c_\xi = \cos(h/\sqrt{2}f)$, $s_\xi = \sin(h/\sqrt{2}f)$. Indeed, no mass term for the T-even combinations (u_{L+}, d_{L+}) is generated. The coupling k is in general a matrix in flavour space for both quarks and leptons. As first noted in [162], in analogy with the CKM transformations, the matrix k^i_j is diagonalised by two $U(3)$ matrices

$$k^i_j = (V_H)^i_k (k_D)^k_l (U_H)^l_j. \quad (4.24)$$

The matrix V_H acts on the left handed fields while U_H acts on the right-handed Ψ_c fields. The gauge interactions in the T-parity eigenbasis are given qualitatively by

$$g\bar{Q}_{-i} \mathbb{A}_- Q^i_+ + g\bar{Q}_{+i} \mathbb{A}_- Q^i_-, \quad (4.25)$$

where the A_- and Q_- are the T-odd gauge bosons and fermions respectively, while the Q_+ are the T-even fermions. Rotating to the mass eigenbasis, using H and L indices for heavy and light, these interactions can be re-expressed as

$$g\bar{Q}_{Hi}V_{Hj}^\dagger A_H \begin{pmatrix} (V_u)_k^j u_L^k \\ (V_d)_k^j d_L^k \end{pmatrix} + g \begin{pmatrix} \bar{u}_{Lk}(V_u^\dagger)_i^k \\ \bar{d}_{Lk}(V_d^\dagger)_i^k \end{pmatrix} A_H V_{Hj}^i Q_H^j, \quad (4.26)$$

where

$$Q_H^i = \begin{pmatrix} u_H^i \\ d_H^i \end{pmatrix}. \quad (4.27)$$

The rotations relevant to flavour physics are then

$$(V_H^\dagger)_k^i (V_u)_j^k \equiv (V_{Hu})_j^i, \quad (V_H^\dagger)_k^i (V_d)_j^k \equiv (V_{Hd})_j^i, \quad (4.28)$$

which are related through the Standard Model CKM matrix

$$V_{Hu}^\dagger V_{Hd} = V_{\text{CKM}}. \quad (4.29)$$

For simplicity, in the following we will assume the matrix k to be diagonal and flavour independent, forcing the T-odd fermions to be degenerate within different generations. The latter relations (4.28) and (4.29) then reduce to the usual SM definition of the CKM matrix, with the mirror fermion matrix V_H as the identity matrix: this is called the minimal flavour violating scenario of LHT. For each generation of quarks and leptons, the following up- and down-type mass eigenstates are generated at $\mathcal{O}(v^2/f^2)$ via (4.23)

$$m_{u_H} = \sqrt{2}kf \left(1 - \frac{1}{8} \frac{v^2}{f^2}\right) \quad m_{d_H} = \sqrt{2}kf. \quad (4.30)$$

Hence, one obtains a total of twelve additional T-odd fermions, partners to the six quarks, the three charged leptons and the three neutrinos. One should note that the up-type mass receives also a contribution from EWSB, since a coupling with the Higgs doublet is present in (4.23) proportional to c_ξ and s_ξ .

The next task is to write invariant Yukawa-like terms to give mass to the T-even (SM) combinations u_{L+} and d_{L+} . In particular, in order to reduce the fine-tuning due to the SM top loop, the top Yukawa sector must realise a collective symmetry breaking pattern as well. One usually introduces the singlet fields T_{L_1} and T_{L_2} (and their right-handed counterparts) which are embedded, together with the previously defined q_1 and q_2 doublets, into the complete $SU(5)$ multiplets $\Psi_{1,t} = (q_1, T_{L_1}, \mathbf{0}_{1 \times 2})^T$ and $\Psi_{2,t} = (\mathbf{0}_{1 \times 2}, T_{L_2}, q_2)^T$. The $SU(5)$ - and T-invariant Yukawa-like Lagrangian for the top sector then reads

$$\begin{aligned} \mathcal{L}_t = & - \frac{\lambda_1 f}{2\sqrt{2}} \epsilon_{ijk} \epsilon_{xy} [(\bar{\Psi}_{1,t})_i \Sigma_{jx} \Sigma_{ky} - (\bar{\Psi}_{2,t}(\Sigma))_i \Sigma'_{jx} \Sigma'_{ky}] t'_R \\ & - \lambda_2 f (\bar{T}_{L_1} T_{R_1} + \bar{T}_{L_2} T_{R_2}) + \text{h.c.} \end{aligned} \quad (4.31)$$

Here, the indices i, j, k run over 1, 2, 3 and x, y over 4, 5, and $\Sigma' = \langle \Sigma \rangle \Omega \Sigma^\dagger \Omega \langle \Sigma \rangle$ is the image of Σ under T-parity (4.16). Under T-parity, the new singlet fields transform as

$$\begin{aligned}
 T : \quad & T_{L_1} \leftrightarrow -T_{L_2} \\
 & T_{R_1} \leftrightarrow -T_{R_2} \\
 & t'_R \rightarrow t'_R.
 \end{aligned} \tag{4.32}$$

The presence in (4.31) of two different couplings λ_1 and λ_2 is due to the collective symmetry breaking mechanism.

The top Lagrangian (4.31) finally contains the following terms

$$\mathcal{L}_t \supset -\lambda_1 f \left(\frac{s_\Sigma}{\sqrt{2}} \bar{t}_{L+} t'_R + \frac{1+c_\Sigma}{2} \bar{T}'_{L+} t'_R \right) - \lambda_2 f (\bar{T}'_{L+} T'_{R+} + \bar{T}'_{L-} T'_{R-}) + \text{h.c.}, \tag{4.33}$$

for which $c_\Sigma = \cos(\sqrt{2}h/f)$ and $s_\Sigma = \sin(\sqrt{2}h/f)$. The T-parity eigenstates are defined as $t_{L+} = (t_{L_1} - t_{L_2})/\sqrt{2}$ and $T'_{L\pm} = (T_{L_1} \mp T_{L_2})/\sqrt{2}$, $T'_{R\pm} = (T_{R_1} \mp T_{R_2})/\sqrt{2}$ as before. Among the terms that we have neglected in (4.33), there are the interaction terms of the T-odd eigenstate t_{L-} , which does not acquire any mass term from \mathcal{L}_t while obtaining its mass from \mathcal{L}_k as explained before. In \mathcal{L}_t a different T-odd Dirac fermion $T_- \equiv (T'_{L-}, T'_{R-})$ obtains a high-scale mass

$$m_{T_-} = \lambda_2 f. \tag{4.34}$$

The T-even combinations in \mathcal{L}_t , these are (t_{L+}, t'_R) and (T'_{L+}, T'_{R+}) , mix among each other:

$$-\mathcal{L}_t \supset (\bar{t}_{L+} \bar{T}'_{L+}) \mathcal{M} \begin{pmatrix} t'_R \\ T'_{R+} \end{pmatrix} + \text{h.c.} \quad \text{where} \quad \mathcal{M} = \begin{pmatrix} \frac{\lambda_1 f}{\sqrt{2}} \sin\left(\frac{\sqrt{2}h}{f}\right) & 0 \\ \lambda_1 f \cos^2\left(\frac{h}{\sqrt{2}f}\right) & \lambda_2 f \end{pmatrix}. \tag{4.35}$$

The mass terms are diagonalised by defining the linear combinations

$$\begin{aligned}
 t_L &= \cos\beta \cdot t_{L+} - \sin\beta \cdot T'_{L+} & T_{L+} &= \sin\beta \cdot t_{L+} + \cos\beta \cdot T'_{L+} \\
 t_R &= \cos\alpha \cdot t'_R - \sin\alpha \cdot T'_{L+} & T_{R+} &= \sin\alpha \cdot t'_R + \cos\alpha \cdot T'_{R+},
 \end{aligned} \tag{4.36}$$

where we used the dimensionless ratio $R = \lambda_1/\lambda_2$ as well as the leading order expressions of the mixing angles

$$\sin\alpha = \frac{R}{\sqrt{1+R^2}} \equiv \sqrt{x_L}, \quad \sin\beta = \frac{R^2}{1+R^2} \frac{v}{f} \equiv x_L \frac{v}{f}. \tag{4.37}$$

Considering only the largest corrections induced by EWSB, the mass spectrum is given by

$$m_t = \lambda_2 x_L v \left[1 + \frac{v^2}{f^2} \left(-\frac{1}{3} + \frac{1}{2} x_L (1 - x_L) \right) \right] \tag{4.38}$$

and

$$m_{T_+} = \frac{f}{v} \frac{m_t}{\sqrt{x_L(1-x_L)}} \left[1 + \frac{v^2}{f^2} \left(\frac{1}{3} - x_L(1-x_L) \right) \right]. \tag{4.39}$$

R and λ_2 are considered to be free parameters. However we can fix λ_2 requiring that, for given (f, R) , m_t corresponds to the experimental top mass value: this way, the only free parameters in the T-even top sector are f and R .

It is to be noted that in reference [156] the authors have performed a study to fix the allowed range for R : by calculating the $J = 1$ partial-wave amplitudes in the coupled system of $(t\bar{t}, T\bar{T}_+, b\bar{b}, WW, Zh)$ states to estimate the tree level unitarity limit of the corresponding scattering amplitudes: the reported upper bound is

$$R \lesssim 3.3. \quad (4.40)$$

The other two generations of T-even up-type quarks acquire their mass through analogous terms as (4.31), but with the $T_{L_{1,2}}$ missing, since the Yukawa couplings are small and one does not have to worry about the quadratic divergences: no additional partners are then introduced in the spectrum besides the T-odd fermion u_H which acquire mass via (4.23).

Regarding the Yukawa interaction for the down-type quarks and charged leptons, two possible constructions of T-invariant Lagrangians are commonly known [157] and usually denoted as *Case A* and *Case B*, respectively. No additional partners are introduced as the quadratic corrections to the Higgs mass are negligible and do not require the introduction of the collective symmetry breaking mechanism in this sector. A prototype Lagrangian is given by [157],

$$\mathcal{L}_d = -\frac{i\lambda_d f}{2\sqrt{2}} \epsilon_{ij} \epsilon_{xyz} [(\bar{\Psi}'_2)_x \Sigma_{iy} \Sigma_{jz} X - (\bar{\Psi}'_1 \langle \Sigma \rangle)_x \Sigma'_{iy} \Sigma'_{jz} X'] d'_R, \quad (4.41)$$

with the same notation as in (4.31), and $\Psi'_{1,2}$ the T-parity images of $\Psi_{1,2}$ (4.21). X is needed to achieve gauge invariance, transforming as a singlet under both $SU(2)_{1,2}$ and with $U(1)_{1,2}$ charges $(1/10, -1/10)$, while X' is the image of X under T-parity. Two choices are indeed possible for X , corresponding to the previously mentioned *Case A* and *Case B* respectively, namely $X = (\Sigma_{33})^{-1/4}$ and $X = (\Sigma_{33})^{1/4}$, where Σ_{33} is the $(3, 3)$ component of the non-linear sigma model field Σ .

The free parameters of this sector are fixed in order to reproduce the SM masses. It turns out that the down-type and charged lepton couplings to the Higgs get corrections of order $\mathcal{O}(v^2/f^2)$ with respect to their SM values, in the expansion of the non-linear sigma model. Furthermore, a higher suppression is registered in the *Case B* implementation, namely

$$\frac{g_{hd\bar{d}}}{g_{hd\bar{d}}^{\text{SM}}} = 1 - \frac{1}{4} \frac{v_{\text{SM}}^2}{f^2} + \mathcal{O}\left(\frac{v_{\text{SM}}^4}{f^4}\right) \quad \text{Case A} \quad (4.42)$$

$$\frac{g_{hd\bar{d}}}{g_{hd\bar{d}}^{\text{SM}}} = 1 - \frac{5}{4} \frac{v_{\text{SM}}^2}{f^2} + \mathcal{O}\left(\frac{v_{\text{SM}}^4}{f^4}\right) \quad \text{Case B}, \quad (4.43)$$

where we defined the Higgs coupling as $\mathcal{L}_d \supset g_{hd\bar{d}} h d \bar{d}$ and the SM value clearly is $g_{hd\bar{d}}^{\text{SM}} = m_d/v_{\text{SM}}$.

Since the coupling of the bottom quark to the Higgs is highly relevant for the Higgs phenomenology, a different pattern is expected from the two different down-type Yukawa implementations, providing a distinctive phenomenology in the Higgs sector [82, 157]. On the

other hand, the Higgs phenomenology has a rather small impact on the topologies considered in direct searches. For this reason, we will focus only on the *Case A* implementation throughout the chapter. For sake of completeness, the results of the Higgs and EWPT combined analysis for *Case B* will be provided in the appendix B.3.

4.3 LHT Phenomenology

As presented in section 4.2, the LHT model can be parametrised by only three free parameters, under the assumption of flavour independence in the mirror fermion sector. The parameter f is the analogue of the pion decay constant in low-energy QCD and corresponds to the scale at which the global symmetry in the strong sector is spontaneously broken. Moreover f , or rather $(v/f)^2$, determines the amount of fine-tuning needed in the Higgs potential to stabilise loop corrections. As Little Higgs theories were designed to overcome the little hierarchy problem, it is natural to demand a small fine-tuning and therefore a relatively low value of f . For example a scale $f \approx 2$ TeV implies a fine-tuning of the order of 1%. Of course, the very definition of fine-tuning has not an absolute physical meaning, and the interpretation of fine-tuning is also not totally physical. We leave it to the reader to judge whether a fine-tuning stronger than 1% would still be considered natural or not. Though, we will show that only with the full 14 TeV run one can reach more contrived values for the f parameter.

To become more specific, the naturalness of the model is usually quantified by observing how much the contributions from the heavy states ($\delta\mu^2$) exceed the observed value of the Higgs mass squared parameter (μ_{obs}^2), as originally proposed in [77]

$$\Delta = \frac{|\delta\mu^2|}{\mu_{\text{obs}}^2}, \quad \mu_{\text{obs}}^2 = \frac{m_h^2}{2}. \quad (4.44)$$

For example, if the new contributions to the Higgs mass squared parameter exceed μ_{obs}^2 by a factor of 5, that is $\Delta = 5$, one says that the model requires 20% of fine-tuning. Clearly, the lower the value of fine-tuning, the worse is the naturalness of the model. The dominant log-divergent contribution to the Higgs mass squared parameter comes from the top and its T_+ heavy partner loops, and is given by [77]

$$\delta\mu^2 = -\frac{3\lambda_t^2 m_T^2}{8\pi^2} \log \frac{\Lambda^2}{m_T^2} \quad (4.45)$$

where $\Lambda = 4\pi f$ is the cut-off of the non-linear sigma model, λ_t is the SM top Yukawa coupling and m_T is the mass of the heavy top partner. In the next sections we will quantify the required amount of fine-tuning using equation (4.44).

The other two parameters k and $R = \lambda_1/\lambda_2$ parametrise the couplings in the mirror fermion sector (4.23) and in the top partner sector (4.31), respectively. Therefore to constrain the symmetry breaking scale f in a consistent way, it is needed to exclude regions in parameter space while varying k and R within their theoretical or experimental bounds, see equations (4.40) and (4.56). The model phenomenology changes drastically for different values of these two free parameters, as we will describe in the next sections.

4.3.1 Particle Spectrum and Decay Modes

Generally speaking, the model is realised in such a way that only the new partners of the SM fields acquire a mass from the global (local) spontaneous symmetry breaking $SU(5) \rightarrow SO(5)$ ($[SU(2) \times U(1)]^2 \rightarrow [SU(2) \times U(1)]_{\text{diag}}$) at the scale f , while the SM states remain massless. EWSB further generates corrections of order v^2/f^2 to the partner masses, and weak scale v masses for the other SM states analogously to the original Higgs mechanism. Once the values of the gauge coupling constants and of the parameters in the scalar potential are fixed, the mass of the gauge boson- and scalar partners are completely determined by the scale f . General features are the identification of the heavy photon A_H as the lightest T-odd particle, therefore being stable unless the quark partners q_H become even lighter. This happens if

$$\begin{aligned} m_{u_H} < m_{A_H} & \quad \text{if} \quad k < \frac{g'}{\sqrt{10}} \left(1 - \frac{1}{2} \frac{v^2}{f^2} + \dots \right) \\ m_{d_H} < m_{A_H} & \quad \text{if} \quad k < \frac{g'}{\sqrt{10}} \left(1 - \frac{5}{8} \frac{v^2}{f^2} + \dots \right) \end{aligned} \quad (4.46)$$

which corresponds to values of $k \lesssim 0.1$. The heavy W and Z partners are degenerate up to corrections of order v^2/f^2 , both being lighter than the different components of the complex triplet ϕ , which are also degenerate at the order we are considering.

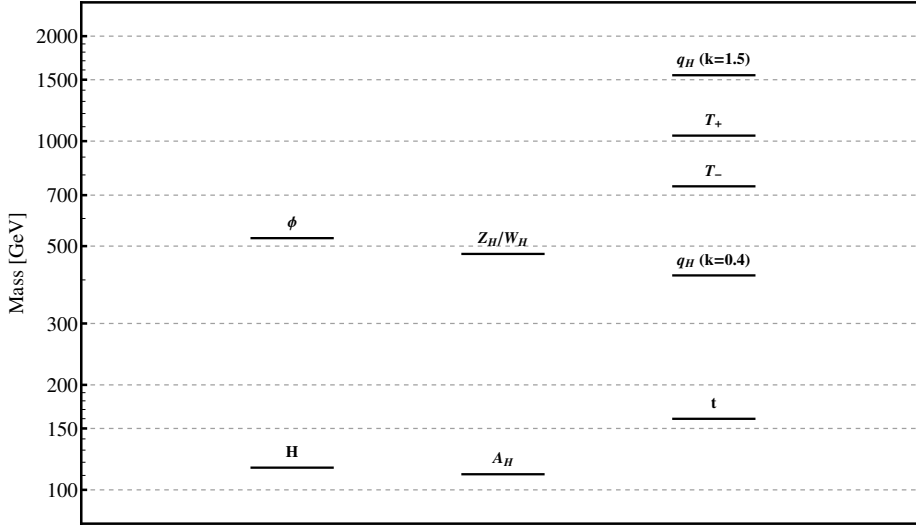


Figure 4.1. LHT partner masses showing the effect of k on the heavy quark masses. f and R are fixed to 800 GeV and 1.0 respectively.

On the other hand, the LHT model requires the presence of other free parameters in the fermion sectors, namely k and $R = \lambda_1/\lambda_2$ as described before, making the fermion spectrum dependent on those values besides the scale f . In particular the top partners T_+ and T_- are always heavier than all bosonic partners, as one can partially see from figure 4.1. There we have fixed $R = 1.0$ minimising the T_+ mass (4.39). The T_- mass (4.34) is proportional to R^{-1} , but it is always heavier than all bosonic partners in the allowed range $R \lesssim 3.3$, too.

It is further noted that the T-even top partner T_+ is always heavier than its T-odd partner T_- , with their mass splitting proportional to R . The mass of the quark partners depends on the value of k , and they are heavier than all the gauge boson partners if

$$\begin{aligned}
 m_{u_H} > m_{W_H}, m_{Z_H} & \quad \text{if } k > \frac{g}{\sqrt{2}} \\
 m_{d_H} > m_{W_H}, m_{Z_H} & \quad \text{if } k > \frac{g}{\sqrt{2}} \left(1 - \frac{1}{8} \frac{v^2}{f^2} + \dots \right).
 \end{aligned} \tag{4.47}$$

This corresponds to $k \gtrsim 0.45$, making the decay $q_H \rightarrow V_H q$ kinematically allowed, where we defined $V_H \equiv W_H^\pm, Z_H$. For $k \lesssim 0.45$ the only kinematically allowed decay of the quark partners is $q_H \rightarrow A_H q$. A compressed mass spectrum is generated in the region $0.1 \lesssim k \lesssim 0.2$ where the mass difference between q_H and A_H is rather small. For even smaller values of k , namely $k \lesssim 0.1$, the quark partners become lighter than the heavy photon A_H and thereby stable. We can safely say that this region can be considered as excluded or in high tension with the experimental observations. In particular R-hadron constraints from the LHC [163] and coloured particle constraints from cosmological observations [164], strongly disfavour stable charged particles. In figure 4.1 we plot a typical mass spectrum of the LHT partners for reference values $f = 800$ GeV, $R = 1.0$ and $k = 1.5$ or $k = 0.4$.

Particle	Decay	BR _{k=1.0}	BR _{k=0.4}	Particle	Decay	BR _{k=1.0}	BR _{k=0.4}
d_H	$W_H^- u$	63%	0%	Φ^\pm	$A_H W^\pm$	100%	100%
	$Z_H d$	31%	0%		$\Phi^{\pm\pm}$	$A_H (W^\pm)^2$	99%
	$A_H d$	6%	100%	A_H		stable	
u_H	$W_H^+ d$	61%	0%	W_H^\pm	$A_H W^\pm$	100%	2%
	$Z_H u$	30%	0%		$u_H d$	0%	44%
	$A_H u$	9%	100%		$d_H u$	0%	27%
T_H^+	$W^+ b$	46%	46%		$l_H^\pm \nu$	0%	13.5%
	$Z t$	22%	22%		$\nu_H l^\pm$	0%	13.5%
	$H t$	21%	21%	Z_H	$A_H H$	100%	2%
	$T_H^- A_H$	11%	11%	$d_H d$	0%	40%	
T_H^-	$A_H t$	100%	100%	$u_H u$	0%	30%	
Φ^0	$A_H Z$	100%	100%	$l_H^\pm l^\mp$	0%	14%	
Φ^P	$A_H H$	100%	100%	$\nu_H \nu$	0%	14%	

Table 4.1. An overview of the decay modes with the corresponding branching ratios of all new LHT particles for $f = 1$ TeV and $R = 1.0$. Two scenarios are listed, where the heavy quarks q_H are either lighter ($k = 0.4$) or heavier ($k = 1.0$) than the boson partners. The heavy leptons decay analogously to the heavy quarks and the decays involving generic up or down quarks have to be considered as summed over all flavours.

Given the previous discussion, it is clear that the decay modes of the quark partners and of the gauge boson partners mostly depend on the value of k . All branching ratios have indeed

a mild dependence on f and R . In table 4.1 we present the typical branching ratios for two different benchmark scenarios, namely $k = 1.0$ and $k = 0.4$ with $f = 1$ TeV, $R = 1.0$.

4.3.2 Production Modes and Experimental Signatures

In this section we will discuss, in order of decreasing cross section at the LHC, the production of the different LHT new particles, updating the results presented in [156]. Notice that due to T-parity, only the T-even top partner T_+ could be singly produced, while all other particles have to be pair produced, highly reducing the available phase space with increasing masses. The plots in this section depict the production cross sections as a function of the symmetry breaking scale f and are done for the benchmark point $R = 1.0$ and $k = 1.0$, unless stated otherwise.

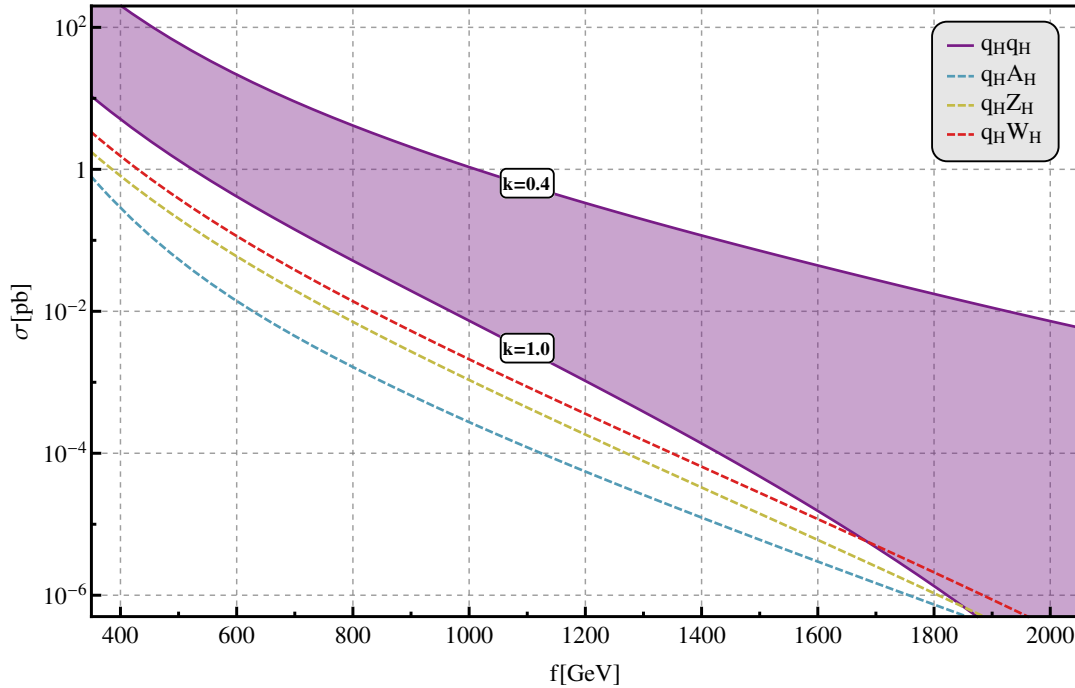


Figure 4.2. Pair production and associated production cross section of the quark partners q_H at the LHC operating at 8 TeV, for reference values of $R = 1.0$ and $k = 1.0$. The pair production line width corresponds to values of $k \in [0.4, 1.0]$.

Since the LHC is a hadron collider, the pair production of quark partners q_H will be significant, especially if their masses are not too large. Opposite sign quark partners can be dominantly produced via QCD processes, but also via electroweak processes involving a heavy W_H or Z_H , A_H in the t -channel. Among the production of a quark partner in association with a gauge boson partner, the dominant contribution comes from the associated production with a heavy W_H , because of the different strength of the couplings between q_H and V_H . In figure 4.2 we plot pair and associated productions of quark partners at LHC8. Since the mass of the quark partners is proportional to k , the q_H pair production is expected to decrease faster with respect to the associated productions for higher values of k : the width of the pair production line corresponds indeed to values of $k \in [0.4, 1.0]$.

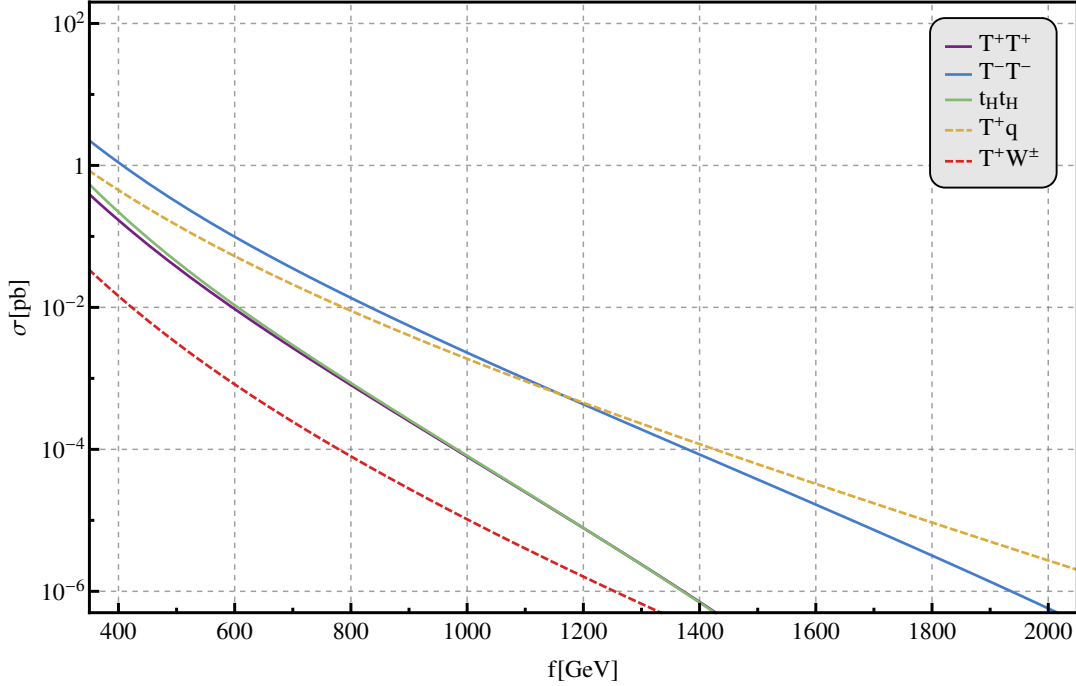


Figure 4.3. Production cross section of LHT top partners at the LHC operating at 8 TeV, for reference values of $R = 1.0$ and $k = 1.0$.

Because of the mass spectrum described in section 4.3.1, the T-odd T_- has the largest pair production cross section compared with the pair production of T_+ and t_H (for $k \gtrsim 0.7$). Clearly, lower values of k reduce the mass of the quark partners q_H , making their pair production the dominant process. With increasing values of f , both T_+ and T_- become heavier, making the single production of the T_+ in association with a light quark (through a diagram involving a t -channel W with an initial state bottom quark) comparable in size or even larger than the T_- pair production. The dominant associated production of the T_+ with a SM gauge boson is the one involving the W^\pm , which is suppressed with respect to the other production modes since the bT_+W coupling is proportional to v/f .

The qualitative behaviour described above can be slightly different by changing the values of k and R . In particular $R \ll 1$ can be considered as the decoupling limit of both T_+ and T_- , making both pair and associated productions vanishing, while for $R > 1$ the mass splitting between T_- and T_+ increases, making the T_- pair production sizably larger than the associated $T_+ q$ production. In figure 4.3 we plot the different production cross sections of the top partners T_+ and T_- fixing $R = 1.0$ and $k = 1.0$.

With generally smaller cross sections, the different production modes for pairs of heavy gauge bosons $V_H V_H$, with $V_H \equiv W_H^\pm, Z_H, A_H$ are plotted in figure 4.4. Their dependence on the parameters is smoother with respect to the fermion production modes, affected only by the masses of the fermionic partners exchanged in the t -channel. The $V_H V_H$ pair production is generated via s -channel exchange of SM gauge bosons or via t -channel exchange of fermionic partners.

The production modes involving the heavy triplet scalar components ($\phi^0, \phi^P, \phi^+, \phi^{++}$)

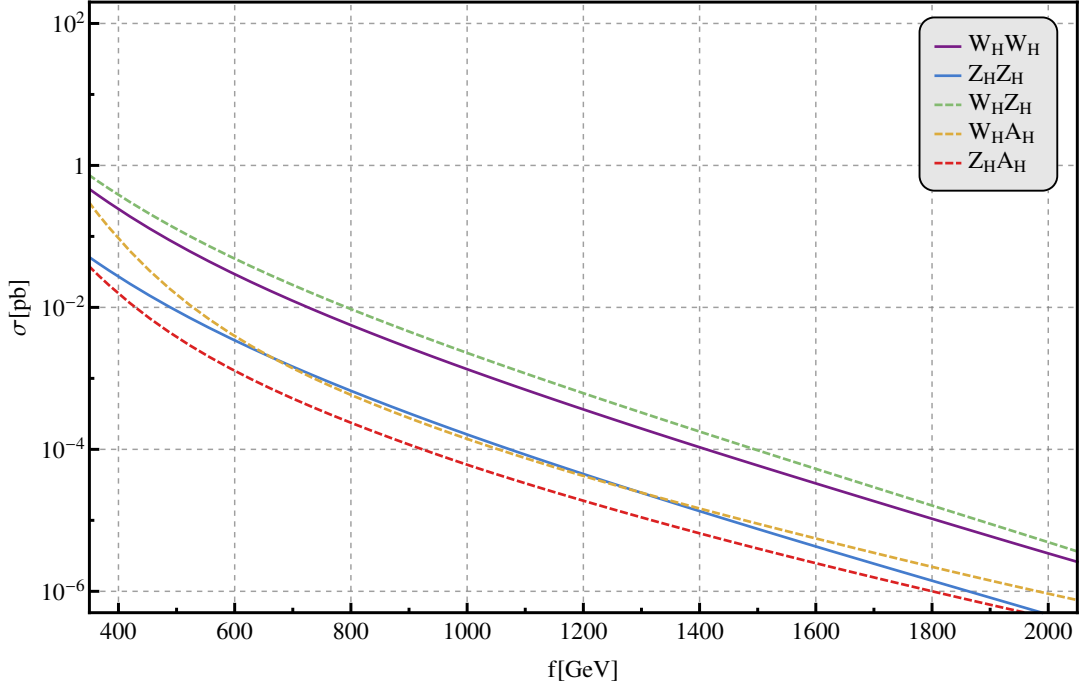


Figure 4.4. Production cross section of LHT gauge bosons partners at the LHC operating at 8 TeV, for reference values of $R = 1.0$ and $k = 1.0$.

will not be considered here, neither the ones involving the lepton partners l_H, ν_H . These production cross sections are parametrically smaller, therefore not affecting the LHC phenomenology relevant for our studies. Given the production and decay modes, it is straightforward to categorise the relevant signatures of the model with respect to the LHC searches, for which a table is presented in appendix B.2.

4.4 Experimental Searches

In this section the constraints on LHT parameter space from high energy physics experiments are discussed. We first discuss the electroweak precision constraints, then the Higgs data, and finally the direct LHC searches for new particles.

4.4.1 Electroweak Precision Observables

Historically, the most severe constraints on the parameter space of the different implementations of the Little Higgs paradigm have always arisen from EWPT [150–152]. The most serious constraints resulted from tree level corrections to precision electroweak observables due to the exchange of additional heavy gauge bosons present in these theories. In the class of product group models, this has been the reason for introducing T-parity which exchanges the gauge groups, as explained in section 4.2.1, making almost all new heavy particles T-odd and all SM particles T-even. Tree level couplings of light states with only one heavy particle are thereby forbidden, and no large contributions from higher dimensional operators — obtained by integrating out the heavy fields — are generated. The lower bound on the

symmetry breaking scale f from EWPT is then relaxed, making the new particles eventually observable at the LHC. On the other hand, single production of new heavy particles is forbidden and pair production leads to smaller production cross sections.

In the LHT model in particular, the only new particle which is T-even is the T-even top partner T_+ . However, it can contribute at tree level only to observables involving the SM top quark, such as its couplings to W and Z bosons: since these couplings have not been measured experimentally yet, no constraints arise at tree level from the T-even top partner as well. The leading contributions to electroweak observables arise therefore from one loop diagrams involving the new T-even and T-odd states. We refer to the literature [82, 158, 159, 165] for a comprehensive review.

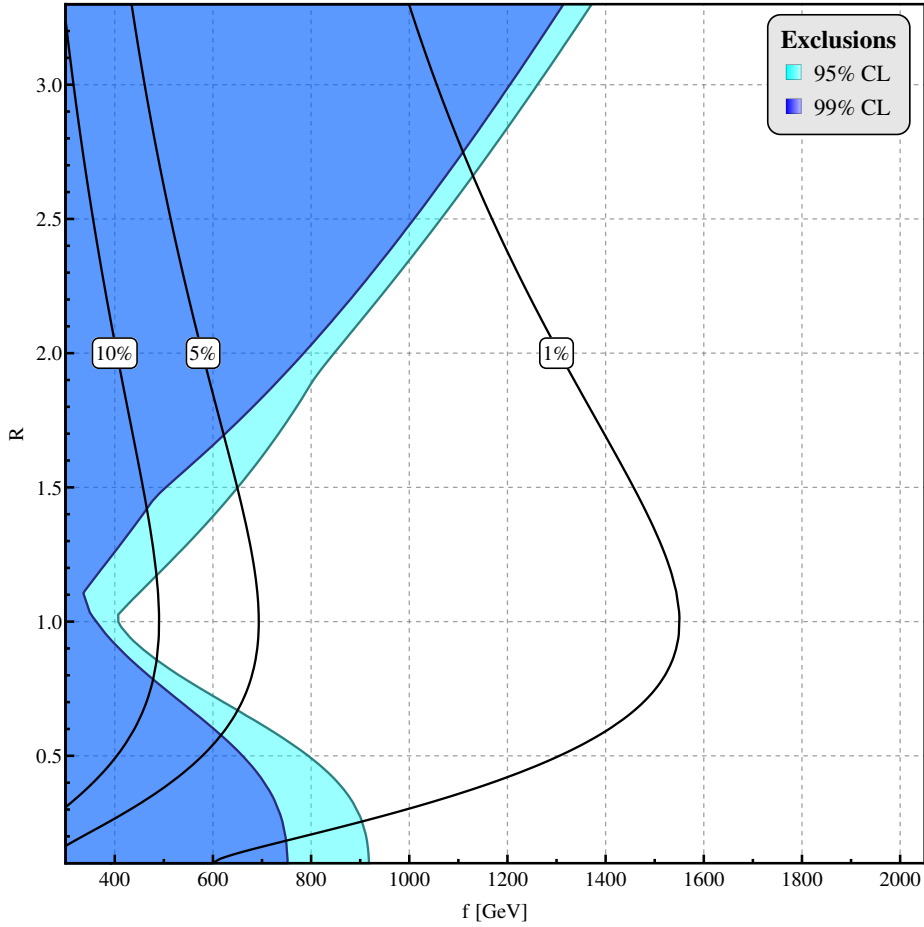


Figure 4.5. Excluded parameter space regions at 95% and 99% CL from EWPT. The thick black lines represent contours of required fine-tuning.

Following most of the details of the analysis realised in [82], including 21 different low-energy and Z -pole precision observables for $m_h = 124.5$ GeV [166], a χ^2 analysis in the (f, R) plane results in a lower bound on the symmetry breaking scale

$$f \gtrsim 405 \text{ GeV} \quad \text{at } 95\% \text{ CL}, \tag{4.48}$$

see figure 4.5. In this updated analysis we included also the T-odd fermion contributions to the T parameter and fit the value of k minimising the χ^2 for each point in the (f, R) parameter space, letting k range between the lower bound arising from the direct searches presented in section 4.4.3 — which is at least $k = 0.6$ for any given f — and the effective operator bound to be discussed below in equation (4.56). Note that the rather low value in equation (4.48) results from the dip around $R \sim 1$, where the LHT contributions to the EWPT are minimised. The value in equation (4.48) is the overall exclusion limit at 95% CL, independent of R . The thick black lines in figure 4.5 denote the levels of fine-tuning as defined at the beginning of section 4.3 and in equation (4.45).

4.4.2 Higgs Searches

A new era of Higgs physics has been entered since the discovery of the Higgs-like bosonic resonance. Besides EWPT, flavour constraints and direct searches of particles, the Higgs sector has become a useful framework for testing the validity of BSM models.

It is conventional for the experimental collaborations to express the results of the SM-like Higgs searches in terms of a signal strength modifier μ , defined as the factor by which the SM Higgs signal is modified for a given value of m_h :

$$\mu^i = \frac{n_S^i}{n_S^{\text{SM},i}} = \frac{\sum_p \sigma_p \cdot \epsilon_i^p}{\sum_p \sigma_p^{\text{SM}} \cdot \epsilon_i^p} \cdot \frac{\text{BR}_i}{\text{BR}_i^{\text{SM}}} \quad (4.49)$$

where i and p refer to a specific Higgs decay channel and production mode, respectively. Furthermore n_S^i is the total number of expected Higgs signal events evaluated in a chosen model passing the selection cuts, and ϵ_i^p is the cut efficiency for a given process (p, i) . For each Higgs decay channel considered, the ATLAS and CMS collaborations report the best-fit value $\hat{\mu}$ for a given hypothesis on m_h , while the cut efficiencies (or equivalently the signal composition in terms of the different production modes) are instead only partially reported. Considering a generic Higgs process (p, i) the cut efficiency ϵ_i^p can be expressed as

$$\epsilon_i^p = \frac{n_S^{\text{SM},i} \cdot \zeta_i^p}{\mathcal{L} \cdot \sigma_p^{\text{SM}} \cdot \text{BR}_i^{\text{SM}}} \quad (4.50)$$

where $n_S^{\text{SM},i} \cdot \zeta_i^p$ is the fraction of the SM expected signal events produced via the process (p, i) passing the selection cuts, \mathcal{L} is the integrated luminosity, and σ_p^{SM} , BR_i^{SM} are the SM cross section and branching ratio of the considered process (p, i) , respectively. It should be noted that $\sum_p \zeta_i^p = 1$, while $\sum_p \epsilon_i^p < 1$ in general. If the signal composition in terms of the different production modes ($\zeta_p^i, \forall p$) is reported, equation (4.49) then simplifies to

$$\mu^i = (c_g \cdot \zeta_g^i + c_V^2 \cdot \zeta_V^i + c_t^2 \cdot \zeta_t^i) \frac{\text{BR}_i}{\text{BR}_i^{\text{SM}}} \quad (4.51)$$

where g, V, t refer to gluon, vector and top initiated productions respectively, and where

$$\begin{aligned} \sigma_g^{\text{BSM}} &= c_g \cdot \sigma_g^{\text{SM}}, \\ \sigma_V^{\text{BSM}} &= c_V^2 \cdot \sigma_V^{\text{SM}}, \\ \sigma_t^{\text{BSM}} &= c_t^2 \cdot \sigma_t^{\text{SM}}. \end{aligned} \quad (4.52)$$

The rescaling factors c_g , c_V and c_t are model dependent and parametrise the rescaling of the $h \rightarrow gg$ partial width and of the hVV ($V \equiv W, Z$) or $ht\bar{t}$ vertices with respect to their SM values respectively, see [82, 167] for more details. For the channels where the signal composition is not reported, one is forced to neglect the efficiencies from equation (4.49), thus making the BSM predictions less reliable.

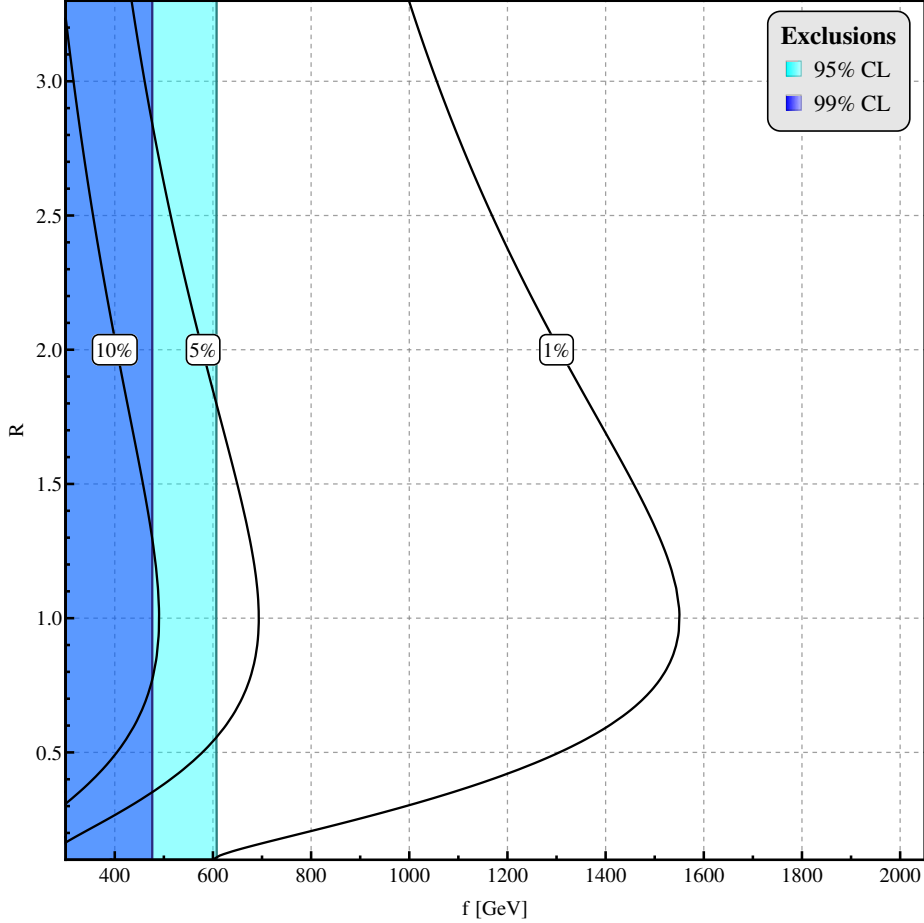


Figure 4.6. Excluded parameter space regions at 95% and 99% CL from ATLAS and CMS 25 fb^{-1} Higgs searches. The thick black lines represent contours of required fine-tuning.

The most recent results made public by both collaborations cover up to 25 fb^{-1} of analysed data for most of the 7+8 TeV Higgs searches. In this thesis we report an update of the analysis in the (f, R) plane realised in [82] with the updated dataset as first summarised in [167]. For completeness we report the explicit values used in the fit in appendix B.1. Unlike in the original analysis [82], we do not reconstruct the 8 TeV likelihood functions when only the 7 TeV and combined 7+8 TeV results are reported, while we use the 7+8 TeV data as if it were all coming from an 8 TeV run, as suggested in [167]. The only error incurred doing this is from a different weighting that would arise in the separate production modes, but this fractional difference is negligible.

The updated lower bound on the symmetry breaking scale, obtained from figure 4.6, is

$$f \gtrsim 607 \text{ GeV} \quad \text{at} \quad 95\% \text{ CL.} \quad (4.53)$$

It should be noted that with the inclusion of the 25 fb^{-1} dataset, Higgs searches have finally overwhelmed EWPT in driving the lower bound on the LHT symmetry breaking scale f , at least in the region around $R \sim 1$, where the EWPT exclusion is the lowest. The regions of required fine-tuning are also presented in the plot.

4.4.3 Direct LHC Searches

In this section we discuss the impact of direct LHC searches from the 8 TeV run for the Littlest Higgs with T-parity. To obtain the exclusion limits from recasting the existing analyses we first implemented the LHT model in FeynRules [113] combining the Feynman rules presented in [153–155]¹. The FeynRules package has been used to export the model to the UFO [168] format in order to interface it with the MadGraph [112] Monte Carlo generator. The model is then validated by reproducing the known results from the literature for both production cross sections and decay of the heavy particles in the model. Furthermore, cross checks for the implementation with the event generator WHIZARD [169, 170] and its FeynRules interface [171] have been made. The results in section 4.3 are in agreement with the established literature [154, 156] on LHT models.

MadGraph is used to generate parton level events which are then interfaced into the Pythia 6.42 [114] parton shower. The result is further processed in Delphes 3.0 [172] to simulate either the ATLAS or CMS detector in a fast manner. Different analyses published by ATLAS and CMS can then be recasted for the LHT model to extract exclusion limits. In particular, for each considered analysis, we evaluated the efficiencies of the analysis-dependent cuts applied to a LHT signal which could mimic the experimental final state topology under consideration². The predicted visible cross section is then simply given by a reweighting of the signal cross section times the evaluated efficiency. The experimental 95% CL upper bound on the visible cross section can finally be used to determine the possible exclusion of the corresponding parameter space point.

Since most of the final states mimic supersymmetry final states with significant amounts of missing transverse energy, we mostly discuss these searches in the following paragraphs. However, we begin with a paragraph on constraints from effective operators bounds. A phenomenologically interesting feature of the LHT model is the power counting of k which leads to an upper bound and not a lower bound for the particles running in the loop. Then we discuss the supersymmetry searches by ATLAS and CMS bearing in mind the determination of the lower exclusion limit on the scale f . This is most easily done in processes where only the parameters f and k play a role and the exclusion limits can be given in the (f, k) plane. These are then summarised in the next section.

¹The FeynRules model implementation is available upon request by the authors.

²A Mathematica package for this purpose has been developed and is also available upon request.

Effective Operator Bounds

The T-odd quark partners of the SM fermions can generate four-fermion operators via box diagrams involving the exchange of NGBs [158]. Assuming a diagonal and flavour-independent matrix k , the following set of four-fermion operators is generated

$$\mathcal{O}_{4-f} = -\frac{k^2}{128\pi^2 f^2} \bar{\psi}_L \gamma^\mu \psi_L \bar{\psi}'_L \gamma_\mu \psi'_L + \mathcal{O}\left(\frac{g}{k}\right), \quad (4.54)$$

where ψ and ψ' are (possibly distinct) SM fermions. On the other hand these four-fermion operators may also be generated through strongly coupled physics above the scale $\Lambda = 4\pi f$. An estimate for these contributions is

$$\mathcal{O}_\Lambda \approx \pm \frac{C_\Lambda}{16\pi^2 \Lambda^2} \bar{\psi}_L \gamma^\mu \psi_L \bar{\psi}'_L \gamma_\mu \psi'_L, \quad (4.55)$$

where the coupling C_Λ should be roughly $\mathcal{O}(1)$.

Experimental bounds on four-fermion interactions provide an upper bound on the T-odd fermion masses, which then yield an upper bound on k for a given value of f . Possible constraints at the LHC come from operators involving four quarks, for example searches in the angular distribution of dijets [119, 120]. These experimental searches give constraints on the operator coefficient in the range of $\Lambda = 15$ TeV for constructive interference which we are considering here. Although these searches are promising candidates to further constrain the parameter k , the most stringent bounds are actually still from LEP searches. The strongest constraint comes from the $eedd$ operator $\Lambda_{4-f} = 26.4$ TeV [158, 166]. This requires the coefficient of the four-fermion operator to be smaller than $2\pi/\Lambda_{4-f}^2$, and yields the following upper bound for k

$$k^2 < 256\pi^3 \frac{f^2}{\Lambda_{4-f}^2} \pm \frac{C_\Lambda}{2\pi^2}. \quad (4.56)$$

This bound is plotted in the total exclusion plot at the end of this section in figure 4.11, assuming $C_\Lambda = 0$ for simplicity. Possible improvements from LHC experiments regarding these bounds are discussed in section 4.5.3.

Monojet & \cancel{E}_T

Both ATLAS and CMS have presented experimental searches with 8 TeV data for final states containing no leptons, one hard jet, missing transverse energy and at most a second hard jet with $p_T > 30$ GeV [173, 174]. The ATLAS search defines four signal regions with both the p_T of the leading jet and the \cancel{E}_T to exceed 120, 220, 350, 500 GeV, respectively. The CMS analysis, however, only defines signal regions in the missing transverse energy, which are $\cancel{E}_T > 250, 300, 350, 400, 450, 500, 550$ GeV, whilst requiring the leading jet $p_T > 110$ GeV. Additional suppression of QCD dijet background is handled by the two experiments in a different manner. ATLAS requires the azimuthal separation between the \cancel{E}_T direction and the second leading jet, if present, to be greater than 0.5. On the other hand, CMS only retains a two jet event if the azimuthal separation between the jets is less than 2.5. In the absence of any deviation from the Standard Model, both experiments quote 95% CL upper bounds on the signal visible cross section for all the signal regions defined above.

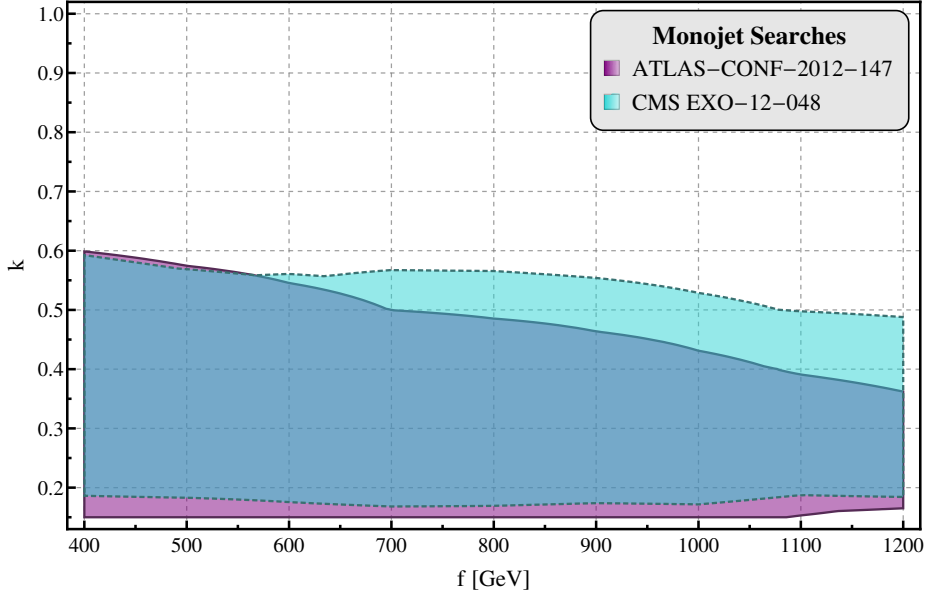


Figure 4.7. 95% CL exclusion limits from monojet & \cancel{E}_T direct searches at LHC8. The different contours represent the excluded regions from the latest monojet searches by ATLAS and CMS.

Both monojet searches are suitable for final state topologies containing one or two hard jets and missing transverse energy. Hence, both LHT production modes $pp \rightarrow q_H q_H$ and $pp \rightarrow q_H A_H$ may contribute, provided the heavy quark partner decays to a quark and a heavy photon $q_H \rightarrow A_H q$. Therefore these searches have the highest exclusion power in the low- k region ($0.2 \lesssim k \lesssim 0.6$). Indeed for $0.2 \lesssim k \lesssim 0.6$ the heavy quarks decay entirely into $A_H q$, giving the required final state topology. For higher values of k , the decays into heavy gauge bosons become kinematically allowed ($q_H \rightarrow W_H/Z_H q$), highly reducing the branching ratio $q_H \rightarrow A_H q$. In figure 4.7 one can observe the excluded contours by recasting both ATLAS and CMS monojet & \cancel{E}_T analysis.

Jets & \cancel{E}_T

This category comprises all searches with at least two signal jets, missing transverse energy and no leptons in the final state. In the past, searches of this kind have been studied in the context of the LHT model using Tevatron and early CMS data [175, 176]. In the last year, numerous searches interpreted in terms of supersymmetric final states have been presented by ATLAS and CMS for the 8 TeV data. All these searches have been analysed and the searches relevant for the LHT final states are the analyses by ATLAS [177, 178] and CMS [179]. The first ATLAS search is optimised for squarks and gluinos and the second for stops, whereas the CMS search looks more generally at squarks, sbottoms and gluinos.

The ATLAS squark and gluino search [177] defines signal regions which require at least two, three, four, five or six jets, respectively. For those signal regions the Standard Model backgrounds are reduced using cuts on $\Delta\phi$ between the jets and the missing transverse energy and stringent cuts on $\cancel{E}_T/m_{\text{eff}}$ and m_{eff} . In the LHT scenario these final states correspond to pair production of heavy gauge bosons and heavy quark partners or mixed

states like $V_H q_H$, with subsequent decays $q_H \rightarrow V_H q$, $V_H \rightarrow V_{SM} A_H$, and all hadronic decays of the SM gauge bosons V_{SM} .

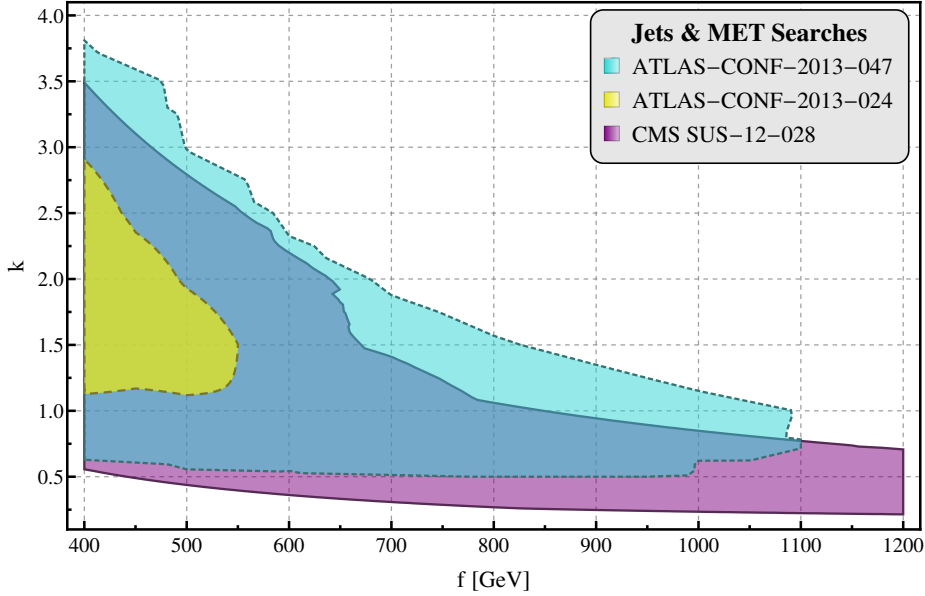


Figure 4.8. 95% CL exclusion limits from jets & \cancel{E}_T direct searches at LHC8. The different contours represent the excluded regions from the latest jets & \cancel{E}_T searches by ATLAS and CMS.

The other ATLAS analysis [178] is optimised for searches of stop pair production, where each stop decays exclusively to a hadronically decaying top and the LSP. The analysis requires at least six hard jets ($p_T > 35$ GeV), of which at least two must originate from bottom quarks. Three signal regions with significant missing transverse energy $\cancel{E}_T > 200, 300, 350$ GeV are defined and two trijet systems should each roughly reconstruct the top mass. To further suppress the Standard Model background, cuts are placed on $\Delta\phi$ between the three highest- p_T jets and \cancel{E}_T . On top of that the transverse mass m_T between the \cancel{E}_T and the b-tagged jet closest in $\Delta\phi$ to the \cancel{E}_T direction is required to be greater than 175 GeV. A possible LHT production mode is pair production of the T-odd top t_H with subsequent stop like decay. Another production mode is two heavy quark partners where at least one of the quarks decays like $q_H \rightarrow Z_H q$, giving the required two b -jets.

The CMS analysis [179] for squarks, including sbottoms, and gluinos looks at events with multiple jets, some of them b -jets, and significant missing energy. The analysis defines five signal regions tailored for the specific supersymmetry final states as $(N_{\text{jet}}, N_b) = (2 - 3, 0); (2 - 3, 1 - 2); (\geq 4, 1 - 2); (\geq 4, 0); (\geq 4, \geq 2)$. In order to suppress Standard Model background there are cuts on the transverse momenta of the jets and the scalar sum of the transverse momenta of the jets. Furthermore, the α_T variable is used to protect against jet energy mismeasurement and is generalised to multi-jet final systems. The first signal region is a perfect fit for the production and decay $q_H q_H \rightarrow (A_H q) + (A_H q)$ which is efficient for low values of $k \lesssim 0.6$. The signal regions with at least four jets are instead efficient for the complementary region of $k \gtrsim 0.6$, where we can look at pair production of heavy gauge bosons and quark partners as well as the associated productions $V_H q_H$ with all hadronic

final states, as already mentioned for the ATLAS analyses.

Each of the above searches provide 95% CL upper bounds on the visible cross sections in the absence of any signal. The results from recasting the analysis are provided in figure 4.8.

Leptons, Jets & \cancel{E}_T

In this section all searches involving leptons, at least two jets and missing transverse energy are considered, where some of the jets may be b-tagged. Indeed, several searches exist by ATLAS and CMS that match the latter final states. Here we only consider the constraining searches for the LHT model, in particular these are [180–183].

A search for supersymmetry using a single isolated lepton, at least four jets and missing transverse energy has been performed by ATLAS [180]. The lepton in the event can be either an electron or a muon, where both cases are considered separately and define a signal region each. Events with more than one lepton are vetoed. Each of the four jets in the event need to have $p_T > 80$ GeV and additional kinematic cuts to suppress Standard Model background are: $\cancel{E}_T > 250$ GeV, $m_T(l, \cancel{E}_T) > 250$ GeV, $\cancel{E}_T/m_{\text{eff}} > 0.2$ and $m_{\text{eff}}^{\text{inc}} > 800$ GeV. In terms of LHT topologies, the production of two heavy quarks, which then decay to heavy gauge bosons $q_H \rightarrow W_H q$ or $\rightarrow Z_H q$ with at least one leptonically decaying W at the end of the decay chain, results in exactly this final state.

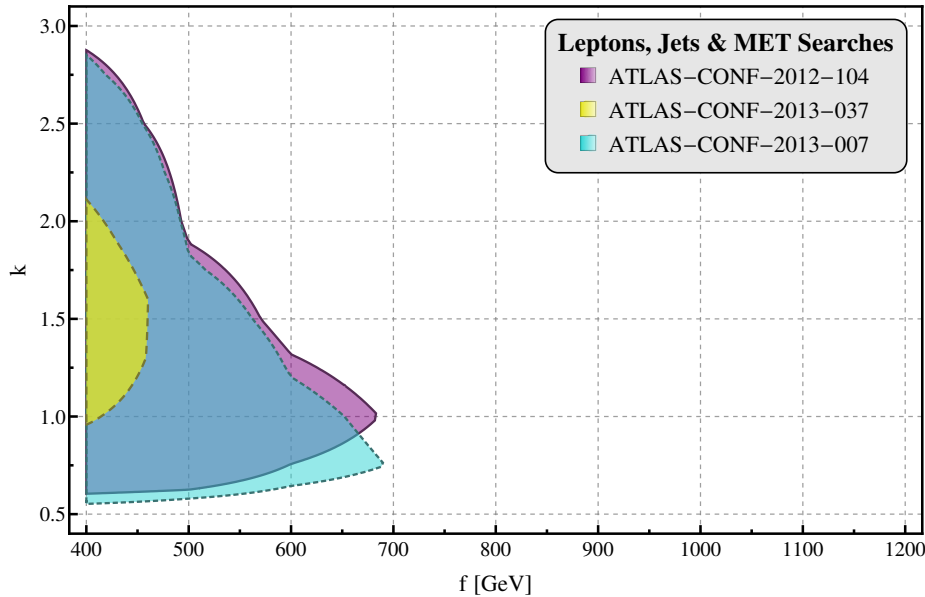


Figure 4.9. 95% CL exclusion limits from leptons, jets & \cancel{E}_T direct searches at LHC8.

There is also a supersymmetry analysis focussing on stops by ATLAS [181], which is updated in [182]. In this scenario the stop either decays into a top quark and the LSP or each top squark decays to a bottom quark and the lightest chargino. Therefore the analysis requires one isolated lepton, at least four jets of which at least one is b-tagged and significant missing transverse energy. Events with more than one lepton are vetoed and each of the signal regions implements various cuts used in supersymmetry searches like \cancel{E}_T , m_{eff} , m_T and m_{T2} . Additionally for the signal regions involving top quarks, it is required to reconstruct the

mass of the hadronically decaying top. The LHT production modes which may contribute are the same as before (pair production of heavy quark partners) with subsequent decays into gauge boson partners W_H, Z_H , but with semi-leptonic decays of the SM gauge bosons. As before, b -jets may arise from the decay of the Higgs boson from the $Z_H \rightarrow H A_H$ decay chain, or from the decay chain of the T-odd top partner $t_H \rightarrow t A_H$.

The ATLAS search [183], which was originally optimised for searches of gluino pair production, looks for two same sign leading leptons in combination with at least three jets and a significant amount of missing transverse energy. This search is divided into three signal regions with different number of jets and b -jets, but since the only final state in our model with two same sign leptons contains at most two additional jets, we only considered the first signal region. This signal region requires at least three jets: for our signal we rely on initial and final state QCD radiation for one additional jet, which is easily possible since the jets in this analysis only need to have $p_T > 40$ GeV. Further requirements on the event kinematics are: $\cancel{E}_T > 150$ GeV, $m_T(l, \cancel{E}_T) > 100$ GeV and $m_{\text{eff}} > 400$ GeV. The only decay chain to achieve this final state is pair production of same charge quark partners $pp \rightarrow q_H q_H$ with subsequent decays into gauge boson partners W_H with all leptonic decays for the W s. A similar analysis by CMS [184] is not efficient because it requires at least two b -tagged jets, for which there is no LHT process that matches this final state.

From the searches described in this paragraph, 95% CL exclusion limits in the (f, k) plane can be extracted similar to the methods described before. The results from the recast are presented in figure 4.9. From this we conclude that searches for both a single and two leptons perform similarly, as long as no b -jets in the final state are required.

4.4.4 Combined Exclusion Limits

It is interesting to combine and compare the results from electroweak precision physics, Higgs precision physics and direct searches at the LHC.

EWPO & Precision Higgs

By combining the χ^2 analyses carried out separately for EWPT and the Higgs sector, as plotted in figure 4.10, the lower bound on the symmetry breaking scale is

$$f \gtrsim 694 \text{ GeV} \quad \text{at} \quad 95\% \text{ CL.} \quad (4.57)$$

By looking at this combination, the allowed fine-tuning is now worse than 10% over the whole parameter space, while still a small region could allow for a $\gtrsim 5\%$ fine-tuning. Results for the *Case B* implementation of the down-type Yukawa couplings are provided in appendix B.3.

Direct LHC Searches

Gathering all the exclusion limits from the aforementioned direct searches, the combined total exclusion limit in the (f, k) plane is presented in figure 4.11. From these combined results the following lower bound on the symmetry breaking scale can be deduced:

$$f \gtrsim 638 \text{ GeV} \quad \text{at} \quad 95\% \text{ CL.} \quad (4.58)$$

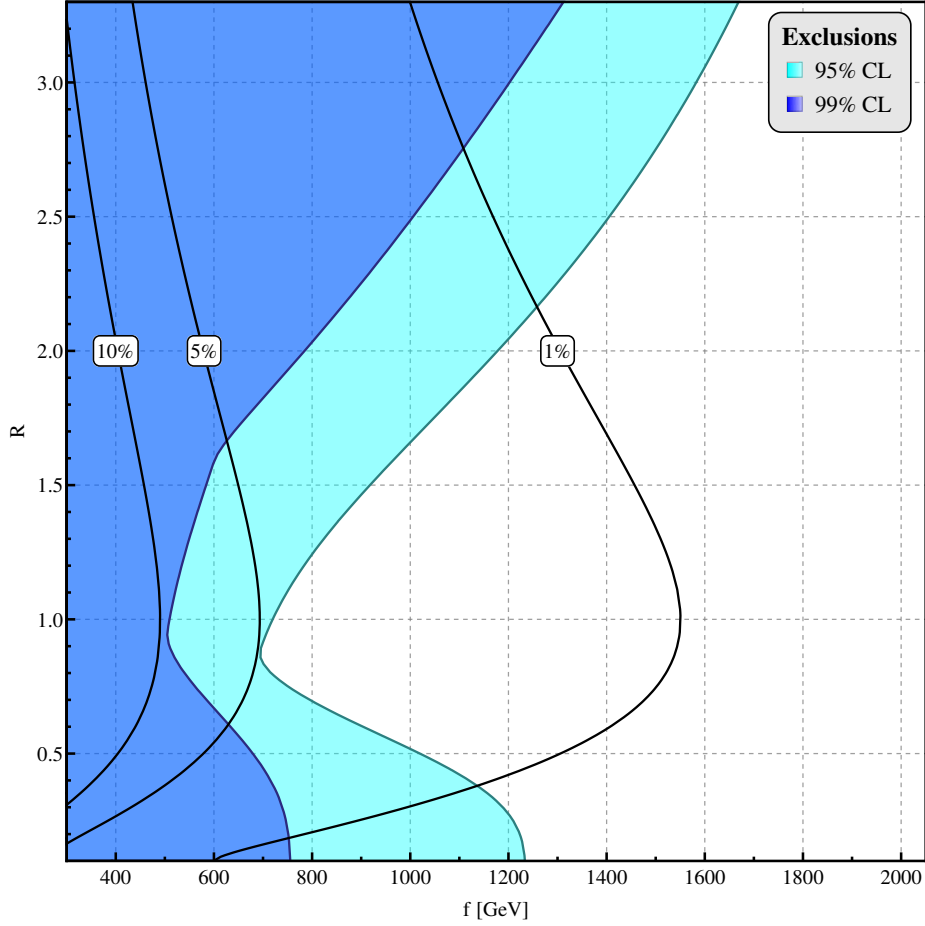


Figure 4.10. Excluded parameter space regions at 95% and 99% CL from combination of EWPT and Higgs sector datasets. The thick black lines represent contours of required fine-tuning. The down-type Yukawa couplings are assumed to be from *Case A*.

From the combination we can observe that the exclusion is dominated by all-hadronic searches. Furthermore, the requirement of b-jets or leptons in the final state only reduces the exclusion power for an LHT signal. This is mainly due to lower cross sections from reduced branching ratios for b-jets and leptons.

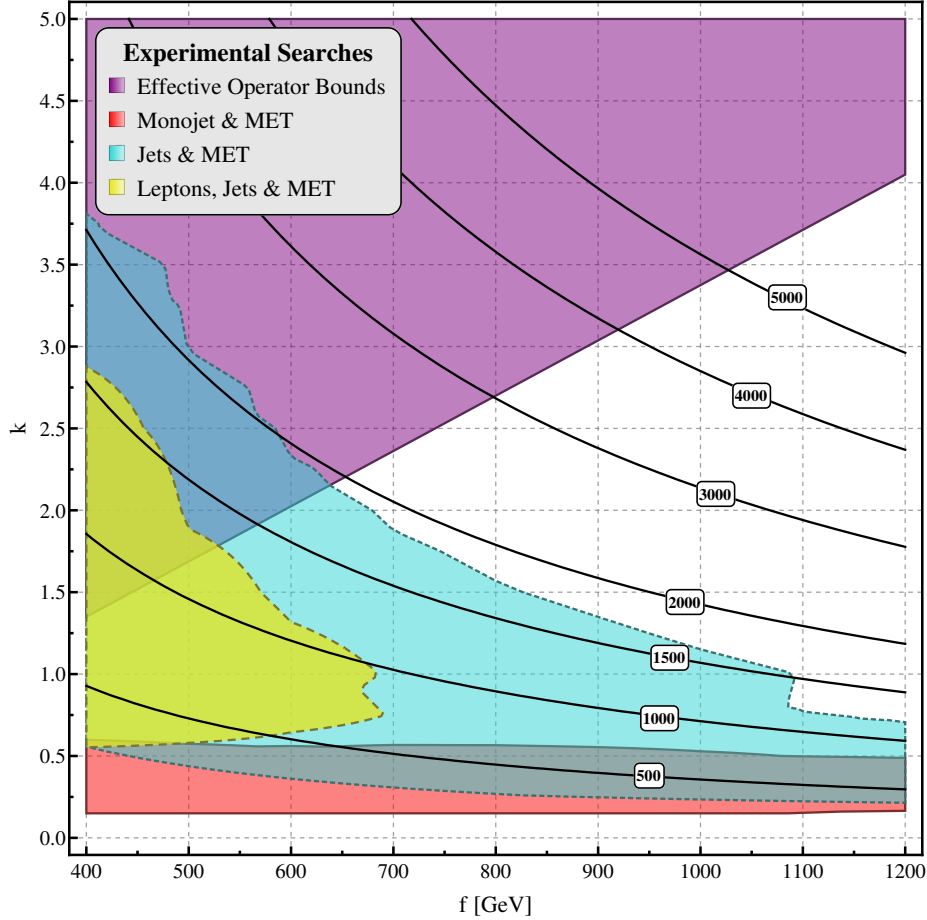


Figure 4.11. 95% CL exclusion limits from direct searches at LHC8 displayed in the (f, k) plane. The different categories comprise limits from operator bounds and searches from monojets, jets and leptons plus jets. The contour lines show the mass of the heavy quark partners.

4.5 Optimising Current SUSY Searches

The current exclusion limits in the (f, k) plane predominantly arise from three different direct searches: four-fermion operator bounds, monojet plus missing energy and jets plus missing energy. In this section we optimise the direct searches and show their effects on the parameter space of the LHT model.

Using the tools for event generation as described before in the text, we generated event samples for some signal benchmark points in the (f, k) parameter space and for the background processes. We made sure to have significant statistics in order to obtain a reliable evaluation of the different cut efficiencies. The optimisation is performed for a centre of mass energy of 8 TeV, in analogy with the latest supersymmetric searches. Following the set-up of the existing experimental analyses, we identified useful sets of kinematic cuts in order to reduce the backgrounds. These cuts are optimised by varying their values within sensible domains, and then evaluating the efficiencies for both signal and backgrounds as a function of the kinematic cuts. By reweighting the signal and background cross sections

with the evaluated efficiencies, we obtained a map of the ratio S/\sqrt{B} , where S is the considered signal and B is the sum of all possible backgrounds, as a function of the cut values. The maximised S/\sqrt{B} ratio determines an optimised set of cut values which guarantees the highest exclusion or discovery power for the particular signal considered.

Once the optimised selection cuts are obtained, we multiplied the evaluated background efficiencies with the corresponding production cross sections. In this way we could determine the total number of expected background events, assuming an integrated luminosity as reported in the experimental analyses. We then used a standard CLs frequentist approach [185] to calculate the model independent 95% CL upper limit on the possible number of BSM signal events. In particular, we calculated the p -values of the signal plus background and the background only hypothesis, assuming Poisson probability for the number of observed events, and constructed a CLs variable including systematic errors on the background. To retrieve the expected signal upper bound, the number of observed events has been fixed to the number of expected events from the Standard Model. The upper bounds on the number of signal events can then finally be translated into exclusion regions in the (f, k) plane. This procedure is outlined for both monojet plus missing energy and jets plus missing energy signatures in the next sections.

4.5.1 Monojet & \cancel{E}_T Search

Both the monojet searches by ATLAS [173] and CMS [174] are designed to reach out into the more compressed parts of the supersymmetry spectrum. In the LHT framework, too, the reach of these searches is in the compressed part of parameter space, namely for lower values of k . This region is constrained by $m_{A_H} \leq m_{Q_H} \leq m_{V_H}$, which roughly implies $0.1 \lesssim k \lesssim 0.45$. In this region of parameter space the production modes $pp \rightarrow q_H q_H$ and $pp \rightarrow q_H A_H$ dominate in terms of production cross section, see table B.3. These production modes lead to final states with one or two jets and significant amounts of missing transverse energy. This is explained by the fact that the heavy quarks uniquely decay as $q_H \rightarrow A_H q$ for these low k values. Even for higher values of k the same final state is still a possibility: however, the branching ratio for this heavy quark decay rapidly decreases to 6 – 9%. Nevertheless we will still investigate the sensitivity of the monojet search also for higher values of $k \lesssim 1.0$.

First the backgrounds and the ATLAS and CMS monojet analyses are discussed, then the procedure of optimising the kinematic cuts and finally potential exclusion contours in the (f, k) plane are obtained. Since the two experimental analyses are based on different amounts of integrated luminosity, we decided to use a reference value of 20 fb^{-1} for the monojet proposal.

Backgrounds & Analyses

The dominant backgrounds for monojet searches are $Z(\rightarrow \nu\nu) + \text{jets}$ and $W + \text{jets}$, with sub-leading contributions from $Z/\gamma^*(\rightarrow l^+l^-) + \text{jets}$, multi-jet, $t\bar{t}$ and diboson (WW, ZZ, WZ) processes. Each of these processes has been simulated using the Monte Carlo chain described previously. The background samples have been generated applying the detector specifications as reported in the ATLAS analysis.

Cut	BM1	BM2	BM3	ATLAS	CMS
MET (\cancel{E}_T)	170 GeV	520 GeV	370 GeV	120	250
First jet p_T	120 GeV	470 GeV	250 GeV	120	110
Second jet p_T	80 GeV	310 GeV	180 GeV	✗	✗
Lepton veto	✓	✓	✓	✓	✓
Two jet veto	✓	✓	✓	✓	✓
$\Delta\phi(\cancel{E}_T, j_2) \geq$	0.5	0.5	0.5	0.5	✗
$\Delta\phi(j_1, j_2) \leq$	2.5	2.5	2.5	✗	2.5
S_{exp}^{95}	1745	8.4	99.9	45136	3694

Table 4.2. Cut-flow table for the monojet & \cancel{E}_T optimisation. In analogy with the existing analyses the lepton veto dismisses any event with an electron ($p_T > 10$ GeV), a muon ($p_T > 10$ GeV) or a tau ($p_T > 20$ GeV). The two jet veto removes all events with more than two jets satisfying $p_T > 30$ GeV and $\eta < 4.5$. Shown in the first three columns are the optimised cuts for the chosen benchmark points. The last two columns show one of the signal regions of the ATLAS and CMS analysis [173, 174], for comparison and validation with the experimental results. S_{exp}^{95} is the upper bound on the number of signal events obtained with the statistics method described at the beginning of section 4.5.

Both the ATLAS and CMS analyses use roughly the same set of cuts to suppress the backgrounds. They share a lepton veto and a two jet veto, which forbids any final state with leptons or more than two hard jets. Furthermore they use cuts on $\Delta\phi$ between the missing energy and the second leading jet, and between the first and the second leading jet, by ATLAS and CMS, respectively. On top of these basic cuts, signal regions are defined which set varying cuts on the missing transverse energy in the event and the p_T of the leading jet. The ATLAS search defines four signal regions with both the p_T of the leading jet and the \cancel{E}_T to exceed 120, 220, 350, 500 GeV, respectively. The CMS analysis however only defines signal regions in the missing transverse energy, which are $\cancel{E}_T > 250, 300, 350, 400, 450, 500, 550$ GeV, whilst requiring the leading jet $p_T > 110$ GeV. The two reference signal regions based on the ATLAS and CMS analyses are shown in the last two columns of table 4.2.

Benchmark	$f(\text{GeV})$	k	Cut	Range
BM1	1600	0.2	\cancel{E}_T	[120, 600] GeV
BM2	2000	0.4	$p_T(j_1)$	[100, 600] GeV
BM3	600	0.8	$p_T(j_2)$	[0, 450] GeV

Table 4.3. Benchmark scenarios (left) and ranges for the kinematic cuts (right) for the monojet proposal.

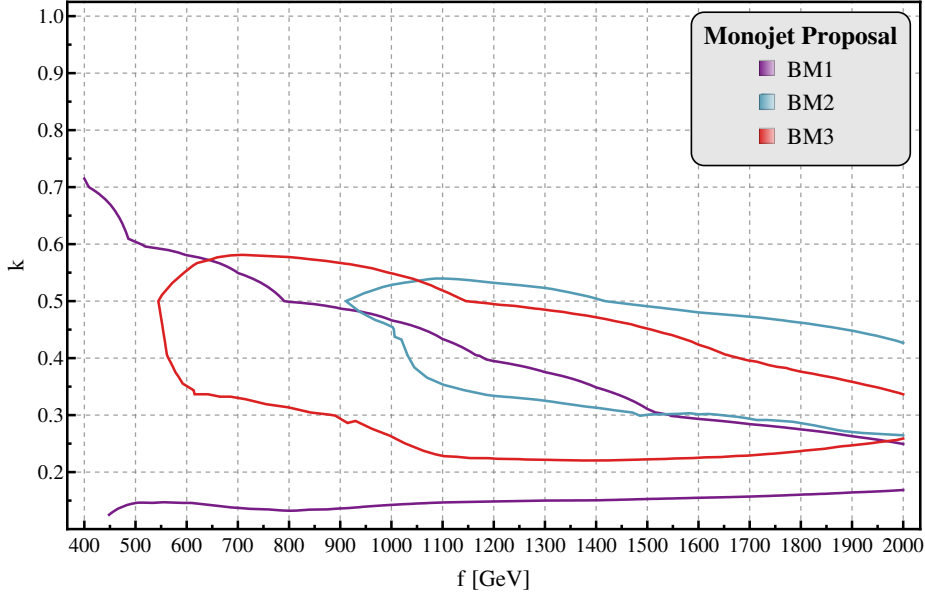


Figure 4.12. 95% CL potential exclusion limits from the proposed optimised monojet search at LHC8 with 20 fb^{-1} displayed in the (f, k) plane. The different contours correspond to different signal regions.

Cut-flow

As discussed before, a set of kinematic cuts, including the ranges in which they are varied, is defined in table 4.3. The minimum values for both the \cancel{E}_T and p_T cut are needed to allow for efficient triggering in both ATLAS and CMS detectors for the monojet searches. Then the optimal values for these cuts are determined for a set of benchmark scenarios, which are listed in table 4.3 as well. In contrast to the monojet searches by ATLAS and CMS we do allow for a p_T cut on the sub-leading jet, since our signal mainly consists of two jets. This topology has also been studied in [186]. Such a cut will aid significantly in the suppression of the background. For each of these benchmark points an optimal S/\sqrt{B} is obtained for the values shown in table 4.2 and these cuts are then used to define three signal regions.

In general we observe that both the missing transverse energy cut and the cuts on the p_T of the jets increase proportional to the mass gap between the heavy quark and the heavy photon. This can be explained simply by the fact that the mass difference $m_{Q_H} - m_{A_H}$ will be translated to transverse momenta of both the jet and the heavy photon. Hence, the result will be high p_T for the jets and a high missing transverse energy for high mass gaps.

Exclusion Limits

After having used the cut-flow procedure we essentially have an experimental monojet search with three signal regions corresponding to the three benchmark points. For each of the benchmark points we obtained the corresponding upper bounds on the visible cross sections, by dividing the signal upper bounds from table 4.2 by the luminosity. These limits can then be compared to the signal visible cross section as a function of f and k and exclusion contours can be drawn. The exclusion contours per signal region are provided in

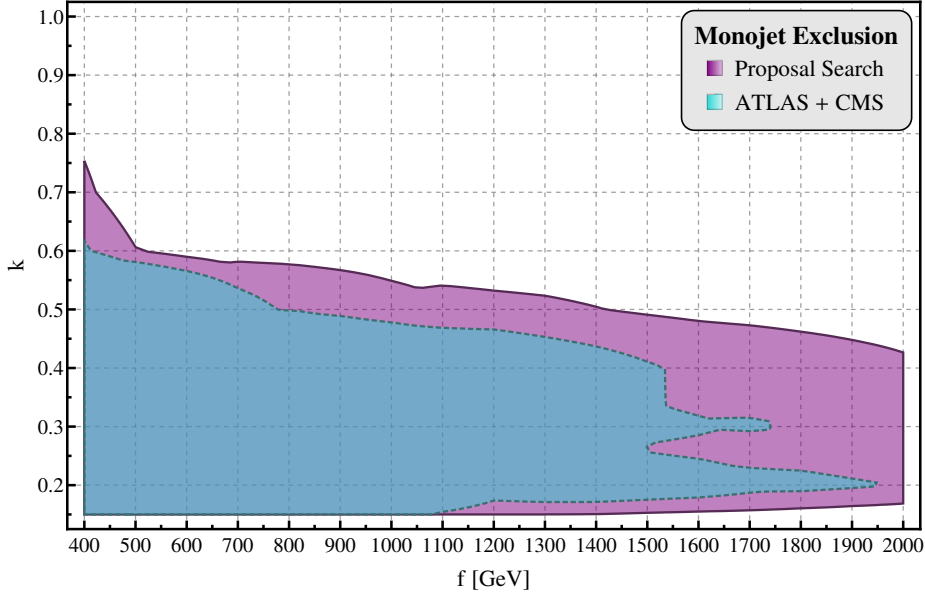


Figure 4.13. Comparison between the monojet proposal exclusion limits and the limits from the experimental signal regions. The upper bounds on the visible cross sections in both cases have been obtained using our statistics method. This is to ensure a comparison which does not depend on the background simulations nor the statistics method.

figure 4.12.

The combined exclusion limit from all signal regions is given in figure 4.13, together with the result of the recasting procedure for the monojet analyses for comparison. Here we used the upper bound on the visible cross section evaluated with our statistics method for both the proposed signal regions as well as for the recasting of the experimental ATLAS and CMS signal regions. This has been done in order to show that the increased exclusion power is genuinely due to the optimisation procedure. The results show that the range of the monojet proposal extends into the high f regions for all k values between 0.2 and 0.6. Above $k = 0.6$ the decay $q_H \rightarrow A_H q$ is too much suppressed and the cross sections are too low, whereas below $k = 0.2$ the spectrum is becoming compressed, reducing the proposal's sensitivity. In conclusion, there is room for improvement especially in the high f regime, which will be vital in the future for excluding f beyond a TeV.

4.5.2 Jets & \cancel{E}_T Search

The highest exclusion sensitivity for the LHT parameter space, as clearly pointed out in section 4.4.4, is achieved in jets & \cancel{E}_T final state topologies. This is mainly due to the higher available LHT signal cross section for this topology, see table B.3. As described in section 4.4.3, there are two available analyses scrutinising possible BSM signals in the jets & \cancel{E}_T final state. The ATLAS analysis [177] is optimised for searches of squarks and gluinos, while the CMS analysis [179] is more general and searches for squarks, sbottoms and gluinos. The goal in this section is to reformulate the set-up of the ATLAS analysis assuming an LHT signal instead of a SUSY signal for which the analysis has been realised.

In this way we will be able to propose an optimised set of selection cuts in order to reach the highest possible exclusion power for the LHT signal.

Experimental Analysis

We decided to focus on the ATLAS signal regions which require a hard p_T cut on the third- and fourth-leading jet (SR B and SR C in ATLAS notation). The corresponding selection cuts used to reduce the backgrounds are summarised in table 4.4.

Cut	SR BM	SR BT	SR CM	SR CT
Lepton veto			✓	
$n_{\text{jets}} \geq$	3			4
$\cancel{E}_T >$			160 GeV	
$p_T(j_1) >$			130 GeV	
$p_T(j_n) >$			60 GeV	
$\Delta\phi(j_{1,2,3}, \cancel{E}_T)_{\text{min}} >$			0.4	
$\cancel{E}_T/m_{\text{eff}}(n_j) >$	0.3	0.4		0.25
$m_{\text{eff}}(\text{incl.}) >$	1.8 TeV	2.2 TeV	1.2 TeV	2.2 TeV

Table 4.4. Selection cuts used in the ATLAS analysis [177] for the signal regions B (3j) and C (4j).

Notice that signal jets need to satisfy $p_T > 40$ GeV and $|\eta| < 2.8$, while signal electrons (muons) $p_T > 20$ (10) GeV and $|\eta| < 2.8$ (2.4). The $\cancel{E}_T/m_{\text{eff}}(n_j)$ cut in any n -jet channel uses a value of m_{eff} constructed by the scalar sum of the transverse momenta only of the n leading jets (and \cancel{E}_T), while the $m_{\text{eff}}(\text{incl.})$ selection includes all jets with $p_T > 40$ GeV besides the \cancel{E}_T . For the cut on the minimal azimuthal separation between the \cancel{E}_T direction and the reconstructed jets, only the three leading jets are considered. An additional requirement of $\Delta\phi(j, \cancel{E}_T) > 0.2$ is placed on all jets with $p_T > 40$ GeV.

Backgrounds

The dominant SM background processes are $W + \text{jets}$, $Z + \text{jets}$, top quark pairs, diboson, single top and multiple jets productions. The majority of the $W + \text{jets}$ background is composed by $W \rightarrow l\nu$ events in which no charged lepton is reconstructed, or $W \rightarrow \tau\nu$ with a hadronically decaying τ . The largest part of the $Z + \text{jets}$ background comes from the $Z \rightarrow \nu\nu$ component, generating large \cancel{E}_T . Top quark single and pair production followed by semi-leptonic decays (both to a light charged lepton or to a τ lepton) can generate \cancel{E}_T , too, and pass the jet and lepton requirements at a non-negligible rate. Missing transverse energy in the multi-jet background originates from the misreconstruction of jet energies in the calorimeters. The background samples have been generated applying the detector specifications as reported in the ATLAS analysis.

Cut-flow

Three different samples for the signal events were generated using three different choices of the free parameters f and k , with substantially different kinematic properties involved. These are summarised in table 4.5. The ranges of the kinematic cuts in which they are varied to obtain an optimal set-up are reported in table 4.5 as well.

Benchmark	f (GeV)	k	Cut	Range
BM1	600	1.0	n_{jets}	3 or 4
BM2	700	2.0	\cancel{E}_T	[100, 500] GeV
BM3	1000	1.0	$p_T(j_1)$	[100, 400] GeV
			$p_T(j_n)$	[40, 100] GeV
			$m_{\text{eff}}(\text{incl.})$	[1.2, 3.0] TeV

Table 4.5. Benchmark scenarios (left) and ranges for the kinematic cuts (right) for the jets & \cancel{E}_T proposal.

The lepton veto and an additional cut of $\Delta\phi(j_{1,2,3}, \cancel{E}_T)_{\text{min}} > 0.4$ are applied in each signal region, in order to further reduce the different backgrounds. Clearly, if a cut on the p_T on the n -th leading jet is applied ($p_T(j_n)$), at least n signal jets are required to be present in the final state. For each benchmark point, an optimal S/\sqrt{B} ratio is obtained for the values shown in table 4.6.

Cut	BM1 _{3j}	BM2 _{3j}	BM3 _{3j}	BM1 _{4j}	BM2 _{4j}	BM3 _{4j}
Lepton veto	✓					
n_{jets}	3			4		
\cancel{E}_T	200 GeV	340 GeV	400 GeV	200 GeV	300 GeV	400 GeV
$p_T(j_1)$	120 GeV	380 GeV	180 GeV	140 GeV	320 GeV	180 GeV
$p_T(j_n)$	100 GeV	100 GeV	100 GeV	70 GeV	80 GeV	100 GeV
$\Delta\phi(j_{1,2,3}, \cancel{E}_T)_{\text{min}}$	0.4					
$m_{\text{eff}}(\text{incl.})$	1.2 TeV	2.8 TeV	2.1 TeV	1.2 TeV	2.6 TeV	2.1 TeV
S_{exp}^{95}	298	3.5	11.3	154	3.5	4.2

Table 4.6. Cut-flow table for the jets & \cancel{E}_T optimisation. In analogy with the existing analysis the lepton veto dismisses any event with an electron (muon) with $p_T > 20$ (10) GeV and $|\eta| < 2.8$ (2.4). S_{exp}^{95} is the upper bound on the number of signal events obtained with the statistics method described at the beginning of section 4.5.

A few general observations can be made. First of all, the required cut on the effective mass (m_{eff}) increases with both f and k : this is indeed a consequence of the increasing mass splitting between the *mother* and *daughter* particles in the decay chain, namely the heavy quark q_H and the heavy photon A_H , respectively. If one considers the (light) quarks as massless, the effective mass in the heavy quark pair production could be indeed approximated with

$m_{\text{eff}} \sim 2(m_{q_H} - m_{A_H})$. A second observation is that the required \cancel{E}_T cut grows with f , namely again with the mass difference between q_H and A_H . From the previous observations it clearly follows that if a hard cut on m_{eff} is required together with a milder cut on \cancel{E}_T , at least a very hard jet is required in the spectrum: this is indeed the case for the benchmark points with relatively low values of f and higher values of k .

Compared to the values of table 4.4, one can see that an increased exclusion power could generically be gained by increasing the values of the cuts on the effective mass m_{eff} and on the missing energy \cancel{E}_T , especially for regions in the parameter space with higher values of f and k .

Exclusion Limits

Assuming an experimental search with the set-up summarised in table 4.6, we evaluated for each signal region the upper bound on the number of BSM signal events, under the hypothesis of exact overlap between background expectation and experimental yield, as described at the beginning of section 4.5.

This gave us the opportunity to validate our methods, namely the reliability of our background samples, the recasting procedure and of the statistics method. By applying the set-up of the original ATLAS analysis on our background samples, we were able indeed to compare the expected number of background events with the reported numbers in the experimental results, as well as the expected upper bounds on BSM events. The result of this comparison is summarised in table 4.7: the results are clearly consistent within the reported uncertainties.

	SR BM	SR BT	SR CM	SR CT	SR D
ATLAS analysis [177]					
Total bkg	33 ± 7	2.4 ± 1.4	210 ± 40	1.6 ± 1.4	15 ± 5
S_{exp}^{95}	$17.0^{+6.6}_{-4.6}$	$5.8^{+2.9}_{-1.8}$	$72.9^{+23.6}_{-18.0}$	$3.3^{+2.1}_{-1.2}$	$13.6^{+5.1}_{-3.5}$
Recasting procedure					
Total bkg	30.2 ± 9.1	3.2 ± 1.6	218.5 ± 43.7	2.4 ± 1.2	15.2 ± 4.5
S_{exp}^{95}	21.0	5.4	90.2	4.3	12.2

Table 4.7. Procedure validation: comparison between reported experimental results [177] and recasting procedure. In particular, the total number of background events and the corresponding 95% CL expected upper bound on BSM signal events (S_{exp}^{95}) are shown.

The upper bounds on the visible cross section within the optimised signal regions can be extracted from the last row of table 4.6. These limits can then be compared to the LHT signal visible cross section as a function of f and k , and exclusion contours can be drawn. In particular, the exclusion contours per signal region are reported in figure 4.14. It should be noted that only the signal regions requiring at least four jets in the final state are included in the latter plot, since it turned out that they possess higher exclusion power than the corresponding signal regions which require at least three jets.

In figure 4.15 the combined exclusion limits from all signal regions are drawn, together with the result of the recasting procedure of the ATLAS analysis. It is to be noted that in the latter plot we used the upper bound on the visible cross section evaluated with our statistics method for both the proposed signal regions as well as for the recasting of the ATLAS signal regions. From figure 4.15 we can see that there is only small room for improvement in the jets & \cancel{E}_T final state topology, if one relies only on the set-up of the existing experimental searches. The improvement of the exclusion in the f -direction can be estimated to roughly 50 GeV for fixed value of k .

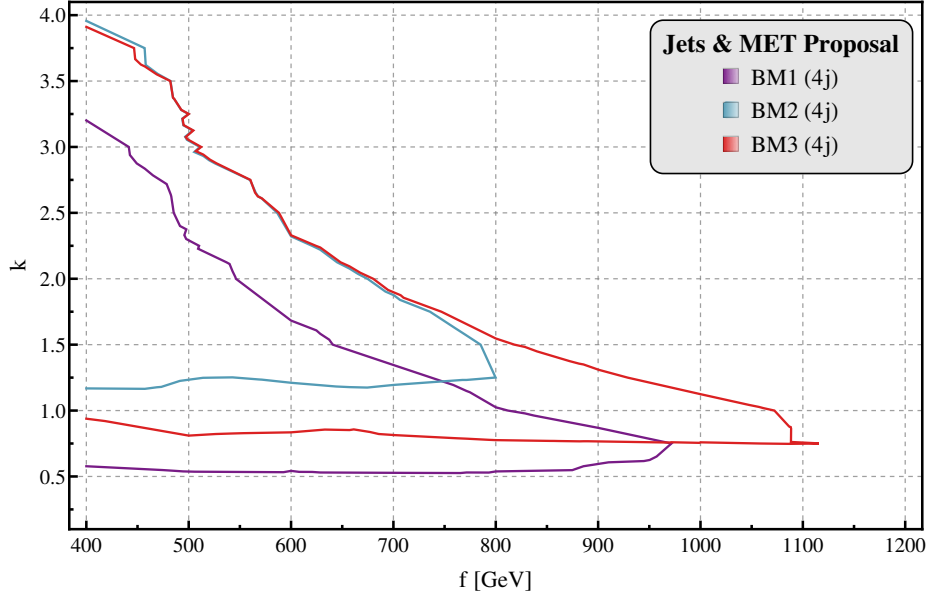


Figure 4.14. 95% CL potential exclusion limits from the proposed optimised jets & \cancel{E}_T search at LHC8 with 20.3 fb^{-1} displayed in the (f, k) plane. The different contours correspond to different signal regions.

4.5.3 Operator Bounds

As an aside to supersymmetric searches also operator bounds are important. Although the operator bounds on four-fermion operators come with an intrinsic uncertainty from non-perturbative physics above the scale Λ , they provide both a viable and crucial method to constrain LHT parameter space. The peculiarity of the box diagrams generating four-fermion contact interactions [158], is that they provide an upper bound for k given a scale f . On the other hand, the direct searches rather give a lower bound on k , hence the interplay between both allows to constrain the LHT model in the (f, k) plane. From equation (4.56) one can immediately see that increasing the scale of non-flavour violating four-fermion operators beyond the 25 TeV range will exclude even larger portions of parameter space for even lower values of k . We do expect LHC to improve these bounds, since at the moment only 7 TeV analyses for operator bounds of this form are available [119, 120]. Moreover, 8 TeV results on two-quark two-lepton operators recently appeared [187, 188], already constraining Λ to roughly 25 TeV, and we do expect the 14 TeV results to be

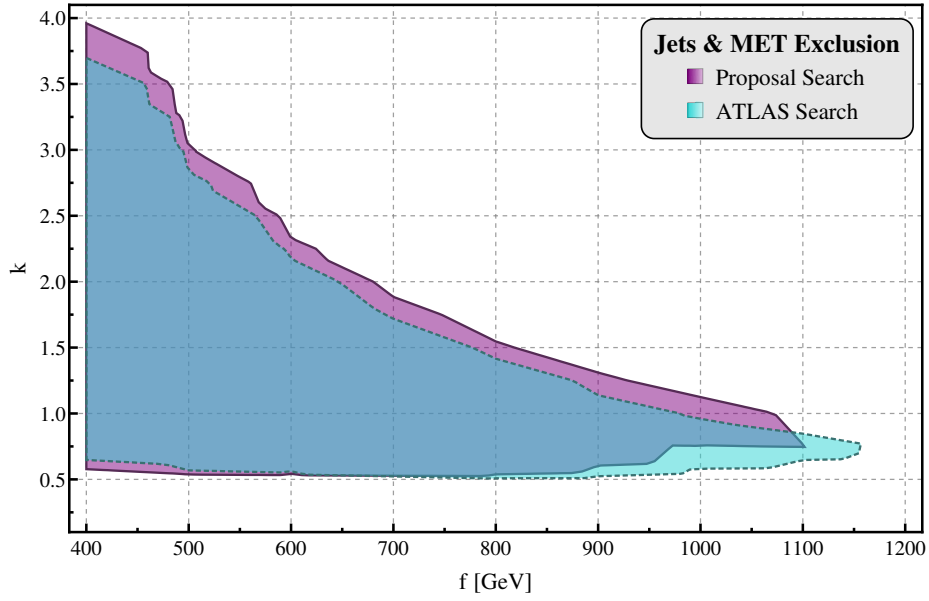


Figure 4.15. Comparison between the jets & \cancel{E}_T proposal exclusion limits and the limits from the experimental signal regions. The upper bounds on the visible cross sections in both cases have been obtained using our statistics method. This to ensure a comparison which does not depend on the background simulations nor the statistics method.

really constraining for LHT parameter space. However, a more thorough analysis of the constraints from LHC should be performed due to the large centre of mass energy compared to LEP, more details on the issues that appear in this case are presented in the next chapter.

Chapter 5

Hadron Collider EFT

This chapter is based on the publication [189] about effective operators at hadron colliders written solely by myself, therefore no further specification of my involvement is provided.

5.1 Introduction

In the previous two chapters we have seen how effective operators have been used to constrain the parameter space of strongly coupled models. In this chapter more details about effective operators at hadron colliders will be provided. Moreover, it will be shown that it is not straightforward to apply effective operator constraints directly to the parameter spaces of strongly coupled models. However, before discussing the topic in full detail a short introduction to the topic is presented here.

The first runs of the LHC at 7 and 8 TeV have not provided us with any signal for new physics beyond the Standard Model. However, these runs have proven to be very effective in excluding regions in parameter space of many BSM theories using direct searches. On the other hand, model independent methods like effective operators have been used to set limits on the same parameter spaces. For example fermionic contact interactions have been probed in dijet events by ATLAS [119, 190, 191] and CMS [120, 192–194]. For evaluating the full exclusion potential from LHC, limits from direct searches and effective operator bounds need to be combined for BSM theories. The translation of effective operator limits to parameter regions of BSM theories is the subject of this chapter.

The experimental analyses consider a set of effective operators and set upper limits on the size of their coefficients, parametrising the deviation from the Standard Model. Typically the coefficient is written as $2\pi/\Lambda^2$ for dimension six operators and a lower bound on Λ is quoted. BSM theories generically have heavy particles, which generate effective operators of the types constrained by experiment when integrated out [195, 196]. To translate the bound on the effective operator to the full theory — the BSM theory — two ingredients are necessary: the analytic expression for the effective operator in terms of full theory parameters and the domain of validity for the effective theory. Then exclusion limits in the parameter space of the full theory can be derived from the experimental results.

As a benchmark for this analysis the most explored channel at the LHC is used: the dijet angular analysis constraining four-quark operators of dimension six. Beyond the Standard Model theories that can be constrained by limits on four-quark operators are typically strongly coupled models. These models contain particles similar to the heavy partners of the Z boson or the gluon, known as Z' or G' bosons. A non-exhaustive list contains colour octets from compositeness [35, 41, 83] (see also chapter 3), flavoured Z' models [197] and explanations for the top forward backward asymmetry [198] using axigluons [199]. In

appendix C.1 a toy model is constructed based on Z' or G' models. The relevant parameters are the mass of the particle and the coupling strength to quarks. For these toy models the width of the Z' and G' depends solely on the mass and the coupling strength, therefore not introducing any additional parameters. However, for other BSM theories this may be different and the width must be considered independently.

The translation of effective operator bounds to BSM theories is an important method to constrain full theory parameter spaces. In this study the errors made in this translation are quantified and are connected with the kinematic parameters of the experiment and the theoretical model. An important quantity is the effective theory expansion parameter which is the ratio of the transfer energy in the events and the mass scale of the full theory. The non-negligible effect of this expansion parameter on the exclusion regions in the full theory parameter space is scrutinised. Conclusively, it is shown that these effects are crucial and should be taken into account.

This chapter is based on a toy model which is described in appendix C.1 and the relevant cross sections calculated in appendix C.2. These details are not needed for a basic understanding of the study in this chapter, but are added to ease understanding and usage of the results. First some general aspects of effective operators at hadron colliders are discussed in section 5.2. Then in section 5.3 the existing experimental analyses for constraining effective operators are reviewed and applied to the toy model. For these analyses the exclusion potential is compared between the full and the effective descriptions of the toy models in section 5.4. Finally, in the general conclusions in chapter 6 the conclusions are presented and recommendations are made for using effective operators at hadron colliders.

5.2 Effective Operators

In this section effective operators are discussed in general. First hadron colliders are discussed, identifying which kind of effective operators might be constrained. After that beyond the Standard Model physics is connected to these operators, justifying a certain class of toy models. Effective field theories only work at low energies compared to the energy scale of the full theory. The errors introduced in the effective approach are quantified by an expansion in energy scales, which forms the basis of the work. This section is then concluded with a first comparison between the full and effective theory description, when the translation from effective theory limits to the full theory parameter space is discussed.

5.2.1 Bounds from Hadron Colliders

For an analysis of constraining effective operators at a hadron collider it is first useful to make the comparison with lepton colliders. Lepton colliders are generally known for their very precise measurements and therefore harsh limits on precision observables and effective operators. Precise measurements and high luminosities lead to strong limits on effective operators compared to the centre of mass energy of the collider. For example the limit from LEP for the four-fermion operator $eedd$ equals 26 TeV [166]. Hadron colliders are very different, first of all composite particles like protons are being collided and therefore not all and also an unknown amount of the centre of mass energy of the collider is passed to the

partons. These partons — quarks and gluons — then interact to produce mostly hadronic final states, presenting another source of imprecision. However, what hadron colliders lack in precision they compensate in centre of mass energy. Hence, also possibly providing a source for constraining effective operators to high energy scales.

The essential difference when looking at effective field theories in both types of colliders is the difference in energy scales between the limits set on the operators and the processes involved at the collider. For a lepton collider nowadays the centre of mass energy is typically around 250 GeV and the limits reach up to more than 10 TeV. The energy scale of the full theory behind the effective theory must roughly be in the same ballpark as the limits on the effective theory. The reasoning being that full theories operating at lower energy scales would have been excluded by these limits. Therefore, we know that the effective theory provides a good description of the physics at centre of mass energy at a lepton collider. For a hadron collider the typical centre of mass energies are around 10 TeV, resulting in partonic centre of mass energies of 2 to 4 TeV. The typical limits set by the LHC — the most energetic hadron collider — are around 10 TeV. We see that the scale separation is much lower¹ and the validity of the effective description should be subject to investigation. In hadron colliders usually protons or antiprotons are collided and these collisions produce a range of Standard Model particles. However, the range of particles is severely dominated by QCD production and therefore jet final states, which are hadronised light quarks or gluons. Therefore, if we are looking into what kind of effective operators can be constrained by hadron colliders, the first that come to mind are those involving quarks or gluons. Indeed, from the dimension six operators that parametrise BSM physics [195, 196], the most investigated effective operators at the LHC are four-quark operators of the type

$$\frac{2\pi\zeta}{\Lambda^2} (\bar{q}_L\gamma^\mu q_L) (\bar{q}_L\gamma^\mu q_L). \quad (5.1)$$

In here $\zeta = \pm 1$ accounts for destructive and constructive interference, respectively, and Λ is the energy scale of the effective theory. Up to now the LHC has not set any bounds on effective operators involving two or more gluons and therefore the scope of this article is limited to four-quark operators. These operators form a direct contribution to the dijet cross section $pp \rightarrow jj$ at hadron colliders. Then if one measures distributions of dijet cross sections at hadron colliders these can be compared with theoretical predictions for the background (QCD) and the signal (effective operators). The comparison, in absence of any deviations from the background, then leads to exclusion limits on coefficients of the effective operators.

The experimental collaborations ATLAS [119, 190, 191] and CMS [120, 192–194] have been pursuing this strategy and have set limits on the effective operators like the one in equation (5.1). Currently, the highest limits are set by CMS from analysing the p_T spectrum of the leading jet [194]. These limits are

$$\Lambda^+ = 9.9 \text{ TeV and } \Lambda^- = 14.3 \text{ TeV} \quad (5.2)$$

¹This issue is even more urgent if we take into account that the typical scales of BSM physics range from 1 to 5 TeV.

for destructive and constructive interference, respectively. Although not relevant for this work the experimental collaborations also constrain effective operators using monojet plus missing transverse energy final states [173, 174]. These analyses constrain operators consisting of two quarks and two invisible particles, and are relevant for dark matter searches. The validity of the effective description for these experimental results has been discussed in a series of papers [200–203] and has been compared to specific models in [204–206]. Moreover, in the Higgs sector similar analyses have been performed in references [207, 208].

5.2.2 BSM Physics

In general, new physics beyond the Standard Model produces quarks rather than gluons, so in that sense the four-quark operator already matches topologies in BSM physics. Generically, strongly coupled theories are susceptible to effective operator limits, due to their relatively large couplings. High values for the couplings of new resonances to quarks automatically generate large effective operators coefficients. Moreover, the parameter space of these models can not be fully probed by direct resonance searches. A fact caused by the large couplings of these particles, making them very wide and reducing the effectiveness of resonance searches. Therefore, effective operators are a vital method to constrain strongly coupled BSM models.

For example, in composite Higgs models with partial compositeness, Standard Model quarks are a mixture of elementary and composite quarks. Some flavour implementations allow for large mixing with the composite sector and then the SM quarks have large couplings to a heavy partner of the gluon — in these models called the colour octet [35, 41, 83]. The colour octet — being sufficiently heavy — can be integrated out to obtain a four-quark effective operator. Analogously, models explaining the Standard Model flavour using Z' bosons lead to the same four-quark effective operator [197]. Another example is the introduction of an axigluon to explain the top forward-backward asymmetry [199]. This model predicts a new resonance which when integrated out produces the four-quark operator, as well.

In summary, typically strongly coupled BSM theories predict bosonic resonances with couplings to Standard Model quarks. These resonances are in most cases heavy copies of the electroweak gauge bosons or the gluon. For that purpose two toy models are introduced: a Z' boson which is a heavy partner of the Z boson and a G' boson which is the gluon's partner. Both partners couple universally to the Standard Model quarks governed by a single coupling constant². This coupling constant g and the mass m are the fundamental parameters of the model, the details for both toy models can be found in appendix C.1. The coefficients of the effective operators corresponding to the full theory are obtained in section C.1.3 and also depend on m and g . Then when translating the experimental limits on effective operators to the full theory it is most conveniently done in the mass versus coupling plane. This also allows for a direct interpretation in many BSM models. This study is focussed on the validity of the EFT description and not in particular on constraining Z' and G' bosons, see references [209, 210] for constraints from LHC on these types of models.

²Universal couplings to Standard Model quarks is of course not a general feature of BSM physics and depends heavily on the flavour implementation. However, for the purpose of determining the validity of the effective description simplicity prevails over completeness.

5.2.3 EFT Expansion

An effective field theory is the low-energy description of some full theory with heavy particles. The effective description is in general valid if it describes processes involving energies much smaller than the energy scale of the full theory. The energy scale of the full theory is determined by the masses of the particles in that theory. The higher dimensional operators in the effective theory are obtained if heavy particles in the full theory are integrated out. This can be done through diagrammatic matching and a detailed example is given in appendix C.1.3. Generically in the full theory the propagators of the massive particles are expanded around zero transfer momenta $q = 0$ to obtain the EFT expansion

$$\frac{g^2}{q^2 - m^2} = -\frac{g^2}{m^2} \left[1 + \frac{q^2}{m^2} + \mathcal{O}\left(\frac{q^4}{m^4}\right) \right]. \quad (5.3)$$

A coupling g has been introduced and the particle in the full theory has mass m . It is shown in appendix C.1.3 and specifically in equation (C.18) that the width of the particle does not play a role if the transfer energy q^2 goes to zero. The first term in the expansion will be the coefficient in front of a dimension six operator and the other terms in the expansion will be coefficients for higher dimensional operators involving derivatives.

In the EFT expansion from equation (5.3) q^2 is the energy transferred by the heavy particle in the diagram. For four-quark operators that can be in all channels, so $q^2 = \hat{s}, \hat{t}$ or \hat{u} . Usually the EFT description is considered valid or applicable if q^2 is smaller than m^2 , since then a converging series is ensured. However, experiments only probe the leading order operator and are neglecting terms of the order of q^2/m^2 . This introduces large errors when translating back from effective to full theory if the energy at which the experiments operate are close to the mass scale of the full theory.

The experimental results, in the absence of new physics, constrain dimension six operators like in equation (5.1). Comparing these limits to the coefficient in front of the effective operator will constrain the full theory parameter space

$$\frac{g^2}{m^2} < \frac{2\pi}{\Lambda^2}. \quad (5.4)$$

A graphical representation of this limit is given in figure 5.1 and the sign indicating interference effects has been absorbed in Λ . It is to be noted that the naive EFT limit constrains a region above a straight diagonal line in the mass versus coupling plane. Naively the effective description is valid if $m^2 > \langle q^2 \rangle$, however, more realistically the EFT limit will have an error which scales as $\langle q^2 \rangle / m^2$. The realistic exclusion can only be obtained by performing the actual analysis and depends on whether the full theory is over or underestimating the cross section relevant for the analysis.

For hadron colliders, however, due to the composite nature of the proton the transfer energy is not an exactly known quantity and is not the same for all events used in the experimental analysis. The transfer energy depends on the kinematic requirements of the analysis, see [200–202] for a detailed discussion. Therefore, as a measure for the expansion parameter the average transfer energy should be used. This average is an analysis dependent quantity and

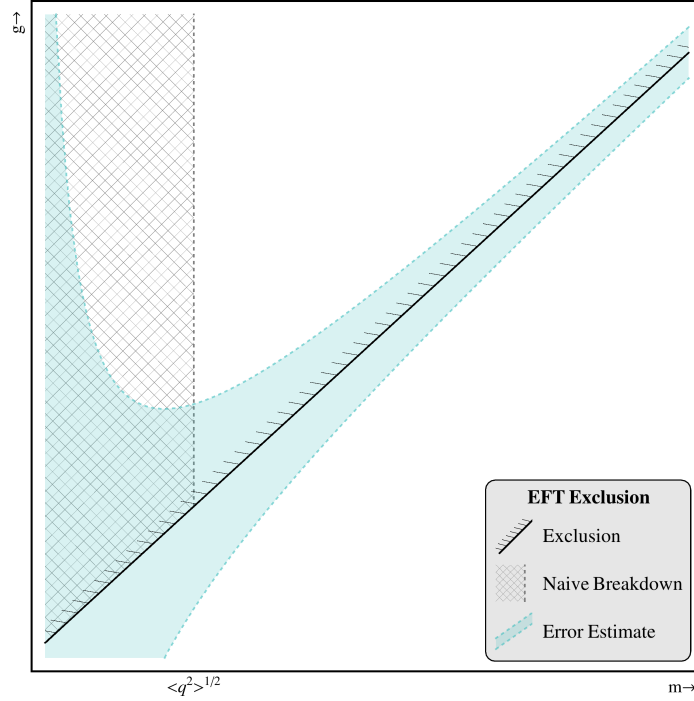


Figure 5.1. Estimation of the exclusion potential of effective operators in the full theory mass versus coupling parameter space. The effective theory description naively breaks down in the part of parameter space covered by the dashed grey region, where $m^2 < \langle q^2 \rangle$. In reality the error of the effective description is given by the light blue area which scales as $\langle q^2 \rangle / m^2$. This figure is just an indication of the effects and actual results are derived in later sections.

further discussion is postponed until section 5.4.1, where this quantity is actually calculated. To allow for a good estimation of the validity of the effective description it is recommendable that experimental analyses quote the average transfer energies in the events used for setting limits on effective operators³.

Beyond the Standard Model theories may predict Z' or G' like particles which have additional couplings beyond the usual couplings to SM quarks. These additional couplings may be to other heavy particles and increase the width of the Z' or G' like particle. However, these couplings will not affect the production cross section of the dijet final state considered in the experimental analyses. Hence, the effect of these couplings is solely through the additional width of the particle, which can be parametrised as Γ_{BSM} . Then, if we look at the scaling of Γ_{BSM} with the transferred momentum q^2 it is expected to have the same scaling as in equation (C.12) with m_q replaced by the mass of the heavy particle decayed into. From this it immediately follows that also the effect of additional widths can be neglected when looking at the first term of the effective operator expansion, as q^2 goes to zero.

³A similar recommendation has been proposed in reference [207] where running and mixing effects for effective operators have been discussed.

5.3 Experimental Analyses

In this section the analyses for obtaining limits on the effective operators are discussed. Both the full and the corresponding effective theory are analysed according to the ATLAS and CMS prescriptions in order to find out the differences in exclusion potential. Therefore, the experimental analyses are discussed first and then the theoretical application to the limit setting is reviewed in the next section. The understanding of the experimental analyses begins with the calculation of differential dijet cross sections for QCD, the full theory and the effective theory. These cross sections are calculated differentially with respect to \hat{t} in appendix C.2 and we base this analysis on

$$\frac{d\sigma}{d\hat{t}}(\hat{s}, \hat{t}, \hat{u}, \alpha), \quad (5.5)$$

where α denotes the collection of the relevant theory parameters for either QCD, the full theory or the effective theory. In the experimental setting the partonic cross sections need to be transformed to realistic cross sections using parton density functions. Moreover, to apply kinematic cuts, the cross sections should be differential in certain kinematic variables. These steps are discussed in the rest of this section for the different experimental analyses.

5.3.1 Differential Cross Sections

For four-fermion effective operators there have been two types of analyses to date at the LHC: dijet angular distributions [119, 120, 190–193] and leading jet p_T spectrum [194]. The first type and the necessary kinematics are discussed in this section. However, the first step from partonic cross sections to an actual analysis in a hadron collider is folding with parton distribution functions. For the partonic cross sections differential in \hat{t} the identification

$$\frac{d^3\sigma}{dx_1 dx_2 d\hat{t}}(pp \rightarrow 34) = f_1(x_1) f_2(x_2) \frac{d\sigma}{d\hat{t}}(12 \rightarrow 34) \quad (5.6)$$

gives the full cross section. In this formula $12 \rightarrow 34$ denotes the partonic process and x_1, x_2 are the momentum fractions for partons 1 and 2. However, this is still differential in \hat{t} and not in variables used in experiments like the rapidity of the dijet system $Y = \frac{1}{2}(y_3 + y_4)$ and the invariant mass of the dijet system $m_{\text{dijet}}^2 = \hat{s}$. The momentum fractions in terms of these variables are

$$x_1 = \sqrt{\frac{\hat{s}}{s}} e^Y \quad x_2 = \sqrt{\frac{\hat{s}}{s}} e^{-Y}, \quad (5.7)$$

where s is the centre of mass energy of the pp collider. From this the differential cross section in the variable defined before can be deduced as

$$\frac{d^3\sigma}{dY d\hat{s} d\hat{t}} = x_1 f_1(x_1) x_2 f_2(x_2) \frac{d\sigma}{d\hat{t}} \frac{1}{\hat{s}}. \quad (5.8)$$

The integration limits on Y and \hat{s} are determined by the individual experimental analysis and the variable \hat{t} might still be converted to an experimental observable. Note that the limits on Y are also influenced by the limits on the momenta fraction $0 < x < 1$, which give

$$|Y| < \frac{1}{2} \log \frac{s}{\hat{s}}. \quad (5.9)$$

By construction the partonic centre of mass energy is limited by the collider's centre of mass energy $\hat{s} < s$, providing an upper limit for the \hat{s} integration.

5.3.2 Angular Distribution

In the analyses based on the angular distribution, events are selected by cuts on the total rapidity of the system Y and are grouped in invariant mass \hat{s} bins. This can be reconstructed by integrating equation (5.8) over these kinematic variables. The remaining data is then binned in the variable

$$\chi \equiv e^{|y_3 - y_4|} = - \left(1 + \frac{\hat{s}}{\hat{t}} \right), \quad (5.10)$$

which represents the angular distribution of the dijet system. It is therefore necessary to obtain the cross section differential in χ rather than \hat{t} . Calculating the Jacobian from equation (5.10) — finding $\frac{d\sigma}{d\chi} = \frac{d\sigma}{d\hat{t}} \frac{d\hat{t}}{d\chi} = \frac{d\sigma}{d\hat{t}} \frac{\hat{t}^2}{\hat{s}}$ — and inserting it in to equation (5.8) one obtains

$$\frac{d\sigma}{d\chi} = \int_{\hat{s}_{\min}}^{\hat{s}_{\max}} d\hat{s} \int_{Y_{\min}}^{Y_{\max}} dY x_1 f_1(x_1) x_2 f_2(x_2) \frac{d\sigma}{d\hat{t}} \frac{\hat{t}^2}{\hat{s}^2}. \quad (5.11)$$

Both angular analyses [119, 120] set the integration limits roughly to $|Y| < 1.1$. Then the data is binned in \hat{s} , where the most significant bin in the CMS analysis is $\hat{s} > 3$ TeV. This analysis then looks for differences between QCD and the effective operator in the $\frac{1}{\sigma} \frac{d\sigma}{d\chi}$ distribution. This distribution is shown in figure 5.2 for QCD, the toy models and their corresponding effective theories.

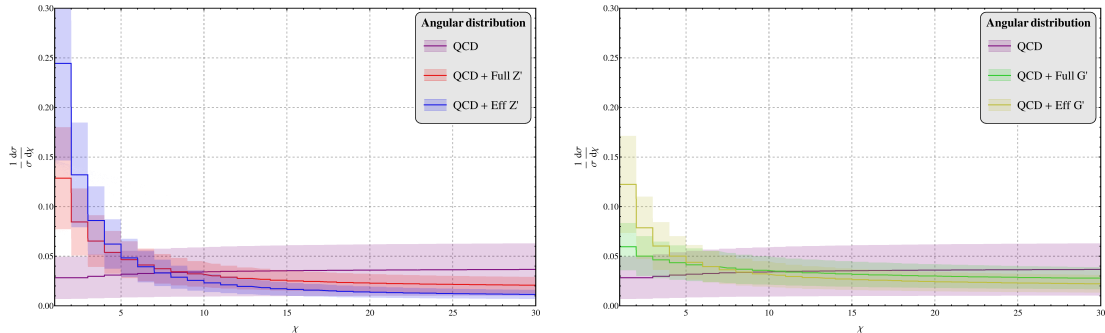


Figure 5.2. Reconstruction of the experimental angular distributions for QCD, for the Z' model (left) and the G' model (right) with parameters $m = 2000$ GeV and $g = 1.5$. This distribution has been obtained for the centre of mass energy integration from $\sqrt{\hat{s}_{\min}} = 3$ TeV to $\sqrt{\hat{s}_{\max}} = 5$ TeV. The bands around the different distributions represent the combination of statistical and systematic errors, more details are given in section 5.3.4.

Error Estimation

For the production of an actual $\frac{1}{\sigma} \frac{d\sigma}{d\chi}$ distribution, the χ range is binned and the bin content is calculated using

$$\left. \frac{1}{\sigma} \frac{d\sigma}{d\chi} \right|_{\chi_{\min}}^{\chi_{\max}} = \frac{N(\chi_{\min} < \chi < \chi_{\max})}{N_{\text{total}}}. \quad (5.12)$$

Since each of the bins is a ratio of number of events, it is straightforward to obtain the error from the systematic errors on the cross section and the statistical error on the number of events. The error on the angular distribution is then readily calculated as

$$\delta \left(\frac{1}{\sigma} \frac{d\sigma}{d\chi} \right) = \sqrt{(\delta N(\chi_{\min} < \chi < \chi_{\max}))^2 + (\delta N_{\text{total}})^2}. \quad (5.13)$$

5.3.3 F_χ Variable

The ATLAS analyses use a single parameter which measures the isotropy of the dijet events. This is defined as

$$F_\chi \equiv \frac{N_{\text{central}}}{N_{\text{total}}}, \quad (5.14)$$

where N_{central} is the number of events in the central region with $1 < \chi < \chi_{\text{central}}$ and N_{total} is the total number of events with $1 < \chi < \chi_{\text{max}}$. This parameter can depend on \hat{s} , for that purpose we explicitly write the \hat{s}_{\min} and \hat{s}_{\max} in equation (5.11) and define the integral over χ as

$$\sigma(\chi_{\text{int}}, \hat{s}_{\min}, \hat{s}_{\max}) = \int_1^{\chi_{\text{int}}} d\chi \frac{d\sigma}{d\chi}(\hat{s}_{\min}, \hat{s}_{\max}). \quad (5.15)$$

The total cross section thus depends on three integration boundaries, from which we can formally define F_χ as

$$F_\chi(\hat{s}_{\min}, \hat{s}_{\max}) = \frac{\sigma(\chi_{\text{central}}, \hat{s}_{\min}, \hat{s}_{\max})}{\sigma(\chi_{\text{max}}, \hat{s}_{\min}, \hat{s}_{\max})}. \quad (5.16)$$

In the most recent ATLAS analysis [119] the event selection criteria $|Y| < 1.1$ and $\hat{s} > 800$ GeV are used. The boundaries for the χ limits are $\chi_{\text{central}} = 3.32$ and $\chi_{\text{max}} = 30.0$, the F_χ parameter is then binned in \hat{s} . An example distribution is shown in figure 5.3 for QCD, the toy models and their corresponding effective theories.

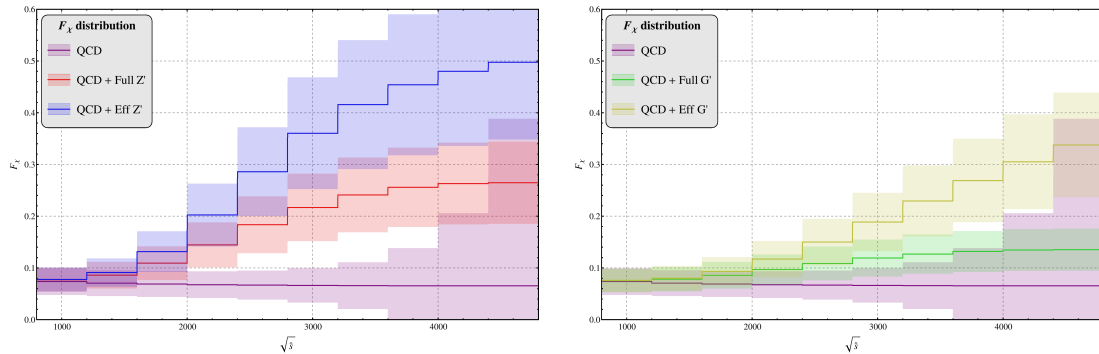


Figure 5.3. Reconstruction of the experimental F_χ distributions for QCD, for the Z' model (left) and the G' model (right) with parameters $m = 2000$ GeV and $g = 1.5$. The bands around the different distributions represent the combination of statistical and systematic errors, more details are given in section 5.3.4.

Error Estimation

The statistical error on F_χ is determined by the number of events in the respective mass bins for both the central and the total region in χ as shown in equation (5.14). Then similarly as for the errors on the $\frac{1}{\sigma} \frac{d\sigma}{d\chi}$ distribution in equation (5.13) the errors on the number of events propagate as

$$\delta F_\chi = \sqrt{(\delta N_{\text{central}})^2 + (\delta N_{\text{total}})^2}. \quad (5.17)$$

5.3.4 Error Analysis

In the next section the comparison between the background — pure QCD — and a possible signal is made. For these types of comparisons a detailed account for the different errors affecting the angular distributions is needed. The distributions discussed in sections 5.3.2 and 5.3.3 are dependent on the number of events in certain bins. The error on that number of events is obtained by propagating the errors on the number of events using the results from the error estimation paragraphs in the previous sections. In the following we describe the error on the number of events.

In the theoretical limit setting procedure the data is assumed to equal the background prediction including the total error on the background coming from statistic and systematic uncertainties. For the QCD background we consider statistical errors on the number of events to be Poisson distributed. The systematic errors originate from experimental effects and from theoretical uncertainties. The systematic uncertainties from experimental effects are described in the respective analyses [119, 120] and range up to 15% for the highest mass bin in the angular distribution. Theoretical uncertainties are estimated by varying the renormalisation and factorisation scales by half and twice their values and this results in errors up to at most 30% for both distributions. A conservative measure for the total systematic uncertainty for the QCD background is then 35%.

The limit setting for the signal does not involve any statistical errors and purely depends on the systematic uncertainties from theory calculations. As for the QCD background these uncertainties are estimated by varying the renormalisation and factorisation scales by half and twice their values. For the signal, which is for each of the two toy models, the errors are similar to the background and range up to 30%. The distributions shown in figures 5.2 and 5.3 include all the errors discussed in this section based on events with a centre of mass energy of 7 TeV and using 5 fb^{-1} of integrated luminosity.

5.4 Results

The goal of this work is to quantify the difference between the full and effective theory exclusions limits in the mass versus coupling plane analogous to figure 5.1. For this an experimental measure based on the angular analyses needs to be introduced. We already observe that there is a significant deviation between the full and effective description for both the experimental angular distributions $\frac{1}{\sigma} \frac{d\sigma}{d\chi}$ and F_χ presented in figures 5.2 and 5.3. We base our theoretical measure on the F_χ distribution, similar to the analysis in reference [119], since this observable is a ratio. For the F_χ distribution many systematic effects cancel, making it a sensitive probe for deviations from QCD.

In the ATLAS analysis the F_χ data is binned in the $\hat{s} = m_{jj}^2$ variable comparable to figure 5.3 and they look for deviations between experimental data and background predictions in these bins. The simplest theoretical measure would be taking a single large bin in \hat{s} and performing a χ^2 analysis on difference between the theory predictions for the full and effective theory and the data, see for example reference [118]. However, this implies less sensitivity to the kinematic details of the distribution and moreover less similarity with the actual experimental method. Therefore we adopt a more detailed χ^2 measure based on the full set of bins⁴. From figure 5.3 a reasonable binning is determined to be in $\sqrt{\hat{s}}$ ranging from 1200 GeV to 4000 GeV with steps of 400 GeV. Then a χ^2 analysis on the F_χ variable with the errors as described in section 5.3.4 is repeated for different values of the coupling and mass of the toy model. These results are then transformed into a 95% CL exclusion contour in the mass versus coupling plane, presented in figure 5.4.

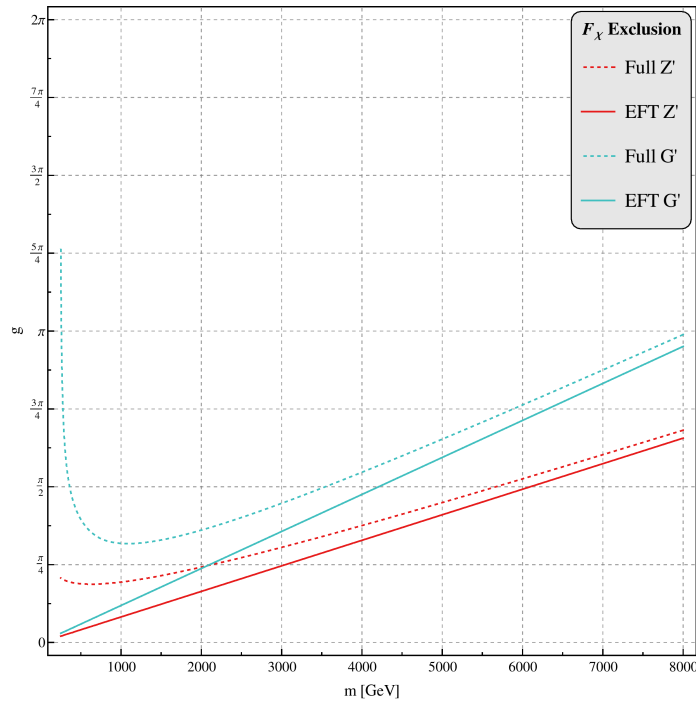


Figure 5.4. Comparison of exclusion limits in the mass versus coupling plane between effective and full theory. The shaded regions are the exclusions for the full theory Z' and G' and the solid lines mark the excluded regions for the effective theory equivalents. This is based on binned F_χ theoretical measure as described in the text.

The results in this section are obtained for a centre of mass energy of 7 TeV and an integrated luminosity of 5 fb^{-1} . This corresponds roughly to the analysis presented in reference [119] and therefore allows for a good comparison with limits obtained in there. Even though the operators corresponding to the Z' and G' models from equation (C.13) are different from the ones studied in reference [119], a rough comparison can be made. The limits in figure

⁴The ATLAS analysis uses a different statistical method to look for deviations, namely the tail hunter method [211]. However, the deviation between this method and a χ^2 analysis is not expected to be significant.

5.4 correspond to the values

$$\Lambda_{Z'} = 13.8 \text{ TeV} \quad \Lambda_{G'} = 9.5 \text{ TeV}, \quad (5.18)$$

and we observe an approximate agreement with the results from the ATLAS analysis. In the next section the deviation between the full and effective theory is quantified and compared to the effective field theory expansion.

5.4.1 EFT Expansion Check

In this section the error made by using the effective description for excluding the full theory parameter space is quantified. From a theoretical viewpoint, the error introduced by the effective expansion is governed by the ratio of the transfer energy and the mass of the particle being integrated out as presented in equation (5.3). As the series is truncated at the first order, the deviation of the effective partonic cross section compared with the full cross section is expected to be given roughly by q^2/m^2 . However, for the limit setting the difference in the total cross sections is also influenced by the parton density functions, the kinematic requirements and the statistical analysis being used. Therefore, the scaling of the deviation in the exclusion limits of the full theory's parameter space is expected to be modified by these effects.

Deviation

An interesting quantity to measure is the deviation between the effective and full description is the difference between exclusions limits for the coupling constant for a given mass of the full theory particle. This deviation can be defined as

$$\Delta g \equiv \frac{g_{\text{full}} - g_{\text{eff}}}{g_{\text{eff}}}, \quad (5.19)$$

and is represented in figure 5.5 by the solid lines. The figure shows the deviation for the binned F_χ based exclusion described in the previous section and presented as in figure 5.4. It is observed that interestingly the deviation scales to good approximation as $1/m^2$. It is conjectured that the deviation Δg can then be fitted to the function

$$\Delta g \simeq \frac{C^2}{m^2}, \quad (5.20)$$

where C^2 is expected to be a constant times $\langle q^2 \rangle$ — the average transfer energy in the events. This function with a single free parameter C is then fitted to the actual Δg in figure 5.5 and is represented by the dashed lines. For the binned F_χ based exclusions the free parameter is

$$C(Z') = 1.31 \text{ TeV}, \quad C(G') = 1.39 \text{ TeV}. \quad (5.21)$$

The difference between the Z' and G' models is small, which might indicate that the coefficient C is indeed mainly determined by the effects of the parton densities, the kinematics in the analysis and the statistical method. From this perspective, it is interesting to quantify the average transfer energies in the events for the background and the different toy models.

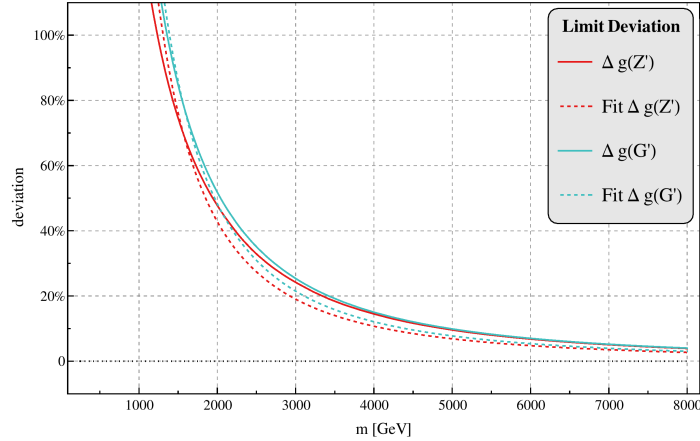


Figure 5.5. Deviation of the full theory description with respect to the effective theory for the binned F_χ based exclusion. The solid lines show the difference between the full and effective description for the limits on the coupling constants given in equation (5.19) as a function of the mass. The dashed lines show the fitted function in equation (5.20) using the fitted result for C .

Average Transfer Energy

In section 5.2.3 the expansion around the energy transfer was introduced to estimate the validity of the EFT at parton level. In order to gain more insight an estimate for the average energy transfer in the events considered in the analysis is needed. For that purpose we need the average values for all the hatted Mandelstam variables, these are given by the expressions

$$\begin{aligned}
 \langle \hat{s} \rangle &= \frac{1}{\sigma_{\text{tot}}} \int_{\hat{s}_{\text{min}}}^{\hat{s}_{\text{max}}} d\hat{s} \int_{\chi_{\text{min}}}^{\chi_{\text{max}}} d\chi \hat{s} \frac{d^2\sigma}{d\hat{s}d\chi} \\
 \langle \hat{t} \rangle &= \frac{1}{\sigma_{\text{tot}}} \int_{\hat{s}_{\text{min}}}^{\hat{s}_{\text{max}}} d\hat{s} \int_{\chi_{\text{min}}}^{\chi_{\text{max}}} d\chi \frac{-\hat{s}}{1+\chi} \frac{d^2\sigma}{d\hat{s}d\chi} \\
 \langle \hat{u} \rangle &= \frac{1}{\sigma_{\text{tot}}} \int_{\hat{s}_{\text{min}}}^{\hat{s}_{\text{max}}} d\hat{s} \int_{\chi_{\text{min}}}^{\chi_{\text{max}}} d\chi \frac{-\hat{s}\chi}{1+\chi} \frac{d^2\sigma}{d\hat{s}d\chi},
 \end{aligned} \tag{5.22}$$

where the normalisation σ_{tot} is defined by

$$\sigma_{\text{tot}} = \int_{\hat{s}_{\text{min}}}^{\hat{s}_{\text{max}}} d\hat{s} \int_{\chi_{\text{min}}}^{\chi_{\text{max}}} d\chi \frac{d^2\sigma}{d\hat{s}d\chi}. \tag{5.23}$$

The averages for an experimental analysis can then be obtained by integrating over the ranges given in the analysis for \hat{s} and χ . For the binned F_χ based theoretical measure the results are depicted in table 5.1 for both the total and the central region in χ .

The experimental collaborations can determine each of the average transfer energies by using the kinematic information on an event by event basis. For each event the kinematic variables \hat{s} and χ are known from measurements on the dijet system. Then, with the use of equation (5.10) and the sum of Mandelstam variables $\hat{s} + \hat{t} + \hat{u} = 0$ (for vanishing quark masses) the quantities \hat{s} , \hat{t} and \hat{u} can be determined for each event. Finally, averaging over all events leads to the determination of the average transfer energies in the experiment.

region	$\sqrt{ \langle \hat{q}^2 \rangle }$	QCD	Full Z'	Eff Z'	Full G'	Eff G'
total	$\sqrt{ \langle \hat{s} \rangle }$	1.43	1.45	1.47	1.44	1.45
total	$\sqrt{ \langle \hat{t} \rangle }$	0.43	0.46	0.49	0.45	0.45
total	$\sqrt{ \langle \hat{u} \rangle }$	1.36	1.37	1.38	1.37	1.37
central	$\sqrt{ \langle \hat{s} \rangle }$	1.43	1.50	1.58	1.46	1.49
central	$\sqrt{ \langle \hat{t} \rangle }$	0.82	0.88	0.93	0.85	0.87
central	$\sqrt{ \langle \hat{u} \rangle }$	1.17	1.22	1.28	1.19	1.21

Table 5.1. Average transfer energies in TeV, which are the hatted Mandelstam variables for both the total region with $\chi < \chi_{\max}$ and the central region with $\chi < \chi_{\text{central}}$. Presented are the absolute values of the Mandelstam variables, however, they are constrained to $\hat{s} > 0$ and $\hat{t}, \hat{u} < 0$. The values correspond to the model parameters $m_{Z'} = m_{G'} = 2$ TeV and $g_{Z'} = g_{G'} = \frac{\pi}{2}$.

5.4.2 Limit Recast

The ultimate goal of the quantification of the deviation is to re-analyse existing limits from effective operators. The full theory effects could be included by performing a rescaling based on the fitted result for the deviation in equation (5.20). These results have been obtained for Z' and G' toy models and could be applied to similar models as well. This would then lead to a more reliable exclusion limit in the mass versus coupling plane of these models, which is crucial for scrutinising a model's parameter space. In the previous section the deviation was quantified for the ATLAS analysis in reference [119]. In appendix C.3 we perform a recast for the colour octet considered in section 3.3, which has been excluded using these ATLAS limits on four-quark effective operators. This example illustrates how considering the full theory effects lead to more reliable exclusion limits.

Consequently, experiments are urged to apply their angular dijet analyses to full models — like the Z' and G' which cover a large class of BSM models — as well. Thereby allowing for a trustworthy quantification of the deviation between the full and effective description, which can then be applied to BSM models.

Chapter 6

Conclusions

In this thesis two different strongly coupled models with phenomenology relevant to the LHC have been discussed, as well as the applicability of effective operator bounds for these models. The conclusions for these three topics are presented separately and are followed by summarising conclusions for strongly coupled models.

Composite Higgs

In this thesis we have investigated the experimental signatures and bounds of partially composite Higgs models where right-handed quarks are largely composite. This scenario is strongly motivated by flavour physics and is until recently experimentally very weakly constrained. The first runs of the LHC are changing this situation and the experimental results are progressively excluding larger regions of parameter space. The most relevant bounds on the right-handed compositeness model were extracted from the latest LHC data. However, existing experimental strategies for the more studied anarchic scenarios and supersymmetry are of a different nature. In particular, right-handed compositeness typically produces jet final states without leptons or missing energy. For this reason existing analyses are in most cases not optimal and could be improved with the dedicated search strategies we provide. The colour octet — a spin one gluon resonance in the right-handed quark compositeness model — is constrained based on dijet searches, both using resonance and angular analyses. In some regions of parameter space these states are excluded up to masses of 3 TeV, but the result is strongly sensitive on the fermionic spectrum. We also derive bounds on the masses of the lightest fermionic partners. These are particularly relevant given their role in guaranteeing the naturalness of the theory. In light of the 125 GeV Higgs discovery some fermions should be lighter than 1 TeV to provide a theory with little fine-tuning. One interesting experimental feature is that single production of the new fermions dominates the bounds, in contrast to anarchic scenarios where at present double production produces the strongest constraints.

We derive an extremely strong bound on the left-handed partners, which are excluded up to 2 TeV in theories that realise MFV. This is obtained from single electroweak production of partners of the up quark studied by the ATLAS collaboration. Right-handed quark partners can be singly produced through the gluon resonances with smaller cross sections and different final states, and the direct bounds are much weaker in this case. Overall our study shows that models that realize MFV are at least as tuned as the anarchic scenarios. This can be avoided by abandoning MFV in favour of theories based on an $SU(2)$ flavour symmetry where the light generations can be more elementary than the top.

The right-handed compositeness scenario motivates more general experimental searches than presently conducted at the LHC. These searches are already possible using the existing

data and experimental analyses with minor modifications. In particular multi-jet signals could be more efficiently captured with a different ordering of jets and then searching for two and three-jet resonances. Moreover, existing dijet studies should be extended to allow for the inclusion of a spectator jet, which might be the leading jet. We hope that the existing experimental analyses will be extended and that our proposals will be pursued by new analyses.

Little Higgs

The second strongly coupled model that has been considered in this thesis is the Littlest Higgs with T-parity. It has been discussed in the context of electroweak precision physics, Higgs precision physics and direct LHC searches, combining constraints from many possible corners of high energy physics. For this purpose an up-to-date overview of the relevant phenomenology for direct searches at the LHC has been presented. This has been used to discuss possible topologies which could mimic supersymmetry searches and therefore be constraining for the LHT parameter space. Based on these topologies the LHT model has been constrained using the recent 8 TeV LHC data from ATLAS and CMS.

The main goal of deriving these constraints was not to provide information on the whole parameter space of the LHT model, but rather to obtain the most stringent limit on the symmetry breaking scale f . This scale is the main parameter of the model as it sets the absolute scale for the global symmetry breaking pattern and gives the connection to its strongly interacting UV completion. Moreover, this scale is also intimately connected to the amount of fine-tuning in the model, and thereby provides a measure of the naturalness of the model. From the combination of EWPT and Higgs precision physics, we derive a lower limit on the symmetry breaking scale f of

$$f \gtrsim 694 \text{ GeV} \quad \text{at} \quad 95\% \text{ CL.}$$

On the other hand, from direct searches the lower limit reads

$$f \gtrsim 638 \text{ GeV} \quad \text{at} \quad 95\% \text{ CL.}$$

From these results we conclude that the implementation of the Littlest Higgs with T-parity is still natural, since the tuning is only of the order of 5%. Furthermore, we observe that direct searches are by now becoming competitive with constraints from indirect measurements like EWPT and Higgs precision physics.

The potential of the LHC for discovering and constraining the LHT model has been analysed, as well. The exclusion possibilities from the monojet & \cancel{E}_T and the jets & \cancel{E}_T searches have been optimised for the LHT model. We performed an exhaustive scan over both the parameters f and k — the coupling in the mirror fermion sector — as well as the relevant kinematic cuts to analyse the exclusion potential of the 8 TeV run with roughly 20 fb^{-1} . The results show that current direct searches can become competitive with indirect searches, though would not be able to push the exclusion limits much beyond. However, direct searches can cover interesting regions of the parameter space, which are left untouched

by precision measurements. In conclusion, the Little Higgs model with T-parity will hold its natural status during the LHC8 era.

Most importantly we would like to stress that we presented a consistent method to constrain the Littlest Higgs model with T-parity using direct searches. Even though at the moment direct searches are less constraining than indirect methods, these form a more direct and therefore more robust method to constrain the LHT parameter space. Improvements in four-fermion operator bounds, as well as the optimised direct searches, can be used by the CMS and ATLAS experiments to either discover or falsify the natural LHT model with the 14 TeV run. Therefore, we hope that the collaborations will extend the kinematic regime of their simplified model searches for supersymmetry, since we have shown that a recasting procedure provides a powerful method to constrain the LHT parameter space.

Hadron Collider EFT

The interpretation of effective operator limits from hadron colliders for strongly coupled models with typical energy scales around the TeV scale is a delicate matter. It is argued that effective operator limits for these theories should be more carefully interpreted in the mass versus coupling plane. In this thesis the pitfalls have been identified and methods to reliably interpret the experimental limits are provided.

For a correct interpretation of effective operator limits at the Large Hadron Collider it is necessary that experimental collaborations provide information on the average transfer energies in their analyses. In section 5.4.1 a procedure which achieves this is outlined for the existing angular analyses. Furthermore, the collaborations are invited to apply the limit setting procedure to generic models like the Z' and G' as well. This allows for more accurate limit setting in the mass versus coupling plane for specific strongly models with similarities to these models.

The reinterpretation of the effective operator limits in the full theory can be obtained through a rescaling procedure based on the quantified deviation in section 5.4.1. The deviation scales as the inverse square of the mass of the particle considered, and this is fitted using the experimental analyses for toy models. The observation that the deviation is not very model dependent implies that this rescaling procedure can be used for a plethora of BSM particles within a reasonable accuracy. In conclusion, a method has been presented which allows for a more reliable scrutinising of BSM parameter spaces while using effective operator limits.

Strongly Coupled Models

The subject of this thesis is strongly coupled models at the Large Hadron Collider. It was shown that strongly coupled physics in the guise of a composite Higgs with partial compositeness and as the Littlest Higgs with T-parity have direct implications for existing and new LHC analyses. Both models provide a unique phenomenology with a plethora of heavy particles and interesting topologies for the LHC. Constraints from LHC have been analysed for the composite Higgs and the Little Higgs model, and increasing exclusion regions were found. However, both models still remain natural if one is willing to live with a little fine-tuning which is still comparable to other descriptions of EWSB like supersym-

metry. Furthermore, it was shown that exclusion limits from effective operators are less constraining than naively expected for strongly coupled BSM physics. From these arguments we conclude that *strongly coupled physics is still a natural and viable description for electroweak symmetry breaking and leads to interesting phenomenology at the Large Hadron Collider.*

Chapter 7

Acknowledgements

This dissertation and my publications would not have been completed without the support and wisdom of many collaborators, colleagues, family and friends over the course of my PhD studies. I would like to take this opportunity and show them my appreciation.

First of all, I am deeply grateful to my advisor Andreas Weiler for his guidance and support during this work. Furthermore, I thank him for having taught me the interesting world of strongly coupled beyond the Standard Model physics and lots of other topics in the broad field of high energy physics.

Secondly, I would like to thank Gudrid Moortgat-Pick for grading this dissertation and for her interesting lectures on the topics of supersymmetry and linear colliders which greatly expanded my view in the field.

I am also very grateful to all my collaborators Michele Redi, Jürgen Reuter, Veronica Sanz, Marco Tonini and Andreas Weiler. I have learned a lot from our discussions and without them the contents of this thesis would be less complete and thorough. Furthermore, I would like to thank my friends here at DESY: Francesco, Francisco, Marco, Marco, Marco, Martin, Paolo, Sara and Stefano for brightening the otherwise so grey atmosphere composed by the DESY campus with their many jokes, gaffes and distractions from work. Moreover, the set of rules they provided for survival in a scientific atmosphere proved to be crucial during seminars and other social events.

Before starting my PhD both my opinion towards physics and my life were elementary, both now have changed, the latter through you my dearest Sonja. It was your attraction that made me partially composite and which completed my life. I will remain forever grateful for the great time we had in Hamburg and your support during the creation of this thesis. Finally, I would like to thank my parents for never pushing me into any direction and giving me the freedom to choose my own path in life — not implying that free will exists at all. And of course also together with the rest of my family and friends back home for their tremendous support throughout my studies and life.

License

This work is licensed under the Creative Commons Attribution-ShareAlike 4.0 International License [212]. Of course this statement needs to be refined, since this is a derivative work depending on lots of different sources. In the high energy physics community there is no general applicable license, therefore it must be assumed that the license is only applicable to the parts of this work which are non-derivative. Moreover, the license is also applicable to derivative parts licensed under a license compatible with the aforementioned license. Furthermore, this work tries to abide to referencing guidelines in the physics community as much as possible. If you feel that your work or ideas have been violated or that this license is not applicable to your work, please do not hesitate to contact me.

Chapter A

Appendix - Composite Higgs

A.1 Right-Handed Composite Model

In this appendix we describe the effective Lagrangian used in our simulations. This is a simple extension of [35], where we will only focus on the quark sector. The composite states are multiplets of the global symmetry $SU(3) \times SU(2)_L \times SU(2)_R \times U(1)_X$. As described in section 3.2 we take the quark partners in the following representations

$$\begin{aligned} \tilde{U} &= (\mathbf{1}, \mathbf{1})_{\frac{2}{3}} & \tilde{D} &= (\mathbf{1}, \mathbf{1})_{-\frac{1}{3}} \\ L_U &= (\mathbf{2}, \mathbf{2})_{\frac{2}{3}} = \begin{pmatrix} U & U_{\frac{5}{3}} \\ D & U_{\frac{2}{3}} \end{pmatrix} & L_D &= (\mathbf{2}, \mathbf{2})_{-\frac{1}{3}} = \begin{pmatrix} D_{-\frac{1}{3}} & U \\ D_{-\frac{4}{3}} & D \end{pmatrix}, \end{aligned} \quad (\text{A.1})$$

where all are in the fundamental representation of $SU(3)$. Focusing on the first generation we consider the following Lagrangian for the composite fermions

$$\begin{aligned} \mathcal{L}_{\text{composite}} &= -\frac{1}{4}\rho_{\mu\nu}^2 + \frac{m_\rho^2}{2}\rho_\mu^2 + \text{Tr} [|D_\mu H|^2] - V(H) \\ &+ \text{Tr} [\bar{L}_U (i\not{D} - m_{L_U}) L_U] + \bar{\tilde{U}} (i\not{D} - m_{\tilde{U}}) \tilde{U} \\ &+ Y_U \text{Tr} [\bar{L}_U \mathcal{H}]_L U_R + \text{h.c.} \\ &+ \{U \rightarrow D\}. \end{aligned} \quad (\text{A.2})$$

We only include the composite Yukawas that are relevant for the generation of the SM flavour structure. Among the spin-1 resonances we consider a massive octet of $SU(3)$ and assume it interacts as a gauge field. The elementary Lagrangian is just QCD with massless quarks

$$\mathcal{L}_{\text{elementary}} = -\frac{1}{4}G_{\mu\nu}^a G^{a\mu\nu} + \bar{q}_L i\not{D} q_L + \bar{u}_R i\not{D} u_R + \bar{d}_R i\not{D} d_R. \quad (\text{A.3})$$

SM quarks mix with the fermions of equal quantum numbers

$$\mathcal{L}_{\text{mixing}} = \Delta_{Lu} \bar{q}_L Q_{Ru} + \Delta_{Rd} \bar{q}_L Q_{Rd} + \Delta_{Ru} \bar{\tilde{U}}_L u_R + \Delta_{Rd} \bar{\tilde{D}}_L d_R + \text{h.c.} \quad (\text{A.4})$$

where the Q_{Ru} and Q_{Rd} are the doublets contained in L_U and L_D respectively. We will assume $\lambda_{Ld} \ll \lambda_{Lu}$. Similarly the gauging of SM symmetries introduces a linear mixing between the SM and the composite spin-one resonances.

Diagonalising the elementary-composite mixings the Lagrangian in the mass basis for the bosons reads

$$\begin{aligned}
 \mathcal{L}_{\text{gauge}} = & -\frac{1}{4}G_{\mu\nu}G^{\mu\nu} + \frac{1}{2}(D_\mu\rho_\nu D_\nu\rho_\mu - D_\mu\rho_\nu D_\mu\rho_\nu) + \frac{M^2}{2\cos^2\theta}\rho_\mu\rho^\mu \\
 & + \frac{ig_s}{2}G_{\mu\nu}[\rho_\mu, \rho_\nu] + 2ig_s \cot 2\theta D_\mu\rho_\nu [\rho_\mu, \rho_\nu] \\
 & + \frac{g_s^2}{4}\left(\frac{\sin^4\theta}{\cos^2\theta} + \frac{\cos^4\theta}{\sin^2\theta}\right)[\rho_\mu, \rho_\nu]^2,
 \end{aligned} \tag{A.5}$$

and for the fermions reads

$$\begin{aligned}
 \mathcal{L}_{\text{fermion}} = & \bar{q}_L i \not{D} q_L + \bar{Q}_u (i \not{D} - m_{Q_u}) Q_u \\
 & + g_s \bar{q}_L (\sin^2 \phi_{Lu} \cot \theta - \cos^2 \phi_{Lu} \tan \theta) \rho_\mu \gamma^\mu q_L \\
 & + g_s \bar{q}_L \left(\frac{\sin \phi_{Lu} \cos \phi_{Lu}}{\sin \theta \cos \theta} \right) \rho_\mu \gamma^\mu Q_{Lu} + \text{h.c.} \\
 & + g_s \bar{Q}_{Lu} (\cos^2 \phi_{Lu} \cot \theta - \sin^2 \phi_{Lu} \tan \theta) \rho_\mu \gamma^\mu Q_{Lu} \\
 & + \{(q_L, Q_u) \rightarrow (q_L, Q_d), (u_R, U_L), (d_R, D_L)\}.
 \end{aligned} \tag{A.6}$$

In the expressions above we have the relations $\tan \theta = g_{e1}/g_\rho$, $\tan \phi = \Delta/m$ and $g_s = g_{e1} \cos \theta$ is the QCD coupling. This is the final form of the Lagrangian which has been implemented in FeynRules [113] to study the LHC phenomenology.

The Higgs vacuum expectation value introduces the following mixings in the up sector

$$\mathcal{L}_{\text{int}}^L = -\frac{Y_{Uv}}{\sqrt{2}} \sin \phi_{Ru} \bar{u}_R [U + U_{2/3}] + \text{h.c.} \tag{A.7}$$

Diagonalising these terms generates the electroweak interactions of equation (3.4) relevant for single production of left-handed partners [128–130].

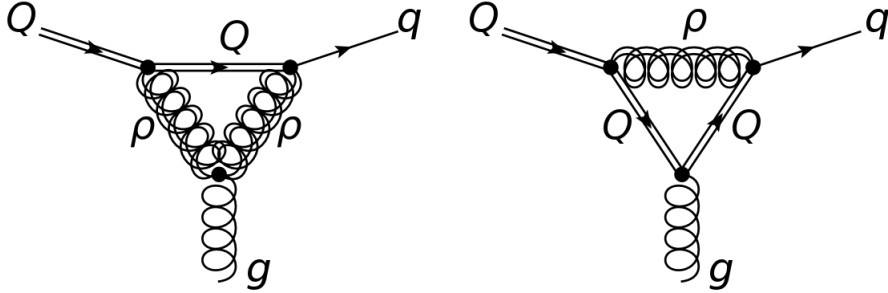


Figure A.1. One-loop new physics contributions to the chromomagnetic operator in partially composite models.

Finally in the effective Lagrangian of the strong sector we include the dimension five operator

$$\mathcal{L}_{\text{chromo}} = \frac{g_s \kappa_0}{m_Q} \bar{Q}_L \sigma_{\mu\nu} T^a q_R G_{\mu\nu}^a + \text{h.c.} \tag{A.8}$$

The chromomagnetic interaction is generated by loops of the strong sector fields, see figure A.1. The naive estimate is $\kappa_0 \sim \frac{g_\rho^2}{16\pi^2}$. We will however be interested in the region $m_Q < m_\rho$. In this case the loops generate

$$\kappa_0 \sim \frac{g_\rho^2}{16\pi^2} \frac{m_Q^2}{m_\rho^2}. \quad (\text{A.9})$$

Dressing the operator with the mixing the interaction (3.5) is obtained. In our numerical evaluation we will use the estimate

$$\kappa = \frac{N_c}{32\pi^2} \frac{m_Q^2}{m_\rho^2} X_R^{QQ} X_R^{Qq}. \quad (\text{A.10})$$

The suppression is relevant phenomenologically because it renders two body and three body decay widths comparable.

A.2 Approximate p_T Distribution

In the following, we derive the approximate cross section given in equation (3.19) for the process $uu \rightarrow uU$. We only include the relevant left-handed couplings, a good approximation for $g_\rho \gg g$ and derive the t -channel expression¹ for a given p_T of the spectator quark. The amplitude squared summed over initial and final states is proportional to

$$|\overline{\mathcal{M}}_{fi}|^2 \propto \frac{\hat{s}(\hat{s} - m_Q^2)}{(\hat{t} - m_\rho^2)^2}. \quad (\text{A.11})$$

This leads to a dependence on the Mandelstam variables in the cross section given by

$$\frac{d^3\sigma}{dy_3 dy_4 d|p_T|} \propto (f(x_1) f(x_2)) \frac{p_T}{S} \frac{\hat{s} - m_Q^2}{(\hat{t} - m_\rho^2)^2}, \quad (\text{A.12})$$

where y_3, y_4 are the rapidities of the daughter particles, S is the centre of mass energy of the collider and $x_{1,2}$ are the usual partonic momentum fractions carried by the initial partons. Recalling that

$$\hat{s} = m_Q^2 + 2p_T^2 + 2p_T \sqrt{m_Q^2 + p_T^2} \cosh \Delta y \quad (\text{A.13})$$

$$\hat{t} = -p_T \left(p_T + \sqrt{m_Q^2 + p_T^2} \exp(-\Delta y) \right) \quad (\text{A.14})$$

$$\hat{u} = -p_T \left(p_T + \sqrt{m_Q^2 + p_T^2} \exp(\Delta y) \right), \quad (\text{A.15})$$

we find

$$\frac{d^3\sigma}{dy_3 dy_4 d|p_T|} \propto (f(x_1) f(x_2)) \frac{p_T^2 \left(\cosh(\Delta y) \sqrt{m_Q^2 + p_T^2} + p_T \right)}{36\pi \left(m_\rho^2 + p_T \left(e^{-\Delta y} \sqrt{m_Q^2 + p_T^2} + p_T \right) \right)^2}. \quad (\text{A.16})$$

¹There is an additional u -channel contribution but since $\Delta y \rightarrow 0$ minimises \hat{s} , see (A.13), we typically have $t \approx u$.

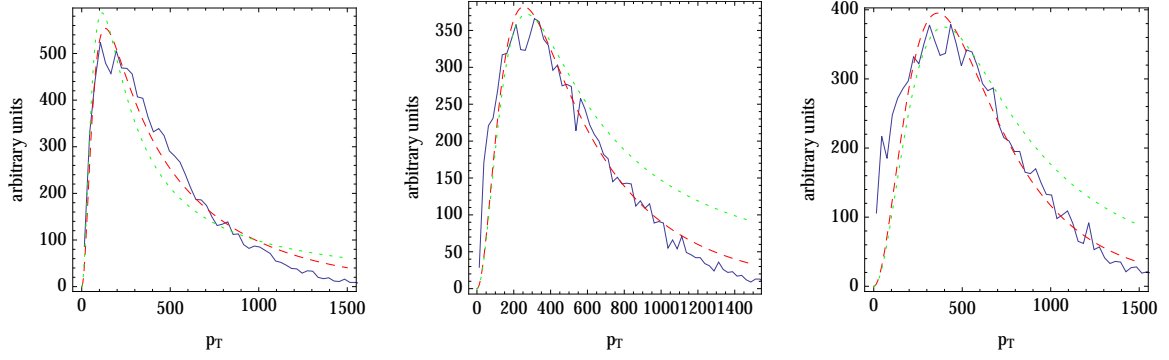


Figure A.2. Comparison between approximate and exact p_T distributions for various values of the fermionic partner and octet masses $(m_Q, m_\rho) = (100, 2500); (250, 2500); (500, 2500)$ GeV with $g_\rho = 6$ and $\sin \phi_{R_{u,d}} = 0.6$. The red line uses the full t -channel propagator, whereas the green line assumes a contact interaction. We use constant α in the plots. Naturally, for very large p_T the ρ dynamics is resolved and taking α constant ceases to be a good approximation.

We can now derive a simple approximation for the p_T distribution. Since $\Delta y \rightarrow 0$ minimises \hat{s} , we can set $\Delta y = 0$ in the following. The parton luminosities are steeply falling functions of \hat{s}/S , therefore we can approximate the remaining integration by the threshold value of the parton luminosities which we model as a steeply falling polynomial $(\hat{s}/S)^{-\alpha}$. We extracted α from the MSTW2008 parton density functions [213]. For heavy colour octets ($m_\rho \gg m_Q, p_T$), we can also ignore the octet propagator. Combining these approximations we find

$$\frac{d\sigma}{d|p_T|} \propto \frac{1}{S} \frac{p_T^2}{m_\rho^4} \left(p_T + \sqrt{m_Q^2 + p_T^2} \right) \left(\frac{p_T^2 + m_Q^2 + p_T \sqrt{m_Q^2 + p_T^2}}{S} \right)^{-\alpha} \quad (\text{A.17})$$

where $\alpha \sim 3-6$ is a slowly varying function of \hat{s} determined by the parton luminosities. The maximum of the p_T distribution is therefore approximately at $(p_T)^{\max} \approx \frac{1.5}{\sqrt{4\alpha-6}} m_Q \approx \frac{1}{2} m_Q$. In figure A.2 we compare the above approximation with a parton level simulation using the full model implementation, validating the result and the approximations.

Chapter B

Appendix - Little Higgs

B.1 Higgs Precision Data

Channel	$\hat{\mu}$ (7 TeV)	$\zeta_i^{(g,V,t)}$ (%)	$\hat{\mu}$ (8 TeV)	$\zeta_i^{(g,V,t)}$ (%)	Refs.
$b\bar{b}$ (VH)	combination	—	$-0.42^{+1.05}_{-1.05}$	(0, 100, 0)	[214]
$b\bar{b}$ (ttH)	3.81 ± 5.78	(0, 30, 70)	—	—	[215]
$\tau\tau$	combination	—	$0.7^{+0.7}_{-0.7}$	(20, 80, 0)	[216]
WW ($0j$)	0.06 ± 0.60	inclusive	$0.92^{+0.63}_{-0.49}$	inclusive	[217]
WW ($1j$)	$2.04^{+1.88}_{-1.30}$	inclusive	$1.11^{+1.20}_{-0.82}$	inclusive	
WW ($2j$)	—	—	$1.79^{+0.94}_{-0.75}$	(20, 80, 0)	
ZZ	combination	—	$1.7^{+0.5}_{-0.4}$	inclusive	[218]
$\gamma\gamma_{(L)}$ (uc ct)	$0.53^{+1.37}_{-1.44}$	(93, 7, 0)	$0.86^{+0.67}_{-0.67}$	(93.7, 6.2, 0.2)	[219] [220]
$\gamma\gamma_{(H)}$ (uc ct)	$0.17^{+1.94}_{-1.91}$	(67, 31, 2)	$0.92^{+1.1}_{-0.89}$	(79.3, 19.2, 1.4)	
$\gamma\gamma_{(L)}$ (uc ec)	$2.51^{+1.66}_{-1.69}$	(93, 7, 0)	$2.51^{+0.84}_{-0.75}$	(93.2, 6.6, 0.1)	
$\gamma\gamma_{(H)}$ (uc ec)	$10.39^{+3.67}_{-3.67}$	(65, 33, 2)	$2.69^{+1.31}_{-1.08}$	(78.1, 20.8, 1.1)	
$\gamma\gamma_{(L)}$ (c ct)	$6.08^{+2.59}_{-2.63}$	(93, 7, 0)	$1.37^{+1.02}_{-0.88}$	(93.6, 6.2, 0.2)	
$\gamma\gamma_{(H)}$ (c ct)	$-4.40^{+1.80}_{-1.76}$	(67, 31, 2)	$1.99^{+1.50}_{-1.22}$	(78.9, 19.6, 1.5)	
$\gamma\gamma_{(L)}$ (c ec)	$2.73^{+1.91}_{-2.02}$	(93, 7, 0)	$2.21^{+1.13}_{-0.95}$	(93.2, 6.7, 0.1)	
$\gamma\gamma_{(H)}$ (c ec)	$-1.63^{+2.88}_{-2.88}$	(65, 33, 2)	$1.26^{+1.31}_{-1.22}$	(77.7, 21.2, 1.1)	
$\gamma\gamma$ (c trans.)	$0.35^{+3.56}_{-3.60}$	(89, 11, 0)	$2.80^{+1.64}_{-1.55}$	(90.7, 9.0, 0.2)	
$\gamma\gamma$ (dijet)	$2.69^{+1.87}_{-1.84}$	(23, 77, 0)	—	—	
$\gamma\gamma$ (m_{jj} high loose)	—	—	$2.76^{+1.73}_{-1.35}$	(45, 54.9, 0.1)	
$\gamma\gamma$ (m_{jj} high tight)	—	—	$1.59^{+0.84}_{-0.62}$	(23.8, 76.2, 0)	
$\gamma\gamma$ (m_{jj} low)	—	—	$0.33^{+1.68}_{-1.46}$	(48.1, 49.9, 1.9)	
$\gamma\gamma$ (E_T^{miss})	—	—	$2.98^{+2.70}_{-2.15}$	(4.1, 83.8, 12.1)	
$\gamma\gamma$ (lepton tag)	—	—	$2.69^{+1.95}_{-1.66}$	(2.2, 79.2, 18.6)	

Table B.1. ATLAS best fits on signal strength modifier μ with signal compositions ζ_i^P (if provided) for gluon (g), vector (V), and top (t) initiated production [167]. If *inclusive* is denoted, the cut efficiencies have been neglected when evaluating μ from equation (4.49). If *combination* is denoted, only the 7+8 TeV combined result is available.

Chapter B: Appendix - Little Higgs

Channel	$\hat{\mu}$ (7 TeV)	$\zeta_i^{(g,V,t)}$ (%)	$\hat{\mu}$ (8 TeV)	$\zeta_i^{(g,V,t)}$ (%)	Refs.
$b\bar{b}$ (VBF)	—	—	$0.7_{-1.4}^{+1.4}$	(0, 100, 0)	[221]
$b\bar{b}$ (VH)	combination	—	$1.0_{-0.5}^{+0.5}$	(0, 100, 0)	[222]
$b\bar{b}$ (ttH)	$-0.81_{-1.75}^{+2.05}$	(0, 30, 70)	—	—	[223]
$\tau\tau$ (0/1j)	combination	—	$0.74_{-0.52}^{+0.49}$	inclusive	
$\tau\tau$ (VBF)	combination	—	$1.38_{-0.57}^{+0.61}$	(0, 100, 0)	[224]
$\tau\tau$ (VH)	combination	—	$0.76_{-1.43}^{+1.48}$	(0, 100, 0)	
WW (0/1j)	combination	—	$0.76_{-0.21}^{+0.21}$	inclusive	
WW (2j)	combination	—	$-0.05_{-0.56}^{+0.73}$	(17, 83, 0)	[225]
WW (VH)	combination	—	$-0.31_{-1.96}^{+2.24}$	(0, 100, 0)	
ZZ (untagged)	combination	—	$0.84_{-0.26}^{+0.32}$	(95, 5, 0)	[226]
ZZ (dijet tag)	—	—	$1.22_{-0.57}^{+0.84}$	(80, 20, 0)	
$\gamma\gamma$ (no tag 0)	$3.78_{-1.62}^{+2.01}$	(61.4, 35.5, 3.1)	$2.12_{-0.78}^{+0.92}$	(72.9, 24.6, 2.6)	
$\gamma\gamma$ (no tag 1)	$0.15_{-0.92}^{+0.99}$	(87.6, 11.8, 0.5)	$-0.03_{-0.64}^{+0.71}$	(83.5, 15.5, 1.0)	
$\gamma\gamma$ (no tag 2)	$-0.05_{-1.21}^{+1.21}$	(91.3, 8.3, 0.3)	$0.22_{-0.42}^{+0.46}$	(91.7, 7.9, 0.4)	
$\gamma\gamma$ (no tag 3)	$1.38_{-1.55}^{+1.66}$	(91.3, 8.5, 0.2)	$-0.81_{-0.42}^{+0.85}$	(92.5, 7.2, 0.2)	
$\gamma\gamma$ (dijet)	$4.13_{-1.76}^{+2.33}$	(26.8, 73.1, 0.0)	—	—	[227]
$\gamma\gamma$ (dijet loose)	—	—	$0.75_{-0.99}^{+1.06}$	(46.8, 52.8, 0.5)	
$\gamma\gamma$ (dijet tight)	—	—	$0.22_{-0.57}^{+0.71}$	(20.7, 79.2, 0.1)	
$\gamma\gamma$ (MET)	—	—	$1.84_{-2.26}^{+2.65}$	(0.0, 79.3, 20.8)	
$\gamma\gamma$ (Electron)	—	—	$-0.70_{-1.94}^{+2.75}$	(1.1, 79.3, 19.7)	
$\gamma\gamma$ (Muon)	—	—	$0.36_{-1.38}^{+1.84}$	(21.1, 67.0, 11.8)	

Table B.2. CMS best fits on signal strength modifier μ with signal compositions ζ_i^P (if provided) for gluon (g), vector (V), and top (t) initiated production [167]. If *inclusive* is denoted, the cut efficiencies have been neglected when evaluating μ from equation (4.49). If *combination* is denoted, only the 7+8 TeV combined result is available.

B.2 LHT Topologies

final state			production modes	$\sigma_{8 \text{ TeV}} \times \text{BR (fb)}$		$\sigma_{14 \text{ TeV}} \times \text{BR (fb)}$	
$\# l^\pm$	$\# \text{ jets}$	\cancel{E}_T		$k = 1.0$	$k = 0.4$	$k = 1.0$	$k = 0.4$
0	1	✓	$q_H A_H$	0.24	1.1×10^2	2.1	4.5×10^2
0	2	✓	$q_H q_H$	0.56	5.6×10^3	5.2	3.2×10^4
0	3	✓	$q_H W_H^\pm$	0.73	14	8.0	77
			$q_H Z_H$	0.76	8.6	8.0	49
0	4	✓	$q_H q_H$	4.0	9.1×10^2	35	5.6×10^3
			$W_H^\pm W_H^\mp$	1.9	low	9.1	low
			$W_H^\pm Z_H$	4.8	low	23	low
			$Z_H Z_H$	0.56	low	3.0	low
0	4	✗	$T^+ q$	2.0	2.0	17	17
0	5	✓	$q_H W_H^\pm$	5.1	✗	54	✗
			$q_H Z_H$	4.1	✗	44	✗
0	6	✓	$q_H q_H$	1.6	9.7×10^2	1.7×10^2	6.0×10^3
			$T^- T^-$	2.5	2.5	25	25
l^\pm	2	✓	$q_H q_H$	0.058	9.0×10^2	1.1	5.6×10^3
			$W_H^\pm W_H^\mp$	0.77	low	3.9	low
			$W_H^\pm Z_H$	2.1	low	10	low
			$T^+ q$	1.3	1.2	10	10
l^\pm	3	✓	$q_H W_H^\pm$	3.5	✗	37	✗
			$q_H Z_H$	0.99	✗	11	✗
l^\pm	4	✓	$q_H q_H$	7.4	9.7×10^2	82	6.0×10^3
			$T^- T^-$	2.2	2.2	21	21
$l^+ l^-$	0	✓	$W_H^\pm W_H^\mp$	0.32	low	1.7	low
$l^+ l^-$	1	✓	$q_H W_H^\pm$	0.54	✗	5.8	✗
$l^+ l^-$	2	✓	$q_H q_H$	1.1	✗	11	✗
			$T^- T^-$	0.47	0.47	4.6	4.6
$l^\pm l^\pm$	2	✓	$q_H q_H$	0.37	✗	2.7	✗

Table B.3. Overview of the relevant final states for LHC8 experimental searches in LHT models. The final states are classified according to the number of leptons and jets and whether they contain missing energy, and all the production modes contributing to each final state are listed. Note that the cross sections depend on f and k , and also R if the mode involves T^\pm . The last columns contain $\sigma \times \text{BR}$ for each of the production modes for fixed $f = 750 \text{ GeV}$ and $R = 1.0$. A ✗ indicates a mode without available phase space, whereas *low* indicates negligible cross section at the LHC.

B.3 EWPO & Precision Higgs: Case B

In this appendix the combined constraints from EWPT and Higgs searches are presented for a second down-type Yukawa coupling scenario, commonly known as *Case B* [157]. By combining the χ^2 analyses carried out separately for EWPT and the Higgs sector, as plotted in figure B.1, the lower bound on the symmetry breaking scale is

$$f \gtrsim 560 \text{ GeV} \quad \text{at} \quad 95\% \text{ CL.} \quad (\text{B.1})$$

The reduced lower bound in *Case B* compared to *Case A* is explained by the higher suppression in the bottom Yukawa coupling (4.42). This yields a higher suppression of the $b\bar{b}$ branching ratio and an enhancement of all other decay rates. This is indeed more aligned with the Higgs results provided by the ATLAS collaboration, where a generic enhancement in the non-fermionic decays of the Higgs is observed. This pattern is not exactly observed in the CMS Higgs results. However, since deviations from the ATLAS results turn out to be dominant in the χ^2 measure, the net result is a weaker exclusion for *Case B*.

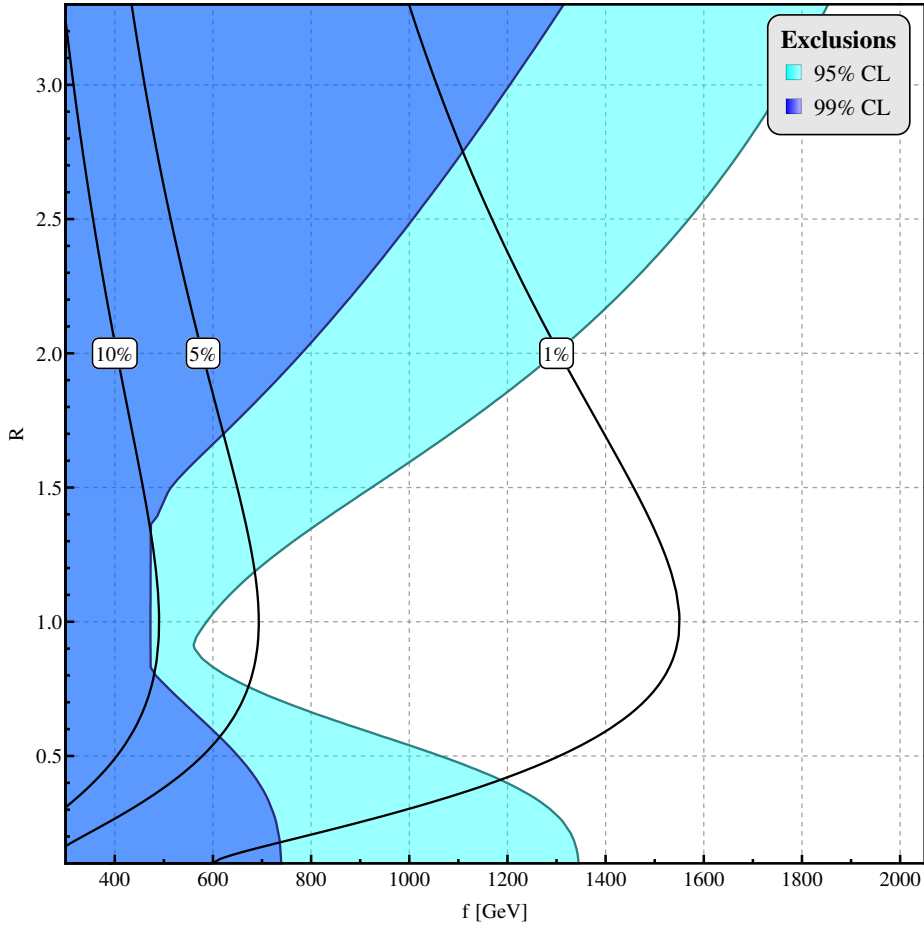


Figure B.1. Excluded parameter space regions at 95% and 99% CL from combination of EWPT and Higgs sector datasets. The thick black lines represent contours of required fine-tuning. Presented here is an alternative description of the Yukawa couplings, known as *Case B*.

Chapter C

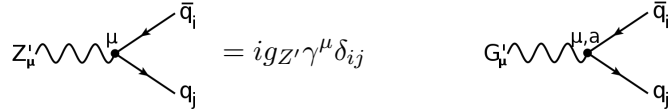
Appendix - Hadron Collider EFT

C.1 Toy Model

The toy model should be as simple as possible while still reproducing the interesting parts of realistic BSM models. Based on Z' models we can construct a single boson which couples uniformly to quarks, also known as the hadronic Z' . Equivalently also a partner for the gluon can be constructed, denoted as G' . These spin-one bosons will be used and their interactions with the Standard Model quarks are governed by the Lagrangians

$$\begin{aligned}\mathcal{L}_{Z'} &\subset -m_{Z'}^2 Z'^\mu Z'_\mu + g_{Z'} \bar{q}_i \gamma^\mu \delta_{ij} q_j Z'_\mu \\ \mathcal{L}_{G'} &\subset -m_{G'}^2 G'^{a\mu} G'_\mu + g_{G'} \bar{q}_i \gamma^\mu T_{ij}^a q_j G'^a_\mu.\end{aligned}\quad (\text{C.1})$$

In here $g_{Z'}$ and $g_{G'}$ are the coupling constants and i, j the colour indices. For these toy models the different transformations under gauge groups and the charges of the quarks are not taken into account. This is not relevant for the analysis in this work, for a comprehensive description discussing anomalies see [209]. Another relevant property of these particles are their masses which are denoted as $m_{Z'}$ and $m_{G'}$ respectively. Together with the coupling constants they form the fundamental parameters of this toy model. The Feynman rule for the $Z' \bar{q}q$ and $G' \bar{q}q$ couplings are



$$\begin{aligned}Z'_\mu \text{ (wavy)} \rightarrow \begin{matrix} \nearrow \bar{q}_i \\ \searrow q_j \end{matrix} &= i g_{Z'} \gamma^\mu \delta_{ij} & G'_\mu \text{ (wavy)} \rightarrow \begin{matrix} \nearrow \bar{q}_i \\ \searrow q_j \end{matrix} &= i g_{G'} \gamma^\mu T_{ij}^a.\end{aligned}\quad (\text{C.2})$$

In the rest of the appendix two additional important properties of the toy model are discussed. First, in the next two sections the width and its effect in the propagator are calculated for both the Z' and the G' and secondly in section C.1.3 the effective operators generated by this toy model are derived.

C.1.1 Widths

A relevant property of any particle in detector based experiment is the width, it influences the detectability in resonance searches. Though, also the width may have an impact on the correctness of the effective description. For our simple bosons the partial widths for decay into a single $q\bar{q}$ pair are given by

$$\begin{aligned}\Gamma_{Z' \rightarrow q\bar{q}} &= \alpha_{Z'} \frac{m_{Z'}^2 + 2m_q^2}{m_{Z'}^2} \sqrt{m_{Z'}^2 - 4m_q^2} \\ \Gamma_{G' \rightarrow q\bar{q}} &= \frac{\alpha_{G'}}{6} \frac{m_{G'}^2 + 2m_q^2}{m_{G'}^2} \sqrt{m_{G'}^2 - 4m_q^2}.\end{aligned}\quad (\text{C.3})$$

Calculation

The starting point for calculating the width of the decay $X \rightarrow q\bar{q}$ is the equation

$$\Gamma_{X \rightarrow q\bar{q}} = \frac{1}{8\pi} \frac{|\vec{p}_{1,2}|}{m_X^2} \int \frac{d\Omega_{cm}}{4\pi} |\mathcal{M}_{X \rightarrow q\bar{q}}|^2, \quad (\text{C.4})$$

where for equal quark masses the relevant kinematic variables — assuming incoming momentum k and outgoing momenta p_1 and p_2 — in this process are

$$\begin{aligned} k^2 &= m_X^2 & p_1^2 &= p_2^2 = m_q^2 \\ 2p_1 \cdot p_2 &= m_X^2 - 2m_q^2 & 2k \cdot p_1 &= 2k \cdot p_2 = m_X^2 \\ |\vec{p}_1| &= |\vec{p}_2| & &= \frac{1}{2} \sqrt{m_X^2 - 4m_q^2}. \end{aligned} \quad (\text{C.5})$$

For Z' the amplitude equals

$$\mathcal{M}_{Z' \rightarrow q\bar{q}} = i g_{Z'} \bar{u}_i(p_1) \gamma^\mu \delta_{ij} v_j(p_2) \epsilon_\mu(k), \quad (\text{C.6})$$

similarly for G' with the replacements $g_{Z'} \rightarrow g_{G'}$, $\delta_{ij} \rightarrow T_{ij}^a$ and $\epsilon_\mu(k) \rightarrow \epsilon_\mu^a(k)$. Then square the amplitude and average over initial spin and colour to obtain

$$|\overline{\mathcal{M}_{Z' \rightarrow q\bar{q}}}|^2 = g_{Z'}^2 \left(-g_{\mu\nu} + \frac{k_\mu k_\nu}{m_{Z'}^2} \right) \text{Tr} \left[(\not{p}_1 + m_q) \gamma^\mu (\not{p}_2 - m_q) \gamma^\nu \right]. \quad (\text{C.7})$$

The same can be obtained for G' with a different factor due to the colour structure and averaging over initial colour. This leads to the identification $|\overline{\mathcal{M}_{G' \rightarrow q\bar{q}}}|^2 = \frac{1}{6} |\overline{\mathcal{M}_{Z' \rightarrow q\bar{q}}}|^2$ with the obvious $Z' \rightarrow G'$ replacements. Evaluating the trace

$$\text{Tr} \left[(\not{p}_1 + m_q) \gamma^\mu (\not{p}_2 - m_q) \gamma^\nu \right] = 4 [p_1^\mu p_2^\nu + p_1^\nu p_2^\mu - g^{\mu\nu} (m_q^2 + p_1 \cdot p_2)] \quad (\text{C.8})$$

and using the kinematic expressions from equation (C.5) the averaged matrix element reduces to

$$|\overline{\mathcal{M}_{Z' \rightarrow q\bar{q}}}|^2 = 4g_{Z'}^2 [m_{Z'}^2 + 2m_q^2]. \quad (\text{C.9})$$

Plugging this expression into equation (C.4) leads to final result given in equation (C.3), concluding the calculation.

C.1.2 Propagator

For the calculation of the dijet cross sections in appendix C.2 and for the determination of the effective operator coefficients in the next section a proper definition for the propagator including the width is needed. In general for Z' like models large widths are a possibility and the usual Breit-Wigner propagator using the narrow-width approximation is not valid. Instead we adopt the methods developed in [228, 229] which imply that for the Z' case the propagator equals

$$\Pi_{Z'}(q^2) = \frac{-ig_{\mu\nu}}{q^2 - m_{Z'}^2 + i\sqrt{q^2} \Gamma_{Z'}(q^2)}. \quad (\text{C.10})$$

For the case of the dijet cross sections the transfer energy q^2 may equal either \hat{s} , \hat{t} or \hat{u} . In this expression the width depends on the transferred momentum in the propagator and is at leading order given by

$$\Gamma_{Z'}(q^2) = \sum_i \Gamma_{Z' \rightarrow q_i \bar{q}_i} \frac{(q^2 - 4m_{q_i}^2)^{\frac{3}{2}}}{(m_{Z'}^2 - 4m_{q_i}^2)^{\frac{3}{2}}} \frac{m_{Z'}^2}{q^2}. \quad (\text{C.11})$$

The width $\Gamma_{Z' \rightarrow q_i \bar{q}_i}$ is given in equation (C.3) in the previous section and the sum is over all six quark flavours. The results for the G' model are exactly the same and are obtained using the replacement $Z' \rightarrow G'$. In the rest of the calculations involving the width or the propagator, the quark masses are neglected, which leads to

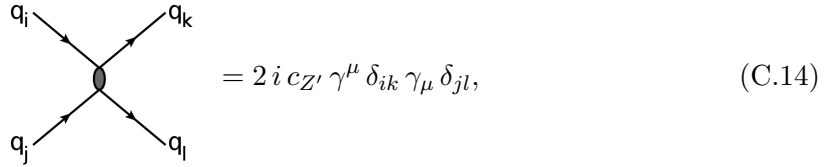
$$\Gamma_{Z'}(q^2) = 6\alpha_{Z'} \sqrt{q^2}. \quad (\text{C.12})$$

C.1.3 Effective Operators

The full theory is given in (C.1) and from this we can obtain an effective theory by integrating out the Z' or G' boson. Among other higher-dimensional operators these two are generated

$$\mathcal{L}^{\text{eff}} = c_{Z'} [\bar{q}_i \gamma^\mu \delta_{ij} q_j]^2 + c_{G'} [\bar{q}_i \gamma^\mu T_{ij}^a q_j]^2. \quad (\text{C.13})$$

The Feynman rule for each of the operators reads



$$= 2i c_{Z'} \gamma^\mu \delta_{ik} \gamma_\mu \delta_{jl}, \quad (\text{C.14})$$

where for the G' boson δ_{ij} is replaced by T_{ij}^a . Note that the combination where k and l are interchanged also exists. From the calculation below when matching the full theory onto this effective theory we find that the coefficients equal

$$c_{Z'} = -\frac{g_{Z'}^2}{2m_{Z'}^2}, \quad c_{G'} = -\frac{g_{G'}^2}{2m_{G'}^2}. \quad (\text{C.15})$$

It is important to note here that the effective operator coefficient does not depend on the width of the Z' or G' particle. The width only enters at non-leading order in the effective expansion of the transfer energy over the mass of the Z' or G' particle.

Calculation

The starting point for the matching are equation (C.1) for the Z' and G' bosons and equation (C.13) for the effective theory. For the matching procedure the process $q_i q_j \rightarrow q_i q_j$ is used, this only leaves the t -channel diagram and simplifies the calculation. In the full theory we have for this amplitude in the case of the Z'

$$\mathcal{M}_{ij \rightarrow ij}^{\text{full}} = \bar{u}_k(k_3) [ig_{Z'} \gamma^\mu \delta_{ki}] u_i(k_1) \frac{-ig_{\mu\nu}}{q^2 - m_{Z'}^2 + i\sqrt{q^2} \Gamma_{Z'}(q^2)} \bar{u}_l(k_4) [ig_{Z'} \gamma^\nu \delta_{kl}] u_j(k_2). \quad (\text{C.16})$$

In the effective theory we find — using the Feynman rule from equation (C.14) — the amplitude

$$\mathcal{M}_{ij \rightarrow ij}^{\text{eff}} = 2ic_{Z'} \bar{u}_k(k_3) [\gamma^\mu \delta_{ki}] u_i(k_1) \bar{u}_l(k_4) [\gamma_\mu \delta_{lj}] u_j(k_2). \quad (\text{C.17})$$

Expanding the propagator around $q^2 = 0$ in the full theory gives

$$\frac{1}{q^2 - m_{Z'}^2 + i\sqrt{q^2} \Gamma_{Z'}(q^2)} = -\frac{1}{m_{Z'}^2} \left[1 + \frac{q^2}{m_{Z'}^2} \left(1 + i \frac{\Gamma_{Z'}}{m_{Z'}} \right) + \dots \right]. \quad (\text{C.18})$$

Then taking the leading order term from this equation leads to the matched coefficients in equation (C.15). The calculation for G' follows exactly the same procedure, however, with the replacements $Z' \rightarrow G'$ and $\delta_{ij} \rightarrow T_{ij}^a$.

C.2 Dijet Cross Sections

In this appendix the partonic cross sections for dijet production at the LHC are calculated and tabulated for QCD in combination with the toy model from appendix C.1. Knowing the exact and analytical expressions for all these cross section is essential for the understanding of the experimental limits and the transition between effective and full theory. Since the toy model involves only quarks as external particles for the dijet production, interference with QCD amplitudes involving external gluons is not present. Therefore these processes are presented first and can be directly obtained from the literature [118, 230, 231], the analytic cross sections differential in \hat{t} are

$$\begin{aligned} \frac{d\sigma}{d\hat{t}}(gq_i \rightarrow gq_i)_{\text{QCD}} &= \frac{4\pi\alpha_s^2}{9\hat{s}^2} \left[-\frac{\hat{u}}{\hat{s}} - \frac{\hat{s}}{\hat{u}} + \frac{9}{4} \frac{\hat{s}^2 + \hat{u}^2}{\hat{t}^2} \right] \\ \frac{d\sigma}{d\hat{t}}(gg \rightarrow q_i\bar{q}_i)_{\text{QCD}} &= \frac{\pi\alpha_s^2}{6\hat{s}^2} \left[\frac{\hat{u}}{\hat{t}} + \frac{\hat{t}}{\hat{u}} - \frac{9}{4} \frac{\hat{t}^2 + \hat{u}^2}{\hat{s}^2} \right] \\ \frac{d\sigma}{d\hat{t}}(gg \rightarrow gg)_{\text{QCD}} &= \frac{9\pi\alpha_s^2}{2\hat{s}^2} \left[3 - \frac{\hat{t}\hat{u}}{\hat{s}^2} - \frac{\hat{s}\hat{u}}{\hat{t}^2} - \frac{\hat{s}\hat{t}}{\hat{u}^2} \right]. \end{aligned} \quad (\text{C.19})$$

In this work all partonic cross sections will be presented differential in \hat{t} , because of their simple structure and easy convolution with the parton density functions in the performed analysis. The relevant production processes only involving external quarks are $q_i q_i \rightarrow q_i q_i$ and $q_i q_j \rightarrow q_i q_j$ where $i \neq j$. These also include interference effects between QCD and the toy model and therefore need a dedicated calculation. The full details of the calculation are not presented, but a rigorous outline is given in the paragraphs below. At the end of this appendix in equation (C.26) the resulting cross sections are presented.

Amplitudes

Now we discuss the production processes $q_i q_i \rightarrow q_i q_i$ and $q_i q_j \rightarrow q_i q_j$ where $i \neq j$. The first takes place through t - and u -channel exchange, whereas the second is an exact copy of the first with only t -channel exchange. Hence the calculation is done only for the first process and for the second process the contributions from t -channel are then extracted. As

a starting point, all amplitudes relevant for the process are listed for QCD, the full theory and the effective theory (both t -channel and u -channel)

$$\begin{aligned}
 \mathcal{M}_{\text{QCD}}^{\hat{t}} &= i \frac{g_s^2}{\hat{t}} [\bar{u}_i(k_3) \gamma^\mu T_{ij}^a u_j(k_1)] [\bar{u}_k(k_4) \gamma_\mu T_{kl}^a u_l(k_2)] \\
 \mathcal{M}_{\text{QCD}}^{\hat{u}} &= -i \frac{g_s^2}{\hat{u}} [\bar{u}_i(k_4) \gamma^\mu T_{ij}^a u_j(k_1)] [\bar{u}_k(k_3) \gamma_\mu T_{kl}^a u_l(k_2)] \\
 \mathcal{M}_{\text{full}}^{\hat{t}} &= i \frac{g_{Z'}^2}{\hat{t} - m_{Z'}^2 + i\sqrt{\hat{t}} \Gamma_{Z'}(\hat{t})} [\bar{u}_i(k_3) \gamma^\mu \delta_{ij} u_j(k_1)] [\bar{u}_k(k_4) \gamma_\mu \delta_{kl} u_l(k_2)] \\
 \mathcal{M}_{\text{full}}^{\hat{u}} &= -i \frac{g_{Z'}^2}{\hat{u} - m_{Z'}^2 + i\sqrt{\hat{u}} \Gamma_{Z'}(\hat{u})} [\bar{u}_i(k_4) \gamma^\mu \delta_{ij} u_j(k_1)] [\bar{u}_k(k_3) \gamma_\mu \delta_{kl} u_l(k_2)] \\
 \mathcal{M}_{\text{eff}}^{\hat{t}} &= 2ic_{Z'} [\bar{u}_i(k_3) \gamma^\mu \delta_{ij} u_j(k_1)] [\bar{u}_k(k_4) \gamma_\mu \delta_{kl} u_l(k_2)] \\
 \mathcal{M}_{\text{eff}}^{\hat{u}} &= -2ic_{Z'} [\bar{u}_i(k_4) \gamma^\mu \delta_{ij} u_j(k_1)] [\bar{u}_k(k_3) \gamma_\mu \delta_{kl} u_l(k_2)]. \tag{C.20}
 \end{aligned}$$

For the coloured resonance G' one needs to make the replacements $Z' \rightarrow G'$ and $\delta_{ij} \rightarrow T_{ij}^a$ in the last four amplitudes. The different colour structure affects the interference terms and some of those may be non-zero for the G' where they would vanish for the Z' . We allow the effective operator coefficients $c_{Z'}$ and $c_{G'}$ from equation (C.15) to be complex, furthermore the full theory propagators also include imaginary parts proportional to the width.

Definitions

Per process we want to calculate the spin and colour averaged amplitude

$$|\overline{\mathcal{M}}|^2 = \frac{1}{3^2} \sum_{\text{colour}} \frac{1}{2^2} \sum_{\text{spin}} \mathcal{M}_X \mathcal{M}_Y^*, \tag{C.21}$$

where \mathcal{M}_X and \mathcal{M}_Y are a combination of any of the amplitudes from equations (C.20). Some useful traces, where k_1 and k_2 are incoming momenta and k_3 and k_4 are outgoing momenta, are given by

$$\begin{aligned}
 \text{tr}[k_3 \gamma^\mu k_1 \gamma^\nu] \cdot \text{tr}[k_4 \gamma_\mu k_2 \gamma_\nu] &= 8(\hat{s}^2 + \hat{u}^2) \\
 \text{tr}[k_4 \gamma^\mu k_1 \gamma^\nu] \cdot \text{tr}[k_3 \gamma_\mu k_2 \gamma_\nu] &= 8(\hat{s}^2 + \hat{t}^2) \\
 \text{tr}[k_3 \gamma^\mu k_1 \gamma^\nu k_4 \gamma_\mu k_2 \gamma_\nu] &= -8\hat{s}^2. \tag{C.22}
 \end{aligned}$$

Moreover, for this momenta configuration and all initial and final state particles massless we have the differential cross section

$$\frac{d\sigma}{d\hat{t}} = \frac{|\overline{\mathcal{M}}|^2}{16\pi\hat{s}^2}. \tag{C.23}$$

Squared Amplitudes

The calculation of squaring the amplitudes from equation (C.20) can be split up in a pre-factor and four spinor structures (t -channel colour octet, u -channel colour octet, t -channel

colour singlet and u -channel colour singlet)

$$\begin{aligned}
 \mathcal{M}_{(8)}^{\hat{t}} &= [\bar{u}_i(k_3)\gamma^\mu T_{ij}^a u_j(k_1)] [\bar{u}_k(k_4)\gamma_\mu T_{kl}^a u_l(k_2)] \\
 \mathcal{M}_{(8)}^{\hat{u}} &= [\bar{u}_i(k_4)\gamma^\mu T_{ij}^a u_j(k_1)] [\bar{u}_k(k_3)\gamma_\mu T_{kl}^a u_l(k_2)] \\
 \mathcal{M}_{(1)}^{\hat{t}} &= [\bar{u}_i(k_3)\gamma^\mu \delta_{ij} u_j(k_1)] [\bar{u}_k(k_4)\gamma_\mu \delta_{kl} u_l(k_2)] \\
 \mathcal{M}_{(1)}^{\hat{u}} &= [\bar{u}_i(k_4)\gamma^\mu \delta_{ij} u_j(k_1)] [\bar{u}_k(k_3)\gamma_\mu \delta_{kl} u_l(k_2)].
 \end{aligned} \tag{C.24}$$

To calculate all contributions from equation (C.20) to the $q_i q_i \rightarrow q_i q_i$ process all possible sixteen contractions from equation (C.21) are needed. These are summarised as

$$\begin{aligned}
 \left| \overline{\mathcal{M}_{(8)}^{\hat{t}}} \right|^2 &= \frac{4}{9} (\hat{s}^2 + \hat{u}^2) & \left| \overline{\mathcal{M}_{(8)}^{\hat{u}}} \right|^2 &= \frac{4}{9} (\hat{s}^2 + \hat{t}^2) \\
 \left| \overline{\mathcal{M}_{(1)}^{\hat{t}}} \right|^2 &= 2 (\hat{s}^2 + \hat{u}^2) & \left| \overline{\mathcal{M}_{(1)}^{\hat{u}}} \right|^2 &= 2 (\hat{s}^2 + \hat{t}^2) \\
 \overline{\mathcal{M}_{(8)}^{\hat{t}} \mathcal{M}_{(8)}^{\hat{u}*}} &= \overline{\mathcal{M}_{(8)}^{\hat{u}} \mathcal{M}_{(8)}^{\hat{t}*}} = \frac{4}{27} \hat{s}^2 \\
 \overline{\mathcal{M}_{(1)}^{\hat{t}} \mathcal{M}_{(1)}^{\hat{u}*}} &= \overline{\mathcal{M}_{(1)}^{\hat{u}} \mathcal{M}_{(1)}^{\hat{t}*}} = -\frac{2}{3} \hat{s}^2 \\
 \overline{\mathcal{M}_{(8)}^{\hat{t}} \mathcal{M}_{(1)}^{\hat{t}*}} &= \overline{\mathcal{M}_{(1)}^{\hat{t}} \mathcal{M}_{(8)}^{\hat{t}*}} = 0 \\
 \overline{\mathcal{M}_{(8)}^{\hat{u}} \mathcal{M}_{(1)}^{\hat{u}*}} &= \overline{\mathcal{M}_{(1)}^{\hat{u}} \mathcal{M}_{(8)}^{\hat{u}*}} = 0 \\
 \overline{\mathcal{M}_{(8)}^{\hat{t}} \mathcal{M}_{(1)}^{\hat{u}*}} &= \overline{\mathcal{M}_{(1)}^{\hat{u}} \mathcal{M}_{(8)}^{\hat{t}*}} = -\frac{8}{9} \hat{s}^2 \\
 \overline{\mathcal{M}_{(8)}^{\hat{u}} \mathcal{M}_{(1)}^{\hat{t}*}} &= \overline{\mathcal{M}_{(1)}^{\hat{t}} \mathcal{M}_{(8)}^{\hat{u}*}} = -\frac{8}{9} \hat{s}^2.
 \end{aligned} \tag{C.25}$$

To obtain the final result for the different cross sections one needs to combine the pre-factors from equation (C.20) with the results from equation (C.25) and insert them into equation (C.23).

Results

For the $q_i q_i \rightarrow q_i q_i$ process we then find the following results (with the colour coding t -

channel, u -channel, t - u channel interference)

$$\begin{aligned}
 \frac{d\sigma}{d\hat{t}} \Big|_{\text{QCD}} &= \frac{4\pi\alpha_s^2}{9\hat{s}^2} \left[\frac{\hat{s}^2 + \hat{u}^2}{\hat{t}^2} + \frac{\hat{s}^2 + \hat{t}^2}{\hat{u}^2} - \frac{2}{3} \frac{\hat{s}^2}{\hat{t}\hat{u}} \right] \\
 \frac{d\sigma}{d\hat{t}} \Big|_{Z'_{\text{full}}}^{\text{pure}} &= \frac{2\pi\alpha_{Z'}^2}{\hat{s}^2} \left[\frac{\hat{s}^2 + \hat{u}^2}{(\hat{t} - m_{Z'}^2)^2 + \hat{t}\Gamma_{Z'}^2(\hat{t})} + \frac{\hat{s}^2 + \hat{t}^2}{(\hat{u} - m_{Z'}^2)^2 + \hat{u}\Gamma_{Z'}^2(\hat{u})} + \frac{2}{3}\hat{s}^2 P(\hat{t}, \hat{u}, Z') \right] \\
 \frac{d\sigma}{d\hat{t}} \Big|_{Z'_{\text{full}}}^{\text{int}} &= \frac{16\pi\alpha_s\alpha_{Z'}}{9\hat{s}^2} \left[\frac{\hat{s}^2}{\hat{t}} Q(\hat{u}, Z') + \frac{\hat{s}^2}{\hat{u}} Q(\hat{t}, Z') \right] \\
 \frac{d\sigma}{d\hat{t}} \Big|_{Z'_{\text{eff}}}^{\text{pure}} &= \frac{|c_{Z'}|^2}{2\pi} \left[\frac{\hat{s}^2 + \hat{u}^2}{\hat{s}^2} + \frac{\hat{s}^2 + \hat{t}^2}{\hat{s}^2} + \frac{2}{3} \right] \\
 \frac{d\sigma}{d\hat{t}} \Big|_{Z'_{\text{eff}}}^{\text{int}} &= \frac{8\alpha_s \text{Re}(c_{Z'})}{9\hat{s}} \left[\frac{\hat{s}}{\hat{t}} + \frac{\hat{s}}{\hat{u}} \right] \\
 \frac{d\sigma}{d\hat{t}} \Big|_{G'_{\text{full}}}^{\text{pure}} &= \frac{4\pi\alpha_{G'}^2}{9\hat{s}^2} \left[\frac{\hat{s}^2 + \hat{u}^2}{(\hat{t} - m_{G'}^2)^2 + \hat{t}\Gamma_{G'}^2(\hat{t})} + \frac{\hat{s}^2 + \hat{t}^2}{(\hat{u} - m_{G'}^2)^2 + \hat{u}\Gamma_{G'}^2(\hat{u})} - \frac{2}{3}\hat{s}^2 P(\hat{t}, \hat{u}, G') \right] \\
 \frac{d\sigma}{d\hat{t}} \Big|_{G'_{\text{full}}}^{\text{int}} &= \frac{8\pi\alpha_s\alpha_{G'}}{9\hat{s}^2} \left[\frac{\hat{s}^2 + \hat{u}^2}{\hat{t}} Q(\hat{t}, G') + \frac{\hat{s}^2 + \hat{t}^2}{\hat{u}} Q(\hat{u}, G') - \frac{1}{3} \left(\frac{\hat{s}^2}{\hat{t}} Q(\hat{u}, G') + \{ \hat{t} \leftrightarrow \hat{u} \} \right) \right] \\
 \frac{d\sigma}{d\hat{t}} \Big|_{G'_{\text{eff}}}^{\text{pure}} &= \frac{|c_{G'}|^2}{9\pi} \left[\frac{\hat{s}^2 + \hat{u}^2}{\hat{s}^2} + \frac{\hat{s}^2 + \hat{t}^2}{\hat{s}^2} - \frac{2}{3} \right] \\
 \frac{d\sigma}{d\hat{t}} \Big|_{G'_{\text{eff}}}^{\text{int}} &= \frac{4\alpha_s \text{Re}(c_{G'})}{9\hat{s}} \left[\frac{\hat{s}^2 + \hat{u}^2}{\hat{s}\hat{t}} + \frac{\hat{s}^2 + \hat{t}^2}{\hat{s}\hat{u}} - \frac{1}{3} \frac{\hat{s}}{\hat{t}} - \frac{1}{3} \frac{\hat{s}}{\hat{u}} \right].
 \end{aligned} \tag{C.26}$$

In the above equations the functions $P(\hat{x}, \hat{y}, X)$ and $Q(\hat{x}, X)$ are defined as

$$\begin{aligned}
 P(\hat{x}, \hat{y}, X) &\equiv \frac{(\hat{x} - m_X^2)(\hat{y} - m_X^2) + \sqrt{\hat{x}}\Gamma_X(\hat{x})\sqrt{\hat{y}}\Gamma_X(\hat{y})}{\left[(\hat{x} - m_X^2)^2 + \hat{x}\Gamma_X^2(\hat{x}) \right] \left[(\hat{y} - m_X^2)^2 + \hat{y}\Gamma_X^2(\hat{y}) \right]} \\
 Q(\hat{x}, X) &\equiv \frac{\hat{x} - m_X^2}{(\hat{x} - m_X^2)^2 + \hat{x}\Gamma_X^2(\hat{x})}.
 \end{aligned} \tag{C.27}$$

The results for the $q_i q_j \rightarrow q_i q_j$ process can be directly read of from equation (C.26) and are given only by the t -channel contributions. In equation (C.27) the assumption has been made that the combination $\sqrt{\hat{x}}\Gamma_X(\hat{x})$ is real for all values of \hat{x} . Equation (C.12) shows that this holds for vanishing quark masses. This is assumed in the numerical calculations as well, since their effect on the differential cross sections is negligible.

Numerical Calculations

The analytical results derived in this section have to be transformed from partonic dijet cross sections to realistic angular distributions at the LHC. This has been done using the Mathematica package of the MSTW 2008 parton density functions [213]. Furthermore, the integration over angular variables and the extraction of exclusion limits on parameters has been done using Mathematica. A notebook containing all partonic cross sections, the interface with the parton densities and the extraction of limits is available upon request with the author.

C.3 Recast Example

Here we outline the recasting of existing limits from effective operators for the full theory using the original effective operator bound and the quantified deviation between the full and effective theory. As an example the heavy gluon resonance ρ in the model with right-handed partial compositeness discussed in section 3.3 is used. When the ρ is integrated out, the effective operator

$$-\frac{g_\rho^2}{6m_\rho^2} \sin^4 \phi (\bar{q}\gamma^\mu q) (\bar{q}\gamma^\mu q) \quad (\text{C.28})$$

is obtained and was used to constrain the parameter space in the m_ρ versus $\sin \phi$ plane¹. With the use of this example we outline the steps needed to rescale this limit to include the full theory effects.

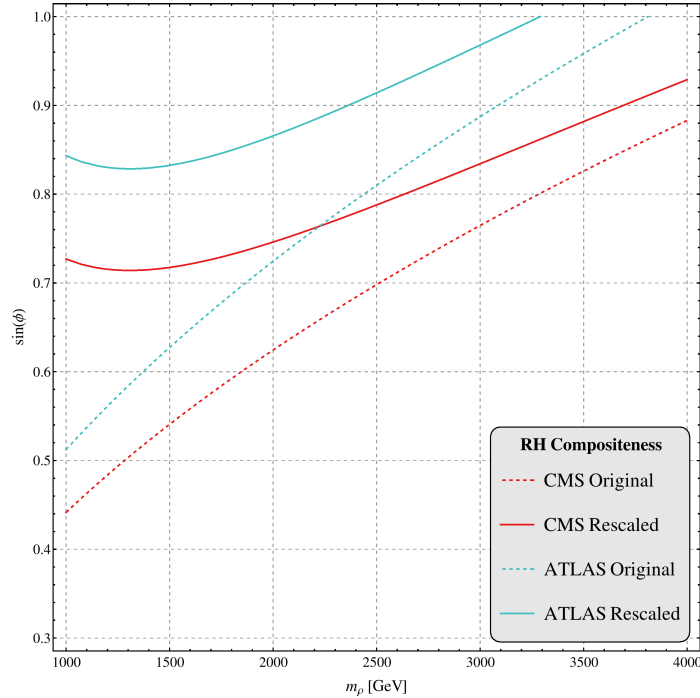


Figure C.1. Recasting of existing effective operator limits using the quantified deviation between effective and full theory for the example of partial right-handed compositeness from chapter 3. A detailed description of the procedure is provided in the text. The dashed lines represent the naive limits from effective operator constraints, whereas the solid lines show the more reliable rescaled limits.

1. The first step is to obtain the experimental limit on either one of the toy models using the effective operator coefficient and compare with the experimental limit

$$|c| = \left| -\frac{g^2}{2m^2} \right| = \frac{2\pi}{\Lambda_{\text{exp}}^2}. \quad (\text{C.29})$$

¹Here we use the simplification of removing the handedness of the Standard Model quarks.

In this case this is the Z' operator and it establishes the exclusion contour in the mass versus coupling plane.

2. Convert the exclusion contour to a limit on the coupling g as a function of the mass m and then use equation (5.20) with the fitted parameter C from equation (5.21) to rescale the exclusion limit. A realistic limit on the full theory behind the Z' toy model using the experimental limit is then obtained.
3. Compare the effective operator coefficients and express the parameters of the model under consideration in terms of the toy model parameters. For the example at hand we obtain

$$g = \sqrt{\frac{1}{3}} g_\rho \sin^2 \phi, \quad (\text{C.30})$$

where m equals m_ρ by definition and drops out.

4. Express the exclusion limits on the toy model in terms of the model parameters using equation (C.30) to obtain realistic exclusion limits for the considered model. For the model considered the limits are expressed in the mass versus $\sin \phi$ plane, using $g_\rho = 3$ for the identification.

Following these steps for the model with right-handed compositeness results for the adjusted exclusion limits are presented in figure C.1. We observe that the exclusion limits are significantly reduced². However, it is noted that the exclusion limits quoted in section 3.3 remain unchanged due to overlap between the exclusion regions from effective operators and dijet resonance searches.

²The deviation between full and effective theory limits has been obtained based on the ATLAS analysis and has also been applied to the CMS limits. Therefore, the rescaled limits should be seen as an indication and a more detailed analysis of the deviation is required.

Bibliography

- [1] **CMS Collaboration**, S. Chatrchyan *et. al.*, *Observation of a new boson at a mass of 125 GeV with the CMS experiment at the LHC*, *Phys.Lett.* **B716** (2012) 30–61, [[arXiv:1207.7235](https://arxiv.org/abs/1207.7235)].
- [2] **ATLAS Collaboration**, G. Aad *et. al.*, *Observation of a new particle in the search for the Standard Model Higgs boson with the ATLAS detector at the LHC*, *Phys.Lett.* **B716** (2012) 1–29, [[arXiv:1207.7214](https://arxiv.org/abs/1207.7214)].
- [3] S. Glashow, *Partial Symmetries of Weak Interactions*, *Nucl.Phys.* **22** (1961) 579–588.
- [4] S. Weinberg, *A Model of Leptons*, *Phys.Rev.Lett.* **19** (1967) 1264–1266.
- [5] A. Salam, *Weak and Electromagnetic Interactions*, *Conf.Proc.* **C680519** (1968) 367–377.
- [6] **ATLAS Collaboration**, “ATLAS Results Overview.” <https://twiki.cern.ch/twiki/bin/view/AtlasPublic>.
- [7] **CMS Collaboration**, “CMS Results Overview.” <https://twiki.cern.ch/twiki/bin/view/CMSPublic/PhysicsResults>.
- [8] F. Englert and R. Brout, *Broken Symmetry and the Mass of Gauge Vector Mesons*, *Phys.Rev.Lett.* **13** (1964) 321–323.
- [9] P. W. Higgs, *Broken symmetries, massless particles and gauge fields*, *Phys.Lett.* **12** (1964) 132–133.
- [10] P. W. Higgs, *Spontaneous Symmetry Breakdown without Massless Bosons*, *Phys.Rev.* **145** (1966) 1156–1163.
- [11] M. Veltman, *The Infrared - Ultraviolet Connection*, *Acta Phys.Polon.* **B12** (1981) 437.
- [12] K. G. Wilson, *The Renormalization Group and Strong Interactions*, *Phys.Rev.* **D3** (1971) 1818.
- [13] E. Gildener, *Gauge Symmetry Hierarchies*, *Phys.Rev.* **D14** (1976) 1667.
- [14] E. Gildener and S. Weinberg, *Symmetry Breaking and Scalar Bosons*, *Phys.Rev.* **D13** (1976) 3333.
- [15] G. 't Hooft, *Naturalness, chiral symmetry, and spontaneous chiral symmetry breaking*, *NATO Adv.Study Inst.Ser.B Phys.* **59** (1980) 135.
- [16] P. Ramond, *Dual Theory for Free Fermions*, *Phys.Rev.* **D3** (1971) 2415–2418.
- [17] A. Neveu and J. Schwarz, *Factorizable dual model of pions*, *Nucl.Phys.* **B31** (1971) 86–112.
- [18] J. Wess and B. Zumino, *A Lagrangian Model Invariant Under Supergauge Transformations*, *Phys.Lett.* **B49** (1974) 52.
- [19] J. Wess and B. Zumino, *Supergauge Transformations in Four-Dimensions*, *Nucl.Phys.* **B70** (1974) 39–50.
- [20] D. B. Kaplan and H. Georgi, *SU(2) x U(1) Breaking by Vacuum Misalignment*, *Phys.Lett.* **B136** (1984) 183.

BIBLIOGRAPHY

- [21] D. B. Kaplan, H. Georgi, and S. Dimopoulos, *Composite Higgs Scalars*, *Phys.Lett.* **B136** (1984) 187.
- [22] **ATLAS Collaboration**, “ATLAS Higgs Overview.”
<https://twiki.cern.ch/twiki/bin/view/AtlasPublic/HiggsPublicResults>.
- [23] **CMS Collaboration**, “CMS Higgs Overview.”
<https://twiki.cern.ch/twiki/bin/view/CMSPublic/PhysicsResultsHIG>.
- [24] **ATLAS Collaboration**, “ATLAS Supersymmetry Overview.”
<https://twiki.cern.ch/twiki/bin/view/AtlasPublic/SupersymmetryPublicResults>.
- [25] **CMS Collaboration**, “CMS Supersymmetry Overview.”
<https://twiki.cern.ch/twiki/bin/view/CMSPublic/PhysicsResultsSUS>.
- [26] **ATLAS Collaboration**, “ATLAS Exotics Overview.”
<https://twiki.cern.ch/twiki/bin/view/AtlasPublic/ExoticsPublicResults>.
- [27] **CMS Collaboration**, “CMS Exotics Overview.”
<https://twiki.cern.ch/twiki/bin/view/CMSPublic/PhysicsResultsEXO>.
- [28] **ILC Collaboration**, J. Brau *et. al.*, *ILC Reference Design Report: ILC Global Design Effort and World Wide Study*, [arXiv:0712.1950](https://arxiv.org/abs/0712.1950).
- [29] **ILC**, G. Aarons *et. al.*, *International Linear Collider Reference Design Report Volume 2: Physics at the ILC*, [arXiv:0709.1893](https://arxiv.org/abs/0709.1893).
- [30] N. Phinney, N. Toge, and N. Walker, *ILC Reference Design Report Volume 3 - Accelerator*, [arXiv:0712.2361](https://arxiv.org/abs/0712.2361).
- [31] **ILC Collaboration**, T. Behnke *et. al.*, *ILC Reference Design Report Volume 4 - Detectors*, [arXiv:0712.2356](https://arxiv.org/abs/0712.2356).
- [32] H. Baer, T. Barklow, K. Fujii, Y. Gao, A. Hoang, *et. al.*, *The International Linear Collider Technical Design Report - Volume 2: Physics*, [arXiv:1306.6352](https://arxiv.org/abs/1306.6352).
- [33] R. Contino, *The Higgs as a Composite Nambu-Goldstone Boson*, [arXiv:1005.4269](https://arxiv.org/abs/1005.4269).
- [34] R. Contino, “Lectures on Electroweak Symmetry Breaking.”
<http://indico.cern.ch/conferenceDisplay.py?confId=206931>.
- [35] R. Contino, T. Kramer, M. Son, and R. Sundrum, *Warped/composite phenomenology simplified*, *JHEP* **0705** (2007) 074, [[hep-ph/0612180](https://arxiv.org/abs/hep-ph/0612180)].
- [36] M. Schmaltz and D. Tucker-Smith, *Little Higgs review*, *Ann.Rev.Nucl.Part.Sci.* **55** (2005) 229–270, [[hep-ph/0502182](https://arxiv.org/abs/hep-ph/0502182)].
- [37] M. Perelstein, *Little Higgs models and their phenomenology*, *Prog.Part.Nucl.Phys.* **58** (2007) 247–291, [[hep-ph/0512128](https://arxiv.org/abs/hep-ph/0512128)].
- [38] S. Weinberg, *Implications of Dynamical Symmetry Breaking*, *Phys.Rev.* **D13** (1976) 974–996.
- [39] L. Susskind, *Dynamics of Spontaneous Symmetry Breaking in the Weinberg-Salam Theory*, *Phys.Rev.* **D20** (1979) 2619–2625.
- [40] N. Arkani-Hamed, A. G. Cohen, and H. Georgi, *Electroweak symmetry breaking from dimensional deconstruction*, *Phys.Lett.* **B513** (2001) 232–240, [[hep-ph/0105239](https://arxiv.org/abs/hep-ph/0105239)].
- [41] M. Redi and A. Weiler, *Flavor and CP Invariant Composite Higgs Models*, *JHEP* **1111** (2011) 108, [[arXiv:1106.6357](https://arxiv.org/abs/1106.6357)].

BIBLIOGRAPHY

- [42] H.-C. Cheng and I. Low, *TeV symmetry and the little hierarchy problem*, *JHEP* **0309** (2003) 051, [[hep-ph/0308199](#)].
- [43] H.-C. Cheng and I. Low, *Little hierarchy, little Higgses, and a little symmetry*, *JHEP* **0408** (2004) 061, [[hep-ph/0405243](#)].
- [44] A. Manohar and H. Georgi, *Chiral Quarks and the Nonrelativistic Quark Model*, *Nucl.Phys.* **B234** (1984) 189.
- [45] G. Giudice, C. Grojean, A. Pomarol, and R. Rattazzi, *The Strongly-Interacting Light Higgs*, *JHEP* **0706** (2007) 045, [[hep-ph/0703164](#)].
- [46] **ALEPH and CDF and D0 and DELPHI and L3 and OPAL and SLD Collaboration**, J. Alcaraz, *Precision Electroweak Measurements and Constraints on the Standard Model*, [arXiv:0911.2604](#).
- [47] A. Djouadi, *The Anatomy of electro-weak symmetry breaking. I: The Higgs boson in the standard model*, *Phys.Rept.* **457** (2008) 1–216, [[hep-ph/0503172](#)].
- [48] M. E. Peskin and T. Takeuchi, *Estimation of oblique electroweak corrections*, *Phys.Rev.* **D46** (1992) 381–409.
- [49] M. E. Peskin and T. Takeuchi, *A New constraint on a strongly interacting Higgs sector*, *Phys.Rev.Lett.* **65** (1990) 964–967.
- [50] M. Golden and L. Randall, *Radiative Corrections to Electroweak Parameters in Technicolor Theories*, *Nucl.Phys.* **B361** (1991) 3–23.
- [51] B. Holdom and J. Terning, *Large corrections to electroweak parameters in technicolor theories*, *Phys.Lett.* **B247** (1990) 88–92.
- [52] K. Agashe, R. Contino, and A. Pomarol, *The Minimal composite Higgs model*, *Nucl.Phys.* **B719** (2005) 165–187, [[hep-ph/0412089](#)].
- [53] R. Contino, Y. Nomura, and A. Pomarol, *Higgs as a holographic pseudoGoldstone boson*, *Nucl.Phys.* **B671** (2003) 148–174, [[hep-ph/0306259](#)].
- [54] R. Contino, L. Da Rold, and A. Pomarol, *Light custodians in natural composite Higgs models*, *Phys.Rev.* **D75** (2007) 055014, [[hep-ph/0612048](#)].
- [55] S. R. Coleman, J. Wess, and B. Zumino, *Structure of phenomenological Lagrangians. 1.*, *Phys.Rev.* **177** (1969) 2239–2247.
- [56] J. Callan, Curtis G., S. R. Coleman, J. Wess, and B. Zumino, *Structure of phenomenological Lagrangians. 2.*, *Phys.Rev.* **177** (1969) 2247–2250.
- [57] R. Rattazzi and A. Zaffaroni, *Comments on the holographic picture of the Randall-Sundrum model*, *JHEP* **0104** (2001) 021, [[hep-th/0012248](#)].
- [58] S. Dimopoulos and L. Susskind, *Mass Without Scalars*, *Nucl.Phys.* **B155** (1979) 237–252.
- [59] M. A. Luty and T. Okui, *Conformal technicolor*, *JHEP* **0609** (2006) 070, [[hep-ph/0409274](#)].
- [60] R. Rattazzi, V. S. Rychkov, E. Tonni, and A. Vichi, *Bounding scalar operator dimensions in 4D CFT*, *JHEP* **0812** (2008) 031, [[arXiv:0807.0004](#)].
- [61] D. B. Kaplan, *Flavor at SSC energies: A New mechanism for dynamically generated fermion masses*, *Nucl.Phys.* **B365** (1991) 259–278.
- [62] L. Randall and R. Sundrum, *A Large mass hierarchy from a small extra dimension*, *Phys.Rev.Lett.* **83** (1999) 3370–3373, [[hep-ph/9905221](#)].

BIBLIOGRAPHY

- [63] M. S. Carena, E. Ponton, J. Santiago, and C. Wagner, *Electroweak constraints on warped models with custodial symmetry*, *Phys.Rev.* **D76** (2007) 035006, [[hep-ph/0701055](#)].
- [64] A. Pomarol and F. Riva, *The Composite Higgs and Light Resonance Connection*, *JHEP* **1208** (2012) 135, [[arXiv:1205.6434](#)].
- [65] R. Grober and M. Muhlleitner, *Composite Higgs Boson Pair Production at the LHC*, *JHEP* **1106** (2011) 020, [[arXiv:1012.1562](#)].
- [66] D. Marzocca, M. Serone, and J. Shu, *General Composite Higgs Models*, *JHEP* **1208** (2012) 013, [[arXiv:1205.0770](#)].
- [67] B. Bellazzini, C. Csáki, and J. Serra, *Composite Higgses*, *Eur.Phys.J.* **C74** (2014) 2766, [[arXiv:1401.2457](#)].
- [68] **ATLAS Collaboration**, *Coupling properties of the new Higgs-like boson observed with the ATLAS detector at the LHC*, tech. rep., ATLAS-CONF-2012-127, ATLAS-COM-CONF-2012-161, 2012.
- [69] **CMS Collaboration**, S. Chatrchyan *et. al.*, *Observation of a new boson with mass near 125 GeV in pp collisions at $\sqrt{s} = 7$ and 8 TeV*, *JHEP* **1306** (2013) 081, [[arXiv:1303.4571](#)].
- [70] **ATLAS Collaboration**, *Updated coupling measurements of the Higgs boson with the ATLAS detector using up to 25 fb⁻¹ of proton-proton collision data*, tech. rep., ATLAS-CONF-2014-009, ATLAS-COM-CONF-2014-013, 2014.
- [71] **CMS Collaboration**, *Precise determination of the mass of the Higgs boson and studies of the compatibility of its couplings with the standard model*, tech. rep., CMS-PAS-HIG-14-009, 2014.
- [72] **ATLAS Collaboration**, G. Aad *et. al.*, *Measurement of the Higgs boson mass from the $H \rightarrow \gamma\gamma$ and $H \rightarrow ZZ^* \rightarrow 4\ell$ channels with the ATLAS detector using 25 fb⁻¹ of pp collision data*, [arXiv:1406.3827](#).
- [73] O. Matsedonskyi, G. Panico, and A. Wulzer, *Light Top Partners for a Light Composite Higgs*, *JHEP* **1301** (2013) 164, [[arXiv:1204.6333](#)].
- [74] M. Redi and A. Tesi, *Implications of a Light Higgs in Composite Models*, *JHEP* **1210** (2012) 166, [[arXiv:1205.0232](#)].
- [75] D. Pappadopulo, A. Thamm, and R. Torre, *A minimally tuned composite Higgs model from an extra dimension*, *JHEP* **1307** (2013) 058, [[arXiv:1303.3062](#)].
- [76] N. Arkani-Hamed, A. G. Cohen, T. Gregoire, and J. G. Wacker, *Phenomenology of electroweak symmetry breaking from theory space*, *JHEP* **0208** (2002) 020, [[hep-ph/0202089](#)].
- [77] N. Arkani-Hamed, A. Cohen, E. Katz, and A. Nelson, *The Littlest Higgs*, *JHEP* **0207** (2002) 034, [[hep-ph/0206021](#)].
- [78] M. Schmaltz and J. Thaler, *Collective Quartics and Dangerous Singlets in Little Higgs*, *JHEP* **0903** (2009) 137, [[arXiv:0812.2477](#)].
- [79] J. Kearney, A. Pierce, and J. Thaler, *Exotic Top Partners and Little Higgs*, *JHEP* **1310** (2013) 230, [[arXiv:1306.4314](#)].
- [80] D. E. Kaplan and M. Schmaltz, *The Little Higgs from a simple group*, *JHEP* **0310** (2003) 039, [[hep-ph/0302049](#)].

BIBLIOGRAPHY

- [81] M. Schmaltz, *The Simplest little Higgs*, *JHEP* **0408** (2004) 056, [[hep-ph/0407143](#)].
- [82] J. Reuter and M. Tonini, *Can the 125 GeV Higgs be the Little Higgs?*, *JHEP* **1302** (2013) 077, [[arXiv:1212.5930](#)].
- [83] M. Redi, V. Sanz, M. de Vries, and A. Weiler, *Strong Signatures of Right-Handed Compositeness*, *JHEP* **1308** (2013) 008, [[arXiv:1305.3818](#)].
- [84] C. Csaki, *TASI lectures on extra dimensions and branes*, [hep-ph/0404096](#).
- [85] R. Sundrum, *Tasi 2004 lectures: To the fifth dimension and back*, [hep-th/0508134](#).
- [86] H. Davoudiasl, S. Gopalakrishna, E. Ponton, and J. Santiago, *Warped 5-Dimensional Models: Phenomenological Status and Experimental Prospects*, *New J.Phys.* **12** (2010) 075011, [[arXiv:0908.1968](#)].
- [87] Y. Grossman and M. Neubert, *Neutrino masses and mixings in nonfactorizable geometry*, *Phys.Lett.* **B474** (2000) 361–371, [[hep-ph/9912408](#)].
- [88] T. Gherghetta and A. Pomarol, *Bulk fields and supersymmetry in a slice of AdS*, *Nucl.Phys.* **B586** (2000) 141–162, [[hep-ph/0003129](#)].
- [89] S. J. Huber and Q. Shafi, *Fermion masses, mixings and proton decay in a Randall-Sundrum model*, *Phys.Lett.* **B498** (2001) 256–262, [[hep-ph/0010195](#)].
- [90] S. J. Huber, *Flavor violation and warped geometry*, *Nucl.Phys.* **B666** (2003) 269–288, [[hep-ph/0303183](#)].
- [91] G. Cacciapaglia, C. Csaki, J. Galloway, G. Marandella, J. Terning, *et. al.*, *A GIM Mechanism from Extra Dimensions*, *JHEP* **0804** (2008) 006, [[arXiv:0709.1714](#)].
- [92] C. Delaunay, O. Gedalia, S. J. Lee, G. Perez, and E. Ponton, *Ultra Visible Warped Model from Flavor Triviality and Improved Naturalness*, *Phys.Rev.* **D83** (2011) 115003, [[arXiv:1007.0243](#)].
- [93] R. Barbieri, G. Isidori, and D. Pappadopulo, *Composite fermions in Electroweak Symmetry Breaking*, *JHEP* **0902** (2009) 029, [[arXiv:0811.2888](#)].
- [94] G. D’Ambrosio, G. Giudice, G. Isidori, and A. Strumia, *Minimal flavor violation: An Effective field theory approach*, *Nucl.Phys.* **B645** (2002) 155–187, [[hep-ph/0207036](#)].
- [95] K. Agashe, G. Perez, and A. Soni, *Flavor structure of warped extra dimension models*, *Phys.Rev.* **D71** (2005) 016002, [[hep-ph/0408134](#)].
- [96] C. Csaki, A. Falkowski, and A. Weiler, *The Flavor of the Composite Pseudo-Goldstone Higgs*, *JHEP* **0809** (2008) 008, [[arXiv:0804.1954](#)].
- [97] M. Blanke, A. J. Buras, B. Duling, S. Gori, and A. Weiler, *$\Delta F=2$ Observables and Fine-Tuning in a Warped Extra Dimension with Custodial Protection*, *JHEP* **0903** (2009) 001, [[arXiv:0809.1073](#)].
- [98] M. Bauer, S. Casagrande, U. Haisch, and M. Neubert, *Flavor Physics in the Randall-Sundrum Model: II. Tree-Level Weak-Interaction Processes*, *JHEP* **1009** (2010) 017, [[arXiv:0912.1625](#)].
- [99] R. Barbieri, D. Buttazzo, F. Sala, and D. M. Straub, *Flavour physics from an approximate $U(2)^3$ symmetry*, *JHEP* **1207** (2012) 181, [[arXiv:1203.4218](#)].
- [100] M. Redi, *Composite MFV and Beyond*, *Eur.Phys.J.* **C72** (2012) 2030, [[arXiv:1203.4220](#)].
- [101] R. Barbieri, D. Buttazzo, F. Sala, D. M. Straub, and A. Tesi, *A 125 GeV composite Higgs*

BIBLIOGRAPHY

- boson versus flavour and electroweak precision tests*, *JHEP* **1305** (2013) 069, [[arXiv:1211.5085](#)].
- [102] K. Agashe, A. Belyaev, T. Krupovnickas, G. Perez, and J. Virzi, *LHC Signals from Warped Extra Dimensions*, *Phys.Rev.* **D77** (2008) 015003, [[hep-ph/0612015](#)].
- [103] K. Agashe, H. Davoudiasl, S. Gopalakrishna, T. Han, G.-Y. Huang, *et. al.*, *LHC Signals for Warped Electroweak Neutral Gauge Bosons*, *Phys.Rev.* **D76** (2007) 115015, [[arXiv:0709.0007](#)].
- [104] B. Lillie, L. Randall, and L.-T. Wang, *The Bulk RS KK-gluon at the LHC*, *JHEP* **0709** (2007) 074, [[hep-ph/0701166](#)].
- [105] K. Agashe, S. Gopalakrishna, T. Han, G.-Y. Huang, and A. Soni, *LHC Signals for Warped Electroweak Charged Gauge Bosons*, *Phys.Rev.* **D80** (2009) 075007, [[arXiv:0810.1497](#)].
- [106] K. Agashe, A. Azatov, T. Han, Y. Li, Z.-G. Si, *et. al.*, *LHC Signals for Coset Electroweak Gauge Bosons in Warped/Composite PGB Higgs Models*, *Phys.Rev.* **D81** (2010) 096002, [[arXiv:0911.0059](#)].
- [107] **ATLAS Collaboration**, *Search for Single Production of Vector-like Quarks Coupling to Light Generations in 4.64 fb⁻¹ of Data at $\sqrt{s} = 7$ TeV*, tech. rep., ATLAS-CONF-2012-137, ATLAS-COM-CONF-2012-167, 2012.
- [108] A. Atre, M. Carena, T. Han, and J. Santiago, *Heavy Quarks Above the Top at the Tevatron*, *Phys.Rev.* **D79** (2009) 054018, [[arXiv:0806.3966](#)].
- [109] C. Delaunay, C. Grojean, and G. Perez, *Modified Higgs Physics from Composite Light Flavours*, *JHEP* **1309** (2013) 090, [[arXiv:1303.5701](#)].
- [110] A. Azatov and J. Galloway, *Light Custodians and Higgs Physics in Composite Models*, *Phys.Rev.* **D85** (2012) 055013, [[arXiv:1110.5646](#)].
- [111] A. Atre, M. Chala, and J. Santiago, *Searches for New Vector Like Quarks: Higgs Channels*, *JHEP* **1305** (2013) 099, [[arXiv:1302.0270](#)].
- [112] J. Alwall, M. Herquet, F. Maltoni, O. Mattelaer, and T. Stelzer, *MadGraph 5 : Going Beyond*, *JHEP* **1106** (2011) 128, [[arXiv:1106.0522](#)].
- [113] N. D. Christensen and C. Duhr, *FeynRules - Feynman rules made easy*, *Comput.Phys.Commun.* **180** (2009) 1614–1641, [[arXiv:0806.4194](#)].
- [114] T. Sjostrand, S. Mrenna, and P. Z. Skands, *PYTHIA 6.4 Physics and Manual*, *JHEP* **0605** (2006) 026, [[hep-ph/0603175](#)].
- [115] S. Ovnyn, X. Roubly, and V. Lemaitre, *DELPHES, a framework for fast simulation of a generic collider experiment*, [arXiv:0903.2225](#).
- [116] E. Richter-Was, D. Froidevaux, and L. Poggioli, *ATLFAST 2.0 a fast simulation package for ATLAS*, .
- [117] M. Cacciari, G. P. Salam, and G. Soyez, *The Anti-k(t) jet clustering algorithm*, *JHEP* **0804** (2008) 063, [[arXiv:0802.1189](#)].
- [118] O. Domenech, A. Pomarol, and J. Serra, *Probing the SM with Dijets at the LHC*, *Phys.Rev.* **D85** (2012) 074030, [[arXiv:1201.6510](#)].
- [119] **ATLAS Collaboration**, G. Aad *et. al.*, *ATLAS search for new phenomena in dijet mass and angular distributions using pp collisions at $\sqrt{s} = 7$ TeV*, *JHEP* **1301** (2013) 029,

BIBLIOGRAPHY

- [arXiv:1210.1718].
- [120] **CMS Collaboration**, S. Chatrchyan *et. al.*, *Search for quark compositeness in dijet angular distributions from pp collisions at $\sqrt{s} = 7$ TeV*, *JHEP* **1205** (2012) 055, [arXiv:1202.5535].
- [121] **ATLAS Collaboration**, *Search for New Phenomena in the Dijet Mass Distribution updated using 13.0 fb^{-1} of pp Collisions at $\sqrt{s} = 8$ TeV collected by the ATLAS Detector*, tech. rep., ATLAS-CONF-2012-148, ATLAS-COM-CONF-2012-180, 2012.
- [122] **CMS Collaboration**, *Search for Narrow Resonances using the Dijet Mass Spectrum in pp Collisions at \sqrt{s} of 8 TeV*, tech. rep., CMS-PAS-EXO-12-016, 2012.
- [123] **CMS Collaboration**, *Search for Narrow Resonances using the Dijet Mass Spectrum with 19.6 fb^{-1} of pp Collisions at $\sqrt{s} = 8$ TeV*, tech. rep., CMS-PAS-EXO-12-059, 2013.
- [124] **ATLAS Collaboration**, *A search for $t\bar{t}$ resonances in the lepton plus jets final state using 4.66 fb^{-1} of pp collisions at $\sqrt{s} = 7$ TeV*, tech. rep., ATLAS-CONF-2012-136, ATLAS-COM-CONF-2012-174, 2012.
- [125] **CMS Collaboration**, S. Chatrchyan *et. al.*, *Search for anomalous t t -bar production in the highly-boosted all-hadronic final state*, *JHEP* **1209** (2012) 029, [arXiv:1204.2488].
- [126] R. Contino and G. Servant, *Discovering the top partners at the LHC using same-sign dilepton final states*, *JHEP* **0806** (2008) 026, [arXiv:0801.1679].
- [127] **ATLAS Collaboration**, *Search for heavy top-like quarks decaying to a Higgs boson and a top quark in the lepton plus jets final state in pp collisions at $\sqrt{s} = 8$ TeV with the ATLAS detector*, tech. rep., ATLAS-CONF-2013-018, ATLAS-COM-CONF-2013-024, 2013.
- [128] J. Mrazek and A. Wulzer, *A Strong Sector at the LHC: Top Partners in Same-Sign Dileptons*, *Phys.Rev.* **D81** (2010) 075006, [arXiv:0909.3977].
- [129] J. Aguilar-Saavedra, *Identifying top partners at LHC*, *JHEP* **0911** (2009) 030, [arXiv:0907.3155].
- [130] A. Atre, G. Azuelos, M. Carena, T. Han, E. Ozcan, *et. al.*, *Model-Independent Searches for New Quarks at the LHC*, *JHEP* **1108** (2011) 080, [arXiv:1102.1987].
- [131] A. Martin and V. Sanz, *Mass-Matching in Higgsless*, *JHEP* **1001** (2010) 075, [arXiv:0907.3931].
- [132] J. Hirn, A. Martin, and V. Sanz, *Benchmarks for new strong interactions at the LHC*, *JHEP* **0805** (2008) 084, [arXiv:0712.3783].
- [133] **LHC New Physics Working Group**, D. Alves *et. al.*, *Simplified Models for LHC New Physics Searches*, *J.Phys.* **G39** (2012) 105005, [arXiv:1105.2838].
- [134] A. Carmona, M. Chala, and J. Santiago, *New Higgs Production Mechanism in Composite Higgs Models*, *JHEP* **1207** (2012) 049, [arXiv:1205.2378].
- [135] G. Panico, M. Redi, A. Tesi, and A. Wulzer, *On the Tuning and the Mass of the Composite Higgs*, *JHEP* **1303** (2013) 051, [arXiv:1210.7114].
- [136] **ATLAS Collaboration**, G. Aad *et. al.*, *Search for Massive Colored Scalars in Four-Jet Final States in $\sqrt{s} = 7$ TeV proton-proton collisions with the ATLAS Detector*, *Eur.Phys.J.* **C71** (2011) 1828, [arXiv:1110.2693].
- [137] **ATLAS Collaboration**, G. Aad *et. al.*, *Search for pair-produced massive coloured scalars in four-jet final states with the ATLAS detector in proton-proton collisions at $\sqrt{s} = 7$ TeV*,

BIBLIOGRAPHY

- Eur.Phys.J.* **C73** (2013) 2263, [[arXiv:1210.4826](#)].
- [138] **CMS Collaboration**, *Search for New Physics in the Paired Dijet Mass Spectrum*, tech. rep., CMS-PAS-EXO-11-016, 2012.
- [139] **CMS Collaboration**, S. Chatrchyan *et. al.*, *Search for three-jet resonances in pp collisions at $\sqrt{s} = 7$ TeV*, *Phys.Lett.* **B718** (2012) 329–347, [[arXiv:1208.2931](#)].
- [140] M. L. Mangano, M. Moretti, and R. Pittau, *Multijet matrix elements and shower evolution in hadronic collisions: $Wb\bar{b} + n$ jets as a case study*, *Nucl.Phys.* **B632** (2002) 343–362, [[hep-ph/0108069](#)].
- [141] M. L. Mangano, M. Moretti, F. Piccinini, R. Pittau, and A. D. Polosa, *ALPGEN, a generator for hard multiparton processes in hadronic collisions*, *JHEP* **0307** (2003) 001, [[hep-ph/0206293](#)].
- [142] J. Reuter, M. Tonini, and M. de Vries, *Littlest Higgs with T-parity: Status and Prospects*, [[arXiv:1310.2918](#)].
- [143] J. Reuter, M. Tonini, and M. de Vries, *Little Higgs Model Limits from LHC - Input for Snowmass 2013*, [[arXiv:1307.5010](#)].
- [144] I. Low, W. Skiba, and D. Tucker-Smith, *Little Higgses from an antisymmetric condensate*, *Phys.Rev.* **D66** (2002) 072001, [[hep-ph/0207243](#)].
- [145] D. Pappadopulo and A. Vichi, *T-parity, its problems and their solution*, *JHEP* **1103** (2011) 072, [[arXiv:1007.4807](#)].
- [146] M. Schmaltz, D. Stolarski, and J. Thaler, *The Bestest Little Higgs*, *JHEP* **1009** (2010) 018, [[arXiv:1006.1356](#)].
- [147] T. A. W. Martin and A. de la Puente, *Darkening the Little Higgs*, [[arXiv:1304.7835](#)].
- [148] W. Kilian, D. Rainwater, and J. Reuter, *Pseudo-axions in little Higgs models*, *Phys.Rev.* **D71** (2005) 015008, [[hep-ph/0411213](#)].
- [149] W. Kilian, D. Rainwater, and J. Reuter, *Distinguishing little-Higgs product and simple group models at the LHC and ILC*, *Phys.Rev.* **D74** (2006) 095003, [[hep-ph/0609119](#)].
- [150] C. Csaki, J. Hubisz, G. D. Kribs, P. Meade, and J. Terning, *Big corrections from a little Higgs*, *Phys.Rev.* **D67** (2003) 115002, [[hep-ph/0211124](#)].
- [151] J. L. Hewett, F. J. Petriello, and T. G. Rizzo, *Constraining the littlest Higgs*, *JHEP* **0310** (2003) 062, [[hep-ph/0211218](#)].
- [152] W. Kilian and J. Reuter, *The Low-energy structure of little Higgs models*, *Phys.Rev.* **D70** (2004) 015004, [[hep-ph/0311095](#)].
- [153] T. Han, H. E. Logan, B. McElrath, and L.-T. Wang, *Phenomenology of the little Higgs model*, *Phys.Rev.* **D67** (2003) 095004, [[hep-ph/0301040](#)].
- [154] J. Hubisz and P. Meade, *Phenomenology of the littlest Higgs with T-parity*, *Phys.Rev.* **D71** (2005) 035016, [[hep-ph/0411264](#)].
- [155] M. Blanke, A. J. Buras, A. Poschenrieder, S. Recksiegel, C. Tarantino, *et. al.*, *Rare and CP-Violating K and B Decays in the Littlest Higgs Model with T⁻ Parity*, *JHEP* **0701** (2007) 066, [[hep-ph/0610298](#)].
- [156] A. Belyaev, C.-R. Chen, K. Tobe, and C.-P. Yuan, *Phenomenology of littlest Higgs model with T⁻ parity: including effects of T⁻ odd fermions*, *Phys.Rev.* **D74** (2006) 115020,

BIBLIOGRAPHY

- [hep-ph/0609179].
- [157] C.-R. Chen, K. Tobe, and C.-P. Yuan, *Higgs boson production and decay in little Higgs models with T-parity*, *Phys.Lett.* **B640** (2006) 263–271, [hep-ph/0602211].
- [158] J. Hubisz, P. Meade, A. Noble, and M. Perelstein, *Electroweak precision constraints on the lightest Higgs model with T parity*, *JHEP* **0601** (2006) 135, [hep-ph/0506042].
- [159] M. Asano, S. Matsumoto, N. Okada, and Y. Okada, *Cosmic positron signature from dark matter in the lightest Higgs model with T-parity*, *Phys.Rev.* **D75** (2007) 063506, [hep-ph/0602157].
- [160] L. Wang, J. M. Yang, and J. Zhu, *Dark matter in little Higgs model under current experimental constraints from LHC, Planck and Xenon*, [arXiv:1307.7780](#).
- [161] S. R. Coleman and E. J. Weinberg, *Radiative Corrections as the Origin of Spontaneous Symmetry Breaking*, *Phys.Rev.* **D7** (1973) 1888–1910.
- [162] J. Hubisz, S. J. Lee, and G. Paz, *The Flavor of a little Higgs with T-parity*, *JHEP* **0606** (2006) 041, [hep-ph/0512169].
- [163] **ATLAS Collaboration**, G. Aad *et. al.*, *Searches for heavy long-lived sleptons and R-Hadrons with the ATLAS detector in pp collisions at $\sqrt{s} = 7$ TeV*, *Phys.Lett.* **B720** (2013) 277–308, [arXiv:1211.1597].
- [164] R. Barbier, C. Berat, M. Besancon, M. Chemtob, A. Deandrea, *et. al.*, *R-parity violating supersymmetry*, *Phys.Rept.* **420** (2005) 1–202, [hep-ph/0406039].
- [165] J. Berger, J. Hubisz, and M. Perelstein, *A Fermionic Top Partner: Naturalness and the LHC*, *JHEP* **1207** (2012) 016, [arXiv:1205.0013].
- [166] **Particle Data Group**, J. Beringer *et. al.*, *Review of Particle Physics (RPP)*, *Phys.Rev.* **D86** (2012) 010001.
- [167] A. Azatov and J. Galloway, *Electroweak Symmetry Breaking and the Higgs Boson: Confronting Theories at Colliders*, *Int.J.Mod.Phys.* **A28** (2013) 1330004, [arXiv:1212.1380].
- [168] C. Degrande, C. Duhr, B. Fuks, D. Grellscheid, O. Mattelaer, *et. al.*, *UFO - The Universal FeynRules Output*, *Comput.Phys.Commun.* **183** (2012) 1201–1214, [arXiv:1108.2040].
- [169] W. Kilian, T. Ohl, and J. Reuter, *WHIZARD: Simulating Multi-Particle Processes at LHC and ILC*, *Eur.Phys.J.* **C71** (2011) 1742, [arXiv:0708.4233].
- [170] M. Moretti, T. Ohl, and J. Reuter, *O’Mega: An Optimizing matrix element generator*, [hep-ph/0102195](#).
- [171] N. D. Christensen, C. Duhr, B. Fuks, J. Reuter, and C. Speckner, *Introducing an interface between WHIZARD and FeynRules*, *Eur.Phys.J.* **C72** (2012) 1990, [arXiv:1010.3251].
- [172] J. de Favereau, C. Delaere, P. Demin, A. Giammanco, V. Lemaître, *et. al.*, *DELPHES 3, A modular framework for fast simulation of a generic collider experiment*, [arXiv:1307.6346](#).
- [173] **ATLAS Collaboration**, *Search for New Phenomena in Monojet plus Missing Transverse Momentum Final States using 10 fb^{-1} of pp Collisions at $\sqrt{s} = 8$ TeV with the ATLAS detector at the LHC*, tech. rep., ATLAS-CONF-2012-147, 2012.
- [174] **CMS Collaboration**, *Search for new physics in monojet events in pp collisions at $\sqrt{s} = 8$ TeV*, tech. rep., CMS-PAS-EXO-12-048.

BIBLIOGRAPHY

- [175] M. S. Carena, J. Hubisz, M. Perelstein, and P. Verdier, *Collider signature of T-quarks*, *Phys.Rev.* **D75** (2007) 091701, [[hep-ph/0610156](#)].
- [176] M. Perelstein and J. Shao, *T-Quarks at the Large Hadron Collider: 2010-12*, *Phys.Lett.* **B704** (2011) 510–514, [[arXiv:1103.3014](#)].
- [177] **ATLAS Collaboration**, *Search for squarks and gluinos with the ATLAS detector in final states with jets and missing transverse momentum and 20.3 fb⁻¹ of $\sqrt{s} = 8$ TeV proton-proton collision data*, tech. rep., ATLAS-CONF-2013-047, 2013.
- [178] **ATLAS Collaboration**, *Search for direct production of the top squark in the all-hadronic $t\bar{t}b\bar{a}r + e\text{miss}$ final state in 21 fb⁻¹ of pp collisions at $\sqrt{s} = 8$ TeV with the ATLAS detector*, tech. rep., ATLAS-CONF-2013-024, 2013.
- [179] **CMS Collaboration**, S. Chatrchyan *et. al.*, *Search for supersymmetry in hadronic final states with missing transverse energy using the variables α_T and b-quark multiplicity in pp collisions at $\sqrt{s} = 8$ TeV*, [arXiv:1303.2985](#).
- [180] **ATLAS Collaboration**, *Search for supersymmetry at $\sqrt{s} = 8$ TeV in final states with jets, missing transverse momentum and one isolated lepton*, tech. rep., ATLAS-CONF-2012-104, 2012.
- [181] **ATLAS Collaboration**, *Search for direct top squark pair production in final states with one isolated lepton, jets, and missing transverse momentum in $\sqrt{s} = 8$ TeV pp collisions using 13 fb⁻¹ of ATLAS data*, tech. rep., ATLAS-CONF-2012-166, 2012.
- [182] **ATLAS Collaboration**, *Search for direct top squark pair production in final states with one isolated lepton, jets, and missing transverse momentum in $\sqrt{s} = 8$ TeV pp collisions using 21 fb⁻¹ of ATLAS data*, tech. rep., ATLAS-CONF-2013-037, 2013.
- [183] **ATLAS Collaboration**, *Search for strongly produced superpartners in final states with two same sign leptons with the ATLAS detector using 21 fb⁻¹ of proton-proton collisions at $\sqrt{s} = 8$ TeV.*, tech. rep., ATLAS-CONF-2013-007, 2013.
- [184] **CMS Collaboration**, S. Chatrchyan *et. al.*, *Search for new physics in events with same-sign dileptons and b jets in pp collisions at $\sqrt{s} = 8$ TeV*, *JHEP* **1303** (2013) 037, [[arXiv:1212.6194](#)].
- [185] G. Cowan, K. Cranmer, E. Gross, and O. Vitells, *Asymptotic formulae for likelihood-based tests of new physics*, *Eur.Phys.J.* **C71** (2011) 1554, [[arXiv:1007.1727](#)].
- [186] D. Choudhury, D. K. Ghosh, and S. K. Rai, *Dijet Signals of the Little Higgs Model with T-Parity*, *JHEP* **1207** (2012) 013, [[arXiv:1202.4213](#)].
- [187] **ATLAS Collaboration**, G. Aad *et. al.*, *Search for contact interactions and large extra dimensions in the dilepton channel using proton-proton collisions at $\sqrt{s} = 8$ TeV with the ATLAS detector*, [arXiv:1407.2410](#).
- [188] **CMS Collaboration**, *Search for Contact Interactions in Dilepton Mass Spectra in pp Collisions at $\sqrt{s} = 8$ TeV*, tech. rep., CMS-PAS-EXO-12-020, 2014.
- [189] M. de Vries, *Four-Quark Effective Operators at Hadron Colliders*, [arXiv:1409.4657](#).
- [190] **ATLAS Collaboration**, G. Aad *et. al.*, *Search for Quark Contact Interactions in Dijet Angular Distributions in pp Collisions at $\sqrt{s} = 7$ TeV Measured with the ATLAS Detector*, *Phys.Lett.* **B694** (2011) 327–345, [[arXiv:1009.5069](#)].
- [191] **ATLAS Collaboration**, G. Aad *et. al.*, *Search for New Physics in Dijet Mass and Angular*

BIBLIOGRAPHY

- Distributions in pp Collisions at $\sqrt{s} = 7$ TeV Measured with the ATLAS Detector*, *New J.Phys.* **13** (2011) 053044, [[arXiv:1103.3864](#)].
- [192] **CMS Collaboration**, V. Khachatryan *et. al.*, *Search for Quark Compositeness with the Dijet Centrality Ratio in pp Collisions at $\sqrt{s} = 7$ TeV*, *Phys.Rev.Lett.* **105** (2010) 262001, [[arXiv:1010.4439](#)].
- [193] **CMS Collaboration**, V. Khachatryan *et. al.*, *Measurement of Dijet Angular Distributions and Search for Quark Compositeness in pp Collisions at $\sqrt{s} = 7$ TeV*, *Phys.Rev.Lett.* **106** (2011) 201804, [[arXiv:1102.2020](#)].
- [194] **CMS Collaboration**, S. Chatrchyan *et. al.*, *Search for contact interactions using the inclusive jet p_T spectrum in pp collisions at $\sqrt{s} = 7$ TeV*, *Phys.Rev.* **D87** (2013), no. 5 052017, [[arXiv:1301.5023](#)].
- [195] W. Buchmüller and D. Wyler, *Effective Lagrangian Analysis of New Interactions and Flavor Conservation*, *Nucl.Phys.* **B268** (1986) 621–653.
- [196] B. Grzadkowski, M. Iskrzyński, M. Misiak, and J. Rosiek, *Dimension-Six Terms in the Standard Model Lagrangian*, *JHEP* **1010** (2010) 085, [[arXiv:1008.4884](#)].
- [197] A. J. Buras, F. De Fazio, and J. Girrbach, *$\Delta I = 1/2$ rule, ε'/ε and $K \rightarrow \pi\nu\bar{\nu}$ in $Z'(Z)$ and G' models with FCNC quark couplings*, *Eur.Phys.J.* **C74** (2014) 2950, [[arXiv:1404.3824](#)].
- [198] J. Aguilar-Saavedra, D. Amidei, A. Juste, and M. Perez-Victoria, *Asymmetries in top quark pair production*, [arXiv:1406.1798](#).
- [199] S. Jung, P. Ko, Y. W. Yoon, and C. Yu, *Correlation of top asymmetries: loop versus tree origins*, [arXiv:1405.5313](#).
- [200] G. Busoni, A. De Simone, E. Morgante, and A. Riotto, *On the Validity of the Effective Field Theory for Dark Matter Searches at the LHC*, *Phys.Lett.* **B728** (2014) 412–421, [[arXiv:1307.2253](#)].
- [201] G. Busoni, A. De Simone, J. Gramling, E. Morgante, and A. Riotto, *On the Validity of the Effective Field Theory for Dark Matter Searches at the LHC, Part II: Complete Analysis for the s-channel*, [arXiv:1402.1275](#).
- [202] G. Busoni, A. De Simone, T. Jacques, E. Morgante, and A. Riotto, *On the Validity of the Effective Field Theory for Dark Matter Searches at the LHC Part III: Analysis for the t-channel*, [arXiv:1405.3101](#).
- [203] O. Buchmueller, M. J. Dolan, and C. McCabe, *Beyond Effective Field Theory for Dark Matter Searches at the LHC*, *JHEP* **1401** (2014) 025, [[arXiv:1308.6799](#)].
- [204] H. An, L.-T. Wang, and H. Zhang, *Dark matter with t-channel mediator: a simple step beyond contact interaction*, *Phys.Rev.* **D89** (2014) 115014, [[arXiv:1308.0592](#)].
- [205] M. Papucci, A. Vichi, and K. M. Zurek, *Monojet versus rest of the world I: t-channel Models*, [arXiv:1402.2285](#).
- [206] O. Buchmueller, M. J. Dolan, S. A. Malik, and C. McCabe, *Characterising dark matter searches at colliders and direct detection experiments: Vector mediators*, [arXiv:1407.8257](#).
- [207] C. Englert and M. Spannowsky, *Effective Theories and Measurements at Colliders*, [arXiv:1408.5147](#).
- [208] A. Biekötter, A. Knochel, M. Kraemer, D. Liu, and F. Riva, *Vices and Virtues of Higgs EFTs at Large Energy*, [arXiv:1406.7320](#).

BIBLIOGRAPHY

- [209] B. A. Dobrescu and F. Yu, *Coupling-mass mapping of dijet peak searches*, *Phys.Rev.* **D88** (2013), no. 3 035021, [[arXiv:1306.2629](#)].
- [210] G. D. La Rochelle and M. Elmer, *Heavy Z': resonant versus non-resonant searches*, [arXiv:1406.2547](#).
- [211] G. Choudalakis, *On hypothesis testing, trials factor, hypertests and the BumpHunter*, [arXiv:1101.0390](#).
- [212] Creative Commons, "Creative Commons Attribution-ShareAlike 4.0 International (CC BY-SA 4.0)." <http://creativecommons.org/licenses/by-sa/4.0/>. Accessed: 10-09-2014.
- [213] A. Martin, W. Stirling, R. Thorne, and G. Watt, *Parton distributions for the LHC*, *Eur.Phys.J.* **C63** (2009) 189–285, [[arXiv:0901.0002](#)].
- [214] **ATLAS Collaboration**, *Search for the Standard Model Higgs boson produced in association with a vector boson and decaying to bottom quarks with the ATLAS detector*, tech. rep., ATLAS-CONF-2012-161, 2012.
- [215] **ATLAS Collaboration**, *Search for the Standard Model Higgs boson produced in association with top quarks in proton-proton collisions at $\sqrt{s} = 7$ using the ATLAS detector*, tech. rep., ATLAS-CONF-2012-135, 2012.
- [216] **ATLAS Collaboration**, *Search for the Standard Model Higgs boson in $H \rightarrow \tau\tau$ decays in proton-proton collisions with the ATLAS detector*, tech. rep., ATLAS-CONF-2012-160, 2012.
- [217] **ATLAS Collaboration**, *Measurements of the properties of the Higgs-like boson in the $WW^{(*)} \rightarrow \ell\nu\ell\nu$ decay channel with the ATLAS detector using 25 fb^{-1} of proton-proton collision data*, tech. rep., ATLAS-CONF-2013-030, 2013.
- [218] **ATLAS Collaboration**, *Measurements of the properties of the Higgs-like boson in the four lepton decay channel with the ATLAS detector using 25 fb^{-1} of proton-proton collision data*, tech. rep., ATLAS-CONF-2013-013, 2013.
- [219] **ATLAS Collaboration**, *Observation of an excess of events in the search for the Standard Model Higgs boson in the gamma-gamma channel with the ATLAS detector*, tech. rep., ATLAS-CONF-2012-091, 2012.
- [220] **ATLAS Collaboration**, *Measurements of the properties of the Higgs-like boson in the two photon decay channel with the ATLAS detector using 25 fb^{-1} of proton-proton collision data*, tech. rep., ATLAS-CONF-2013-012, 2013.
- [221] **CMS Collaboration**, *Search for the standard model Higgs boson produced in vector boson fusion, and decaying to bottom quarks*, tech. rep., CMS-PAS-HIG-13-011, 2013.
- [222] **CMS Collaboration**, *Search for the standard model Higgs boson produced in association with W or Z bosons, and decaying to bottom quarks*, tech. rep., CMS-PAS-HIG-13-012, 2013.
- [223] **CMS Collaboration**, *Search for Higgs boson production in association with top quark pairs in pp collisions*, tech. rep., CMS-PAS-HIG-12-025, 2012.
- [224] **CMS Collaboration**, *Search for the Standard-Model Higgs boson decaying to tau pairs in proton-proton collisions at $\sqrt{s} = 7$ and 8 TeV*, tech. rep., CMS-PAS-HIG-13-004.
- [225] **CMS Collaboration**, *Evidence for a particle decaying to W^+W^- in the fully leptonic final state in a standard model Higgs boson search in pp collisions at the LHC*, tech. rep., CMS-PAS-HIG-13-003.

BIBLIOGRAPHY

- [226] **CMS Collaboration**, *Properties of the Higgs-like boson in the decay H to ZZ to $4l$ in pp collisions at $\sqrt{s} = 7$ and 8 TeV*, tech. rep., CMS-PAS-HIG-13-002.
- [227] **CMS Collaboration**, *Updated measurements of the Higgs boson at 125 GeV in the two photon decay channel*, tech. rep., CMS-PAS-HIG-13-001.
- [228] G. Gounaris and J. Sakurai, *Finite width corrections to the vector meson dominance prediction for $\rho \rightarrow e^+e^-$* , *Phys.Rev.Lett.* **21** (1968) 244–247.
- [229] J. H. Kühn and A. Santamaria, *Tau decays to pions*, *Z.Phys.* **C48** (1990) 445–452.
- [230] E. Eichten, I. Hinchliffe, K. D. Lane, and C. Quigg, *Super Collider Physics*, *Rev.Mod.Phys.* **56** (1984) 579–707.
- [231] S. Davidson and S. Descotes-Genon, *Constraining flavoured contact interactions at the LHC*, [arXiv:1311.5981](https://arxiv.org/abs/1311.5981).